Unité de formation et d'Enseignement

Imagerie des exoplanètes : du système optique à la fréquence des géantes gazeuses

présentée et soutenue publiquement le 18 décembre 2020

pour l'obtention d'une

Habilitation à diriger des recherches

par

Raphaël Galicher

Composition du jury

Président :	Daniel Rouan	Observatoire de Paris-PSL
Rapporteurs :	Magali Deleuil	Université Aix-Marseille
	Dimitri Mawet	California institute of technology
	Rémi Soummer	Space telescope science institute
Examinateurs :	Marc Ferrari	Université Aix-Marseille
	Anne-Marie Lagrange	Université Grenoble Alpes

Laboratoire d'Études Spatiales et d'Instrumentation en Astrophysique — UMR 8109

Mis en page avec la classe thloria.

Remerciements

Paragraphe compliqué à écrire que celui des remerciements. Non pas que j'ai du mal à remercier mais parce qu'à l'aube de mes quarante ans, je suis sûr d'oublier certaines personnes qui font que j'écris ce document.

Un livre ne suffirait pas à lister les raisons pour lesquelles je les remercies alors je me contente d'une seule phrase : merci du fond du cœur à mes parents qui m'ont appris à être curieux, à chercher à comprendre et, quand j'y arrive, à m'adapter à la situation. Ce sont trois forces essentielles quand on exerce le métier d'enseignant-chercheur.

Un grand merci à Pierre-Marie, Jean-Baptiste et Antoine-Laurent qui, me croisant au hasard d'un couloir du lycée Masséna à Nice, m'ont suggéré de venir faire une prépa avec eux plutôt que des études de STAPS. Je me serais certainement épanoui en tant que professeur d'EPS mais le sort en a décidé autrement.

Je remercie toutes les personnes que j'ai eu la chance de rencontrer depuis mon premier pas dans le monde de l'astronomie professionnelle en 2002, à l'Observatoire de la Côte d'Azur, dans les observatoires hawaiiens, en Île-de-France pendant le master, à l'institut d'astrophysique Herzberg, au VLT, sur le mont Palomar, dans les consortia GPI et Sphere, etc. Échanger avec des collègues aux quatre coins de la planète est une véritable richesse. Et ils ont tous influencé à leur manière ce manuscrit.

Depuis que j'ai gravi la côte de Meudon pour la première fois en 2005 (en rollers s'il-vous-plaît), mon chemin a croisé à l'Observatoire de Paris celui de plusieurs belles personnes qui m'ont offert des bouts d'elles tant sur le plan scientifique qu'humain. Il y a les enseignants et les amis du M2 A&A de 2005, les collègues des DU ECU/SU, ceux qui ont partagé les missions au Bénin et au Gabon, et les administratifs dont le travail, indispensable à nos projets de recherche, est souvent oublié. Merci à vous tous !

Je remercie spécialement l'équipe très haute dynamique du Lesia avec qui j'ai la chance de pouvoir travailler sérieusement, rigoureusement et, dans la bonne humeur. C'est un plaisir de mener des études à vos côtés. Merci à Elsa, Anthony, Johan, Olivier, Simone, tous les ingénieurs, et tous les étudiants qui travaillent avec nous, de la licence à la thèse en passant par les écoles ingénieurs et les apprentis.

Enfin, le mot merci est trop petit pour exprimer ma reconnaissance envers Pierre. Déjà quinze ans que nous nous sommes rencontrés pour la première fois. J'ai l'impression que c'était hier. Travailler à ses côtés et discuter de tout et de rien avec lui m'enrichit chaque jour un peu plus. Pierre, merci pour tout !

À mes parents,
à ma soeur,

Table des matières

Partie III Note d'accompagnement

Annexes

Première partie

Curriculum vitæ

Raphaël Galicher

Born on 1981, no children, Associate Professor (Maître de Conférences) University of Paris, LESIA, UMR8109

Research

Responsabilities

Since 2020 **SPHERE+/VLT**, *co-I*, upgrade of the SPHERE+ instrument for exoplanet imaging.

Since 2012 **THD2 bench**, *co-PI (∼ 10 persons)*, laboratory R&D for high contrast imaging, comparing, associating and optimizing very high contrast imaging techniques for the exoplanet imagers of future telescopes (space, balloon, and ground).

2012 – 2016 **Sphere/VLT pipeline**, *co-leader*, development of the automatic pipeline to reduce all IRDIS/IFS data of the SPHERE 5 year survey: astrometry, spectro-photometry of exoplanets.

Instrumentation

Since 2010 **Broadband coronagraphy**, development of broadband phase and amplitude masks.

Since 2006 **Wavefront control high contrast imaging**, from lab to current instruments like SPHERE.

2013 – 2016 **Broadband wavefront sensing**, development of a focal plane wavefront sensor.

2010 – 2012 **Gemini Planet imager**, detector linearity, wavefront control for coronagraphy.

2009 – 2010 **Spices mission**, optical design and science cases for a mission proposed to ESA.

Astrophysics

Since 2014 **Exoplanetary systems**, astrometry and spectro-photometry of giant exoplanets and brown dwarfs orbiting HR 8799, Fomalhaut, HD 95086, etc ; and disk imaging.

2012 – 2018 **Occurrence of giant exoplanets**, 14-year survey (Keck, Gemini Nord et Sud, HST, VLT) to determine the giant planet frequency.

Teaching: courses

Responsabilities

Since 2019 **Mechanics, optics, electronics**, *Licence 1*, lecture, lab, ∼ 190 students/year.

Since 2014 **Optics**, *Engineering School 1st year*, lecture, tutorial, lab, ∼ 20 students/year.

2014 – 2019 **Wave and vibration**, *Licence 2*, lab, ∼ 150 students/year.

2014 – 2016 **Exoplanet science**, *Master 1*, Lecture, ∼ 20 students/year.

Participation

Since 2017 **Personal and professional project**, *Engineering School 1st year*, ∼ 60 students/year.

Since 2018 **Signal Processing**, *Engineering School 1st year*, lab, ∼ 30 students/year.

2018 – 2019 **Mechanics**, *Licence 1*, tutorial, ∼ 30 students/year.

2017 – 2018 **Electronics**, *Engineering School 1st year*, lab, ∼ 30 students/year.

2014 – 2018 **Flux in Physics**, *Licence 2*, tutorial, lab, ∼ 30 students/year.

2012 – 2017 **High angular resolution**, *Master 2*, lab, ∼ 15 students/year.

2012 – 2014 **Simple and coupled harmonic oscillators**, *Licence 3*, tutorial, lab, ∼ 30 students/year.

2012 – 2014 **Optics**, *Licence 3*, tutorial, lab, ∼ 30 students/year.

2008 – 2010 **Astronomy and astrophysics**, *University degree*, Lecture, ∼ 60 students/year.

2006 – 2009 **Sound and vibration**, *Licence 3*, tutorial, lab, ∼ 30 students/year.

2006 – 2009 **Optics**, *Licence 3*, tutorial, lab, ∼ 30 students/year.

Observatoire de Paris, 5, place Jules Janssen – 92195 Meudon France
+33695344395 • ☎ +33145077583 • ✉ *raphael.galicher at obspm.fr*

Administrative responsabilities

Since 2020 **Nominated member of the education council**, Physics department, University of Paris.

Since 2020 **Course allocation**, allocating $\sim 14{,}000$ hours over ~ 160 teachers and temporary workers.

Since 2020 **Nominated member of the scientific council**, Paris Observatory.

Since 2019 **Elected substitute member of the council of University**, CNU section 34.

Since 2018 **Elected member of the laboratory council**, LESIA department, Paris Observatory.

Since 2015 **Elected member of the council of the Physics department**, University of Paris.

2013 – 2018 **Elected member of the laboratory council**, LESIA department, Paris Observatory.

2006 – 2008 **Student representative**, Doctorale School of Astronomy and Astrophysics (ED127).

Committees

Since 2016 **Engineering projects**, *EIDD (2nd/3rd years)*, ∼2 defenses per year.

2020 **ATER Selection committee**, *Université de Paris*, Physics department.

2020 **ATER Selection committee**, *Observatoire de Paris*

2020 **PhD thesis**, *Université PSL*, A. Potier.

2018 **PhD thesis**, *Onera*, O. Herscovici-Schiller.

2017 **PhD thesis**, *Observatoire de la Côte d'Azur*, M. Beaulieu.

2016 **PhD thesis**, *Université Denis Diderot*, J.-R. Delorme.

2011 **Science projects**, *Univ. of Victoria, Canada (<12th grade students)*, ~ 20 defenses.

2010 **Projects in Astrophysics**, *Observatoire de Paris (L2)*, ∼20 defenses.

Public outreach

Conferences

Since 2006 **Festival of Science**, *University of Paris, Paris Observatory, Palais de la découverte.*

Since 2014 **Main à la pâte**, *<9th grade*, Discovering spectrometry from experiments, exoplanets.

2014 **Observatory of Côte d'Azur**, Exoplanet HD 95086b.

2014 **Institut d'optique**, *Astronomy club*, High contrast imaging and exoplanet science.

2013 **Science ouverte**, *science camp for undergraduate students*, Models in Physics.

Videos and interviews

2018 **Exoplanète: observez-les toutes**, Radio-program La Méthode Scientifique, France Culture.

2017 **Expedition Earth**, Interview at VLT/Chili, BBC and France 5.

2016 **What is teaching?**, Filming Physics Lab at the University Denis Diderot.

2014 **"There are planets everywhere"**, Video "Explore and Understand the Univers".

2012 **"How to become an astrophysicist?"**, Okapi interview for undergraduate students.

2009 **What is being an astrophysicist?**, Onisep interview for undergraduate students.

Projects in Africa

2013 **Solar eclipse, Gabon**, Conferences & observations in schools and public places.

2006 – 2015 **Eclipses, Benin**, conferences & observations in schools and public places, helping one astronomy club for school education, creation of a library in Savalou (sending books/computers).

Others

2020 **Consulting**, Interview by a writer of hard-SF about exoplanets.

Since 2006 **Consulting**, *<9th grade teachers*, Astrophysics projets and visits of the Paris Observatory.

Since 2006 **Presenting current researches**, Undergraduate and graduating students visiting LESIA.

2018 **National workshop**, consulting at the French science academy for the European project Learning from Innovation and Networking in STEM (LINKS) with *La main à la pâte*.

2015 **Consulting**, Interview by a film-maker about teaching at the university.

Supervision

Post-doctorate

Since 2019 **Supervisor**, *L. Leboulleux*, Speed up AO numerical simulation, SPHERE+ preparation.
Since 2018 **Co-supervisor**, *G. Singh*, Focal plane wavefront sensing for ground telescopes.
2016 – 2018 **Co-supervisor**, *T. Schmidt*, Exoplanet & circumstellar disk imaging with SPHERE/VLT.
2016 – 2018 **Co-supervisor**, *F. Patru*, Optimizing coronagraph fabrication.

PhD thesis

2017 – 2020 **Co-supervisor**, *A. Potier*, Université PSL, Comparison of imaging technics and applications.
2019 (2 months) **Co-supervisor**, *B. Gerard*, Univ. of Victoria, Lab demonstration for Gemini Planet Imager.
2015 – 2018 **Co-supervisor**, *C. de Jonge*, SRON, Active correction of chromatic aberrations.
2013 – 2016 **Supervisor**, *J.-R. Delorme*, Univ. Denis Diderot, Coronagraphy and wavefront sensing.

Engineering project

2016 (6 months) **Supervisor**, *A. Capomassi & B. Steir*, Engineering School of University Denis Diderot (EIDD, 3rd year), Optical simulation of atmospheric turbulence on the THD2 bench.
2016 (3 months) **Supervisor**, *Z. Bouharras*, EIDD (2nd year), Polarization & coronagraphy in lab.
2007 (6 months) **Co-supervisor**, *J. Totems*, Institut d'Optique Graduate School (2nd year).

Master 2

2020 (5 months) **Co-supervisor**, *C. Desgrange*, Observatoire de Paris, Polarization in high contrast imaging.
2020 (6 months) **Supervisor**, *R. Dubroeucq*, INSA Rennes, High contrast imaging at low signal-to-noise ratio.
2019 (4 months) **Co-upervisor**, *C. Lopez*, Sorbonne Université, High contast imaging in broadband.
2013 (4 months) **Supervisor**, *J.-R. Delorme*, Univ. Denis Diderot, Achromatic focal plane wavefront sensing.

Master 1

2018 (4 months) **Co-supervisor**, *S. Meziani*, Observatoire de Paris, Coronagraphic phase mask 4Q++.
2017 (4 months) **Co-supervisor**, *M. El Morsi*, Observatoire de Paris, Speckle temporal modulation.
2017 (4 months) **Supervisor**, *T. Madeleine*, ENS Saclay, Frequency of giant exoplanets from observations.
2017 (1 week) **Co-supervisor**, *W. Kai*, Univ. of Shanghai, Laboratory tests of a coronagraph in lab.
2017 (1 month) **Co-supervisor**, *Y. Komuro*, Univ. of Hokkaido, Laboratory tests of a coronagraph in lab.

Intership

2017 (1 week) **Supervisor**, *M. Babot*, Project on adaptive optics systems (French TIPE/CPGE).
2016 (1 week) **Supervisor**, *J. Gumbs*, 12th-grade student, Data processing for exoplanet imaging.
2013 (1 week) **Supervisor**, *C. Meunier*, Project on Doppler effect (French TIPE/CPGE).

Collaborations

Since 2014 **University of Hokkaiddo**, *Japan*, N. Murakami, Broadband coronagraphy.
Since 2012 **SPHERE consortium**, *Europe*, Automatic Pipeline, exoplanet and disk studies.
Since 2012 **Observatory Côte d'Azur**, *France*, P. Martinez, High contrast imaging on E-ELT.
Since 2012 **NRC-CNRC**, *Canada*, C. Marois, Studies for the GPI upgrade ; balloon projects; consulting.
2015 – 2020 **SRON**, *Netherlands*, R. Huisman, M. Min, Active correction of chromatic aberrations.
2015 – 2019 **Caltech University**, *USA*, D.Mawet, Correction of aberrations at the Palomar Observatory.
2017 – 2018 **ETHZ**, *Switzerland*, J. Kuhn, Broadband coronagraphy and wavefront sensing.
2016 – 2018 **University of Shanghai**, *China*, Q. Cao, Broadband coronagraphy.
2006 – 2018 **GEPI**, *France*, F. Boussaha, Fabrication of phase masks.
2014 – 2017 **NAOJ**, *Japan*, J. Nishikawa, Broadband coronagraphy.
2012 – 2014 **LAM**, *France*, K. Dohlen, M. N'Diaye, Broadband coronagraphy.

Conferences (oral contributions)

Since 2017 **Physics day**, University Paris Diderot, France
2017 **Optimal Optical Coronagraph (invited)**, Leiden, Netherlands
2013 **ESPC**, London, UK
2013 **SPIE (invited)**, San Diego, USA
2013 **IAUS299**, Victoria, Canada
2012 **Gemini Science Meeting**, San Francisco, USA
2012 **High Contrast Imaging & Spectroscopy**, *2 talks*, Santiago, Chile
2012 **Observing Planetary Systems II**, Santiago, Chile
2010 **In The Spirit Of Lyot II**, Paris, France
2010 **SPIE**, San Diego, USA
2009 **Towards Other Earths**, Porto, Portugal
2009 **4th Sino-French Workshop "Origins" (invited)**, Tongling, China
2008 **SF2A**, Paris, France
2007 **In the Spirit of Bernard Lyot conference**, Berkeley, USA
2007 **SF2A**, Grenoble, France

Publications (23 1st author publications – 12 refereed articles– and 168 as co-author)

2020 **R. Galicher, E. Huby, P. Baudoz, O. Dupuis**, *A&A*, 635, id. A11
2019 **R. Galicher, P. Baudoz, J.-R. Delorme, et al.**, *A&A*, 631, id. A143
2018 **R. Galicher, A. Boccaletti, D. Mesa, et al.**, *A&A*, 615, id. A92
2016 **R. Galicher, C. Marois, B. Macintosh, et al.**, *A&A*, 594, id. A63
2014 **R. Galicher, J. Rameau, M. Bonnefoy, et al.**, *A&A*, 565, L4
2013 **R. Galicher, C. Marois, B. Zuckerman, B. Macintosh**, *ApJ*, 769, id. 42
2011 **R. Galicher, C. Marois, B. Macintosh, T. Barman, Q. Konopacky**, *ApJ*, 739, L24
2011 **R. Galicher, P. Baudoz, J. Baudrand**, *A&A*, 530, id. A43
2010 **R. Galicher, P. Baudoz, G. Rousset, et al.**, *A&A.*, 509, id. A31
2008 **R. Galicher, P. Baudoz, G. Rousset**, *A&A*, 488, 912
2007 **R. Galicher and P. Baudoz**, *CRPhy*, 8, Issue $3-4$, 333.
2005 **R. Galicher, O. Guyon, M. Otsubo, et al.**, *PASP*, 117, 411
Since 2010 **Books of engineering exam solutions**, *H&K Edition*, Co-author, ISBN 9782351413340, 9782351410646, 9782351410370, 9782351413494, 9782351413517
2020 **Manga "Relativité"**, *H&K Edition*, Co-author, ISBN 9782351413679
2018 **Manga "Mécanique"**, *H&K Edition*, Co-author, ISBN 9782351413385

Education

2006 – 2009 **PhD Thesis**, *University Denis Diderot*, Paris, France, summa cum lauda
2005 – 2006 **Master 2**, *University Denis Diderot*, rank 1, Astronomy & Astrophysics.
2004 – 2005 **Agrégation**, France, rank 17., French physics teaching certification.
2002 – 2006 **École Normale Supérieure**, Paris, France., honors, General Physics.

Observatoire de Paris, 5, place Jules Janssen – 92195 Meudon France
+33695344395 • ☎ +33145077583 • ✉ *raphael.galicher at obspm.fr*

Event organization

2020 **Festival of Science**, *Paris Observatory*, co-organizer.

2015 – 2019 **High angular resolution (HRAA) day**, Yearly summary of the HRA projects lead at LESIA.

2012 – 2016 **Seminars**, Seminars for the HRAA team at LESIA (one seminar a month).

2008 **Creation of the Elbereth conference**, Conference for and by PhD students working in astronomy in the Paris area (60 persons).

2005 **Creation of the "Tournoi de la rue d'Ulm"**, Free volleyball tournament (100 persons).

Observatoire de Paris, 5, place Jules Janssen – 92195 Meudon France
+33695344395 • ☎ +33145077583 • ✉ *raphael.galicher at obspm.fr*

Deuxième partie

Dossier de synthèse

Chapitre 1

Contexte

1.1 Exoplanètes

1.1.1 Diversité

Au début des années 1990, seules les planètes de notre système solaire sont connues et leur formation est, pense-t-on, bien comprise : les planètes se forment par accrétion dans un disque de gaz et de poussières qui se crée autour de l'étoile naissante ; les planètes géantes se forment loin de leur étoile, là où elles peuvent capturer tout le matériau nécessaire à leur formation ; les planètes telluriques se forment proche de leur étoile, là où il y a moins de gaz et de poussières (Safronov, 1972). C'est alors que Mayor & Queloz (1995) réalisent la première détection d'une exoplanète orbitant autour d'une étoile de la séquence principale : 51 Pegasi b, une planète géante gazeuse ($0,46\ M_{\text{J}}$) orbitant très proche de son étoile hôte à $0,05$ unité astronomique (UA). Et les centaines d'exoplanètes découvertes les années suivantes confirment d'une part que 51 Pegasis b n'est pas une exception et d'autre part qu'il existe une grande diversité d'exoplanètes qui n'ont pas leur pendant dans notre système solaire. Pour preuve la figure 1.1 qui présente la masse des planètes du système solaire et des exoplanètes connues au 1er avril 2020 en fonction de leur demi-grand axe. Et la diversité concerne également les autres paramètres qui caractérisent les systèmes exoplanétaires : excentricité, rayon, résonance orbitale, paramètres de l'étoile hôte, etc.

1.1.2 Techniques de détection

Pour détecter et étudier la diversité des exoplanètes, plusieurs techniques sont utilisées : vitesse radiale (Wright & Gaudi, 2013; Santos, 2008), transit (Winn, 2010), astrométrie (Perryman *et al.* , 2014), micro-lentille gravitationnelle (Bennett, 2008), chronométrage (Wolszczan, 2015), imagerie (Lagrange, 2014). Aucune ne peut sonder l'ensemble de l'espace des paramètres : paramètres de l'orbite exoplanétaire, masse de l'exoplanète, âge du sytème stellaire, type de l'étoile hôte, etc. Par exemple, la figure 1.1 met en évidence que la technique des transits ne détecte que des planètes qui orbitent à moins de $\simeq 1$ UA de leur étoile tandis qu'aujourd'hui, l'imagerie découvre des planètes au-delà de $\simeq 1$ UA. De plus, chaque technique ne permet de déterminer que certains paramètres caractérisant le sytème exoplanétaire ; le tableau 1.1 montre en vert les paramètres qui peuvent être estimés directement, à partir des paramètres stellaires (rayon, masse, densité, photométrie, âge), ou à partir de modèles « sûrs »(e.g. lois de Képler) et, en orange les paramètres qui sont estimés à partir de modèles ou d'hypothèses « non sûrs »(e.g. existence de plusieurs modèles) ou dans des cas particuliers (e.g. les masses dynamiques pour les systèmes multi-planétaires détectés par imagerie).

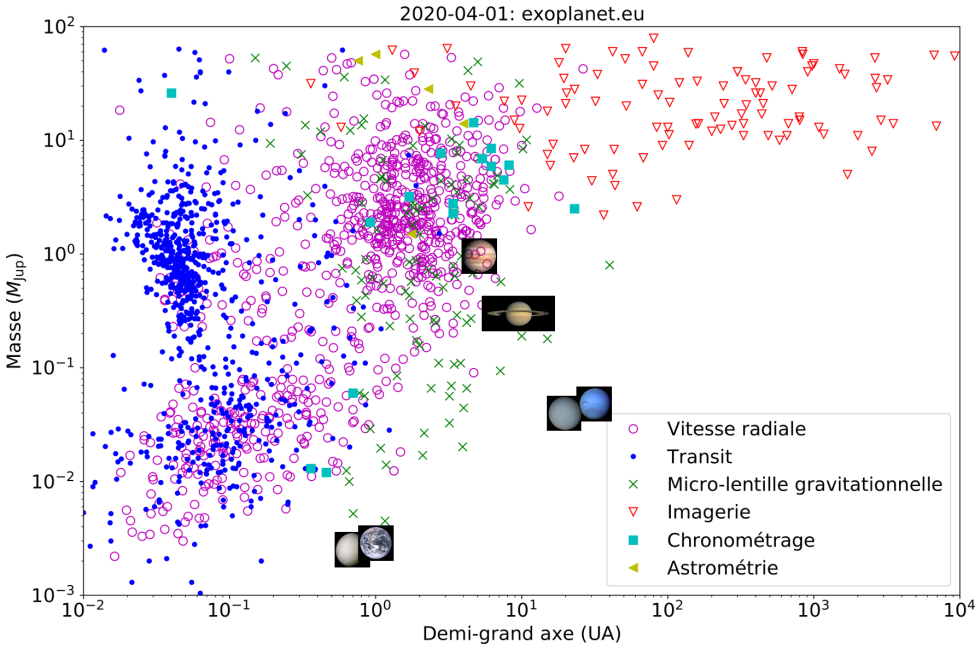

FIGURE 1.1 – *Masse des exoplanètes en fonction de leur demi-grand axe. Les points correspondent aux exoplanètes connues le 1er avril 2020 et symboles et couleurs précisent la technique utilisée pour leur découverte.*

	Vitesse radiale	Transit	Astrométrie	Micro-lentille gravitationnelle	Imagerie	Chronométrage (pulsar)
Masse planétaire	Minimale					
Inclinaison de l'orbite						
Période orbitale						
Demi-grand axe						
Excentricité						
Rayon						
Spectre						
Gravité de surface planétaire						

TABLE 1.1 – *Paramètres mesurables en fonction de la technique utilisée.* **Case verte** *: estimation directe, à partir des paramètres stellaires (rayon, masse, densité, photométrie, âge), ou à partir de modèles « sûrs »(e.g. lois de Képler).* **Case orange** *: estimation à partir de modèles ou d'hypothèses « non sûrs »(e.g. existence de plusieurs modèles) ou dans des cas particuliers.*

Pour étudier les exoplannètes dans leur ensemble (différents types et tous les paramètres les caractérisant), il est donc indispensable d'utiliser toutes les techniques de détection en parallèle.

1.1.3 Que cherche-t-on à comprendre ?

1.1.3.1 Formation planétaire

Après 25 ans d'observations, plus de 4000 exoplanètes ont été détectées et pour expliquer la diversité de leurs paramètres orbitaux, de leurs masses et de leurs rayons (Santos, 2008;

Santos & Faria, 2018), les modèles de formation planétaire ont été adaptés. L'exemple que je présente souvent en conférence grand public pour expliquer comment un modèle évolue en science physique est le modèle de migration planétaire (Goldreich & Tremaine, 1980; Lin *et al.* , 1996) qui explique comment des planètes géantes gazeuses migrent vers leur étoile après s'être formées selon les modèles proposés avant la découverte des exoplanètes.

Aucun modèle de formation planétaire (Boss, 2006a,b,c; Pollack *et al.* , 1996; Mordasini *et al.* , 2009, etc) ne permet cependant d'expliquer l'ensemble des observations et il reste de nombreuses questions ouvertes : quels processus dominent en fonction de la distance à l'étoile, de la masse de l'étoile, de la masse du disque circumstellaire, etc ; quels sont les détails de chacun des processus ?

Pour répondre à ces questions, il est indispensable d'une part d'augmenter le nombre d'exoplanètes détectées pour permettre des études statistiques et d'autre part d'étudier en détail les systèmes pour lesquels nous avons accès à un grand nombre d'informations (exoplanètes détectées par plusieurs techniques par exemple). On remarque sur la figure 1.1 qu'une catégorie d'exoplanètes est peu étudiée jusqu'à aujourd'hui : celles qui orbitent aux alentours et au-delà de la limite de glace de leur système ($\simeq 5\,UA$ pour une étoile de type solaire). Pour compléter l'échantillon, il est donc important de détecter de tels objets par :

— imagerie pour les géantes gazeuses jeunes en 2020, et pour des planètes de plus en plus légères et matures dans les années à venir.
— astrométrie avec la mission Gaia pour des planètes de type Jupiter orbitant à $\lesssim 5\,\mathrm{UA}$; publication des résultats prévue en 2021 (Gaia Collaboration *et al.* , 2016).
— vitesse radiale pour les planètes autour de 5 UA, et plus loin dans les années à venir.

1.1.3.2 Atmosphère exoplanétaire

Malgré le grand nombre d'équipes travaillant dans le domaine, deux paramètres caractérisant les exoplanètes restent à ce jour peu mesurés : leur température et la composition de leur atmosphère. Ceci vient du fait que presque la totalité des exoplanètes ont été détectées par des techniques indirectes, c'est-à-dire sans mesurer la lumière réfléchie, émise ou transmise par la planète. La détection directe d'une exoplanète est pourtant possible dans trois cas :

1. Pendant un transit primaire, une petite fraction de la lumière stellaire traverse les hautes couches de l'atmosphère planétaire avant d'être détectée par l'instrument. Cela a permis de détecter quelques molécules dans l'atmosphère d'exoplanètes qui orbitent très proches de leur étoile (Snellen *et al.* , 2010; Alonso-Floriano *et al.* , 2019; von Essen *et al.* , 2019; Espinoza *et al.* , 2019, , etc). Les molécules détectées sont souvent exotiques comparées aux molécules trouvées dans les atmosphères des planètes du système solaire car la température effective des exoplanètes détectées par transit est élevée.

2. En comparant le spectre stellaire mesuré pendant le transit secondaire au spectre mesuré en dehors du transit (somme du spectre stellaire et du spectre émis par la planète), on en déduit le flux thermique émis par l'exoplanète. De nouveau, cette technique ne permet d'étudier que des exoplanètes qui orbitent très proche de leur étoile et dont la température effective est élevée (Deming *et al.* , 2005; Charbonneau *et al.* , 2005; Alonso, 2018).

3. Par imagerie on peut séparer angulairement l'image de l'exoplanète et celle de l'étoile. On mesure alors le flux émis et réfléchi par l'exoplanète soit par photométrie, soit par spectrométrie. Remarque : je regroupe sous le terme « imagerie » tout instrument qui permet de séparer angulairement l'image de l'exoplanète de celle de l'étoile quelle que soit la façon d'analyser la lumière exoplanétaire (photométrie, spectromètre intégral de champ, couplage avec un spectromètre à haute résolution spectrale).

Peu de détections directes ont été réalisées à cause de la faiblesse des signaux à mesurer. Mais quand cela a été fait, la comparaison du spectre mesuré, ou la photométrie, aux modèles théoriques d'atmosphères (Charnay *et al.* , 2018, et articles qu'ils citent) a permis de déterminer en partie la composition chimique et la température de l'atmosphère de l'exoplanète. Ces comparaisons nous ont aussi montré notre méconnaissance des atmosphères exoplanétaires. Cela n'est pas surprenant puisque les systèmes exoplanétaires détectés à ce jour ne ressemblent pas au système solaire : planètes très chaudes détectées par transit ou géantes gazeuses jeunes détectées par imagerie. Les modèles d'atmosphère planétaire ne peuvent donc pas être utilisés directement pour expliquer les spectres exoplanétaires. Comme pour les modèles de formation planétaire, il est indispensable d'augmenter le nombre de détections pour améliorer les modèles.

1.1.3.3 Vie extraterrestre

Pour le grand public et certains scientifiques, l'étude des exoplanètes est synonyme de recherche d'une vie extraterrestre. Cette question est certes passionnante mais les scientifiques se doivent d'être honnêtes envers le grand public et envers eux-mêmes : nous ne sommes pas encore capables de répondre à cette question.

À ce jour, la recherche d'une vie extraterrestre se résume à rechercher une vie qui nous ressemblerait (chimie du carbone, respiration de dioxygène). La première étape est de définir un ensemble de bio-marqueurs, c'est-à-dire un ensemble de signatures spectrales dont la détection dans un spectre, seule observable accessible, nous permettrait d'affirmer qu'une vie similaire à la nôtre a été détectée. La question est donc : « quel est l'ensemble de bio-marqueurs qui ne laisserait aucun doute ? ». Le grand nombre d'articles avec comité de lecture dont le titre contient *biomarker* est une preuve qu'il n'y a pas consensus (128 articles entre janvier et mi-avril 2020). Une difficulté est que beaucoup de molécules produites par les êtres-vivants sur Terre peuvent également être créées par des phénomènes géologiques (Harman & Domagal-Goldman, 2018). Une autre difficulté est que les marqueurs de vie peuvent être très différents en fonction des êtres vivants considérés (organismes unicellulaires ou pluricellulaires, bactéries, etc). Cela signifie que même avec un spectre étendu et à haute résolution spectrale, nous ne pourrions pas affirmer qu'une vie extraterrestre similaire à la vie terrestre a été détectée. À cela s'ajoute le fait que, en 2020, les seuls spectres que nous mesurons sont soit à résolution spectrale modérée, voire basse, ou sur des domaines spectraux très restreints.

Devant la difficulté du problème, les astrophysiciens ont cherché à le simplifier. Puisque la vie sur Terre ne pourrait pas exister sans eau liquide, ils en ont conclu qu'une planète qui pourrait abriter la vie doit avoir de l'eau liquide à l'état stable à sa surface. Ils ont alors déterminé la zone autour de chaque étoile où de l'eau liquide pourrait exister à l'état stable à la surface d'une planète rocheuse. Au lieu d'appeler cela la « zone d'eau liquide », la communauté a préféré « zone habitable »(Kasting *et al.* , 1993), certainement plus vendeur auprès du grand public et des politiques. La définition de cette zone a évolué mais le terme est resté (Ramirez, 2018). Un article récent fait remarquer que les biologistes travaillent sur le sujet de l'habitabilité d'une planète depuis trente ans et que les astrophysiciens pourraient utiliser les résultats de leur travaux (Méndez *et al.* , 2020).

Il faut également être conscient que la recherche actuelle de vie extra-terrestre est très réductrice puisque nous cherchons uniquement ce que nous connaissons (la vie terrestre). Pourquoi n'existerait-il pas d'autres formes de vie ? Difficile de répondre à cette question avant d'avoir découvert une autre forme de vie. Le serpent se mord la queue. Nous pourrions aller plus loin et nous demander ce qu'est la vie, question encore débattue dans la communauté scientifique.

En conclusion, la recherche d'une vie extraterrestre reste une question scientifique importante

et des travaux sont menés pour que l'on puisse y répondre dans les décennies à venir : définition de la vie, reproduction des conditions d'apparition de la vie en laboratoire, missions proposées sur Mars, Ganymède et Europe qui pourraient ou auraient pu accueillir de la vie similaire à celle que nous connaissons. Cependant, en 2020, les raisons scientifiques qui nous poussent à détecter et caractériser les exoplanètes sont la compréhension de la formation des planètes et l'étude de leur atmosphère. La recherche d'une vie extraterrestre est un objectif à très long terme.

1.2 Imagerie haute dynamique

1.2.1 Pourquoi l'imagerie ?

L'imagerie présente trois intérêts majeurs pour la communauté scientifique.

1. Elle détecte des exoplanètes dans la partie externes des systèmes expolanétaires, objets peu étudiées jusqu'à présent.
2. Elle permet d'étudier les intéractions entre exoplanètes et disques circumstellaires, ce qui aide à comprendre la formation planétaire.
3. Elle mesure le spectre de la lumière reçue de l'exoplanète.

L'imagerie permet donc contraindre les modèles de formation planétaire et d'étudier les atmosphères exoplanétaires en déterminant leur composition chimique.

1.2.2 Une luciole près d'un phare maritime

En conférence grand public, on utilise souvent l'analogie entre faire l'image d'une Terre autour d'un Soleil et faire l'image depuis Paris d'une luciole [1] volant à un mètre d'un phare maritime [2] qui serait à New-York [3] (Figure 1.2). Cette analogie met en avant les deux principales difficultés de l'imagerie que sont la faible séparation angulaire (une fraction de seconde d'angle) et le très grand rapport de luminosité (10^4 à 10^{10}) entre l'étoile et l'exoplanète.

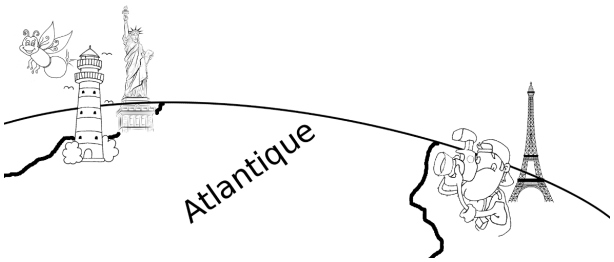

FIGURE 1.2 – *Analogie : Faire l'image d'une planète Terre est équivalent à faire l'image d'une luciole volant à un mètre d'un phare maritime qui se trouve à 6000 km.*

Pour ces raisons, l'imagerie des exoplanètes est souvent qualifiée d'imagerie à haute dynamique et elle fait appel à une instrumention spécifique. En 2020, quelques instruments permettent de mesurer les spectres émis par des exoplanètes géantes gazeuses jeunes qui orbitent loin de leur étoile (§ 1.3). Afin d'étudier des planètes matures, plus légères ou plus proches de leur étoile par cette technique, des progrès instrumentaux sont nécessaires (§ 2).

1. Harvey & Stevens (1928) ont mesuré que l'intensité émise par une *Pyrophorus noctilucus* est 2.10^{-3} candela.
2. Un phare maritime à longue portée émet facilement une intensité de 10^7 candela.
3. Considérons que la Terre est plate pour cette analogie.

1.3 Instruments coronographiques en 2020

1.3.1 Coronographe

La figure 1.3 schématise les instruments d'imagerie haute dynamique en visible et proche-infrarouge actuellement en service derrière les télescopes au sol. Pour obtenir l'image d'une

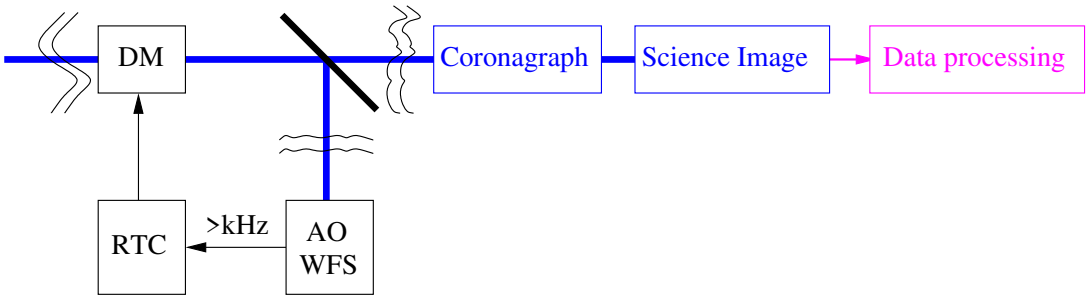

FIGURE 1.3 – *Schéma fonctionnel des instruments d'imagerie à haute dynamique de 2020 : Le faisceau lumineux en bleu est séparé, généralement spectralement, entre voie d'analyse de l'optique adaptative (AO, boîtes noires) et voie scientifique qui utilise un coronographe (boîtes bleues). Une fois enregistrées, les données sont combinées pour extraire le signal d'intérêt (en magenta).*

exoplanète, il faut utiliser dans la voie scientifique (boîtes bleues sur la figure) un filtre optique qui atténue la lumière de l'étoile sans modifier l'image de l'exoplanète. De nombreux coronographes stellaires ont été proposés, testés et validés en laboratoire pour cela [4]. Plusieurs de ces composants sont aujourd'hui partie intégrante d'instruments dans l'espace (ACS et STIS du *Hubble Space Telescope*) et d'instruments au sol : Sphere/VLT (Beuzit *et al.* , 2019), GPI/Gemini (Macintosh *et al.* , 2014), SCExAO/Subaru (Lozi *et al.* , 2018), MagAO/Magellan (Close *et al.* , 2018), NIRC2/Keck (McLean & Sprayberry, 2003), NICI/Gemini (Chun *et al.* , 2008), NIRI/Gemini (Hodapp *et al.* , 2003), NACO/VLT (Rousset *et al.* , 2003; Lenzen *et al.* , 2003).

1.3.2 Coronographes et aberrations

Avant d'aller plus loin, modélisons la formation d'image à travers un système coronographique. Utilisons le modèle de Fraunhoffer et considérons un coronographe parfait qui élimine la tache de diffraction d'une source ponctuelle placée à l'infini sur l'axe optique [5] (Cavarroc *et al.* , 2006). Cet instrument fonctionne parfaitement si la surface d'onde est plane en amont du coronographe. En revanche, s'il existe une aberration optique, une partie de la lumière stellaire n'est pas filtrée par le coronographe et elle est diffractée sous forme de tavelures dans l'image coronographique ; chaque tavelure est une copie de la tache de diffraction de l'instrument, décalée par rapport à l'axe optique, c'est-à-dire ressemblant à l'image d'une source ponctuelle hors-axe comme une exoplanète.

Par exemple, en présence d'une aberration de phase dans la pupille de diamètre D, de faible amplitude a_n et de période spatiale D/n, quand on centre l'image de l'étoile sur le coronographe, on observe au premier ordre deux tavelures stellaires dans l'image coronographiées. Elles

4. J'inclus dans cette famille les apodiseurs de pupille.
5. Cette modélisation ne fonctionne pas pour les apodiseurs qui minimisent l'intensité diffractée dans une région donnée du plan focal. La performance d'un apodiseur reste cependant limitée par les aberrations.

se trouvent aux positions angulaires $\pm n\,\lambda/D$ et leur intensité est a_n^2 fois celle de l'image non coronographiée de l'étoile (figure 1.4). De cette modélisation, on déduit que :

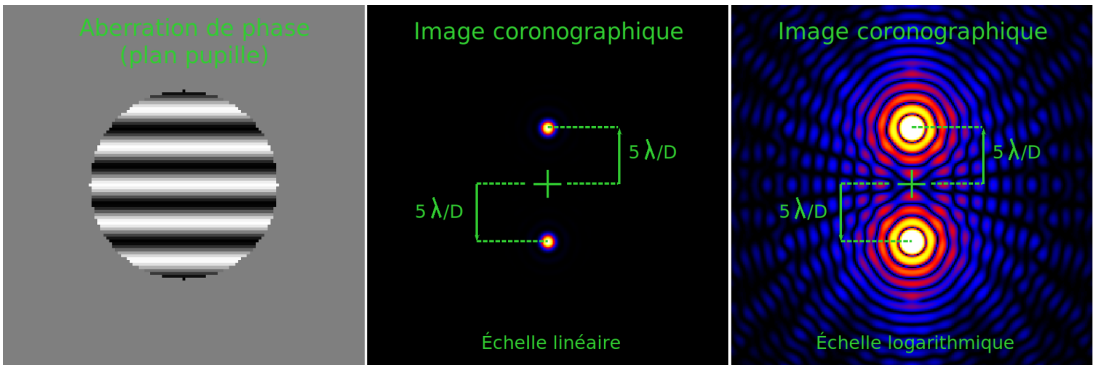

FIGURE 1.4 – *Simulations numériques : image coronographique composée de deux tavelures à $\pm 5\,\lambda/D$ de l'axe optique (échelles linéaire au centre et logarithmique à droite) obtenue avec un coronographe parfait et une aberration sinusoïdale avec 5 périodes dans la pupille (gauche).*

1. Si on utilise un miroir déformable qui possède N actionneurs dans un diamètre de pupille, seule l'intensité des tavelures qui se trouvent à moins de $N\,\lambda/(2D)$ de l'axe optique pourra être modifiée. Cette région est la zone d'influence du miroir déformable.
2. Pour une aberration de phase d'amplitude 2 nm et une longueur d'onde d'observation de $1,5\,\mu$m, on trouve un contraste, rapport entre les intensités du résidu stellaire et de l'étoile non coronographiée, $C = (2\,\pi \times 2/1500)^2 \simeq 7 \times 10^{-5}$. Il s'agit de l'ordre de grandeur du contraste mesuré dans les images brutes de Sphere. Quand on intègre sur les fréquences spatiales qui créent des tavelures dans la zone d'influence du miroir déformable pour Sphere, on trouve que l'écart-type des aberrations vaut $10-20$ nm. Il s'agit principalement d'erreurs de phase dues aux défauts de polissage des optiques de l'instrument.
3. Pour détecter une planète Terre autour d'un Soleil, il faudrait atteindre au moins un contraste de 10^{-10}, ce qui correspond à une aberration de quelques picomètres par fréquence spatiale pour une observation dans l'infrarouge. Ceci est bien en-deçà des erreurs de polissage des optiques et nous ne pourrons pas l'atteindre par construction [6].

1.3.3 Aberrations turbulentes et quasi-statiques

Quand on observe avec un instrument coronographique, deux situations se présentent :

1. Les aberrations dont le temps de vie est beaucoup plus court que le temps de pose dominent (e.g. en présence de turbulence atmosphérique). Un halo stellaire surmonté de tavelures variant d'une image à l'autre domine les images coronographiques (Singh *et al.* , 2019). Le signal d'une exoplanète est noyé dans le bruit de photon du halo stellaire et il peut facilement être confondu avec les tavelures résiduelles. De plus, la présence du halo signifie que la résolution angulaire est dégradée. Dans ces conditions, il n'est pas envisageable de détecter une exoplanète et pour compenser les aberrations rapides, les instruments actuels utilisent un système d'optique adaptative (paragraphe 1.3.4).

6. Même si on pouvait déposer les atomes un à un pour épouser au mieux la forme de l'optique à fabriquer, l'aberration serait supérieure au picomètre par fréquence spatiale à cause de la « granularité » des atomes.

2. Les aberrations quasi-statiques dont le temps de vie est plus long que le temps de pose dominent. Cela se produit quand les aberrations rapides sont bien corrigées par l'optique adaptative ou quand l'instrument est dans l'espace ou derrière un ballon stratosphérique. Dans ce cas, un champ de tavelures quasi-statiques domine les images coronographiques. La difficulté est alors de différentier l'image d'une exoplanète d'une tavelure stellaire, ce que l'on fait grâce aux techniques d'imagerie différentielle (paragraphe 1.3.5).

1.3.4 Optique adaptative

Comme les coronographes sont très sensibles aux aberrations de la surface d'onde (schématisées par les traits noirs sur la figure 1.3), et en premier lieu à celles dues à la turbulence atmosphérique, on utilise un système d'optique adaptative. Il s'agit d'une boucle d'asservissement qui compense en temp réel les déphasages introduits par la turbulence atmosphérique. Un analyseur de surface d'onde (AO WFS) estime les aberrations de phase en amont du coronographe à partir d'une partie de la lumière incidente qui est extraite de la voie scientifique grâce à une séparatrice[7]. Un *real time computer* (RTC) calcule alors les commandes à envoyer à un miroir déformable (DM) pour minimiser les aberrations de phase mesurées. Comme le temps de cohérence moyen de la turbulence atmosphérique est de l'ordre de la milliseconde, la boucle d'optique adaptative doit fonctionner à plus de 1 kHz.

L'optique adaptative minimise ainsi les aberrations de phase mesurées dans la voie d'analyse. On obtient alors une image coronographique brute comme celle présentée sur la gauche de la figure 1.5 : l'intensité du halo et des tavelures stellaires a été réduite à l'intérieur de la zone d'influence du miroir déformable délimitée par l'anneau de tavelures brillantes à la fréquence de coupure du système ($N\,\lambda/(2D)$, voir le paragraphe 1.3.2). Il reste cependant des tavelures à l'intérieur de cette zone car les aberrations corrigées par l'optique adaptatives sont différentes de celles existantes dans la voie scientifique. En effet, les faisceaux lumineux traversent des optiques différentes dans la voie d'analyse et dans la voie scientifique après la séparatrice. On parle d'aberrations différentielles ou *non common path aberrations* (NCPA). Quand les conditions d'observation sont bonnes (i.e. bon seeing, peu de vent, peu de nuage), les NCPA sont la principale limitation des instruments actuels ; les images coronographiques brutes sont alors dominées par des tavelures au mieux $10^4 - 10^5$ fois moins brillantes que l'image de l'étoile non coronographiée (image de gauche sur la figure 1.5). Cela signifie qu'à partir d'une seule image, on ne peut détecter que des objets au mieux $10^4 - 10^5$ fois moins brillants que l'étoile pointée.

1.3.5 Imagerie différentielle

Peu d'exoplanètes sont suffisamment brillantes pour être détectées dans les images brutes pleines de tavelures stellaires. Des stratégies d'observation ont donc été mises au point pour extraire le signal d'un objet astrophysique du champ de tavelures :

1. imagerie différentielle angulaire (ADI, Schneider *et al.* , 1998, 1999; Marois *et al.* , 2006) : on fait l'hypothèse que les aberrations sont localisées dans un plan, généralement la pupille de l'instrument ; on immobilise ce plan tout en laissant le champ d'observation tourner autour de l'axe optique (en utilisant la rotation diurne de la Terre ou en faisant tourner l'instrument dans l'espace) ; on enregistre une séquence d'images. De cette manière, le champ de tavelures est le même dans toutes les images tandis que l'image de l'objet astrophysique ne se forme pas au même endroit sur le détecteur d'une image à l'autre.

7. Il s'agit généralement d'une dichroïque.

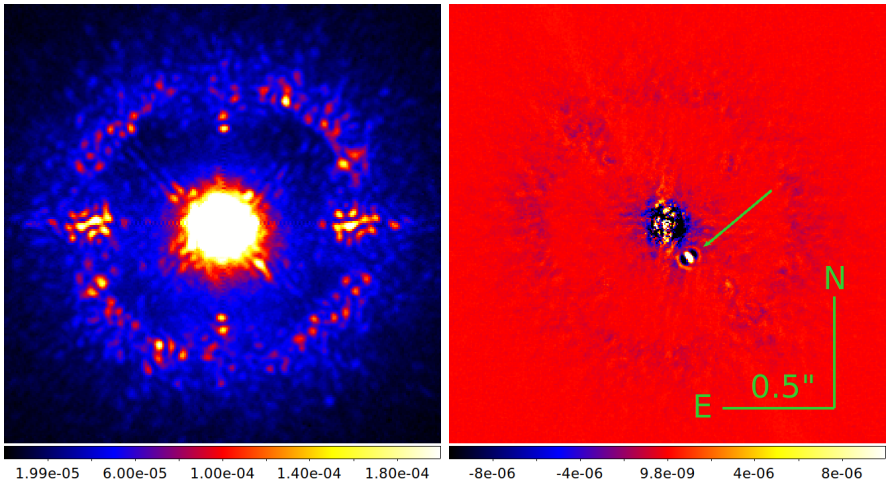

FIGURE 1.5 – *Images coronographiques enregistrées par l'instrument Irdis/Sphere/VLT.* **Gauche** *: image brute de temps de pose* 2 *s dominée par des tavelures stellaires.* **Droite** *: image réduite par ADI à partir d'une séquence de* 200 *images brutes. La planète BetaPictoris b est détectée (pointée par une flèche). Les échelles donnent le flux normalisé par celui de l'étoile.*

2. imagerie différentielle spectrale (SDI, Racine *et al.* , 1999; Thatte *et al.* , 2007) : on fait l'hypothèse que les aberrations sont des aberrations de phase dues à des différences de marche achromatiques et/ou que les spectres de l'étoile et de l'exoplanète sont différents ; l'intensité et la position des tavelures ne varient donc pas comme celles de l'objet astrophysique entre des images enregistrées à différentes longueurs d'onde.
3. imagerie différentielle polarimétrique (PDI, Baba & Murakami, 2003) : on suppose que la lumière reçue de l'exoplanète ou du disque circumstellaire est partiellement polarisée tandis que celle de l'étoile, et donc des tavelures, ne l'est pas.
4. imagerie différentielle par étoile de référence (RDI, Beuzit *et al.* , 1997) : on observe l'étoile cible, puis une étoile de référence ayant des caractéristiques similaires (position dans le ciel, magnitude, type spectral). Les champs de tavelures sont alors similaires mais l'image de l'objet astrophysique n'est présent qu'autour de l'étoile cible.

Une fois les images enregistrées, plusieurs méthodes ont été proposées pour extraire l'image de l'objet astrophysique en utilisant les variations différentes de son intensité et de sa position par rapport à celles des tavelures : *classical* ADI (Marois *et al.* , 2006), Loci (Lafrenière *et al.* , 2007a), TLoci (Marois *et al.* , 2014; Galicher *et al.* , 2011), PCA (Soummer *et al.* , 2012; Amara & Quanz, 2012), Andromeda (Cantalloube *et al.* , 2015), Paco (Flasseur *et al.* , 2018), etc. Toutes ces techniques réalisent des combinaisons linéaires des images enregistrées (Galicher *et al.* , 2018) à l'exception d'Andromeda et Paco qui modélisent ces images. Grâce à ces techniques (représentées par la boîte *data processing* sur la figure 1.3), des objets à plusieurs unités astronomiques de leur étoile et jusqu'à quelques 10^6 fois moins lumineux peuvent être détectés dans les images fournies par les instruments en 2020. Ces objets peuvent être des exoplanètes géantes gazeuses jeunes et donc, relativement brillantes par rapport à leur étoile (image de droite sur la figure 1.5). Il peut également s'agir de disques circumstellaires de poussières. Les instruments tels Sphere/VLT et GPI/Gemini ont d'ailleurs permis la détection dans le proche-infrarouge d'une multitude de disques circumstellaires dont la plupart des propriétés photométriques, polarimétriques et géométriques ne sont pas encore expliquées (Figure 1.6).

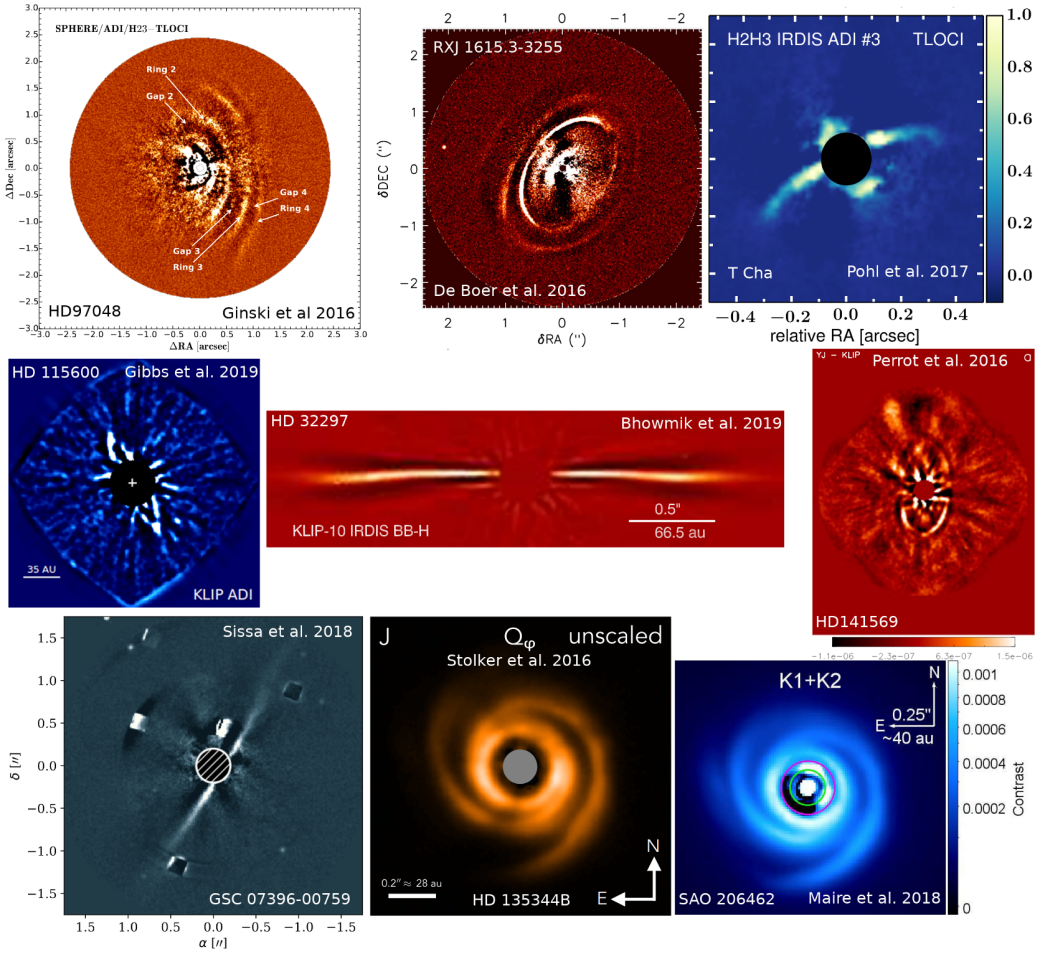

FIGURE 1.6 – *Images de disques circumstellaires obtenues avec Sphere/VLT (Ginski* et al. *, 2016; de Boer* et al. *, 2016; Pohl* et al. *, 2017; Gibbs* et al. *, 2019; Bhowmik* et al. *, 2019; Perrot* et al. *, 2016; Sissa* et al. *, 2018; Stolker* et al. *, 2016; Maire* et al. *, 2017).*

1.3.6 Quelle performance ?

Dans les instruments actuels, l'utilisation d'une optique adaptative rapide ($\simeq 1\,$kHz) et de coronographes plus efficaces que le coronographe de Lyot classique permet de détecter à $0,3$ arcsec de l'étoile des objets jusqu'à 1500 fois moins brillants que ce que ne pouvaient faire les instruments de la génération précédente comme NACO [8]. Plusieurs objets sub-stellaires ont été détectés autour d'étoiles jeunes et j'ai pu mener ou participer à différentes études (paragraphe 3.1). Seulement, les exoplanètes sont des objets très ténus et pour détecter par imagerie [9] des planètes plus légères que Jupiter et plus âgées que quelques 100 millions d'années à moins de 5 UA de leur étoile, il faut de nouveau gagner au moins le même facteur en contraste, ce qui requiert une nouvelle génération d'instruments.

8. Comparaison des courbes de contraste de Beuzit *et al.* (2019) et de Launhardt *et al.* (2020).
9. Ce terme inclut l'imagerie en large bande spectrale et l'imagerie via un spectromètre intégral de champ.

Chapitre 2

L'imagerie d'exoplanètes de demain

2.1 Un type d'instrument par objectif scientifique

L'instrument idéal fournirait une mesure spectro-polarimétrique de la lumière exoplanétaire avec une résolution spectrale de plusieurs centaines de milliers et avec la possibilité d'observer des planètes de tous types (solides et gazeuses, jeunes et matures) à toutes séparations angulaires de l'étoile. De la sorte, nous pourrions étudier la composition chimique des atmosphères en fonction des paramètres orbitaux, des propriétés de l'étoile hôte, de leur âge, etc. La technologie actuelle ne permet pas d'imaginer un tel instrument mais plusieurs projets existent avec deux approches complémentaires : la caractérisation fine du spectre et de l'astrométrie d'exoplanètes connues et la détection de nouvelles exoplanètes.

2.1.1 Caractérisation spectrale fine

Des équipes utilisent les spectrographes à haute résolution spectrale dans des cas particuliers (planètes jeunes et brillantes comme β-Pictoris b, Snellen *et al.* , 2010), voire couplent un instrument d'imagerie à haute dynamique avec un tel spectrographe (Jovanovic *et al.* , 2016; Mawet *et al.* , 2018, 2019; Vigan, 2019). Cela permet de mesurer à haute résolution spectrale une partie du spectre de l'exoplanète, et ainsi d'étudier la composition chimique de son atmosphère. En revanche, cette approche ne peut être utilisée que pour caractériser une exoplanète dont la position a été mesurée par un autre instrument. Il faut donc un travail collaboratif entre les équipes qui utilisent les instruments d'imagerie pour découvrir et caractériser spectralement les exoplanètes à des résolutions modérées, et celles qui utilisent les instruments de spectroscopie à haute, voire très haute, résolution spectrale.

D'autres équipes cherchent à détecter des exoplanètes très faiblement séparées de leur étoile. Pour cela, elles utilisent l'interférométrie optique. L'instrument Gravity/VLT est un bel exemple (Gravity Collaboration *et al.* , 2017). Il a permis d'affiner les mesures astrométriques de la planète HR 8799 e et d'extraire un spectre de résolution spectrale modérée ($R = \lambda/\Delta\lambda = 500$, Gravity Collaboration *et al.* , 2019). Cet instrument pourra mesurer avec une grande précision le mouvement orbital d'exoplanètes connues et mesurer leur spectre à résolution modérée. En revanche, il n'est pas envisageable de faire une campagne d'observation pour découvrir de nouvelles exoplanètes avec GRAVITY puisqu'un seul point du champ de vue est étudié par séquence d'observation. Là encore, une synergie avec d'autres instruments d'imagerie est indispensable.

2.1.2 Nouvelles détections et caractérisations

Comme expliqué ci-dessus, pour mesurer un spectre à haute résolution spectrale ou l'astrométrie par interférométrie avec une précision de quelques microsecondes d'angle, il est indispensable de savoir où se trouve l'exoplanète dans le champ d'observation. C'est pour cela que plusieurs équipes proposent de nouveaux instruments d'imagerie qui feront une recherche systématique de nouvelles exoplanètes plus ténues et plus proches de leur étoile que ce que ne font les instruments en 2020 (Macintosh *et al.* , 2018; Mennesson *et al.* , 2018; Gong *et al.* , 2019; Boccaletti *et al.* , 2020a; Gaudi *et al.* , 2020). La suite de ce document concerne ces instruments.

2.2 Instruments coronographiques de demain au sol

La différence majeure entre les instruments d'aujourd'hui et la prochaine génération est qu'aujourd'hui, on utilise un coronographe derrière un système d'optique adaptative tandis que demain, les deux sous-systèmes devront interagir.

2.2.1 Coupler deux boucles d'asservissement

Reprenons la vision binaire du paragraphe 1.3.3 « temps de vie des aberrations plus court ou plus long que le temps d'exposition de l'image scientifique ». Cette vision est une simplification. Dans la réalité, il y a une distribution continue des temps de vie (Macintosh *et al.* , 2005; Milli *et al.* , 2016; Goebel *et al.* , 2018). La vision binaire permet cependant d'identifier deux sous-

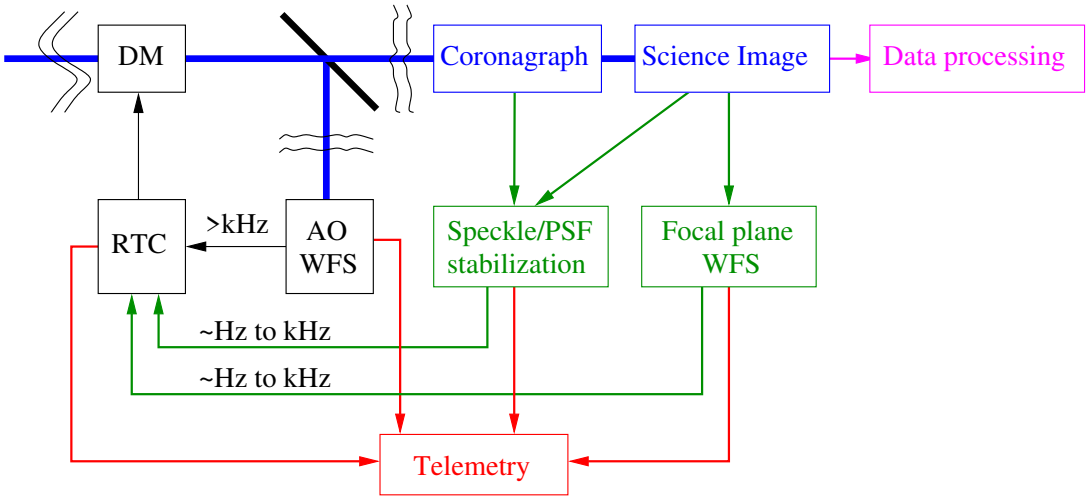

FIGURE 2.1 – *Schéma fonctionnel des futurs instruments d'imagerie à haute dynamique au sol : même schéma que sur la figure 1.3 avec deux boucles supplémentaires associées à celle de l'optique adaptative : une boucle de stabilisation qui utilise la lumière rejetée par le coronographe pour estimer les aberrations de basses fréquences spatiales et une boule de correction utilisant un analyseur en plan focal (Focal plane WFS).*

systèmes prévus dans la nouvelle génération d'instruments au sol tels Sphere+(Boccaletti *et al.* , 2020a), GPI2.0 (Chilcote *et al.* , 2018), SCExAO (Lozi *et al.* , 2018), KPIC (Mawet *et al.* , 2018) et dont le schéma fonctionnel est représenté dans la figure 2.1 :

1. **Un système d'optique adaptative** (OA, en noir sur la figure) plus performant (plus rapide, plus d'actionneurs sur le miroir déformable) que les meilleurs systèmes actuels (e.g. Saxo et GPI, Fusco *et al.* , 2016; Macintosh *et al.* , 2014) pour compenser les aberrations variant plus rapidement que le temps d'exposition. Ainsi, on augmentera le nombre de nuits (actuellement $\sim 30\,\%$) où le halo d'OA est suffisamment faible pour que les images coronographiques soient dominées par des tavelures quasi-statiques.

2. **Un deuxième étage d'optique adaptative** pour minimiser en continu pendant les observations l'intensité des tavelures dues à des aberrations variant plus lentement que le temps d'exposition. Ce système devra estimer les commandes à envoyer aux éléments correcteurs (certainement des miroirs déformables, DM) à partir de l'image scientifique en utilisant un analyseur de surface d'onde en plan focal (*Focal plane WFS* en vert sur la figure) car toute séparation de faisceau ou modification des optiques du système entre l'analyse et l'image scientifique introduirait des aberrations différentielles (NCPA).

Coupler ces deux boucles permettra de minimiser l'intensité des tavelures dans une zone de l'image coronographique qu'on appelle le *dark hole* (DH, Malbet *et al.* , 1995). Sur le schéma un seul DM est représenté mais il y en aura sûrement plusieurs pour compenser les défauts de phase et d'amplitude de l'onde. De plus, les deux boucles n'utiliseront pas forcément les mêmes DM.

La figure 2.2 (Singh *et al.* , 2019) montre des images coronographiques enregistrées sur le banc THD2 de R&D (paragraphe 3.2.1 et Galicher *et al.* , 2014; Baudoz *et al.* , 2018b) en présence d'aberrations turbulentes partiellement corrigées par une optique adaptative de type Saxo/Sphere et d'aberrations statiques (simulant des NCPA). Dans l'image de gauche, l'optique adaptative corrige les aberrations associées aux tavelures à moins de $20\,\lambda/D$ de l'axe optique et laisse un halo stellaire au-delà (anneau brillant blanc et jaune) ; les aberrations statiques non corrigées par l'optique adaptative sont à l'origine des tavelures en-deçà de $20\,\lambda/D$. Celles-ci empêchent la détection d'une exoplanète dont l'image aurait la même forme.

Dans l'image de droite, le halo stellaire est toujours présent mais l'intensité des tavelures statiques a été minimisée dans un *dark hole* (tirets blancs) en utilisant un deuxième étage d'optique adaptative incluant un analyseur de surface d'onde en plan focal (FPWFS, paragraphe 2.2.2). Ainsi, si une planète se trouve à l'intérieur du *dark hole*, nous pourrions la détecter.

2.2.2 Analyseur de surface d'onde en plan focal

Pour minimiser l'intensité des tavelures stellaires quasi-statiques dans l'image scientifique, il faut estimer, à partir de cette image, le champ électrique E_S qui est associé aux tavelures. Cela est fait grâce à un analyseur de surface d'onde en plan focal (FPWFS). Or, dans les longueurs d'onde visible et infrarouge, les détecteurs mesurent l'intensité I_S qui est proportionnelle au carré du champ électrique [10]. Le FPWFS ne peut donc pas estimer directement E_S à partir de $I_S = |E_S|^2$ (l'information sur la phase du champ est perdue au moment de l'enregistrement de l'image). Pour mesurer E_S, plusieurs FPWFS ont été proposés (voir la revue par Jovanovic *et al.* , 2018) pour moduler I_S spatialement (Baudoz *et al.* , 2006; Galicher *et al.* , 2008; Galicher *et al.* , 2010; Delorme *et al.* , 2016a; Gerard *et al.* , 2018; Gerard & Marois, 2020) ou temporellement (Bordé & Traub, 2006; Give'On *et al.* , 2007; Sauvage *et al.* , 2012; Paul *et al.* , 2013). Une fois E_S mesuré, il faut contrôler un ou des miroirs déformables pour minimiser $I_S = |E_S|^2$ comme expliqué dans le paragraphe suivant.

10. Plus précisément, à la moyenne temporelle du vecteur de Poynting.

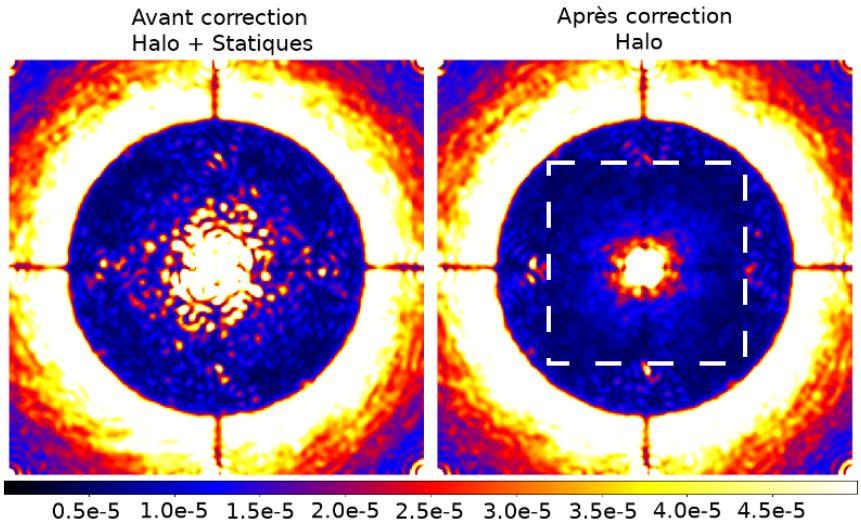

FIGURE 2.2 – *Images coronographiques obtenues en laboratoire sur le banc très haute dynamique (THD2) en simulant des aberrations turbulentes et des aberrations statiques sans (gauche) et avec (droite) un deuxième étage de correction pour créer un dark hole.*

2.2.3 Minimisation en plan focal vs optique adaptative

On fait souvent le lien entre le niveau des aberrations de phase dans la pupille et le contraste obtenu dans l'image coronographique (exemple : paragraphe 1.3.2). C'est un héritage des travaux sur les systèmes classiques d'optique adaptative qui effectivement minimisent les aberrations de phase en plan pupille. En imagerie à haute dynamique, l'objectif n'est pas de minimiser les aberrations de phase et d'amplitude en plan pupille mais de minimiser l'intensité des tavelures dans l'image scientifique derrière le coronographe (donc en plan focal). Mazoyer (2014) a montré que les deux ne sont pas équivalents. On peut s'en convaincre en étudiant l'image coronographique en présence d'une aberration sinusoïdale (image de droite de la figure 1.4). Les ondes diffractées autour des deux positions $\pm n\,\lambda/D$ interfèrent entre elles et modulent l'intensité stellaire résiduelle dans toute l'image scientifique. Voyons comment on peut tirer profit ou être limité par ces interférences en supposant qu'on utilise un miroir déformable avec N actionneurs dans le diamètre de la pupille et en considérant deux cas :

1. **Minimisation des aberrations en plan pupille** (optique adaptative classique) : on annule les aberrations de phase pour toutes les fréquences spatiales accessibles par le miroir déformable (cas idéal). On annule alors l'intensité des tavelures en-deçà de $N\,\lambda/(2\,D)$ de l'axe optique. Cependant, les tavelures qui sont au-delà de cette limite diffractent une partie de leur énergie vers les séparations inférieures à $N\,\lambda/(2\,D)$. Il en résulte un résidu de tavelures stellaires en-deçà de $N\,\lambda/(2\,D)$.
2. **Minimisation de l'intensité des tavelures en plan focal** (imagerie à haute dynamique) : on minimise cette fois-ci le champ électrique des tavelures stellaires à l'intérieur de la zone d'intérêt (le *dark hole*) qui s'étend au maximum jusqu'à la fréquence de coupure $N\,\lambda/(2\,D)$ (paragraphe 3.2 et Malbet *et al.* , 1995; Bordé & Traub, 2006; Pueyo *et al.* , 2009; Beaulieu *et al.* , 2017; Baudoz *et al.* , 2018a). Au premier ordre, cela revient à minimiser les aberrations de fréquences spatiales inférieures à $N\,\lambda/(2\,D)$ comme dans le cas précédent. Mais, la minimisation en plan focal permet également de modifier les

aberrations de fréquences inférieures à $N\,\lambda/(2\,D)$ pour minimiser le champ électrique diffracté par les aberrations de plus hautes fréquences spatiales. La minimisation est donc plus efficace et c'est de cette manière que l'on crée un *dark hole* (de forme carrée dans l'image de droite de la figure 2.2).

2.2.4 Imagerie différentielle et télémétrie

Même en utilisant deux étages de correction, il restera des tavelures dans l'image scientifique. Elles seront de moindre intensité que dans les instruments actuels mais elles existeront toujours. C'est pour cela que nous continuerons à utiliser des techniques d'imagerie différentielle pour détecter a posteriori des sources moins brillantes que les tavelures enregistrées (*data processing* sur la figure). D'après notre expérience avec les instruments actuels, nous pourrons rendre ces étalonnages a posteriori plus efficaces de plusieurs façons :

1. **Stabiliser le champ de tavelures pour ADI et RDI** grâce à des sous-systèmes appelés *low order wavefront sensor* (LOWFS, paragraphe 3.2.1), qui analyseront la lumière stellaire rejetée par le coronographe pour stabiliser les aberrations résiduelles dans la voie scientifique (Singh *et al.* , 2014; Huby *et al.* , 2015; Miller *et al.* , 2018). Il ne s'agit pas de minimiser le champ de tavelures mais de maintenir l'instrument dans un état donné en stabilisant principalement des aberrations de bas ordre spatial : centrage de l'étoile sur le coronographe (en utilisant un miroir tip-tilt), centrage de la pupille et focus. Cette stabilisation sera très utile aux techniques ADI et RDI (*Speckle/PSF stabilization* sur la figure). Cette boucle d'asservissement s'ajoute aux deux boucles du paragraphe 2.2.1.
2. **Enregistrer les paramètres caractérisant l'état de l'instrument**. Cette télémétrie (en rouge sur la figure) sera utile pour faire de la reconstruction d'images et optimiser le traitement des données a posteriori (Vievard *et al.* , 2019).
3. **Développer de nouveaux algorithmes SDI** pour traiter les données enregistrées par un *integral field spectrometer* (IFS). Chaque donnée est une images 2D constituée de multiples spectres de résolution spectrale R (un pour chaque élément de résolution angulaire de la scène observée). En 2020, la première étape est toujours de reconstruire un cube spectral d'images 2D (une image 2D de la scène pour chaque bande spectrale de résolution R). Cette opération introduit forcément du bruit numérique et n'a pas d'autre justification que notre désir de « voir » les images de la scène. Il faudrait réfléchir à des algorithmes qui traitent directement les images 2D issues de l'IFS, quitte à faire une reconstruction une fois que l'intensité des tavelures aura été minimisée pour « voir » l'image finale.
4. **Utiliser des techniques basées sur l'incohérence des lumières** venant de l'étoile et de son environnement. De telles techniques (REF) permettraient de sonder l'environnement proche de l'étoile, lieu où ADI, SDI et RDI sont limitées :
   — ADI/SDI : la modulation des tavelures et de l'image de l'exoplanète sont similaires ;
   — RDI : il est compliqué de maintenir stables les tavelures proches de l'axe optique quand on pointe le télescope vers une autre étoile.

2.2.5 Coronographes

Un autre sous-système qui pourra aussi être amélioré dans les futurs instruments est le coronographe. Jusqu'à aujourd'hui, les grandes campagnes d'observation ont été réalisées avec des coronographes de Lyot avec (Soummer, 2005) ou sans (Schneider *et al.* , 1998) apodisation. D'autres coronographes (Ruane *et al.* , 2018) permettraient pourtant d'observer plus proche de

l'étoile (i.e. plus petit *inner working angle*). Ils sont cependant moins efficaces dans les instruments actuels à cause des NCPA de basses fréquences spatiales (Vigan *et al.* , 2019) ; les tavelures stellaires proches de l'axe optique (entre 1 et $3\,\lambda/D$) diffractent jusqu'à des séparations angulaires de $\simeq 5 - 10\,\lambda/D$ [11] tandis qu'avec un coronographe de Lyot, elles sont optiquement filtrées.

2.3 Instrument coronographique de demain dans l'espace

Les coronographes étant très sensibles aux aberrations optiques, il y aurait un très grand intérêt à utiliser un instrument dans l'espace pour s'affranchir de la turbulence atmosphérique. Dans ce cas, le système d'optique adaptative classique n'est plus nécessaire et le schéma fonctionnel de l'instrument se simplifie (figure 2.3). Une optique active reste cependant indispensable pour

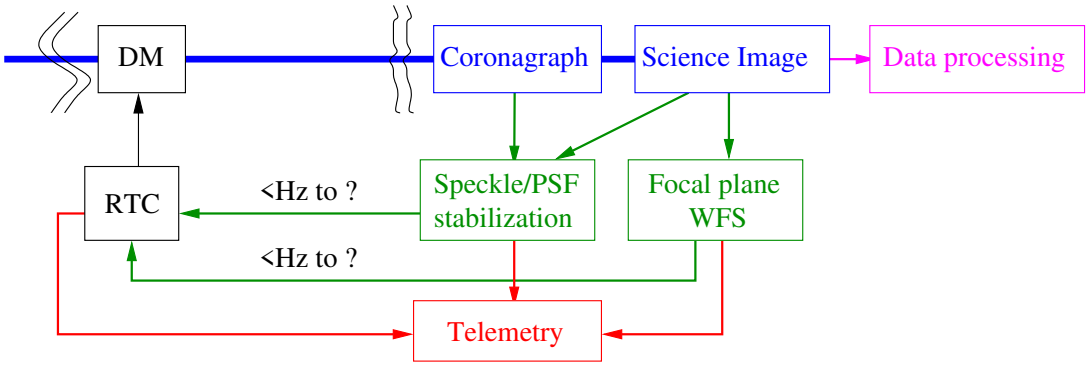

FIGURE 2.3 – *Schéma fonctionnel des futurs instruments d'imagerie haute dynamique dans l'espace : même schéma que sur la figure 2.1 sans le système d'optique adaptative.*

minimiser l'intensité des tavelures stellaires dans l'image scientifique et permettre la détection d'objets plus de 10^6 fois moins lumineux que l'étoile pointée. Comme cette technologie n'a pas encore été utilisée dans l'espace, elle est considérée comme risquée par les agences spatiales et plusieurs travaux sont en cours pour démontrer sa fiabilité derrière des ballons stratosphériques (Bryden *et al.* , 2011; Cook *et al.* , 2015; Côté *et al.* , 2018) et dans la mission spatiale Roman Space Telescope/CGI (Mennesson *et al.* , 2018).

11. Voir la figure de diffraction d'une tavelure sur la figure 1.4.

Chapitre 3

Projet de recherche

Depuis mon stage de master 1 en 2004, je travaille dans le domaine de l'imagerie des exoplanètes. Jusqu'à la fin de ma thèse en 2009, mes travaux étaient purement instrumentaux : R&D en laboratoire sur la coronographie et sur un analyseur de surface d'onde en plan focal (Galicher *et al.* , 2005; Galicher & Baudoz, 2007; Galicher *et al.* , 2008; Galicher *et al.* , 2008; Galicher, 2009; Galicher *et al.* , 2010; Galicher *et al.* , 2011). Je ne les décris pas dans ce document.

Pendant mon post-doctorat ($2010-2012$), je me suis consacré presque exclusivement à l'étude astrophysique des exoplannètes (traitement de données, interprétation, modélisation).

Depuis 2012, date de mon recrutement au Lesia sur un poste de maître de conférences, j'essaie de trouver un équilibre entre études astrophysiques (paragraphe 3.1) et travaux instrumentaux (paragraphe 3.2) sur le temps que je peux effectivement consacrer à la recherche (voir chapitre 2 de la note d'accompagnement). Cette double expertise me permet d'être investi dans plusieurs projets (paragraphe 3.3) avec pour objectifs de comprendre les limitations instrumentales actuelles afin de fabriquer des instruments qui permettent de répondre à des questions astrophysiques.

3.1 Astrophysique

Entre 2010 et 2016, j'ai travaillé sur une campagne de quatorze ans d'observations par imagerie pour déterminer la fréquence des exoplanètes orbitant dans la partie externe de leur système (paragraphe 3.1.1). Ayant fait partie du consortium GPI et étant membre actif du consortium Sphere, j'ai un accès privilégié aux observations et j'ai mené les études astrométriques et spectro-photométriques de quelques objets (paragraphe 3.1.2). J'ai également développé l'outil SpeCal qui est utilisé pour traiter l'ensemble des données enregistrées par le consortium Sphere avec les instruments Irdis et IFS (paragraphe 3.1.3).

3.1.1 Fréquence des planètes géantes gazeuses

L'objectif de mon post-doctorat à l'Institut Herzberg d'astrophysique au Canada était de traiter avec des algorithmes d'imagerie différentielle et de manière homogène l'*international deep planet survey*, 14 ans d'observations de 292 étoiles obtenues avec les instruments du moment : NIRC2, NICI, NIRI, NACO, NICMOS. J'ai découvert seize nouvelles étoiles binaires et deux nouveaux triplets d'étoiles. J'ai identifié 2279 sources ponctuelles dont la quasi-totalité étaient des étoiles de fond de champ [12].

12. Quelques objets restent à ré-observer mais la probabilité pour qu'il s'agissent d'exoplanètes est faible.

J'ai ensuite fait l'étude statistique des détections et des limites de détection pour confirmer que les jeunes Jupiter massifs sont peu fréquents dans la partie externe de leur système (fréquence inférieure à quelques pourcents). Cette fréquence devrait être plus élevée pour les planètes plus légères mais pour la mesurer, il faudra attendre la mise sur ciel des futurs instruments.

La campagne d'observation, le formalisme bayésien, l'étude par simulation Monte Carlo et les résultats sont présentés dans Galicher *et al.* (2016) (chapitre 1 des annexes). Les données réduites (images, courbes de contraste, coordonnées des objets détectés) sont disponibles sur le site `https://lesia.obspm.fr/directimaging`. Cette étude bayésienne similaire à ce qui est fait par d'autres dans la communauté repose sur de nombreuses hypothèses. J'ai d'ailleurs proposé à un étudiant en master 1 d'estimer l'impact de ces hypothèses sur les fréquences obtenues (paragraphe 1.9 de la Note d'accompagnement).

3.1.2 Études d'objets de masse planétaire

En plus des études statistiques, j'ai étudié certains systèmes en particulier dont l'objet qui orbite Folmalhaut (paragraphe 3.1.2.1) ou les planètes autour de HR 8799 (paragraphe 3.1.2.2) et de HD 95086 (paragraphe 3.1.2.3).

3.1.2.1 Fomalhaut b : une exoplanète ou autre chose ?

Au début des années 2010, certains affirmaient que l'objet orbitant Fomalhaut était une planète. D'autres soutenaient que l'objet ne pouvait pas être une planète car aucun signal n'était détecté en infra-rouge (Janson *et al.* , 2012), voire douter de la détection publiée par Kalas *et al.* (2008). J'ai alors décidé de réduire les données HST indépendamment du travail de l'équipe de Paul Kalas. J'ai confirmé que l'objet n'était pas un artefact (figure 3.1). J'ai également mesuré que la source était légèrement étendue, ce qui a été confirmé par d'autres équipes depuis (Gaspar & Rieke, 2020). Pour expliquer l'absence de détection dans l'infrarouge moyen et l'extension de la source, j'ai proposé que le signal de Fomalhaut b est soit la lumière réfléchie par un nuage de poussières orbitant autour d'une exoplanète, soit un nuage de poussières résultant de la collision de deux objets de la ceinture de Kuiper du système Fomalhaut (Galicher *et al.* , 2013b).

3.1.2.2 HR 8799 en bande M

Quelques exoplanètes ont été détectées par imagerie dans le visible et principalement dans le proche infrarouge dans les bandes spectrales Y à L. Très peu d'instruments permettent d'étudier ces objets en bande M ou N. En bande N, les observations, faites au sol, sont dominées par le fond de ciel et il est compliqué d'obtenir des données exploitables même si l'instrument Near/VLT REF nous permet quelques mesures. En bande M, le fond de ciel est moins brillant et j'ai proposé un algorithme pour l'étalonner et extraire le signal de trois des planètes orbitant HR 8799. La mesure du flux dans cette bande spectrale a permis de confirmer que les planètes se trouvaient à la transition entre naines brunes de type L et de type T avec un non-équilibre chimique entre CO et CH_4 (Galicher *et al.* , 2013a, chapitre 2 des annexes).

3.1.2.3 HD 95086

Un autre objet sur lequel j'ai travaillé est la planète HD 95086 b. J'ai traité les données obtenues pendant le temps de vérification scientifique au moment de l'installation de l'instrument GPI et j'ai extrait le signal de la planète en bandes H et K. Nous avons alors confirmé que la planète

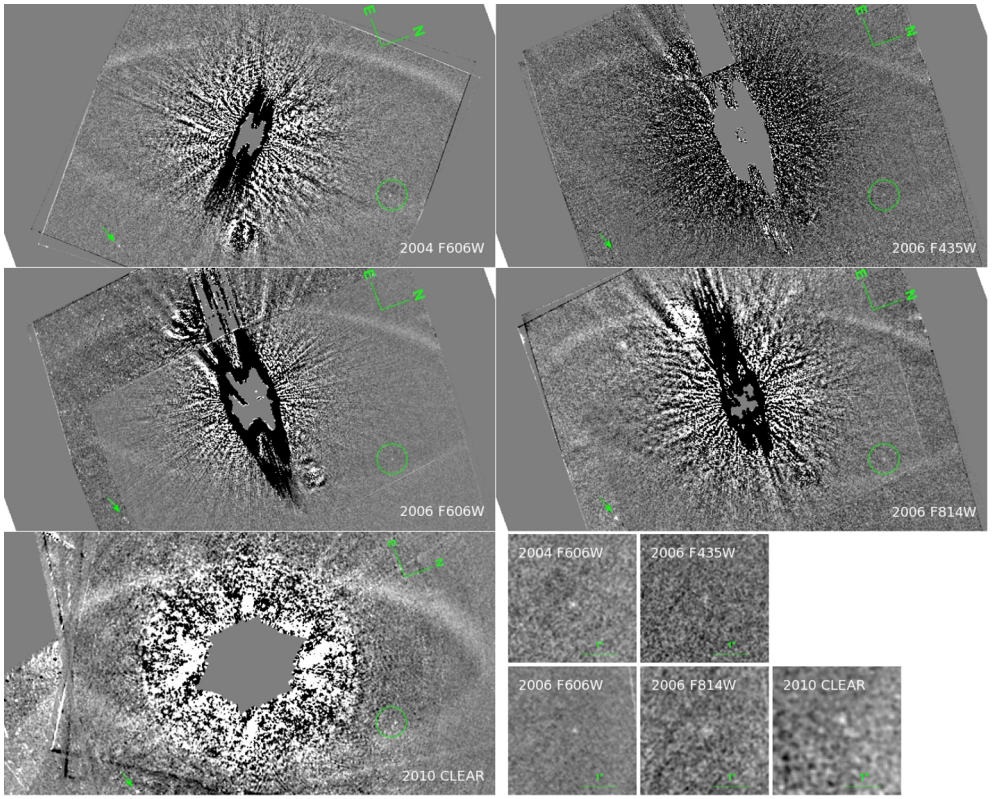

FIGURE 3.1 – *Images de l'environnement de Fomalhaut dans différents filtres spectraux de l'instrument ACS du HST et à différentes époques (précisés en bas à droite de chaque image). Le disque (anneau) et l'objet b (entouré en vert) sont détectés dans toutes les images. Les images en bas à droite sont des zooms sur la région autour de l'objet b. (Galicher* et al. *, 2013b)*

est à la transition L-T des naines brunes. Nous avons aussi montré qu'il y avait trop d'incertitudes à l'époque pour savoir quel modèle d'atmosphère et d'évolution reproduisait au mieux les données. Plus de détails sont fournis dans Galicher *et al.* (2014, chapitre 3 des annexes).

3.1.3 Outil SpeCal pour le consortium Sphere

Pour traiter l'ensemble des données Sphere dans le cadre des *guaranteed time observations* (GTO), une chaine de réduction automatique a été développée (Delorme *et al.* , 2017b). La première étape trie les données et applique les étalonnages classiques (mauvais pixels, *flat*, *sky*) et fournit des cubes d'images coronographiques centrées et l'image associée de l'étoile non coronographiée. Pour les données enregistrées par les instruments Irdis (Dohlen *et al.* , 2008) et IFS (Claudi *et al.* , 2008), j'ai développé la deuxième étape de la chaîne de réduction : SpeCal (pour *Speckle Calibration*, chapitre 4 des annexes, Galicher *et al.* , 2018) qui est utilisé pour :

- étalonner les tavelures stellaires par imagerie différentielle (ADI, SDI, ASDI, RDI) grâce à plusieurs algorithmes (classical ADI, Loci, TLoci, PCA, voir paragraphe 1.3.5) ;
- extraire l'astrométrie et la photométrie des sources ponctuelles détectées ;
- calculer les limites de détection ;
- nourrir la base de données Sphere qui contient tous les résultats des observations (limites de détection, images, astro-spectrophotométrie des sources ponctuelles, télémétrie, etc).

3.2 Instrumentation

Les figures 2.1 et 2.3 donnent les schémas fonctionnels des futurs instruments au sol et dans l'espace tels qu'on les conçoit aujourd'hui. Ils sont plutôt simples mais les choses se compliquent quand on liste tous les composants et toutes les techniques existants pour chaque sous-système. Il existe des dizaines de coronographes stellaires, de nombreux FPWFS, plusieurs algorithmes de contrôles des miroirs déformables. Quelles techniques choisir ? Quelle est la meilleure combinaison coronographe+FPWS+contrôleur ? Chacun a sa réponse mais il n'y a pas de consensus. D'ailleurs, les réponses dépendent certainement des objectifs scientifiques : observations spatiales ou depuis le sol, études d'exoplanètes ou de disques circumstellaires, mesures spectrométriques ou polarimétriques, études de l'environnement très proches de l'étoile.

Une chose est sure, pour trouver la meilleure configuration, il est indispensable de comparer les différentes techniques dans les mêmes conditions. C'est ce que nous faisons en laboratoire avec Pierre Baudoz depuis une dizaine d'années grâce au banc très haute dynamique (THD, paragraphe 3.2.1). Au cours de ces études, entre autres, deux techniques d'analyse de surface d'onde en plan focal ont donné des résultats très intéressants et nous les avons testées sur télescope à l'Observatoire Palomar et au *Very Large Telescope* (paragraphe 3.2.2).

3.2.1 Le banc très haute dynamique

3.2.1.1 Le banc THD

En 2007, la première version du banc THD (figure 3.2) a été développée pour tester en lumière visible à 640 nm un FPWFS (voir paragraphe 2.2.2), la *self-coherent camera* (SCC), associée au coronographe à quatre quadrants (FQPM, Mas *et al.* , 2010; Mazoyer *et al.* , 2013, 2014). Cependant, dès le départ, le banc a été conçu avec un objectif plus large de comparaison

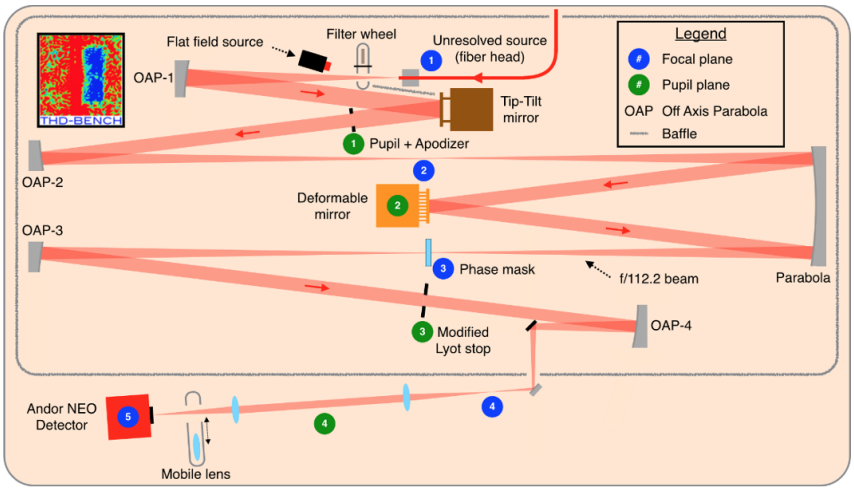

FIGURE 3.2 – *Schéma optique du banc THD1.*

de différentes techniques dans les mêmes conditions dans le domaine visible (400 nm à 900 nm). Pour cela, un accès facile a été privilégié avec possibilité de remplacer rapidement le masque coronographique (plan focal 3 sur la figure) ou d'ajouter des optiques dans des plans pupilles (pastilles vertes) et focaux (pastilles bleues) en amont et en aval du masque coronograhique. Plusieurs filtres spectraux permettaient également d'étudier les performances en fonction de la

longueur d'onde et le banc n'etait constitué que d'optiques réflectives à l'exception d'une fenêtre protectrice devant le miroir déformable. Cela permettait d'avoir un banc optique avec très peu d'aberrations chromatiques.

Sur ce banc, nous avons atténué la lumière stellaire d'un facteur 50 millions à quelques éléments de résolution de l'étoile (contraste de 2×10^{-8} entre 5 et 13 λ/D, Mazoyer *et al.* , 2014) même si l'utilisation d'un seul miroir déformable nous limitait à la moitié du champ d'observation comme le montre la figure 3.3.

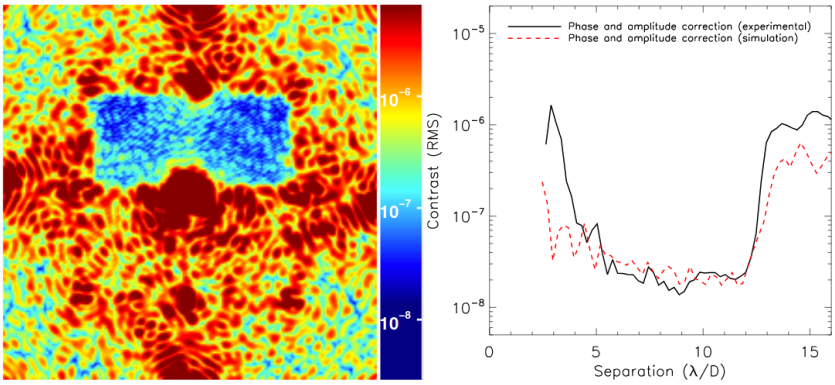

FIGURE 3.3 – **Gauche :** *Image coronographique obtenue sur le banc THD1 montrant un dark hole (DH, zone sombre où l'intensité des tavelures est minimisée).* **Droite :** *Écart-type azimutal de l'intensité du résidu stellaire calculé dans le DH en fonction de la séparation angulaire à l'étoile (en noir) et la prédiction numérique (tirets). Mazoyer* et al. *(2014).*

Le banc THD1 nous a permis de mesurer les performances de plusieurs techniques présentes à différents niveau du schéma fonctionnel d'un instrument spatial (figure 2.3).

- **Tip-tilt**
  - Une boucle d'asservissement LOWFS (paragraphe 2.2.4) pour contrôler le miroir tip-tilt et assurer le centrage de l'image de l'étoile sur le centre du masque coronographique en utilisant la lumière rejetée par le coronographe (Mas *et al.* , 2012b).
- **Imagerie différentielle**
  - SCC pour l'imagerie différentielle basée sur l'incohérence entre les lumières de l'étoile et de son environnement (paragraphe 2.2.4, Baudoz *et al.* , 2012).
- **Coronographes en large bande spectrale**
  - le coronoraphe FQPM à multi-étages (Delorme *et al.* , 2014; Galicher *et al.* , 2014) ;
  - le coronographe *dual zone phase mask* (Delorme *et al.* , 2016b; Galicher *et al.* , 2014).
- **Analyseurs de surface d'onde en plan focal**
  - la SCC associée au coronographe FQPM en lumière quasi-monochromatique (Mas *et al.* , 2012a; Mazoyer *et al.* , 2012, 2013, 2014) ;
  - la SCC à multi-références associées au FQPM à multi-étages et au DZPM (chapitre 5, Delorme *et al.* , 2016a; Galicher *et al.* , 2014).

3.2.1.2 Le banc THD2

En 2014, nous avons ajouté un deuxième miroir déformable dans le train optique (DM-1 sur la figure 3.4), puis un emplacement pour un troisième DM (DM-2), pour pouvoir compenser à la

fois les aberrations de phase et d'amplitude sur l'ensemble du champ d'observation (Baudoz *et al.* , 2018b). Nous avons également ajouté une lame de phase mobile qui permet de simuler une tur-

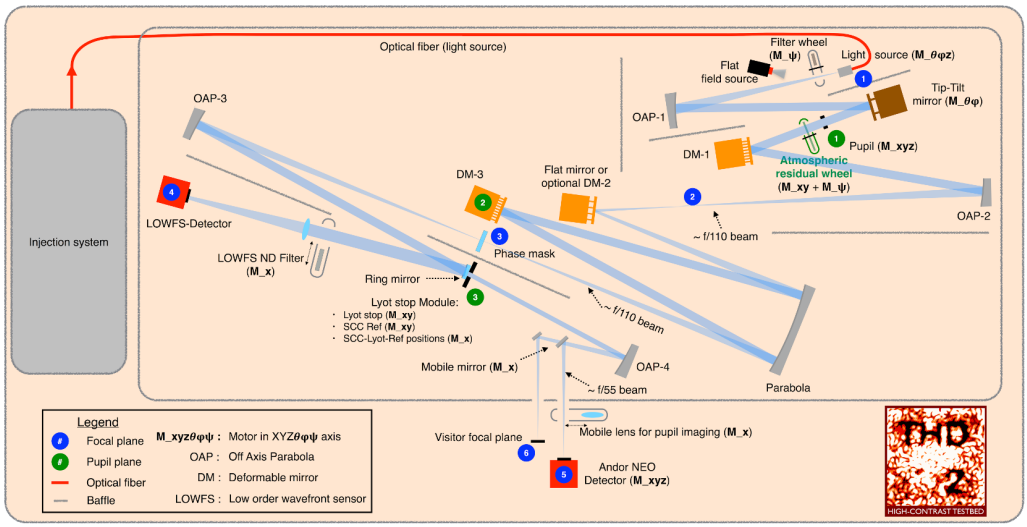

FIGURE 3.4 – *Schéma optique du banc THD2.*

bulence atmosphérique qui aurait été compensée par une optique adaptative de type Saxo/Sphere dans de bonnes conditions d'observation (*Atmospheric residual wheel* sur la figure). Comme dans la première version du banc THD, plusieurs plans focaux et pupilles sont accessibles, ce qui permet de tester de nombreuses techniques dans les mêmes conditions. Enfin, nous avons ajouté de nombreux systèmes qui permettent de mesurer les paramètres de l'environnement : une dizaine de capteurs de température et d'humidité répartis sur le banc, un détecteur pouvant focaliser l'image sur l'optique au choix (étude de la lumière diffusée et de la présence de poussières, Potier *et al.* , 2018), fluxmètre et spectromètre dans le système d'injection (figure 3.5).

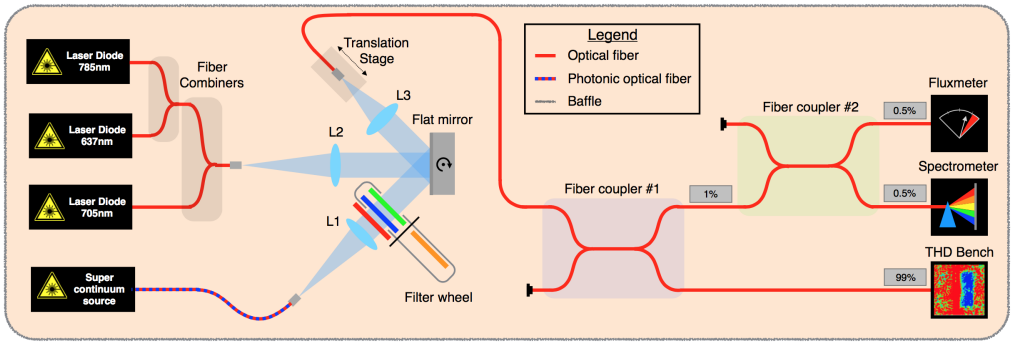

FIGURE 3.5 – *Schéma optique du système d'injection en amont du banc THD2. Utilisation au choix d'une diodes laser (637, 705, 785 nm) ou d'une source supercontinuum (500 à 900 nm) associée à des filtres spectraux, et mesure en permanence pendant l'expérience du flux et du spectre.*

Plusieurs équipes nous ont contactés pour tester leurs composants ou techniques sur le banc THD2 car d'une part, les performances atteintes sont uniques en Europe (Mazoyer *et al.*

, 2019) et d'autre part, le banc est facilement accessible car à l'air libre (et non pas dans le vide comme les bancs du *Jet Propulsion Laboratory*, Cady *et al.* , 2017; Ruane *et al.* , 2019). Ces collaborations nous ont permis de tester, en plus de nos propres techniques, de nombreuses techniques coronographiques et, d'analyse et de contrôle de surface d'onde mises en jeu dans les schémas fonctionnels des futurs instruments pour le sol (figure 2.1) ou pour l'espace (figure 2.3).

- **Coronographes**
  - *Six level phase mask coronagraph* avec l'Université de Shanghai (Patru *et al.* , 2018) ;
  - *Phase apodized pupil Lyot coronagraph* (PAPLC) avec Emiel Por du SRON ;
  - *Eigth octants phase mask* avec Naoshi Murakami de l'Université de Hokkaido ;
  - *Vortex phase mask* avec Jun Nishikawa de NAOJ ;
  - *Vector vortex phase mask* (Lopez et al., in prep.) ;
  - Optimisation de la fabrication des FQPM (Bonafous *et al.* , 2016) ;
  - *Tip-tilt Gaussian mask* avec Ben Gerard et Christian Marois de l'université de Victoria (Gerard *et al.* , 2019b) ;
  - *Wrapped vortex phase mask* (Galicher *et al.* , 2020).
- **Tip-tilt**
  - la boucle d'asservissement du miroir tip-tilt est désormais utilisée systématiquement et elle fonctionne avec tous les coronographes que nous avons testés sauf le PAPLC qui ne rejette pas suffisamment de lumière dans le plan du diaphragme de Lyot.
- **Chromatisme des aberrations** (de Jonge *et al.* , 2018).
- **Diffusion par les optiques** (Potier *et al.* , 2018).
- **Analyseurs et contrôleurs de surface d'onde en plan focal**
  - SCC (analyseur et contrôleur) associée à tous les coronographes testés sauf le PAPLC ;
  - *Pair-wise probing* qui module temporellement le champ électrique et première comparaison entre modulation temporelle et spatiale (Potier *et al.* , 2020a) ;
  - Coffee qui utilise aussi une modulation temporelle (Herscovici-Schiller *et al.* , 2018a,b) ;
  - *Electric field conjugation* (EFC) qui permet de contrôler les miroirs déformables à partir d'une estimation fournies par un FPWFS a été associé à *Pair wise* et Coffee.

Tester ces nombreuses techniques dans des conditions similaires, étudier précisément les possibles limitations (lumière diffusée, effets de polarisation, vibrations du banc, etc) et comparer tout cela avec des simulations numériques nous permettent de comprendre les détails de l'imagerie très haute dynamique [13]. À l'été 2020, nous sommes capables d'atténuer la lumière de l'étoile centrale d'un facteur 500 millions, ce qui signifie que l'intensité du résidu stellaire est 2×10^{-9} celle de l'étoile observée sans coronographe (figure 3.6). Nous ne pourrons pas améliorer la performance en atténuation avec le banc actuel (précision de déplacement des miroirs déformables, vibration du tip-tilt, etc). Cela est cependant suffisant pour préparer les futurs instruments au sol et dans l'espace comme le *coronagraph instrument* du *Roman Space Telescope* (paragraphe 3.3).

3.2.2 Mise en œuvre à Palomar et sur Sphere

Les études paramétriques réalisées par simulations numériques et en laboratoire sur les bancs THD nous ont permis de maîtriser la *self-coherent camera* (SCC) et *pair-wise/EFC*. Ces deux techniques nous permettent indépendamment l'une de l'autre d'atténuer la lumière stellaire d'un facteur 500 millions en laboratoire. Nous avons alors décidé de tester la SCC sur l'instrument *Stellar double coronagraphs* (SDC) au Mont Palomar (paragraphe 3.2.2.1) et *pair-wise/EFC* sur l'instrument Sphere au VLT (paragraphe (3.2.2.2).

13. Et il ne faut jamais oublier que *The devil is in the detail*!

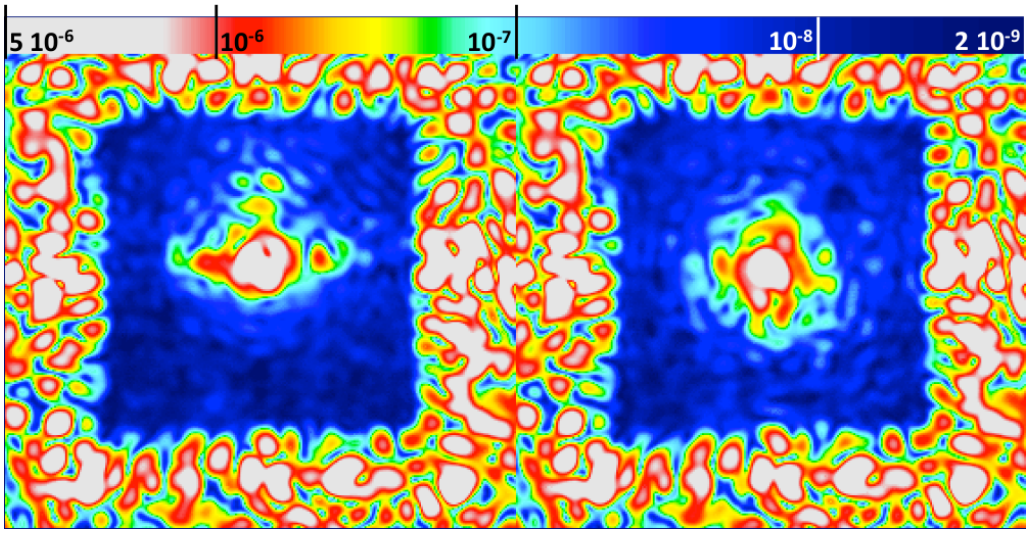

FIGURE 3.6 – *Images coronographiques obtenues sur le THD2 avec un FQPM et une SCC en lumière monochromatique (785 nm) en minimisant l'intensité des tavelures stellaires dans tout le champ autour de l'étoile (droite) et dans la partie basse du champ uniquement (gauche). L'échelle de couleur donne le rapport de flux par rapport à l'étoile (i.e. contraste).*

3.2.2.1 Self-coherent Camera sur le SDC à Palomar

La *self-coherent camera* est une technique très intéressante car elle permet de mesurer le champ électrique à partir d'une unique image coronographique. De plus, on peut utiliser a posteriori la modulation spatiale pour faire de l'imagerie différentielle. Le seul inconvénient de la technique est le besoin d'avoir des optiques deux fois plus grandes que la normale après le diaphragme de Lyot. Cela signifie qu'il n'est généralement pas possible d'implémenter la SCC dans un instrument déjà construit [14] L'instrument *stellar double coronagraph* (SDC, Mawet *et al.* , 2014; Bottom *et al.* , 2016) qui est installé au foyer du télescope Hale de 5 m de diamètre sur le Mont Palomar fait figure d'exception. Une des configurations optiques du SDC nous a permis d'implémenter la SCC associée à un coronographe à masque vortex. Dans cette configuration, c'est comme si nous utilisions un télescope hors-axe de 1, 5 m de diamètre.

Des algorithmes sont utilisés avant chaque nuit pour minimiser les NCPA dans l'instrument SDC à partir de l'image enregistrée sur source interne et sans coronographe. Ils minimisent uniquement les aberrations de phase en plan pupille (voir le paragraphe 2.2.3) et ils ne peuvent pas corriger les aberrations introduites par tous les composants de l'instrument (dont le masque vortex). Quand on enregistre une image coronographique sur source interne après cet étalonnage, on obtient l'image de gauche de la figure 3.7.

L'image de droite montre l'image coronographique obtenue après minimisation des tavelures dans tout le champ grâce à la SCC. Cet étalonnage des NCPA est de bien meilleure qualité que l'étalonnage habituel : l'intensité des tavelures a été diminuée d'un facteur 4 à 20 entre 1, 5 et $5\,\lambda/D$ de l'étoile. Cela augmente considérablement la zone dans laquelle des exoplanètes peuvent être recherchées. L'étalonnage n'est cependant pas aussi marqué que ce qui est fait en laboratoire (« on ne voit pas le DH »). Et ceci est dû à plusieurs raisons. Proche de l'axe optique, la lumière résiduelle vient de la qualité du masque vortex en plan focal, d'une réflexion

14. car la taille des optiques est choisie aussi petite que possible pour rendre l'instrument compact.

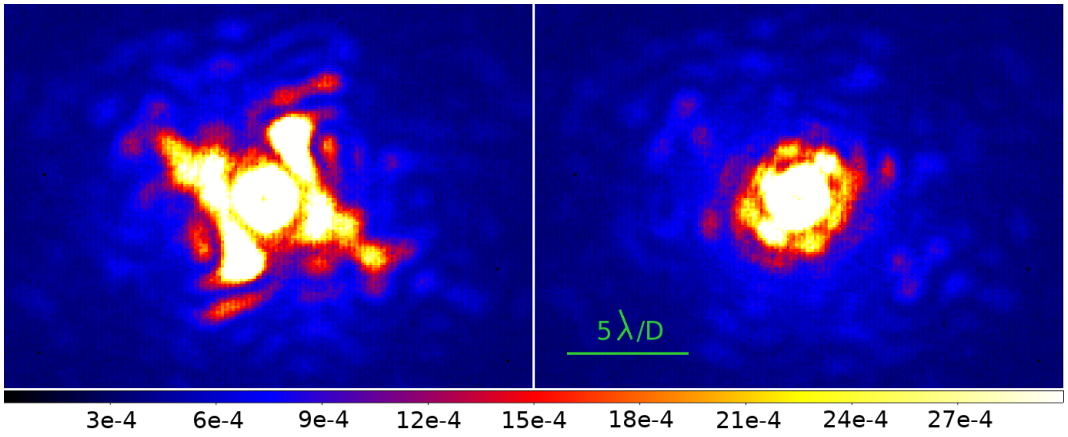

FIGURE 3.7 – *Images coronographiques obtenues sur le SDC avec un masque vortex et un filtre étroit (filtre Br-γ, $\lambda_o = 2,166\,\mu m$, $\Delta\lambda = 0,020\,\mu m$) après étalonnage par la procédure habituelle de l'observatoire (gauche) et après minimisation grâce à la SCC (droite). L'échelle de couleur donne le rapport de flux par rapport à l'étoile (i.e. contraste). Galicher* et al. *(2019)*

sur le diaphragme de Lyot et d'un centrage de l'image stellaire mal stabilisé sur le coronographe (*jitter*) pendant le temps de pose minimum du détecteur ($1,5\,$s). Loin de l'axe optique, nous ne pouvions pas mesurer l'intensité des tavelures par manque de dynamique sur le détecteur. Il n'était donc pas possible de les atténuer. La prochaine étape de démonstration de la SCC comme FPWFS serait de faire le même type de correction pendant des observations sur ciel. Pour cela, il faudrait un détecteur plus rapide que celui utilisé en 2018 au Mont Palomar.

3.2.2.2 Pair wise/EFC sur Sphere au VLT

Une partie de la thèse d'Axel Potier a été d'implémenter les techniques *pair-wise* (PW) et EFC sur le banc THD2 (Potier *et al.* , 2020a). Comme les performances étaient similaires à celles obtenues avec la SCC et comme PW/EFC ne demande aucune modification de la configuration optique, nous avons décidé de tester la technique sur l'instrument Sphere. Ces tests ont été réalisés de jour sur source interne par tranches de une heure ou deux sur le temps libre de Zahed Wahhaj et Julien Milli de l'ESO. Axel Potier a développé un code qui est maintenant presque totalement automatisé et qui permet au *support astronomer* d'utiliser la source interne de l'instrument pour créer en quelques minutes un grand *dark hole* centré sur l'axe optique (image du centre de la figure 3.8) ou un *dark hole* plus profond sur la moitié du champ d'observation (image de droite).

Minimiser l'intensité sur le dark hole centré revient à minimiser les tavelures créées par des aberrations de phase uniquement. Le résidu est constitué des tavelures stellaires créées par les aberrations d'amplitude et par la figure de diffraction du coronographe PAPLC (qui ne filtre pas toute la lumière stellaire même en l'absence d'aberrations). Quand on se restreint à la moitié du champ d'observation (image de droite), on peut minimiser l'intensité de toutes les tavelures, peu importe leur origine. Dans ce cas, le résidu est environ $2,5$ millions de fois moins brillant que l'intensité de l'étoile observée sans coronographe entre $150\,$mas et $650\,$mas (contraste de 4×10^{-7}, Potier *et al.* , 2020b). Cela est plus de 10 fois mieux que la performance actuelle de l'instrument Sphere sur source interne. Nous prévoyons des tests sur ciel pour obtenir le même gain. Si nous réussissons, nous pourrons détecter des objets plus proches et plus ténus de leur étoile que ce qui a été fait jusqu'à aujourd'hui.

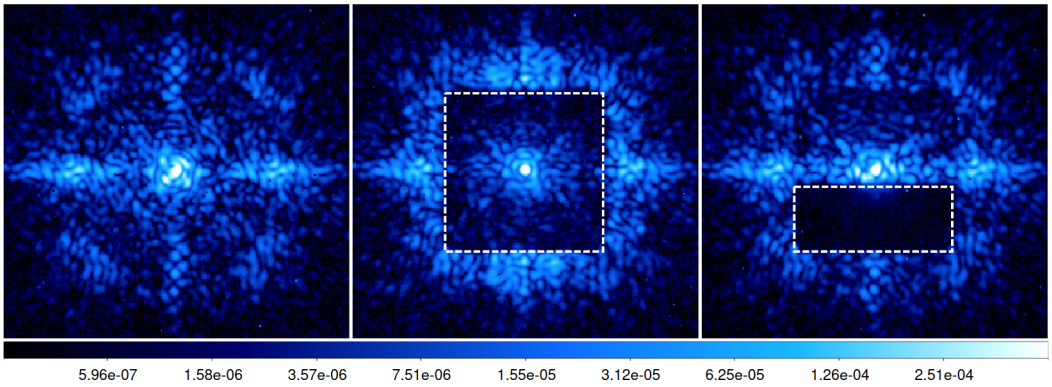

FIGURE 3.8 – *Images coronographiques obtenues sur Sphere avec un apodized pupil Lyot coronagraph (APO1/ALC2) dans le filtre H3 ($\lambda_o = 1,667\,\mu m$, $\Delta\lambda = 0,054\,\mu m$) après étalonnage par la procédure habituelle de l'observatoire (gauche), après minimisation grâce à PW/EFC dans toute la zone d'influence du miroir déformable (centre) et dans la moitié du champ d'observation (droite). L'échelle de couleur donne le rapport de flux par rapport à l'étoile (i.e. contraste). (Potier* et al. *, 2020b)*

3.3 Projets

Dans les années à venir, je prévois de consacrer mon temps de recherche (voir chapitre 2 de la note d'accompagnement) à plusieurs projets dont les principaux sont

Instrument CGI du Roman Space Telescope : Notre équipe du Lesia, l'Onera, le Lam et l'Oca commençons une collaboration, sous la tutelle du Cnes, pour optimiser la rapidité de convergence de la boucle de correction des aberrations quasi-statiques dans l'intrument CGI (FPWFS). Si nos résultats sont positifs, ils pourront être utilisés par le JPL dans l'instrument en vol. L'utilisation du banc THD2 est primordiale dans ce projet pour tester les solutions envisagées dans des conditions extrêmes de contraste. Je participerai à plusieurs niveaux à ce projet : propositions de nouveaux algorithmes, tests en laboratoire, évaluation de l'impact sur les planètes et disques détectables par CGI.

Instrument Sphere+ : Notre équipe du Lesia est PI de la proposition d'améliorations de l'instrument Sphere pour observer l'environnement proche des étoiles [15]. Une des améliorations consiste à ajouter un deuxième étage d'optique adaptative pour entre autres compenser les NCPA. Je travaillerai sur la façon de coupler les différentes boucles et une fois sur ciel, j'étudierai les environnements stellaires (exoplanètes, disques).

Dicos : Il s'agit d'un projet Cnes d'instrument coronographique de démonstration placé derrière un ballon stratosphérique. Je contribuerai au design de la partie haute dynamique (coronographe et boucle d'asservissement).

D'autres projets attireront peut-être mon attention (exploitation des données Micado et JWST par exemple). À plus longs termes, il y aura [16] la définition et l'exploitation des projets Luvoir (Gong *et al.* , 2019) et Habex (Gaudi *et al.* , 2020) et du *planetary camera and spectrograph* pour l'*extremely large telescope* (Kasper *et al.* , 2013). Les projets astrophysiques et instrumentaux intéressants ne manquent pas, le temps oui.

15. Plus proche et plus ténu que ce que ne peut faire Sphere.
16. peut-être avant ma retraite...

Troisième partie

Note d'accompagnement

Chapitre 1

Encadrement d'étudiants et de jeunes chercheurs

1.1 Lucie Leboulleux (post-doc) : Coherence differential imaging

En 2018, j'ai obtenu un financement IrisOcav pour contracter un chercheur postdoctorant pendant deux ans. J'ai sélectionné Lucie Leboulleux qui a commencé à travailler au Lesia en février 2019. Les deux objectifs principaux de son postdoc sont de :

- développer un formalisme mathématique pour accélérer les simulations numériques d'images obtenues en longue pose par des télescopes au sol (i.e. comment simuler une telle image en ne faisant qu'un tirage aléatoire de l'aberration de phase plutôt qu'en moyennant plusieurs dizaines de milliers d'écrans de phase, Leboulleux et al., in prep.).
- simuler numériquement l'interaction entre deux boucles d'asservissement pour préparer l'instrument Sphere+, amélioration de l'instrument Sphere (Boccaletti *et al.* , 2020b).

1.2 Garima Singh (post-doc) : Sphere+ et PCS/ELT

Garima Singh est en postdoctorat au Lesia avec Pierre Baudoz depuis juin 2018 (bourse Marie Curie) et je participe à son encadrement. Elle a travaillé sur l'analyse et le contrôle de surface d'onde en plan focal dans les conditions d'un télescope au sol. Pour cela, elle a utilisé le système de lame de phase motorisée pour simuler en laboratoire un résidu de phase similaire à ce qui est observé derrière l'optique adaptative de l'instrument Sphere (paragraphe 3.2.1.2 du dossier de synthèse). Puis, elle a obtenu en laboratoire les premiers résultats d'une corrrection active d'aberrations de phase statiques derrière une optique adaptative en utilisant la *self-coherent camera* (figure 2.2 du dossier de synthèse). Les études en laboratoire qu'elle a menées seront utiles pour optimiser Sphere+ et le futur instrument PCS/ELT (Kasper *et al.* , 2013).

1.3 Tobias Schmidt (post-doc) : Astro-photométrie avec Sphere

Tobias Schmidt a travaillé deux ans avec Anthony Boccaletti et moi-même (bourse ANR, PI Anne-Marie Lagrange). Il a utilisé la chaîne de réduction de données du consortium Sphere et en particulier, l'outil SpeCal (Galicher *et al.* , 2018) pour extraire des informations sur l'astrométrie et la spectro-photométrie de compagnons substellaires (Delorme *et al.* , 2017; Ginski *et al.* , 2018; Cheetham *et al.* , 2018).

1.4 Fabien Patru (post-doc) : coronographie en large bande

De 2016 à 2018, Fabien Patru a travaillé pour Pierre Baudoz et moi-même. Nous avons caractérisé sur le banc THD2 de nombreux masques de phase coronographiques fabriqués par le laboratoire GEPI : des masques à quatre quadrants (Bonafous *et al.* , 2016) et des *six level phase mask* (SLPM). Le second type de masque est en théorie aussi efficace que le premier mais sur de plus larges bandes spectrales. Fabien a réussi à comprendre la plupart des observations faites en laboratoire grâce à des simulations numériques précises des SLPM (Patru *et al.* , 2018).

1.5 J.-R. Delorme (master 2 et thèse) : analyse de surface d'onde en large bande

Jacques-Robert Delorme m'a contacté en 2013 pour un stage de master 2. Nous avons réalisé les tests préliminaires d'un analyseur de surface d'onde en large bande qui utilise le principe de la *self-coherent camera* : la *multi-reference SCC*. J'ai présenté les résultats du stage à la conférence AO4ELT (Galicher *et al.* , 2013a).

Jacques-Robert a ensuite fait sa thèse de doctorat avec moi. En collaboration avec des collègues du Laboratoire d'astrophysique de Marseille (Ketjil Dohlen et Mamadou N'Diaye), nous avons réussi à atténuer la lumière stellaire d'un facteur $5\,10^7$ entre 5 et $17\,\lambda/D$ sur une bande spectrale de 250 nm autour de 675 nm (37% de bande passante) en utilisant un *dual zone phase mask* (Delorme *et al.* , 2016b). Dans un deuxième temps, Jacques-Robert a continué ses travaux sur la *multi-reference* SCC. Nous avons réussi à estimer et contrôler les aberrations de phase statique à partir de l'image coronographique enregistrée avec une bande passante de 13% (600 nm à 680 nm Delorme *et al.* , 2016a). Jacques-Robert a alors continué sa carrière à Caltech et il vient d'accepter un poste d'*AO scientist* à l'Observatoire Keck.

1.6 Axel Potier (thèse) : analyse et contrôle de surface d'onde

Axel Potier est en thèse avec Pierre Baudoz, Anthony Boccaletti et moi-même. Ses travaux en laboratoire (Potier *et al.* , 2018, 2020a) et sur Sphere (Potier *et al.* , 2020b) ont déjà été présentés aux paragraphes 3.2.1.2 et 3.2.2.2 du dossier de synthèse. Axel soutiendra en septembre 2020 et a été accepté en post-doctorat au *jet propulsion laboratory* à la Nasa.

1.7 Ben Gerard (thèse) : coronographie et imagerie différentielle

Depuis mon post-doctorat à l'institut Herzberg de Victoria en Colombie Britanique, je suis en contact régulier avec Christian Marois. Depuis quelques années, il souhaite implémenter une *self-coherent camera* dans plusieurs instruments (GPI, un instrument à $10\,\mu$m, voire un instrument pour le *Thirty meter telescope*). Pour travailler sur plusieurs idées évoquées au cours de nos discussions, Christian a engagé Ben Gerard. Celui-ci a proposé un masque de phase coronographique optimisé pour l'utilisation de la *self-coherent camera* derrière un télescope terrestre (Gerard *et al.* , 2019a). J'ai obtenu un financement pour la fabrication de ce masque et j'ai accueilli Ben Gerard pendant un mois début 2019 pour que nous testions ce masque sur le banc THD2 (Gerard *et al.* , 2019b).

1.8 Coline Lopez (Master 2) : coronographie en large bande

En 2019, Coline Lopez m'a contacté pour une étude bilbiographique sur les exoplanètes. L'objectif était d'analyser quelques articles scientifiques et de les résumer pour un public de non-spécialistes (principalement les autres étudiants de son master d'optique).

Coline m'a ensuite demandé d'encadrer son stage de master 2. Je lui ai proposé de tester un coronographe *vector vortex* en laboratoire sur le banc THD2. La performance de ce coronographe, constitué essentiellement d'un masque de phase fabriqué en matériaux biréfringents, est peu sensible au chromatisme d'après la théorie. Le stage de Coline nous a montré que pratique et théorie ne sont pas toujours en accord. Nous sommes encore en train d'écrire proprement la propagation des différents états de polarisation dans le montage qui incluent polariseurs linéaires, lame quart d'onde et le *vector vortex*. Nous espérons publié les résultats dans les mois à venir (Lopez et al. in prep).

1.9 Tristan Madeleine (Master 1) : fréquence des exoplanètes

Pour déterminer la fréquence des planètes géantes gazeuses dans la partie externe des systèmes exoplanétaires (demi-grand axe plus grand que 5 unités astronomiques), les données fournies par les instruments d'imagerie sont essentielles car les autres techniques de détection ne permettent pas de sonder ces régions.

Pendant son stage de master 1, Tristan Madeleine devait répondre à la question suivante : Comment varie la fréquence obtenue quand on modifie les différentes hypothèses de travail (distributions supposées, modèle de luminosité) ? Il a alors travaillé sur un échantillon de 356 étoiles (Lafrenière *et al.* , 2007b; Chauvin *et al.* , 2010; Galicher *et al.* , 2016) et il a montré que

- le choix des modèles donnant la luminosité des exoplanètes et le choix des distributions choisies pour les paramètres orbitaux (excentricité et demi-grands axes), ainsi que pour la masse et l'âge de l'exoplanète n'ont qu'un impact mineur sur la fréquence obtenue ;
- il faudrait augmenter énormément la sensibilité des instruments pour pouvoir différentier deux échantillons avec des distributions différentes en masse exoplanétaire ou en demi-grand axe (si aucune nouvelle détection n'est faite).

Ces conclusions seront certainement à revoir quand les limites de détection seront telles que plusieurs dizaine d'exoplanètes auront été détectées par imagerie.

1.10 Mona El Morsi (Master 1) : modulation temporelle d'images coronographiques

Mona El Morsi a fait son stage de master 1 avec Daniel Rouan. Elle étudiait la modulation temporelle de l'intensité des speckles dans une image coronographique. Pour cela, elle utilisait un miroir déformable dont elle faisait varier la forme. Daniel Rouan m'a demandé de co-encadrer le stage. J'ai donc aidé Mona à aligner les optiques sur le banc d'expérimentation, à contrôler le miroir déformable et à établir un protocol expérimental. Nous avons alors interprété les données qu'elles a enregistrées et avons conclu que la technique testée ne permettait pas d'améliorer la qualité des images coronographiques.

1.11 Sofiane Meziani (Master 1) : coronographie stellaire

Daniel Rouan m'a demandé de co-encadrer un autre stagiaire de M1, Sofiane Meziani. L'objectif du stage était de tester un masque de phase coronographique proposé par Daniel Rouan à la conférence *In the Spirit of Lyot* en 2015. J'ai donné accès à Sofiane à un banc optimisé pour la caractérisation des masques de phase et je l'ai aidé à mesurer les performances de son masque.

1.12 Yusuke Komuro (Master 1) : coronographe à huit octants

Naoshi Murakami de l'université de Hokkaido et Jun Nishikawa du *National Observatory of Astronomy of Japan* sont venus en décembre 2015 au Lesia pour tester deux types de coronographes sur le banc THD2 : des masques à huit octants (Murakami *et al.* , 2016) et des masques vortex. Pour la deuxième campagne de tests qui a eu lieu en janvier 2017, j'ai obtenu un financement pour que Yusuke Komuro, étudiant en master 1, puisse rester travailler un mois dans notre équipe. Il a ainsi eu accès au banc THD2 sur lequel nous avons testé un masque coronographique à huit octants et un masque vortex que lui avait laissés ces directeurs Naoshi Murakami et Jun Nishikawa.

1.13 Andréa Capomassi et Benjamin Steir (ingénieurs) : simulation optique d'une OA

Benjamin Steir et Andréa Capomassi étaient étudiants à l'école d'ingénieurs Denis Diderot (EIDD). Leur projet d'ingénieur au sein de notre équipe au Lesia avait pour objectif de concevoir un montage opto-mécanique pour simuler les résidus optiques d'une optique adaptative similaire à Saxo/Sphere (Fusco *et al.* , 2016). Ils ont fait une étude de marché à la fois pour la lame de phase qui introduit les aberrations de phase et pour la mécanique qui doit faire tourner cette lame de phase. Ils ont alors écrit un cahier des charges pour que notre équipe puisse contacter les fournisseurs.

1.14 Zineb Bouharras (ingénieur) : masque de phase polarisant

Pendant son projet d'ingénieur à l'EIDD, Zineb Bouharras a caractérisé optiquement des polariseurs linéaires et des lames quart d'onde. Elle en a déduit la précision de fabrication de ces optiques. Ensuite, elle a utilisé ces polariseurs et lames quart d'onde pour étudier un masque de phase vortex constitué de cristaux liquides polymérisés.

Chapitre 2

Répartition du temps de travail

Une question qui revient souvent quand je donne des conférences à des scolaires ou au grand public est « Quelle est votre journée type ? ». J'explique alors qu'en tant que maître de conférences, je partage mon temps comme indiqué sur la figure 2.1 entre

- (en bleu foncé sur la figure) la recherche (incluant les demandes de financements) ;
- (orange) l'encadrement de personnels (étudiants, ingénieurs, recrutement), l'organisation et la participation à des réunions d'équipe, de projets, de collaboration ;
- (jaune) l'enseignement (incluant la préparation des cours/TD/TP), l'organisation et la participation à des réunions avec les équipes d'enseignants, des jurys de fin de semestre ;
- (vert clair) la coordination, la répartition, le suivi et la validation des services d'enseignement des $\simeq 150$ enseignants-chercheurs de l'UFR de Physique de l'Université de Paris ($\simeq 25\,000$ h, incluant la gestion des vacataires et des missionnaires) ;
- (marron) la diffusion vers le grand public, incluant les scolaires (exemple : organisation de la fête de la science à l'Observatoire de Paris) ;
- (bleu clair) la participation au conseil d'UFR et au conseil des enseignements de l'Université de Paris, au conseil de laboratoire du Lesia, au conseil scientifique de l'Observatoire de Paris, au Conseil national des universités (section 34, suppléant) ;
- (vert foncé) des taches administratives (vérification des lignes de crédits, appel d'offres), l'organisation de séminaires, la rédaction de rapports d'activité pour tutelles et financeurs.

Pour calculer les pourcentages, j'enregistre tous les jours depuis janvier 2019 le nombre d'heures que je consacre à chaque tache.

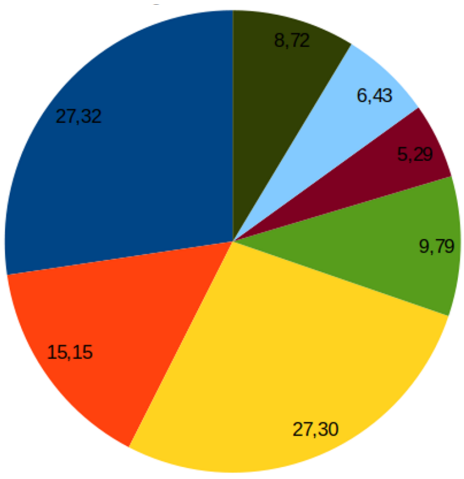

FIGURE 2.1 – *Répartition de mon temps de travail. Temps médian de travail par semaine :* 56 *h.*

Annexes

Chapitre 1

Galicher et al., 2016, AA, 594, A63

The International deep planet survey (paragraphe 3.1.1 du dossier de synthèse).

A&A 594, A63 (2016)
DOI: 10.1051/0004-6361/201527828

Astronomy & Astrophysics

The International Deep Planet Survey

II. The frequency of directly imaged giant exoplanets with stellar mass⋆

R. Galicher[1,2,3], C. Marois[3,4], B. Macintosh[4,5], B. Zuckerman[6], T. Barman[7], Q. Konopacky[8], I. Song[9], J. Patience[10], D. Lafrenière[11], R. Doyon[11], and E. L. Nielsen[5,12]

[1] LESIA, Observatoire de Paris, CNRS, Université Paris Diderot, Université Pierre et Marie Curie, 5 place Jules Janssen, 92190 Meudon, France
e-mail: raphael.galicher@obspm.fr
[2] Groupement d'Intérêt Scientifique PHASE (Partenariat Haute résolution Angulaire Sol Espace) between ONERA, Observatoire de Paris, CNRS and Université Paris Diderot, 75000 Paris, France
[3] National Research Council Canada, 5071 West Saanich Road, Victoria, BC, V9E 2E7, Canada
[4] Lawrence Livermore National Laboratory, 7000 East Ave., Livermore, CA 94550, USA
[5] Kavli Institute for Particle Astrophysics and Cosmology, Stanford University, CA 94305, USA
[6] Department of Physics and Astronomy, University of California, Los Angeles, CA 90095, USA
[7] Lunar and Planetary Laboratory, University of Arizona, Tucson AZ 85721, USA
[8] CASS, University of California San Diego, La Jolla, CA 92093-0424, USA
[9] Department of Physics and Astronomy, University of Georgia, Athens, GA 30602-2451, USA
[10] Arizona State University, Tempe, AZ 85281, USA
[11] Département de Physique, Université de Montréal, C.P. 6128 Succ. Centre-Ville, Montréal, QC H3C 3J7, Canada
[12] SETI Institute, Carl Sagan Center, 189 Bernardo Avenue, Mountain View, CA 94043, USA

Received 25 November 2016 / Accepted 17 July 2016

ABSTRACT

Context. Radial velocity and transit methods are effective for the study of short orbital period exoplanets but they hardly probe objects at large separations for which direct imaging can be used.
Aims. We carried out the international deep planet survey of 292 young nearby stars to search for giant exoplanets and determine their frequency.
Methods. We developed a pipeline for a uniform processing of all the data that we have recorded with NIRC2/Keck II, NIRI/Gemini North, NICI/Gemini South, and NACO/VLT for 14 yr. The pipeline first applies cosmetic corrections and then reduces the speckle intensity to enhance the contrast in the images.
Results. The main result of the international deep planet survey is the discovery of the HR 8799 exoplanets. We also detected 59 visual multiple systems including 16 new binary stars and 2 new triple stellar systems, as well as 2279 point-like sources. We used Monte Carlo simulations and the Bayesian theorem to determine that $1.05^{+2.80}_{-0.70}$% of stars harbor at least one giant planet between 0.5 and 14 M_J and between 20 and 300 AU. This result is obtained assuming uniform distributions of planet masses and semi-major axes. If we consider power law distributions as measured for close-in planets instead, the derived frequency is $2.30^{+5.95}_{-1.55}$%, recalling the strong impact of assumptions on Monte Carlo output distributions. We also find no evidence that the derived frequency depends on the mass of the hosting star, whereas it does for close-in planets.
Conclusions. The international deep planet survey provides a database of confirmed background sources that may be useful for other exoplanet direct imaging surveys. It also puts new constraints on the number of stars with at least one giant planet reducing by a factor of two the frequencies derived by almost all previous works.

Key words. planets and satellites: gaseous planets – planets and satellites: fundamental parameters – methods: observational – methods: data analysis – methods: statistical – instrumentation: high angular resolution

1. Introduction

After the first discoveries of exoplanets by indirect detections in the late 80s and 90s, several teams performed surveys to obtain direct images of substellar objects in the optical and near-infrared. As the instruments were not optimized for high contrast imaging, the first surveys probed brown dwarfs that are brighter than planets and thus, easier to detect. For example, Becklin & Zuckerman (1988), Schroeder et al. (2000), Gizis et al. (2001), Oppenheimer et al. (2001), and Carson et al. (2009) observed nearby stars, while Neuhäuser & Guenther (2005) and Lowrance et al. (2005) surveyed young systems, and Chauvin et al. (2006) targeted stars harboring planets detected by stellar radial velocity. Taking advantage of new observing modes, such as spectral differential imaging (SDI; Marois et al. 2000) and angular differential imaging (ADI; Marois et al. 2006) and using more powerful adaptive optics systems, later surveys of youthful

⋆ Tables 11–15 are only available at the CDS via anonymous ftp to cdsarc.u-strasbg.fr (130.79.128.5) or via http://cdsarc.u-strasbg.fr/viz-bin/qcat?J/A+A/594/A63

Table 1. Target list.

Star	α (J2000.0)	δ (J2000.0)	Spec. type	Dist. (pc)	Age (Myr) median	min	max	Age method or Assoc.	Ref.	IR excess
HIP 682	00:08:25.75	+06:37:00.49	G2V	40	100	30	300	Li/X		Y[c]
QTAND	00:41:17.34	+34:25:16.87	Ge	41	100	30	300	Li/X/UV		–

Notes. The complete list is in Table 11, available at the CDS.

stars probed fainter and fainter substellar companions down to the young gas-giant extrasolar planet regime (Biller et al. 2007; Kasper et al. 2007; Lafrenière et al. 2007a; Nielsen et al. 2008; Metchev & Hillenbrand 2009; Chauvin et al. 2010; Heinze et al. 2010; Rameau et al. 2013; Yamamoto et al. 2013; Biller et al. 2013; Nielsen et al. 2013; Wahhaj et al. 2013; Brandt et al. 2014).

For 14 yr, we had been using Keck II, Gemini North and South, and VLT to run two near-infrared imaging surveys: a Keck adaptive optics search for young exoplanets (Kaisler et al. 2003) and the international deep planet survey (IDPS; Marois 2010). In this paper, we merge the two and call IDPS the resulting survey. The targets were 292 young and nearby stars of A to M spectral types with a majority of massive stars. The main objectives of the IDPS were the detection and spectral characterization of new exoplanets, and the determination of the frequency of stars harboring giant planets with long orbital periods.

A first paper (Vigan et al. 2012) presented a fraction of the A stars of the IDPS. In the current paper, we present the complete survey. The target sample is described in Sect. 2. The observations and instruments that we used are presented in Sect. 3. Then, Sect. 4 details the pipeline that we developed for the uniform data processing of the ∼30 000 frames. The characteristics of all the detected sources (multistellar systems, exoplanets, and field stars) are listed in Sect. 5. Finally, we run a Monte Carlo analysis in Sect. 6 to constrain the frequency of stars with giant planets.

2. Target sample

As for most of exoplanet direct imaging surveys, the target sample is composed of young and nearby stars (Table 1) with a median age of 120 Myr and a median distance of 45 pc (Fig. 1). The youth ensures that giant planets are bright enough in the near-infrared to be detected assuming evolutionary models like COND and DUSTY (Chabrier et al. 2000; Baraffe et al. 2003). The ages in Table 1 are extracted from previous work (Ref. column) or were derived by our team using the following techniques described in Zuckerman & Song (2004): lithium, X-ray, UV emission, UVW velocity, H-alpha, and color-magnitude diagrams.

All types of main-sequence stars were surveyed with a majority of massive stars: 5, 107, 63, 24, 44, and 49 B, A, F, G, K, M stars. The complete sample is composed of 292 stars.

3. Observations

We obtained near-infrared observations with the adaptive optics systems of Gemini North, Gemini South, Keck II, and VLT. We used public HST data to confirm one of our candidates to be a background object. The observations are described in the following sections and in Table 2. The information about the NACO/VLT observations are gathered in Vigan et al. (2012) and they are not included in this paper although we use the associated detection limits for the statistical study (Sect. 6).

3.1. NIRI at Gemini North

At Gemini North, we observed with the NIRI camera (Hodapp et al. 2003) and the ALTAIR adaptive optics system (Herriot et al. 2000). Data were taken from 2004 to 2014 (programs GN-2007B-Q-59, GN-2008A-Q-77, GN-2008B-Q-64, GN-2009A-Q-80, GN-2009B-Q-17, GN-2011B-Q-11, GN-2012B-Q-14, GN-2012B-Q-70, GN-2013A-Q-34, GN-2013B-Q-16, and GN-2014A-Q-18).

The $f/32$ camera was used, yielding a $22'' \times 22''$ field of view and 1024×1024 pixel images. The spatial sampling is 21.4 mas or 22.0 mas per pixel if the Altair field lens is used (LI in Table 2) or not (LO). The lens improves the off-axis AO correction but induces astrometric distortions (Sect. 4.1). Table 3 gives the specifications of the spectral filters that were used. Images with ∼30 s exposure time were recorded in an ADI mode. With NIRI, ADI consists of recording a sequence of many exposures of the target while keeping the instrument rotator off. The camera and the telescope optics thus remain aligned for all exposures, enabling a very accurate point spread function (PSF) correlation between consecutive exposures. Since the field of view rotates when the rotator is off, any off-axis source (companion or background object) moves angularly around the central star with time. For each frame of the sequence, a locally optimized combination of images (LOCI, Lafrenière et al. 2007b; Marois et al. 2010b) produces a reference PSF to subtract. The PSF subtracted frames are then rotated to align north up and they are median combined. Generally, the more the field of view rotates during the sequence, the more efficient the speckle subtraction. Optimal performance is achieved if the observations are acquired as the target is close to the meridian (±1 h from its transit).

During the first observations of each star (apart from 9 that saturated the detector even for the shortest exposure time), unsaturated short exposures were recorded to calibrate the photometry in the ∼30 s images. Sometimes, when observing at a second or later epoch, to save time we did not acquire unsaturated images, observe more targets, and follow more exoplanet candidates.

3.2. NIRC2 at Keck II

Most of the IDPS data were obtained with the NIRC2 instrument (McLean & Sprayberry 2003; Wizinowich 2006) at Keck II during ∼70 nights or half-nights between 2001 and 2014.

Two observing modes were employed, and both of these modes enabled the use of ADI to subtract the speckle pattern. In the position angle mode (PA in Table 2), north points to the same direction in all frames of a given sequence. The field of view is thus fixed while most of the speckle pattern rotates. One can thus discriminate a fixed off-axis source from the rotating speckle pattern. In the vertical angle mode (V), the pupil rotator is kept off

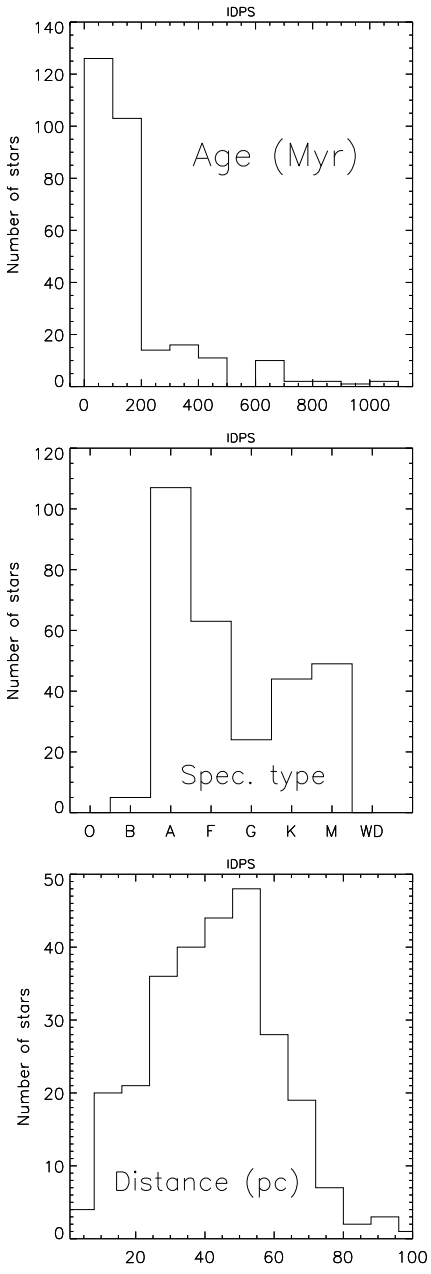

Fig. 1. IDPS star age, spectral type, and distance distributions.

and the field rotates, which is equivalent to the ADI mode used at Gemini. The V mode is usually more effective for speckle calibration, but this mode was not used before 2004 since we were still searching for the best observing strategy at this time.

We sometimes recorded saturated and unsaturated data but usually, we only recorded long exposure sequences using one of the occulting coronagraphic focal plane masks, with diameters of 400, 600, 800, or 1000 mas. The masks are not fully opaque and unsaturated images of the star could be extracted from the long exposures. During the survey, we used several filters that are listed in Table 3.

Most of the data were recorded with the $10'' \times 10''$ narrow field-of-view camera with 9.942 mas/pixels. We also used the $40'' \times 40''$ wide camera with 39.686 mas/pixels (w in Table 2) in peculiar cases to probe planets at more than $10''$ from their star or when the observing conditions where bad.

3.3. NICI at Gemini South

Thirty-four stars were observed with the NICI AO camera (Chun et al. 2008) in 2009, 2012, and 2013 (programs GS-2009B-Q-14, GS-2012B-Q-8, and GS-2013A-Q-24). The camera provided a $18.5'' \times 18.5''$ field of view and a 18 mas plate scale. We recorded 1024×1024 pixel images in one or two filters at the same time (Table 3). All data were taken in ADI mode keeping the Cassegrain rotator off (V mode). Sometimes, the SDI mode was also used observing simultaneously at CH4s and CH4l. We always used the F0.32 (320 mas diameter) or F0.65 (650 mas) occulting focal plane masks. As for NIRC2, the occulting masks were not fully opaque and unsaturated images of the star could be extracted from the long exposures.

3.4. NICMOS on HST and other programs

We reduced public data that were not part of the IDPS to obtain a second epoch for some of our candidates. We used NIRI, NICI, NIRC2, NACO, and NICMOS archive data. We list the programs these data come from in Table 2.

4. Image processing

The pipeline we developed for a uniform processing of all the IDPS sequences can be divided into four main steps. First, flat fielding, sky subtraction, bad-pixel and distortion corrections were applied to each frame of a considered sequence (Sect. 4.1). In the second step, all frames were registered within a pixel (Sect. 4.2). The procedures used for these two first steps depended on the instrument and on the sequence (procedures were not the same for registering saturated or unsaturated data for example). The last two steps consisted of obtaining calibrated high contrast images and were common to all the IDPS sequences. In the third step, a LOCI-like algorithm was applied to each sequence to reduce the speckle intensity and provide a final image with high contrast for each target (Sect. 4.3). In cases where the field-of-view rotation was small, north was aligned up in each frame of the sequence and all the frames were stacked, applying no speckle subtracting algorithm. The fourth step calibrated the contrast level in the final images, estimated the astrometry and the photometry of off-axis sources, and gathered the results in a database (Sect. 4.4).

4.1. Cosmetic corrections

Considering one IDPS sequence, the first step of our data processing was the selection of the frames. If their quality was

Table 2. Observation list.

Star	Date	Nb × Exp × Coadd (s)	FOV rot (deg)	Tel	Filter	Config Coro	Mode	Program
HR9	2001-12-01	8 × 15 × 4	4.4	KE	*K*p	w	PA	
TYC1186-706-1	2008-12-17	9 × 0.5 × 10	1.0	KE	*K*cont	–	PA	A162N2
HIP 107350	2005-07-18	6 × 30 × 1	10.2	GN	CH4s	LO	V	GN-2005A-Q-16
HIP 107412	2007-09-12	139 × 30 × 1	55.6	GN	CH4s	LI	V	–

Notes. The complete list is in Table 12, available at the CDS.

Table 3. Spectral filter specifications.

Tel.	Name	λ_0 (μm)	$\lambda_{min} - \lambda_{max}$ or $\Delta\lambda$
GN	*J*	1.25	1.15–1.33
	H	1.65	1.49–1.78
	CH4s[1]	1.58	6.5%
	K	2.20	2.03–2.36
	*K*s	2.15	1.99–2.30
	*K*p	2.12	1.95–2.30
GS	CH4-H4%S	1.578	4.00%
	CH4-H4%L	1.652	3.95%
	*K*s	2.15	1.99–2.30
KE	*J*	1.248	1.166–1.330
	*H*cont	1.5804	1.5688–1.5920
	FeII[1]	1.6455	1.6327–1.6583
	CH4s[1]	1.5923	1.5295–1.6552
	H	1.633	1.485–1.781
	CH4l[1]	1.6809	1.6125–1.7493
	*K*p	2.124	1.948–2.299
	*K*s	2.146	1.991–2.302
	H2 $v = 1$–0[1,2]	2.1281	2.1112–2.1452
	Br_gamma[1]	2.1686	2.1523–2.1849
	PAH	3.2904	3.2627–3.3182
	*L*p	3.776	3.426–4.126

Notes. GN, GS, and KE stand for Gemini North (NIRI), Gemini South (NICI), and Keck II (NIRC2). [(1)] Associated with a blocker PK-50. [(2)] Called NB2.108 in the fits headers.

degraded because of clouds, high seeing variations, or bad adaptive optics corrections, they were removed from the sequence. When available, a sky frame was subtracted from all frames. In the cases of observations at *L*p or *M*p-bands, the LOCI background subtraction algorithm presented in Galicher & Marois (2011) was used to subtract the background residuals.

Each frame of the sky-corrected sequence was corrected from flat-fielding using calibration data taken at the telescope. Then, the bad and hot pixels were found from the sky and flat images, and their flux was set to the median value of neighboring pixels of the science image. Sometimes, detectors created a horizontal or vertical stripe pattern in NIRI and NICI images (Fig. 2). To remove this pattern, we assumed it to be translation invariant. We estimated the stripe intensity and spatial frequency from the 25 first rows for vertical stripes or columns for horizontal stripes and we subtracted the pattern to the rest of the image.

Then, the field distortions were corrected. For the NIRC2 narrow camera images, we used the solution from Yelda et al. (2010) with an accuracy down to ~0.01 pixel (0.5 mas) for static distortion correction. When observing with the wide camera,

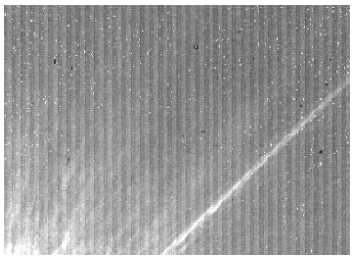

Fig. 2. Stripe pattern induced by detectors in NIRI and NICI images.

we applied the Keck routine revised by Cameron[1] that corrects for distortions down to a ~4 mas level. For NICI distortions, we used the instrument team solutions that have an accuracy of ~35 mas for 2009 data. To correct for NIRI distortions, we compared NIRI and NIRC2 images of the Trapezium region and we created new distortion maps for images taken with or without the Altair field lens (Fig. 3). In both cases, the accuracy of the correction is less than a pixel (<21 mas) close to the center of the detector but reaches 2 to 5 pixels (40–100 mas) further than ~4″ from the center. We did not correct for distortions in NICMOS images and assumed a 1.5 pixel (113 mas) error.

Eventually, we registered all images within ~1 pixels adding zero pixels at the borders of the images to ensure no field-of-view loss when rotating the frames as described in Sect. 4.3.

4.2. Image registration

If images were unsaturated, we used an iterative Gaussian fit procedure to register each frame of the sequence within a fraction of pixel ($\lesssim$1/50). We used the same procedure to register coronagraphic images since the occulting mask transmissions was partially transmissive and left unsaturated images of the central star on the detector. In NIRC2 and NICI coronagraphic images, the central part of the star image, which was attenuated by the focal plane mask, was slightly shifted with respect to the external part of the star image (i.e., the speckles that were not affected by the focal plane mask). We thus registered all the frames using the deflected central star image and compensated for the bias induced by the mask. Several times during the IDPS, we calibrated the mask deflections at Keck II observing the HD 172649 binary system with the 400, 600, 800, and 1000 mas diameter masks at *J*, *H*, and *K*s filters.

For NIRI saturated images, we selected the first frame of the sequence and we masked all the pixels but the regions of the spider diffraction pattern. We then found the position that maximized the correlation of the masked image with its 180 deg

[1] http://www.astro.caltech.edu/~pbc/AO/distortion.pdf

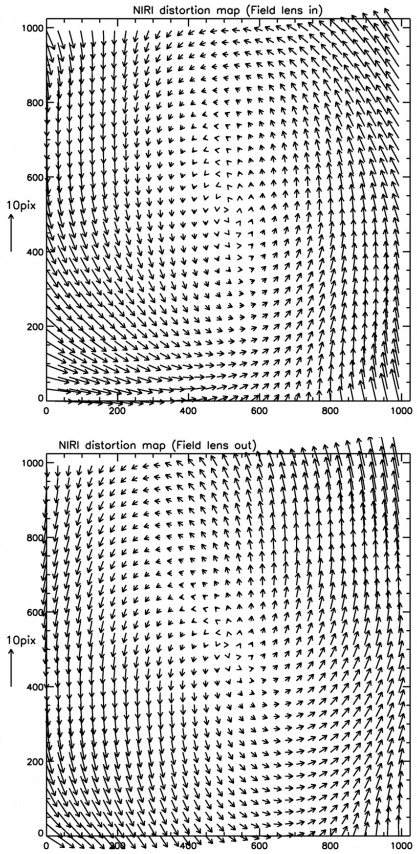

Fig. 3. NIRI distorsion maps for images taken with (*top*) or without (*bottom*) the Altair field lens. Arrows indicate the distortions at each position of the detector. For the sake of visibility, we multiplied their length by 10.

rotation (spiders are symmetrical). Once the first frame was registered within a pixel, we built a new mask to select the spider diffraction pattern and an annulus where speckles were not saturated and where the detector noise was negligible. We registered all the frames of the sequence maximizing their correlation inside the new mask with the first frame. Sizes of the annulus were sequence dependent.

For NIRC2 saturated images, the procedure was very similar but the centering of the first frame was done by hand (∼1 pix error) using the hexagonal diffraction signal as a guide because the spider pattern was not detected.

For NICMOS images, we selected the spider pattern area and found the position that maximized the correlation of the image with its 180 deg rotation.

At this point of the pipeline, all sequences were registered within ≤1 pixel.

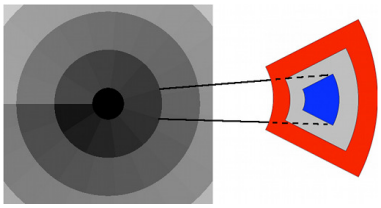

Fig. 4. SOSIE sections of interest (left and right central blue section) and optimizing region (right exterior red region).

4.3. High contrast imaging

For NIRC2 and NIRI data, the speckle pattern was reduced in each frame of the sequence by subtracting an optimized reference image calculated by the SOSIE algorithm (Marois et al. 2010b). To create the reference image, we divided the target image into sections (left in Fig. 4). For each section (blue central region, right in Fig. 4), we selected the frames in the sequence for which the field-of-view rotation would have sufficiently displaced a putative companion (half of the PSF full-width half-maximum, FWHM), and we defined a region (exterior red region) setting a FWHM gap. We found the linear combination of the selected frames that minimized the residual noise in the exterior region. We then subtracted the linear combination in the section of interest (blue central section). This reduced the speckle intensity because the SOSIE coefficients that are needed to subtract the speckles in the blue region are highly correlated with the SOSIE coefficients that are optimized to subtract the speckles in the red region. The FWHM gap avoids self-subtraction of the planet signal. We tested several geometrical shapes for the sections and found that annuli were a good trade-off between computing time and performance (negligible loss in performance). After subtraction, we derived the north axis from the FITS header keywords for each frame and we rotated all frames to align their field of view with north up. We eventually median combined the frames to enhance the signal-to-noise ratio of putative off-axis sources. In the regions of the image where no reference frames were available to apply the SOSIE algorithm (far from the central star if the telescope was dithered during the sequence or close to the center when the field-of-view rotation was small), we did no speckle subtraction and only median combined the frames.

For sequences taken in PA mode (Sect. 3.2), the pupil rotated between frames rather than the field of view. We rotated each frame to create a sequence with a fixed speckle pattern and a rotating field of view. We then applied our SOSIE algorithm.

When only one spectral filter was used with NICI, we used the same SOSIE algorithm as described before. For images taken at two spectral bands simultaneously, we developed a SOSIE-based algorithm that minimizes the speckle intensity using the spectral images (spectral speckle differential imaging) and the ADI images simultaneously (see also Artigau et al. 2008). This data processing was used only for detection. To avoid the issue of calibration in such ADI/SDI SOSIE images (Maire et al. 2014), we used the ADI SOSIE images (no SDI) to derive the photometry of the candidates and the detection limits.

Usually, NICMOS sequences are composed of only 2–6 frames, which limits the SOSIE performance. To improve the speckle subtraction, we built a NICMOS image database (called $I_{\rm DB}$) gathering 1012 images that is similar to what Lafrenière et al. (2009) proposed. To reduce the speckle level

Table 4. Intensity attenuation of the PSF behind the NIRC2 and NICI occulting masks.

Instrument	NIRC2								NICI		
Filter	*J*	*H*	*H*	*H*	*Ks*	*Ks*	*Ks*	*Lp*	CH4l	*H*	*K*
Mask diameter (mas)	800	600	800	1000	400	600	800	800	320	320	320
Attenuation	70	200	40	39	57	29	28	120	300	238	191

in one section of one frame, we selected the frames of the same sequence and the 50 most correlated images I_{DB} in this section. Then, we applied the SOSIE algorithm described previously.

As the ADI observing mode was not used before 2004, the SOSIE algorithm could not be applied to a non-negligible number of sequences taken between 2000 and 2004 with NIRC2. For these sequences, we only rotated all the frames to align the north up and we median combined them. We tested a SOSIE algorithm using a library of PSFs taken the same night with the same instrumental configuration (similar to the NICMOS-HST data processing) but no improvement was achieved. The reason is certainly that aberrations vary over the night in a ground-based telescope (pointing, flexures, temperatures, etc.) and thus, the PSF and the speckle pattern evolve over the night.

4.4. Photometry and astrometry calibrations

As for any ADI or SDI technique used for speckle calibration, the astrometry and photometry are biased in the final images. The procedure we used to estimate these biases requires an unsaturated PSF (Galicher et al. 2011). When unsaturated images were available, they were registered following the procedures described in Sect. 4.2 and we median combined them to obtain the needed unsaturated PSF.

In the case of NIRC2 coronagraphic images, we used the attenuated images of the star that were recorded behind the occulting mask. We compensated for the mask transmissions that were calibrated observing binary systems (Sect. 4.2 and Table 4). For the 600 and 800 mas masks at *H* and *Lp*, we used images of GJ 803 and HR 8799 taken with and without masks for the calibration.

All the NICI data were recorded with an occulting mask and we also used the attenuated image of the star behind the coronagraph as a reference for photometry. From the NICI documentation, the attenuation of the 0.32 arcsec occulting mask was ~300. We used this value for the CH4 bands as the calibration was performed at CH4l. For the *K* and *H*-bands, we used calibrations published in Wahhaj et al. (2011) in which the attenuations were 238 and 191 at *H* and *K*, respectively.

For several data sets, saturated and unsaturated sequences were not recorded using the same filters although their central wavelengths and bandwidths were close. We thus considered the median saturated and unsaturated images. We selected an annulus in which the saturated image was not saturated and where the unsaturated image was not dominated by the detector noise. We integrated the flux over the annulus for both images and we determined the factor that gives the photometry in the saturated image from the measured flux in the unsaturated image. We finally obtained an unsaturated PSF that was calibrated in flux with respect to the saturated data. Doing so, we assumed the PSF pattern was similar in the two filters, which was a good approximation as the filter central wavelengths and bandwidths were similar.

When a binary or planet candidate was detected, we used the calibrated unsaturated PSF to estimate its astrometry and photometry (Galicher et al. 2011). First, we roughly estimated the flux and position (within 1 pixel) of the source in the SOSIE image. The pipeline then created a data cube of frames that only contained the unsaturated PSF at the candidate position on the detector accounting for the field-of-view rotation in each frame and for the smearing of off-axis source images as the field of view could rotate during a single exposure. The SOSIE coefficients that were used to obtain the SOSIE image where the candidate was detected were applied on the candidate data cube. The resulting frames were rotated to align north up. The median of these frames provided the estimation of the candidate image in the SOSIE image (Fig. 5). We then adjusted the estimated image subpixel position and its flux to minimize the integrated flux of the difference between the real and estimated candidate images. We used a 3 FWHM diameter disk for the minimization. The 1σ error bars were the required excursions in position or in flux to increase the minimum residual flux by a factor of $\sqrt{2}$. We empirically determined this factor running tests on sequences in which we injected known fake planets.

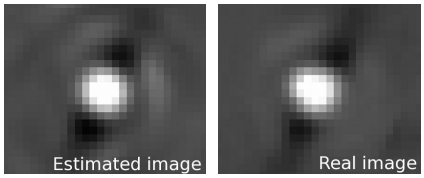

Fig. 5. Estimated (*left*) and real (*right*) images of an off-axis source.

Using the calibrated unsaturated PSF, we also estimated the SOSIE throughput in all SOSIE sections (central blue section in Fig. 4) following a procedure similar to the one used for the candidate position and flux estimation. The image were thus flux calibrated.

For every star (IDPS and public data) with unsaturated data, we produced a contrast curve. When off-axis sources were detected in the image, we added a negative object at their position in the raw datacube to remove them from the image and not bias the contrast at their angular separation (Marois et al. 2010a; Galicher et al. 2011). The noise distribution in ADI processed images is well reproduced by a Gaussian function (Marois et al. 2008a) and we estimated the 5σ noise level where σ is the azymuthal standard deviation of the residual flux in annulii of $1\,\lambda/D$ width rejecting pixels with no flux (out of the field of view). We did not account for the small amount of noise realizations (Mawet et al. 2014) whose impact is negligible at the considered separations. Finally, the 5σ noise levels were divided by the stellar flux estimated from the unsaturated images. Typical contrast curves of the IDPS are plotted in Fig. 6. The shallow curves correspond to the short sequences taken between 2000 and 2004 with NIRC2. The best performance is commonly reached using NIRC2 (after 2004) or NICI. All the IDPS contrast curves are gathered in Table 5.

Table 5. 5σ contrast curves of the IDPS observations.

Star	Date	Filter	0.3″	0.5″	1.0″	1.5″	2.0″	3.0″	4.0″	5.0″	6.0″	7.0″	8.0″	9.0″	10.0″
HR9	2009-11-01	*Ks*	5.3	6.9	9.7	11.6	12.8	13.5	13.6	13.4	12.6	9.8	–	–	–
HR9	2009-12-05	CH4l	8.5	10.0	12.7	13.9	14.7	15.2	15.3	15.3	15.3	15.3	15.7	16.6	15.1

Notes. The complete list is in Table 13, available at the CDS.

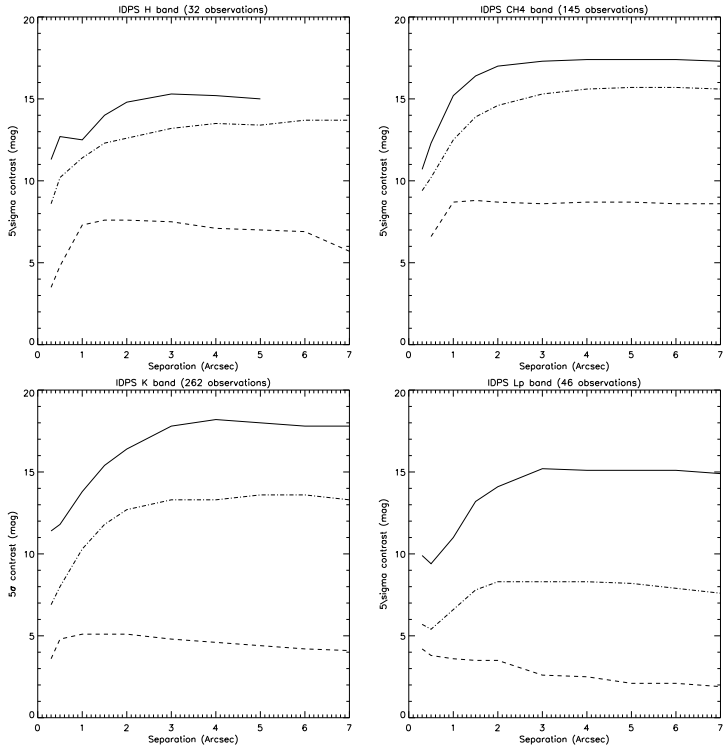

Fig. 6. Typical deep (full line), median (dotted-dashed line), and shallow (dashed line) IDPS 5σ contrast curves against angular separation. *Top left*: *H*-band. *Top right*: CH4-bands. *Bottom left*: *K*-band. *Bottom right*: *L*-band.

Table 6. Targets with crowded field (more than 50 sources).

Name	α (J2000.0)	δ (J2000.0)	Date
2MASS J17150362-2749397	17:15:04	−27:49:40	2010-07-12
HD 324741	17:54:55	−26:49:42	2004-05-24
HIP 89829	18:19:52	−29:16:33	2009-08-31
HIP 93805	19:06:15	−04:52:57	2008-05-31
HIP 99770	20:14:32	+36:48:23	2008-05-22

5. Detections

5.1. Crowded fields

For 5 targets, we detected more than 50 off-axis sources (Table 6). These stars are within 10 deg in latitude from the Galactic plane and the probability that the off-axis sources are background objects is high. Thus, we put a low priority on these stars, and finally, we did not reobserved them.

5.2. Binary and triple systems

During the survey, we detected 59 visual multiple systems with projected separations smaller than 200 AU. Forty of these

Table 7. Binaries detected during the IDPS.

Star	α (J2000.0)	δ (J2000.0)	ρ (arcsec)	θ (deg)	Contrast (Δmag)	Filter	Date	Telescope	Status	Comments/References
TYC1186-706-1	00:23:34.66	+20:14:28.75	1.74 ± 0.01	136.7	0.6	*K*cont	2008-12-17	KE	A[a]	
			1.74 ± 0.01	137.4	0.6	*K*p	2009-07-30	KE	A[a]	

Notes. In the status column, "A" stands for associated with the star and "B" for background object. "?" means unknown status. The complete table is in Table 14 available at the CDS. [(a,b,c)] Companion status confirmed from the IDPS, from previous works, or combining the IDPS and previous works (reference column) respectively.

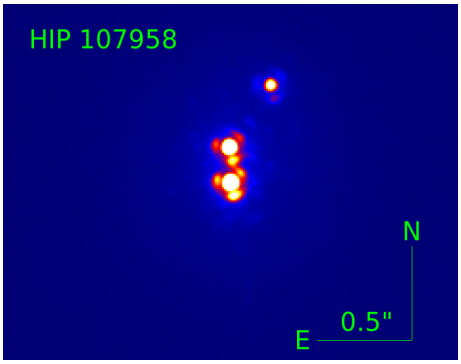

Fig. 7. Multistellar system discovered during the IDPS: HIP 107948.

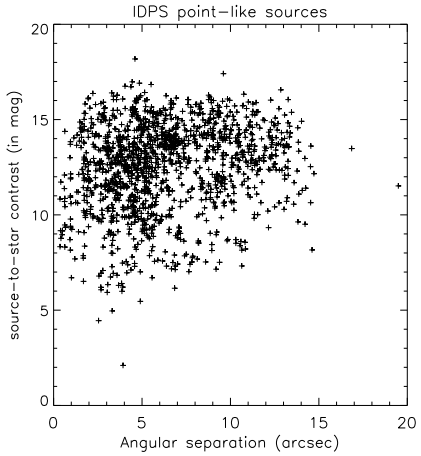

Fig. 8. Contrast of 1396 point-like sources detected in the IDPS as a function of their angular separation.

systems are already known physical binaries and 16 are physical binaries discovered during the IDPS. We also obtained an image of HIP 117452, which is a triple stellar system (De Rosa et al. 2011). Finally, we discovered two triple stars: HIP 104365 (Vigan et al. 2012) and HIP 107948 (Fig. 7). The properties of the binaries (separation, magnitude difference, etc.) are listed in Table 7. We do not derive the stellar type of the companions in this paper.

5.3. Exoplanet detections

One of the main results of the IDPS is the discovery of the four exoplanets orbiting the HR 8799 star (Marois et al. 2008b, 2010b). We also flagged 2279 point-like objects in the IDPS images, corresponding to ∼1100 individual sources detected at 2−3 epochs. We plot in Fig. 8 the contrast and the angular separation with respect to the star for the 1396 IDPS detections whose contrast could be estimated. By observing a given star at multiple epochs and considering proper motions and parallax, we confirmed that most of the detected sources are background objects (Fig. 9). Some candidates have not yet been followed up because of very bad weather or technical problems. The characteristics of the 2279 detected sources are reported in Table 8 and are available on a dedicated website[2].

6. Occurence of stars with giant planets

The detection limits (Table 5) and the four exoplanet detections of the IDPS can be used to run a Monte Carlo statistical analysis (Sects. 6.2 and 6.3) and calculate an upper limit to the frequency of stars that harbor at least one companion of mass and semi-major axis within given intervals (Sect. 6.4). Moreover, as exoplanets were discovered during the survey, we can put a lower limit on this frequency and we study the impact of the hosting star mass (Sect. 6.5.1). We also study the impact of one of the assumptions that is needed to run the Monte Carlo analysis (Sect. 6.5.2). Finally, we compare our results to previous works (Sect. 6.6).

6.1. Sample

We focus our analysis on single star systems rejecting the binaries (Table 7) from the IDPS sample. We also reject the stars with crowded fields (Sect. 5.1) and the stars for which no contrast curve could be derived from the observations. This leaves 229 stars with a median age of 100 Myr and a median distance of 43 pc (dashed lines in Fig. 10).

To increase the number of stars in the sample and, thus, derive a more accurate frequency of stars with giant planets, we combine the IDPS detection limits and detections to the detection limits of two other surveys: Gemini deep planet survey (Lafrenière et al. 2007a) and a NACO/VLT survey (Chauvin et al. 2010). Thanks to previous collaborations with these teams, we know that our detection limits and theirs are consistent. In future works, it would be interesting to combine all the existing surveys ensuring all the detection limits are consistent but this is out of the scope of our paper.

[2] http://lesia.obspm.fr/directimaging/admin/form_user.php

Table 8. substellar candidates and background sources observed during the IDPS.

Star	α (J2000.0)	δ (J2000.0)	ρ (")	θ (deg)	$\delta\rho = \rho\delta\theta$ (mas)	Δm	Filter	M	$m_{\rm min,max}$ ($M_{\rm Jup}$)	$a_{\rm proj}$ (AU)	Date	Tel.	#	Status
HR9	00:06:50.09	−23:06:27.14	19.691	337.347	40	–	Kp	–	–	770.1 ± 13.0	2001-12-01	KE	1	?
HIP 682	00:08:25.74	+06:37:00.48	5.472	268.037	14	15.47 ± 0.49	Ks	–	–	–	2012-09-04	KE	1	B
			4.945	267.774	12	14.73 ± 0.31	Kp	–	–	–	2006-07-18	KE	1	B

Notes. In the status column, "A" stands for associated with the star, whereas "B" is for background object and "F" for false detection. The flag "B?"' means that the errors bars are larger than parallax and proper motion, but given the displacement of all the candidates between the two epochs, we are confident the object is background.

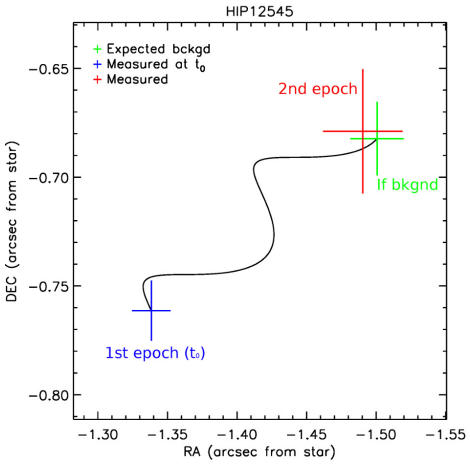

Fig. 9. Example of the astrometry test for comparing the expected position of a background source (blue and green) to the measured positions (blue and red) for a planet candidate around HIP 12545. Crosses include error bars on the measured astrometry and on the stellar parallax and proper motion.

The Lafrenière et al. (2007a) and Chauvin et al. (2010) surveys complete the IDPS because they include more G, K, and M stars (full lines in Fig. 10). The complete sample of 356 stars includes 5, 95, 67, 43, 86, and 60 B, A, F, G, K, M stars. The median age and median distance, which are 100 Myr and 37 pc, are very similar to those of the IDPS. We use this sample in the rest of the paper.

6.2. Formalism and assumptions

The analysis is based on the statistical formalism presented in Lafrenière et al. (2007a). A Monte Carlo simulation is used to create an ensemble of fake planets computing their projected angular separation with respect to their star assuming given distributions of planetary masses and orbital parameters. Then, considering a model of planet atmosphere and the age of the targets, the fake planet fluxes are derived and compared to the detection limits of the survey to determine what fraction of planets should have been detected. Finally, the frequency of stars that harbor at least one exoplanet is derived using the Bayes' theorem. In this section, we briefly outline the main steps of the analysis specifying the assumptions.

We simulate $N_{\rm pla}$ fake planets for each target star. First, we draw $N_{\rm pla}$ semimajor axis values considering a uniform distribution in the interval $[a_{\rm min}, a_{\rm max}]$. These values are converted

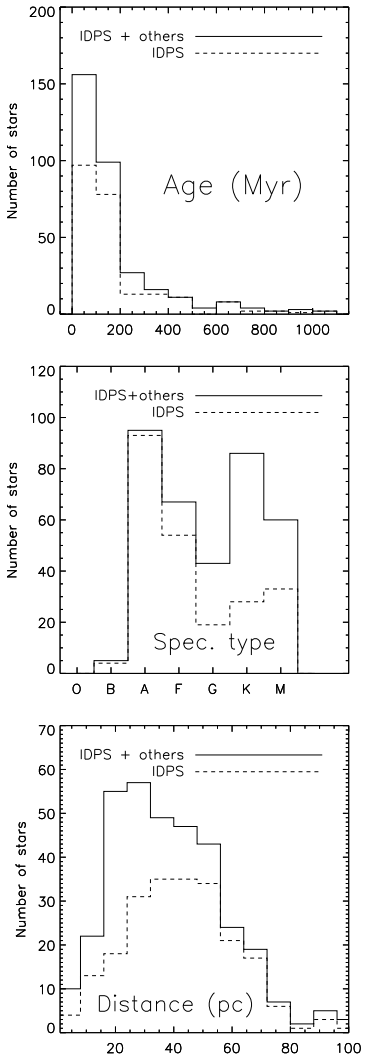

Fig. 10. Distribution of the ages, spectral types, and distances of the IDPS stars with contrast curves (dashed line) and of the sample used for the statistical study (full line).

to planet-star separations following the method of Brandeker et al. (2006) and assuming the orbital eccentricity distribution derived by Kipping (2013) from the radial velocity exoplanet sample, which is a Beta distribution with parameters $a = 0.867$ and $b = 3.03$. The projected physical separations are converted into angular separations based on the distance of the primary star. Then, we draw $N_{\rm pla}$ masses following a uniform distribution in the interval $[m_{\rm min}, m_{\rm max}]$. Each planet mass is converted into flux in the observing spectral band using the COND03 model (Baraffe et al. 2003) and a random age assuming an asymmetric Gaussian distribution for which the 1σ lower age, 1σ upper age, and average age are given in Table 1. The planet-to-star contrast is then derived from the stellar magnitude. As we compare this contrast to a 1D-contrast curve, we add a random noise to account for the variations of the noise in the 2D-reduced image. The random noise is drawn from a Gaussian distribution of standard deviation that is equal to the noise measured at the separation of the fake planet. Finally, we derive the probability p_j of detecting a given planet around the jth star from the fraction of fake planets lying above the 5σ detection limit.

When the star was observed several times, we combine the detection limits (Table 5) taking the deepest contrast at each separation. Doing so, we assume the putative planets do not move in the image from one observation to the others. During the IDPS, the earliest and latest observations of a given star are separated by 3.5 yr in average. Considering the median distance to the stars (~40 pc) and the average minimum angular separation of the observations (0.3″), the closest detectable planets would have a semimajor axis of 12 AU and, thus, an orbital period of ~30 yr for the massive stars ($2\,M_\odot$). The putative planets would then have moved by ~20 pixels in Keck data and 10 pixels in Gemini data between the two observations. Such a motion is small enough so that we can combine the detection limits.

6.3. Exoplanet detection probability

The average of p_j over all j values (i.e., over the complete sample) are plotted in Fig. 11 as a function of the projected planet-star separation for planet masses going from 0.5 to 13 Jupiter masses. For each curve, we set the mass of the $N_{\rm pla} = 100\,000$ random planets ($m_{\rm min} = m_{\rm max}$). The peak sensitivity of the survey occurs for projected separations between 20 and 300 AU. For example, if each star of the sample harbored one $10\,M_{\rm J}$ at 100 AU, we would have detected 75% of them. The sensitivity declines for separations larger than 200 AU because of the median distance of the targets (37 pc) and the ~10″ field of view of NIRC2 (the most used instrument during the IDPS).

6.4. Upper limit on the frequency of stars with giant planets

Using the Bayes theorem, the determination of the p_j yields a credible interval for the frequency of stars with giant planets under the assumptions made about the planet mass and semimajor axis (uniform distributions), stellar age, and atmosphere model. The boundaries of the interval depend on the level of credibility α that is considered (Eq. (6) in Lafrenière et al. 2007a). For $\alpha = 95\%$, Fig. 12 presents the upper limit on the frequency of stars harboring at least one giant planet as a function of the planet mass and the projected separation. The large number of targets and the low detection limits of the IDPS, combined with Lafrenière et al. (2007a) and Chauvin et al. (2010) results, enables us to constrain the frequency of stars harboring exoplanets with masses down to 0.5–1 $M_{\rm J}$. For example, we find that there

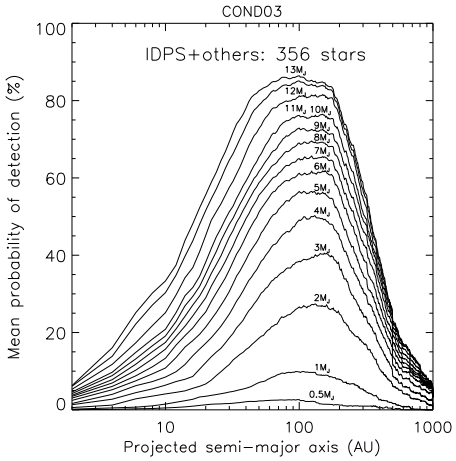

Fig. 11. Mean probability of detecting giant planets during the surveys as a function of the projected semimajor axis for several planetary masses.

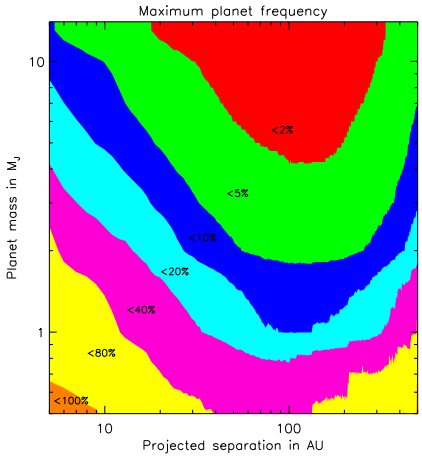

Fig. 12. Upper limit on the frequency of stars harboring at least one giant planet as a function of the planet mass and projected semimajor axis.

are less than 20% of stars harboring one or more 1 $M_{\rm J}$ exoplanets between 30 and 300 AU; and less than 10% of stars with one or more 2 $M_{\rm J}$ exoplanets between 30 and 400 AU.

6.5. Frequency of stars with giant planets

Because substellar objects are detected around stars in our sample (Table 9), we can also put a lower limit on the frequency of stars with giant planets following the formalism presented in Lafrenière et al. (2007a, Eq. (6)). When calculating the frequency of stars harboring at least one giant planet within $[m_{\rm min}, m_{\rm max}]$ and $[a_{\rm min}, a_{\rm max}]$, only the exoplanets of Table 9, whose mass and separation are included in these intervals are considered detected during the survey. For example, the detected

Table 9. Detected substellar objects in our sample.

Star		Planet			
Name	Type	Name	Mass (M_J)	Sep. (AU)	Ref.
HR 8799	A5V	b	5–11	68	1
		c	5–8	38	1
		d	5–10	24	1
		e	5–10	15	2
HD 130948	G1V	b	13–75	47	3
HIP 30034	K2	b	13–14	260	4

References. 1) Marois et al. (2008b); 2) Marois et al. (2010b); 3) Lafrenière et al. (2007a); 4) Chauvin et al. (2010).

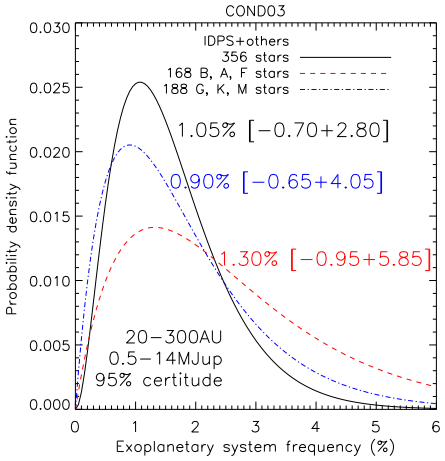

Fig. 13. Probability density function of frequency of stars with at least one giant planet in the given intervals of masses and semimajor axes: $[m_{\rm min}, m_{\rm max}] = [0.5, 14]\,M_J$ and $[a_{\rm min}, a_{\rm max}] = [20, 300]$ AU.

exoplanets for $[m_{\rm min}, m_{\rm max}] = [0.5, 14]\,M_J$ and $[a_{\rm min}, a_{\rm max}] = [20, 300]$ AU are HR 8799 b, c, d, and HIP 30034 b. Also, even if several of the HR 8799 planets are flagged as detected, the HR 8799 system counts for one detection only, i.e., one star with at least one giant planet.

6.5.1. Mass of the hosting star

Under all the assumptions described in the previous sections, we derive the probability density function of the frequency of stars with at least one giant planet of mass in $[m_{\rm min}, m_{\rm max}] = [0.5, 14]\,M_J$ and semimajor axis in $[a_{\rm min}, a_{\rm max}] = [20, 300]$ AU (black full line in Fig. 13). The mode of the distribution (i.e., frequency for which the distribution is maximum) is $1.05^{+2.80}_{-0.70}$%. The error bars give a 95% confidence interval. This means that $1.05^{+2.80}_{-0.70}$% of stars harbors at least one giant planet of 0.5−14 M_J between 20 and 300 AU with a 95% certitude.

Surveying exoplanets with orbital periods shorter than four years around stars of 1 to 5 $M_\odot$ (i.e., semimajor axis of <2 AU) and with masses up to 30 M_J, Reffert et al. (2015) found that the frequency of stars with giant planets depends on the stellar mass, reaching a maximum for hosting stars of ∼1.9 $M_\odot$. We test this assertion on our sample for stars hosting at least one giant planet between 20 and 300 AU and in the range of 0.5 to 14 M_J. We split our sample into 168 massive stars (B, A, F types, >1.1 $M_\odot$, red dashed line) and 188 low-mass stars (G, K, M-types, <1.1 $M_\odot$, blue mixed line) and we overplot the associated probability density functions in Fig. 13. The mode of the distribution for the massive stars is $1.30^{+5.85}_{-0.95}$% with 95% confidence error bars. For the low-mass stars, we find $0.90^{+4.05}_{-0.65}$%. The two confidence intervals overlap and there is no significant difference at a 95% confidence level between the frequencies of massive and low-mass stars that host an exoplanetary system. We cannot extend the Reffert et al. (2015) result to giant planets orbiting at large separations using our sample.

6.5.2. Planet mass and semimajor axis distributions

The various assumptions that are made to performed a statistical analysis impact the final results. Although studying each parameter effect is out of the scope of this paper, we tested one effect. Instead of assuming uniform distributions of planet masses and semimajor axes, we now use power laws similar to what was measured for close-in exoplanets by Cumming et al. (2008). Hence, the number dN of simulated exoplanets whose mass is in the interval $[m, m + {\rm d}m]$ and semimajor axis is in the interval $[a, a + {\rm d}a]$ is proportional to $m^{-1.31}\,a^{-0.61}\,{\rm d}m\,{\rm d}a$. All the other assumptions being the same as before, we obtain that $2.30^{+5.95}_{-1.55}$% of stars harbor at least one giant planet of 0.5−14 M_J between 20 and 300 AU with a 95% certitude. Thus, changing the assumption on the planet mass and semimajor axis distributions, the derived frequency increases by a factor of ∼2: the most probable frequency ranges from 1.05% (uniform distributions, Sect. 6.5.1) to 2.30%, and the 95% interval ranges from [0.35%, 3.85%] (uniform distributions) to [0.75%, 8.25%]. The two 95% intervals overlap but the impact of the assumed planet mass and semimajor axis distributions is obvious in this case.

This result was expected because the power law distributions predict a lot more light and close-in planets than uniform distributions, which are planets the IDPS is less sensitive to. This leads to the open question: which distribution shall we use for the planet mass and semimajor axis? On the one hand, we can argue that the distributions derived by Cumming et al. (2008) come from observations and should be a good a priori. On the other hand, we can wonder whether the formation process is or is not the same for close-in and outer giant planets, and thus, whether the distributions are or are not the same. In any case, future studies are needed to determine the impact of each assumption that is made to derive exoplanet frequencies. In the rest of the current paper, we provide the frequencies for both assumptions on the planet mass and semimajor axis.

6.6. Comparision to other surveys

We compare to previous results the frequencies of stars that harbor at least one giant planet as derived from our sample (Table 10). We use mass and separation intervals as close as possible to those chosen by the other teams and we confirm all results. Having a larger number of stars and deep detection limits, we put stronger constraints reducing the estimated frequencies by a factor of two or more in almost all cases. Also, the difference between the frequencies derived for the two planet mass distributions that we consider (uniform or power laws) is small when we focus on planets more massive than ∼1 M_J. Whereas each team makes different assumptions, all results are consistent with each other. This is interesting and future works should be

Table 10. Frequencies of stars harboring at least one giant planet in given intervals of masses and semimajor axes derived from our work and from previous publications.

Stellar type	Frequency (in %)			Separation (AU)	Planet mass (M_J)	Mass&SMA distribution	Reference
		95% certitude					
	Mode	Min.	Max.				
BA	1.90	0.50	10.05	59–460	4–14	uniform law	This work
BA	2.05	0.50	11.05	59–460	4–14	power law	This work
BA	–	–	20	59–460	>4		Nielsen et al. (2013)[a]
BA	2.70	0.65	14.30	25–940	4–14	uniform law	This work
BA	2.75	0.70	14.70	25–940	4–14	power law	This work
BA	–	–	50	25 – 940	>4		Nielsen et al. (2013)[a]
FGK	1.20	0.30	6.60	25–856	4–14	uniform law	This work
FGK	1.10	0.30	6.05	25–856	4–14	power law	This work
F2-K7	–	–	20	25 – 856	>4		Nielsen & Close (2010)[a]
M	–	–	8.30	9–207	4–14	uniform law	This work
M	–	–	8.60	9–207	4–14	power law	This work
M0-M5	–	–	20	9 – 207	>4		Nielsen & Close (2010)[a]
M	–	–	9.15	10–200	1–13	uniform law	This work
M	–	–	11.85	10–200	1–13	power law	This work
M	–	–	11	10–200	1–13		Bowler et al. (2015)
GKM	1.30	0.35	7.00	30–900	5–14	uniform law	This work
GKM	1.05	0.30	5.85	30–900	5–14	power law	This work
GKM	–	–	2	≥30	≥5		Kasper et al. (2007)[a]
FGKM	–	–	3.30	10–500	0.5–13	uniform law	This work
FGKM	–	–	6.25	10–500	0.5–13	power law	This work
FGKM	–	–	57	10–500	0.5–13		Lafrenière et al. (2007a)
FGKM	–	–	2.75	25–340	0.5–13	uniform law	This work
FGKM	–	–	5.20	25–340	0.5–13	power law	This work
FGKM	–	–	17	25–340	0.5–13		Lafrenière et al. (2007a)
FGKM	–	–	2.40	50–230	0.5–13	uniform law	This work
FGKM	–	–	4.50	50–230	0.5–13	power law	This work
FGKM	–	–	10	50–230	0.5–13		Lafrenière et al. (2007a)
FGKM	0.60	0.15	3.25	100–300	5 – 14	uniform law	This work
FGKM	0.60	0.15	3.30	100–300	5 – 14	power law	This work
FGKM	–	–	15	100–300	>5		Chauvin et al. (2015)[a]
FGKM	0.50	0.15	2.80	50–300	10–14	uniform law	This work
FGKM	0.50	0.15	2.75	50–300	10–14	power law	This work
FGKM	–	–	10	50–300	> 10		Chauvin et al. (2015)[a]
BAFGKM	0.45	0.15	2.60	40–150	1–14	uniform law	This work
BAFGKM	0.75	0.20	4.10	40–150	1–14	power law	This work
BAFGKM	–	–	10	40 – 150	>1		Chauvin et al. (2010)[a]
BAFGKM	0.45	0.15	2.55	10–150	1–20	uniform law	This work
BAFGKM	0.85	0.25	4.70	10–150	1–20	power law	This work
BAFGKM	–	–	6	10–150	1–20		Biller et al. (2013)
BAFGKM	0.35	0.10	1.95	10–100	5–70	uniform law	This work
BAFGKM	0.45	0.15	2.45	10–100	5–70	power law	This work
BAFGKM	1.70	0.52	4.90	10–100	5–70		Brandt et al. (2014)

Notes. Credible intervals are given for confidence levels of 95%. [(a)] The authors do not provide all the upper limits.

done to understand which assumption(s) the derived frequencies mainly depend on.

7. Conclusion

We have completed the IDPS for giant planets around 292 young nearby stars of all spectral types with a majority of massive stars. We developed a pipeline for a uniform processing of the data that have been recorded for 14 yr using several instruments: NIRC2/Keck II, NIRI/Gemini north, NICI/Gemini South, and NACO/VLT. We achieved contrasts of $\sim 12.5 \pm 2.5$ mag at 1″ at H, CH4, K and Lp-bands.

We detected a total of 2279 point-like sources. Most of these sources were confirmed to be background objects. Four were confirmed to be exoplanets. They are the now well-characterized HR 8799 planets (Marois et al. 2008b, 2010b). We also discovered 16 stellar binary systems and 2 triple stars.

We used the Bayesian formalism developed in Lafrenière et al. (2007a) to derive the frequency of stars with giant planets from the detection limits of the survey as well as the confirmed exoplanets. To complete the IDPS sample, we combined our results with the Lafrenière et al. (2007a) and Chauvin et al. (2010) surveys that mainly observed low-mass stars (G, K and M stars). The complete sample includes 356 stars of all spectral types with a median age of 100 Myr and a median distance of 37 pc. We determined that $1.05^{+2.80}_{-0.70}$% of stars harbor at least one giant planet of 0.5−14 M_J between 20 and 300 AU. We also found no evidence that giant planets at large separations are more likely formed around BAF stars than around GKM stars. We confirm previous results reducing the measured frequencies of stars with at least one giant planet by a factor of two or more in almost all cases. The fact that the results of the different studies are consistent is encouraging, but we should keep in mind that each team uses different assumptions (planet atmosphere models, orbital parameter distributions, star aging, etc.) and one might wonder on which assumption(s) the derived frequencies mainly depend. For example, we showed in this paper that the assumption on the planet mass and semimajor axis distributions can change the conclusions and it will be essential to address this question to prepare the interpretation of the Gemini Planet Imager (Macintosh et al. 2008) and the Spectro-Polarimetric High-contrast Exoplanet REsearch (Beuzit et al. 2008) surveys. Most of their targets are part of the IDPS sample but the extreme adaptive optics systems will probe lighter and closer-to-their-star exoplanets, which will complete our knowledge of giant planets at large separations.

Acknowledgements. The authors acknowledge the referee for constructive comments and suggestions. The authors wish to recognize and acknowledge the very significant cultural role and reverence that the summit of Mauna Kea has always had within the indigenous Hawaiian community. We are most fortunate to have the opportunity to conduct observations from this mountain. This research has made use of the SIMBAD database, operated at CDS, Strasbourg, France (Wenger et al. 2000). Some of the data presented herein were obtained at the W. M. Keck Observatory, which is operated as a scientific partnership among the California Institute of Technology, the University of California, and the National Aeronautics and Space Administration. The Observatory was made possible by the generous financial support of the W. M. Keck Foundation. This research has made use of the Keck Observatory Archive (KOA), which is operated by the W. M. Keck Observatory and the NASA Exoplanet Science Institute (NExScI), under contract with the National Aeronautics and Space Administration. Based on observations obtained at the Gemini Observatory (acquired through the Gemini Observatory Archive and the Gemini Science Archive), which is operated by the Association of Universities for Research in Astronomy, Inc., under a cooperative agreement with the NSF on behalf of the Gemini partnership: the National Science Foundation (United States), the National Research Council (Canada), CONICYT (Chile), Ministerio de Ciencia, Tecnología e Innovación Productiva (Argentina), and Ministério da Ciência, Tecnologia e Inovação (Brazil).

References

Argyle, R. W., Alzner, A., & Horch, E. P. 2002, A&A, 384, 171
Artigau, É., Biller, B. A., Wahhaj, Z., et al. 2008, in SPIE Conf. Ser., 1
Baraffe, I., Chabrier, G., Barman, T. S., Allard, F., & Hauschildt, P. H. 2003, A&A, 402, 701
Barrado Y Navascués, D. 2006, A&A, 459, 511
Batalha, C. C., Quast, G. R., Torres, C. A. O., et al. 1998, A&AS, 128, 561
Becklin, E. E., & Zuckerman, B. 1988, Nature, 336, 656
Bergfors, C., Brandner, W., Janson, M., et al. 2010, A&A, 520, A54
Beuzit, J.-L., Feldt, M., Dohlen, K., et al. 2008, in SPIE Conf. Ser., 7014
Biller, B. A., Close, L. M., Masciadri, E., et al. 2007, ApJSS, 173, 143
Biller, B. A., Liu, M. C., Wahhaj, Z., et al. 2013, ApJ, 777, 160
Bowler, B. P., Liu, M. C., Shkolnik, E. L., & Tamura, M. 2015, ApJS, 216, 7
Brandeker, A., Jayawardhana, R., Khavari, P., Haisch, Jr., K. E., & Mardones, D. 2006, ApJ, 652, 1572
Brandt, T. D., McElwain, M. W., Turner, E. L., et al. 2014, ApJ, 794, 159
Caballero, J. A. 2010, A&A, 514, A98
Carson, J. C. 2005, Ph.D. Thesis, Cornell University, New York, USA
Carson, J. C., Hiner, K. D., Villar, III, G. G., et al. 2009, AJ, 137, 218
Chabrier, G., Baraffe, I., Allard, F., & Hauschildt, P. 2000, ApJ, 542, 464
Chauvin, G., Lagrange, A.-M., Udry, S., et al. 2006, A&A, 456, 1165
Chauvin, G., Lagrange, A.-M., Bonavita, M., et al. 2010, A&A, 509, A52
Chauvin, G., Vigan, A., Bonnefoy, M., et al. 2015, A&A, 573, A127
Chen, C. H., Patten, B. M., Werner, M. W., et al. 2005, ApJ, 634, 1372
Chen, C. H., Mittal, T., Kuchner, M., et al. 2014, VizieR Online Data Catalog: J/ApJS/211/25
Chun, M., Toomey, D., Wahhaj, Z., et al. 2008, in SPIE Conf. Ser., 7015
Cumming, A., Butler, R. P., Marcy, G. W., et al. 2008, PASP, 120, 531
Cvetković, Z., Pavlović, R., Damljanović, G., & Boeva, S. 2011, AJ, 142, 73
David, T. J., & Hillenbrand, L. A. 2015, ApJ, 804, 146
De Rosa, R. J., Bulger, J., Patience, J., et al. 2011, MNRAS, 415, 854
De Rosa, R. J., Patience, J., Vigan, A., et al. 2012, MNRAS, 422, 2765
De Rosa, R. J., Patience, J., Wilson, P. A., et al. 2014, MNRAS, 437, 1216
Delfosse, X., Forveille, T., Beuzit, J.-L., et al. 1999, A&A, 344, 897
Desidera, S., Covino, E., Messina, S., et al. 2015, A&A, 573, A126
Docobo, J. A., Alvarez, C., Lahulla, J. F., Lancharesi, V., & Aguirre, A. 2000, Astron. Nachr., 321, 53
Dommanget, J., & Nys, O. 2000, A&A, 363, 991
Dommanget, J., & Nys, O. 2002, VizieR Online Data Catalog: I/274
Eggleton, P. P., & Tokovinin, A. A. 2010, VizieR Online Data Catalog: J/MNRAS/389/869
Elliott, P., Bayo, A., Melo, C. H. F., et al. 2014, A&A, 568, A26
Elliott, P., Huélamo, N., Bouy, H., et al. 2015, A&A, 580, A88
Fabricius, C., & Makarov, V. V. 2000, A&A, 356, 141
Galicher, R., & Marois, C. 2011, in AO4ELT2 Proc., SPIE Conf. Ser., 25
Galicher, R., Marois, C., Macintosh, B., Barman, T., & Konopacky, Q. 2011, ApJ, 739, L41
Gizis, J. E., Kirkpatrick, J. D., Burgasser, A., et al. 2001, ApJ, 551, L163
Hartkopf, W. I., Tokovinin, A., & Mason, B. D. 2012, AJ, 143, 42
Heinze, A. N., Hinz, P. M., Sivanandam, S., et al. 2010, ApJ, 714, 1551
Hernández, J., Calvet, N., Hartmann, L., et al. 2005, AJ, 129, 856
Herriot, G., Morris, S., Anthony, A., et al. 2000, in SPIE Conf. Ser. 4007, ed. P. L. Wizinowich, 115
Hodapp, K. W., Jensen, J. B., Irwin, E. M., et al. 2003, PASP, 115, 1388
Holmberg, J., Nordström, B., & Andersen, J. 2009, A&A, 501, 941
Janson, M., Brandner, W., & Henning, T. 2008, A&A, 478, 597
Janson, M., Carson, J. C., Lafrenière, D., et al. 2012, ApJ, 747, 116
Kaisler, D., Zuckerman, B., & Becklin, B., E. M. 2003, in Scientific Frontiers in Research on Extrasolar Planets, eds. D. Deming, & S. Seager, ASP Conf. Ser., 294, 91
Kasper, M., Apai, D., Janson, M., & Brandner, W. 2007, A&A, 472, 321
Kipping, D. M. 2013, MNRAS, 434, L51
Kraus, A. L., Shkolnik, E. L., Allers, K. N., & Liu, M. C. 2014, AJ, 147, 146
Lafrenière, D., Doyon, R., Marois, C., et al. 2007a, ApJ, 670, 1367
Lafrenière, D., Marois, C., Doyon, R., Nadeau, D., & Artigau, É. 2007b, ApJ, 660, 770
Lafrenière, D., Marois, C., Doyon, R., & Barman, T. 2009, ApJ, 694, L148
Lowrance, P. J., Becklin, E. E., Schneider, G., et al. 2005, AJ, 130, 1845
Macintosh, B., Zuckerman, B., Kaisler, D., et al. 2000, BAAS, 32, 1508
Macintosh, B. A., Graham, J. R., Palmer, D. W., et al. 2008, in SPIE Conf. Ser., 7015
Maire, A.-L., Boccaletti, A., Rameau, J., et al. 2014, A&A, 566, A126
Malo, L., Doyon, R., Lafrenière, D., et al. 2013, ApJ, 762, 88
Mamajek, E. E. 2012, ApJ, 754, L20
Marois, C. 2010, in In the Spirit of Lyot 2010, Int. Conf., 18
Marois, C., Doyon, R., Racine, R., & Nadeau, D. 2000, PASP, 112, 91

Marois, C., Lafrenière, D., Doyon, R., Macintosh, B., & Nadeau, D. 2006, ApJ, 641, 556
Marois, C., Lafrenière, D., Macintosh, B., & Doyon, R. 2008a, ApJ, 673, 647
Marois, C., Macintosh, B., Barman, T., et al. 2008b, Science, 322, 1348
Marois, C., Macintosh, B., & Véran, J. 2010a, in SPIE Conf. Ser., 7736
Marois, C., Zuckerman, B., Konopacky, Q. M., Macintosh, B., & Barman, T. 2010b, Nature, 468, 1080
Marshall, J. P., Löhne, T., Montesinos, B., et al. 2011, A&A, 529, A117
Mawet, D., Milli, J., Wahhaj, Z., et al. 2014, ApJ, 792, 97
McLean, I. S., & Sprayberry, D. 2003, in SPIE Conf. Ser. 4841, eds. M. Iye, & A. F. M. Moorwood, 1
Melis, C., Zuckerman, B., Rhee, J. H., & Song, I. 2010, ApJ, 717, L57
Metchev, S. A., & Hillenbrand, L. A. 2009, ApJS, 181, 62
Moór, A., Ábrahám, P., Derekas, A., et al. 2006, ApJ, 644, 525
Moór, A., Pascucci, I., Kóspál, Á., et al. 2011, ApJS, 193, 4
Moór, A., Szabó, G. M., Kiss, L. L., et al. 2013, MNRAS, 435, 1376
Morales, F. Y., Rieke, G. H., Werner, M. W., et al. 2011, ApJ, 730, L29
Mugrauer, M., Neuhäuser, R., Guenther, E. W., et al. 2004, A&A, 417, 1031
Nakajima, T., & Morino, J.-I. 2012, AJ, 143, 2
Neuhäuser, R., & Guenther, E. W. 2005, in 3th Cambridge Workshop on Cool Stars, Stellar Systems and the Sun, eds. F. Favata, G. A. J. Hussain, & B. Battrick, ESA SP, 560, 841
Nielsen, E. L., & Close, L. M. 2010, ApJ, 717, 878
Nielsen, E. L., Close, L. M., Biller, B. A., Masciadri, E., & Lenzen, R. 2008, ApJ, 674, 466
Nielsen, E. L., Liu, M. C., Wahhaj, Z., et al. 2012, ApJ, 750, 53
Nielsen, E. L., Liu, M. C., Wahhaj, Z., et al. 2013, ApJ, 776, 4
Nordström, B., Mayor, M., Andersen, J., et al. 2004, A&A, 418, 989
Oppenheimer, B. R., Golimowski, D. A., Kulkarni, S. R., et al. 2001, AJ, 121, 2189
Paunzen, E. 1997, A&A, 326, L29
Perryman, M. A. C., & ESA, eds. 1997, The Hipparcos and TYCHO catalogues. Astrometric and photometric star catalogues derived from the ESA HIPPARCOS Space Astrometry Mission, eds. M. A. C. Perryman, & ESA, ESA SP, 1200
Rameau, J., Chauvin, G., Lagrange, A.-M., et al. 2013, A&A, 553, A60
Reffert, S., Bergmann, C., Quirrenbach, A., Trifonov, T., & Künstler, A. 2015, A&A, 574, A116
Rhee, J. H., Song, I., Zuckerman, B., & McElwain, M. 2007, ApJ, 660, 1556
Rieke, G. H., Su, K. Y. L., Stansberry, J. A., et al. 2005, ApJ, 620, 1010
Rodriguez, D. R., & Zuckerman, B. 2012, ApJ, 745, 147
Rodriguez, D. R., Zuckerman, B., Kastner, J. H., et al. 2013, ApJ, 774, 101
Rousseau, J. M., Perie, J. P., & Gachard, M. T. 1996, A&AS, 116, 301
Schroeder, D. J., Golimowski, D. A., Brukardt, R. A., et al. 2000, AJ, 119, 906
Shkolnik, E. L., Anglada-Escudé, G., Liu, M. C., et al. 2012, ApJ, 758, 56
Sion, E. M., Holberg, J. B., Oswalt, T. D., McCook, G. P., & Wasatonic, R. 2009, AJ, 138, 1681
Song, I., Caillault, J.-P., Barrado y Navascués, D., & Stauffer, J. R. 2001, ApJ, 546, 352
Song, I., Zuckerman, B., & Bessell, M. S. 2003, ApJ, 599, 342
Song, I., Zuckerman, B., & Bessell, M. S. 2012, AJ, 144, 8
Tetzlaff, N., Neuhäuser, R., & Hohle, M. M. 2011, MNRAS, 410, 190
Tokovinin, A., Hartung, M., Hayward, T. L., & Makarov, V. V. 2012, AJ, 144, 7
Turon, C., Creze, M., Egret, D., et al. 1993, Bulletin d'Information du Centre de Données Stellaires, 43, 5
Vigan, A., Patience, J., Marois, C., et al. 2012, A&A, 544, A9
Wahhaj, Z., Liu, M. C., Biller, B. A., et al. 2011, ApJ, 729, 139
Wahhaj, Z., Liu, M. C., Nielsen, E. L., et al. 2013, ApJ, 773, 179
Wenger, M., Ochsenbein, F., Egret, D., et al. 2000, A&AS, 143, 9
Wizinowich, P. L. 2006, in ICO20: Optical Design and Fabrication, eds. J. Breckinridge, & Y. Wang, Proc. SPIE, 6034, 1
Yamamoto, K., Matsuo, T., Shibai, H., et al. 2013, PASJ, 65, 90
Yelda, S., Lu, J. R., Ghez, A. M., et al. 2010, ApJ, 725, 331
Zacharias, N., Monet, D. G., Levine, S. E., et al. 2004, in BAAS, 36, 1418
Zuckerman, B., & Song, I. 2004, ARA&A, 42, 685
Zuckerman, B., & Song, I. 2012, ApJ, 758, 77
Zuckerman, B., Song, I., Bessell, M. S., & Webb, R. A. 2001, ApJ, 562, L87
Zuckerman, B., Rhee, J. H., Song, I., & Bessell, M. S. 2011, ApJ, 732, 61
Zuckerman, B., Melis, C., Song, I., et al. 2008, ApJ, 683, 1085
Zuckerman, B., Vican, L., Song, I., & Schneider, A. 2013, ApJ, 778, 5

Chapitre 2

Galicher et al., 2011, ApJL, 739, L41

Imagerie en bande M du système exoplanétaire orbitant HR 8799 (paragraphe 3.1.2.2 du dossier de synthèse).

The Astrophysical Journal Letters, 739:L41 (5pp), 2011 October 1 doi:10.1088/2041-8205/739/2/L41

M-BAND IMAGING OF THE HR 8799 PLANETARY SYSTEM USING AN INNOVATIVE LOCI-BASED BACKGROUND SUBTRACTION TECHNIQUE

Raphaël Galicher[1,2], Christian Marois[1], Bruce Macintosh[3], Travis Barman[4], and Quinn Konopacky[3]
[1] National Research Council Canada, Herzberg Institute of Astrophysics, 5071 West Saanich Road, Victoria, BC, V9E 2E7, Canada; raphael.galicher@nrc-cnrc.gc.ca
[2] Département de Physique, Université de Montréal, C.P. 6128 Succ. Centre-ville, Montréal, QC, H3C 3J7, Canada
[3] Lawrence Livermore National Laboratory, 7000 East Ave., Livermore, CA 94550, USA
[4] Lowell Observatory, 1400 West Mars Hill Road, Flagstaff, AZ 86001, USA
Received 2011 May 16; accepted 2011 June 27; published 2011 September 2

ABSTRACT

Multi-wavelength observations/spectroscopy of exoplanetary atmospheres are the basis of the emerging exciting field of comparative exoplanetology. The HR 8799 planetary system is an ideal laboratory to study our current knowledge gap between massive field brown dwarfs and the cold 5 Gyr old solar system planets. The HR 8799 planets have so far been imaged at *J*- to *L*-band, with only upper limits available at *M*-band. We present here deep high-contrast Keck II adaptive optics *M*-band observations that show the imaging detection of three of the four currently known HR 8799 planets. Such detections were made possible due to the development of an innovative LOCI-based background subtraction scheme that is three times more efficient than a classical median background subtraction for Keck II AO data, representing a gain in telescope time of up to a factor of nine. These *M*-band detections extend the broadband photometric coverage out to $\sim$5 μm and provide access to the strong CO fundamental absorption band at 4.5 μm. The new *M*-band photometry shows that the HR 8799 planets are located near the L/T-type dwarf transition, similar to what was found by other studies. We also confirm that the best atmospheric fits are consistent with low surface gravity, dusty, and non-equilibrium CO/CH_4 chemistry models.

Key words: instrumentation: high angular resolution – methods: data analysis – methods: observational – planetary systems – planets and satellites: atmospheres – techniques: image processing

Online-only material: color figures

1. INTRODUCTION

After more than a decade of searching, the direct exoplanet imaging quest was finally successful in 2008 with the discovery of three planetary systems (Marois et al. 2008b; Kalas et al. 2008; Lagrange et al. 2009). One key advantage of this technique is the detection of the planet's thermal emission. Detailed multi-band photometry and spectrometry can be acquired that can then be compared with atmospheric models to derive the planet's physical characteristics and study the effect of dust and molecular chemistry. With its multiple coeval Jovian planets, the HR 8799 system is an ideal laboratory to study young planets with low temperature/surface gravity atmospheres and bridge the gap between massive field brown dwarfs and the cold solar system planets.

HR 8799 is a 30 Myr old (Marois et al. 2010b; Zuckerman et al. 2011) A5V star located 39.4 pc away (Leeuwen 2007) in the Pegasus constellation. It is classified as a γ Doradus and a λ Bootis star (Gray & Kaye 1999). It also shows an IR excess (Vega-like star) consistent with a debris disk composed of a warm dust disk (6–15 AU), a massive cold dust disk (90–300 AU), and a small dust particle halo extending up to a 1000 AU (Rhee et al. 2007; Su et al. 2009).

Photometry and some spectroscopy of the HR 8799 planets are available in several bands from 1 to 3.8 μm (Marois et al. 2008b, 2010b; Lafrenière et al. 2009; Metchev et al. 2009; Janson et al. 2010; Hinz et al. 2010; Currie et al. 2011; Barman et al. 2011). An initial characterization (Marois et al. 2008b, 2010b; Bowler et al. 2010; Currie et al. 2011; Barman et al. 2011) has been achieved using the available data and state-of-the-art atmospheric models developed for field brown dwarf analysis. It is clear that these planets are quite different than most field brown dwarfs, showing very dusty atmospheres while being cool ($\sim$1000 K) with no sign of methane molecular absorption. *L*- and *M*-band detections/upper limits suggest that this lack of methane is due to a CO/CH_4 non-equilibrium chemistry (Saumon et al. 2003; Cushing et al. 2006; Leggett et al. 2007; Hinz et al. 2010; Bowler et al. 2010; Currie et al. 2011; Barman et al. 2011). Other teams have been able to fit the available photometry with patchy clouds and equilibrium chemistry atmospheres (Marois et al. 2008b; Currie et al. 2011). Accurate *M*-band photometry can help disentangle the various models, but it is hard on a ground-based telescope due to the bright thermal background mainly from the telescope and the adaptive optics system (Lloyd-Hart 2000). This background is particularly hard to remove at Keck, as it varies with time as the instrument image rotator (which is located very near focus) moves and as the AO deformable mirror modulates the rotator-induced background pattern as seen by the detector. As a result, conventional sky/background subtraction routines leave a spatially variable residual that limits final sensitivity.

In this Letter, we present the first *M*-band (4.670 μm) detections of three of the currently four known HR 8799 planets, the longest wavelength at which these planets have been imaged. The observations are discussed in Section 2. The data reduction along with the new very efficient LOCI-based (LOCI: locally optimized combination of images) background subtraction technique are presented in Section 3. Comparisons with field brown dwarfs and new atmospheric fits are shown in Section 5. Conclusions are summarized in Section 6.

2. OBSERVATIONS

The HR 8799 data were obtained on 2009 November 1 and 2 at the Keck II observatory using the adaptive optics system, the NIRC2 near-infrared narrow-field camera (McLean

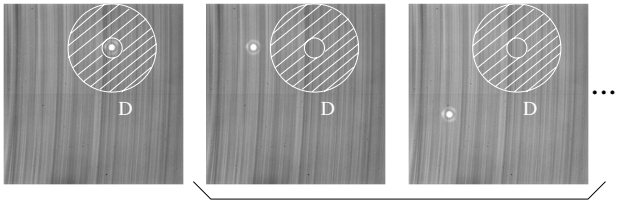

Figure 1. Image I_p where the background has to be subtracted (left) and the D region inside which the LOCI coefficients are optimized using the reference background dither images (right).

& Sprayberry 2003), and the M-band filter ($\lambda_0 = 4.670\,\mu$m and $\Delta\lambda = 0.241\,\mu$m). No coronagraph was used for these observations. For these two nights, 140 unsaturated images (58 for November 1 and 82 for November 2) were acquired, each image consisting of 200 co-adds of 0.3 s, for a total on-source integration time of 140 minutes. The data were taken in angular differential imaging mode (Marois et al. 2006). In that mode, the instrument field rotator is adjusted to track the telescope pupil while leaving the field of view (FOV) to rotate with time. In addition, the telescope was nodded every few minutes between four positions to facilitate the background subtraction. In our data, the total FOV rotation is ∼180 deg for both nights, but both data sets were not acquired through transit (between hour angle [−1.6 hr, −0.4 hr] and [0.6 hr, 1.1 hr] for November 1 and [−1 hr, −0.6 hr] and [0.5 hr, 2.2 hr] for November 2). Although such observing strategy is fine for background limited data, it did limit the amount of speckle subtraction achievable at smaller separations where the data are still speckle noise limited and where planet e is now known to be located (the HR 8799 transit time was actually used during these two nights for L-band imaging to confirm planet e).

3. DATA REDUCTION

The data reduction was performed as follows: we first subtract a dark image, divide by a flat field and mask bad/hot pixels. We then remove known NIRC2 narrow-field camera distortions using the Yelda et al. (2010) solution. The images are rotated by 0.252 deg clockwise to put north up and the plate scale is selected to be 9.952 ± 0002 mas pixel^{-1} to be consistent with the distortion correction of Yelda et al. (2010). After these steps, we subtract the background (Section 3.1) and the speckle noise (Section 3.2) on the two data cubes of 58 (November 1) and 82 (November 2) images separately. We then average the two processed sets to produce a final image.

3.1. LOCI-based Background Subtraction

The telescope was nodded between exposures to record the star at different detector locations. For each image of the sequence, a classical background reduction would consist of subtracting the median of all the images where the star is sufficiently dithered. This standard technique is limited because of the time variations of the thermal background whereas the median uses all the reference background images without distinction. As the background subtraction step is no different than a standard ADI/LOCI speckle subtraction, we have developed a background subtraction routine (Marois et al. 2010a) based on the LOCI algorithm (Lafrenière et al. 2007). This new routine is more efficient than the classical median subtraction as it puts different weights on the background reference images. Let consider the background subtraction in the pth image I_p of the sequence. An annulus (called D, Figure 1) is defined around the star and all reference background images are selected where the star has been sufficiently dithered compared to I_p. The algorithm searches for the linear combination of these images that minimizes the χ^2_p (i.e., the residual noise in D excluding bad pixels) which can be expressed as

$$\chi^2_p\left(\alpha_p^{1\leqslant i\leqslant N}\right) = \sum_{i=1}^{N}\sum_{j=1}^{M}\left[\alpha_p^i\, I_i(x_j) - I_p(x_j)\right]^2 D(x_j), \quad (1)$$

where M is the number of pixels in the image, N is the total number of images in the sequence, x_j is the jth pixel, I_i is the ith image of the sequence, and α_p^i the coefficients to be determined. The inner radius of area D is chosen to avoid the bright star speckle noise that can bias the background minimization algorithm, while its outer radius is chosen to avoid the dithered star images. In our case, the inner and outer radii are 3 and 30 λ/D corresponding to 24 to 240 pixels. We have then imposed $\alpha_p^i = 0$ if the star is at a similar location in I_i as in I_p. The LOCI algorithm then finds the optimal $\alpha_p^{i,\mathrm{best}}$ (Lafrenière et al. 2007; Marois et al. 2010a) that minimizes the χ^2_p. The optimized background image B_p at each pixel for I_p (not only in D) is then

$$B_p = \sum_{i=1}^{N} \alpha_p^{i,\mathrm{best}}\, I_i. \quad (2)$$

The generated reference background image B_p is finally subtracted from I_p. As $\alpha_p^{i,\mathrm{best}} = 0$ for the images where the star is registered at the same location in I_i as in I_p, B_p does not contain any flux from a possible companion. Moreover, if a companion exists in I_p, its impact on the $\alpha_p^{i,\mathrm{best}}$ LOCI coefficients is negligible since the companion flux is much smaller than the thermal background and D is large compared to the companion point-spread function (PSF).

Once the background is subtracted, we sub-pixel register each image using an iterative cross-correlation Gaussian fit to the PSF core (images are unsaturated).

3.2. Median Speckle Subtraction

The speckle subtraction is performed following a basic ADI data reduction as described in Marois et al. (2006). For each data cube, an initial reference PSF is assembled by taking the median of all images and is then subtracted. We then rotate the images to put north up and median combine them. We apply an unsharp mask to the resulting image (median in a $4 \times 4\lambda/D$

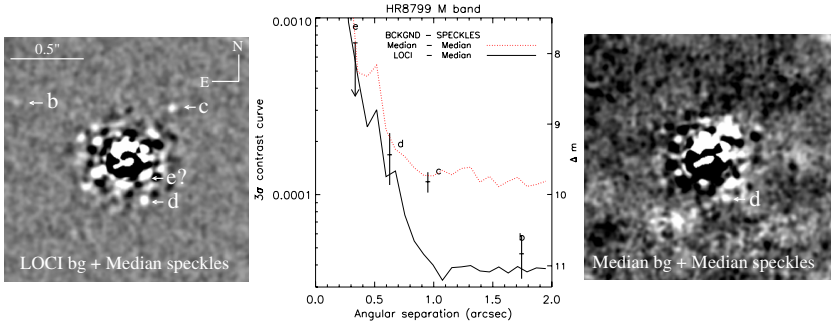

Figure 2. Left panel: final image (average of the November 1 and 2 data) after subtracting the background noise with our new LOCI-based algorithm and the speckle noise with a basic median. Right panel: same reduction, but using a classical median background subtraction. We applied an unsharp mask (median in a $4 \times 4\lambda/D$ box) on the two images and then convolved them by a $0.5\lambda/D$ width Gaussian. The two panels have the same linear intensity scale and FOV. North is up and east is left. Central panel: 3σ radial contrast noise profiles of our resulting median-combined images after subtracting the background with LOCI processing (black full line) or a median (red dashed line). Planets b, c, and d fluxes are also plotted with 1σ error bars along with the planet e flux upper limit.

(A color version of this figure is available in the online journal.)

box) to remove the low spatial frequency noise and convolve it by a $0.5\lambda/D$ width Gaussian to average the high-frequency pixel-to-pixel noise. We finally average the November 1 and 2 images (Figure 2).

Without the LOCI background subtraction, none of the planets would have been detected (right panel, signal-to-noise ratio (S/N) for d is less than 2). With the LOCI background subtraction, HR 8799b, c, and d are detected (left panel, 3–8 S/N). Planet e non-detection is probably due to both sequences not being acquired through transit, thus limiting the amount of speckle noise being removed at small separations from the median subtraction. We tried to apply a more advanced LOCI algorithm (Lafrenière et al. 2007; Marois et al. 2008a, 2010a) to improve the speckle reduction, but as the FOV rotation ranges were small for both nights, no contrast gain was achieved.

4. DATA ANALYSIS

Planet fluxes and positions were obtained by subtracting the planets prior to the speckle reduction using the stellar unsaturated PSF as the template. We also tried subtracting the companions prior to the LOCI-background algorithm and we have confirmed that no bias is introduced by this technique (final flux variations smaller than 0.07%). The subtraction was iterated by moving the planet template and changing its intensity until a minimal noise residual at the planet's location was achieved (inside a $1.5\ \lambda/D$ radius area; Table 1 for the resulting magnitudes). Photometric error bars were calculated in λ/D width annulus. As expected from other wavelengths (Marois et al. 2008b), HR 8799b flux is roughly a third of that of planets c and d. The planet's positions are included in Table 1. The low S/Ns and the large M-band PSF core result in large astrometric errors. A future astrometric HR 8799 paper using shorter wavelength astrometry is in preparation.

Contrast plots (central panel of Figure 2) were obtained by calculating the noise in an annulus having a λ/D width normalized by the stellar PSF flux (after performing the same unsharp mask and convolution of a $0.5\ \lambda/D$ Gaussian). The contrast plots were then normalized at each separation by the estimated point source throughput using simulated ADI median process planets. Figure 2 shows that the LOCI background subtraction (black full line) is up to ~3 times better than a classical background median subtraction (red dotted line). If a classical background subtraction routine is used, an integration time of up to nine times longer is required to reach the same LOCI background subtraction contrast. This new highly efficient LOCI-based background subtraction routine can be used on any data where the background is non-negligible and evolving with time.

Table 1
HR 8799 Planets M-photometry

Planet	b	c	d	e
Separation w.r.t. HR8799a (E,N)″	(1.54, 0.80)	(−0.63, 0.72)	(−0.24, −0.58)	[a]
	±0.019	±0.013	±0.014	
Contrast Δm	10.84 ± 0.30	9.82 ± 0.14	9.44 ± 0.35	>7.85[b]
Absolute M	13.07 ± 0.30	12.05 ± 0.14	11.67 ± 0.35	>10.09[b]
Absolute M (T. Currie et al. 2011, submitted)	>11.37[b]	>11.22[b]	>11.15[b]	
Absolute flux (mJy)	0.91 ± 0.21	2.33 ± 0.25	3.31 ± 0.65	<14.23[b]
Currie's absolute flux (mJy)	<4.36[b]	<5.00[b]	<5.34[b]	

Notes. HR 8799a apparent magnitude is 5.21 and its distance is 39.4 ± 1.0 pc. Magnitude zeropoint is 154 Jy (Cox & Pilachowski 2000).
[a] We use the Marois et al. (2010b) astrometry for planet e.
[b] 3σ upper limits.

5. DISCUSSIONS

It has been shown that the HR 8799 planets are an L-type extension toward lower effective temperatures and lower surface gravities (Marois et al. 2008b; Bowler et al. 2010; Currie et al. 2011; Barman et al. 2011). The planets have also been found to be dusty with evidence of non-equilibrium CO/CH_4 chemistry. If the HR 8799 planets are plotted in $K' - L'$ versus $L' - M'$ diagram (Figure 3) against field brown dwarfs and lower mass stars (Leggett et al. 2007), it is found that the HR 8799 planets are located near the L/T-type dwarf transition. The M-band photometry is thus consistent with what was found previously by

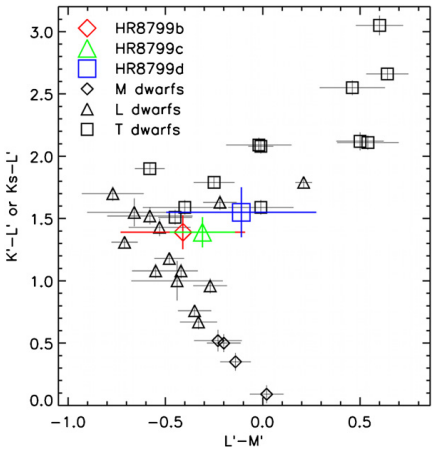

Figure 3. $K-L$ vs. $L-M$ diagram for field brown dwarfs, lower mass stars, and the HR 8799 planets. The planets are located near the end of the L-type sequence, close to the T-type transition.

(A color version of this figure is available in the online journal.)

other studies. From the field brown dwarf best-fit parameters of Figures 4–6 of Leggett et al. (2007), we also find that the planet L- and M-band colors are consistent with dusty atmospheres with vertical mixing. Barman et al. (2011) found a similar result for HR 8799b while considering lower surface gravities.

If we compare our estimated M-band flux to Currie et al. (2011) equilibrium chemistry model predictions, we find that all their best patchy-cloud atmospheric fits are rejected to $\sim 3\sigma$ for HR 8799b. For planets c and d, Currie et al. (2011) use equilibrium chemical models and focus on clouds to interpret the available photometry. The earlier work of Hinz et al. (2010) did compare different chemical models to their M-band upper limits for all three planets, but did not include near-IR photometry. Our new photometry is consistent with some models proposed by the two teams and will help in constraining their fits.

In this Letter, we compare cloudy and non-equilibrium model fits for all of the photometry for the three planets. Such comparison has only been done for planet b so far (Bowler et al. 2010; Barman et al. 2011). Using the same solar-abundance model atmosphere grids and procedures described in Barman et al. (2011), new gravities and effective temperatures are found (Figure 4). For planet b, we find similar model atmosphere parameters as in Barman et al. (2011), but with a slightly higher gravity—$\log(g) = 4$ rather than 3.5. This solar-abundance model has $T_{\rm eff} = 1100$ K and, thus, requires a very small

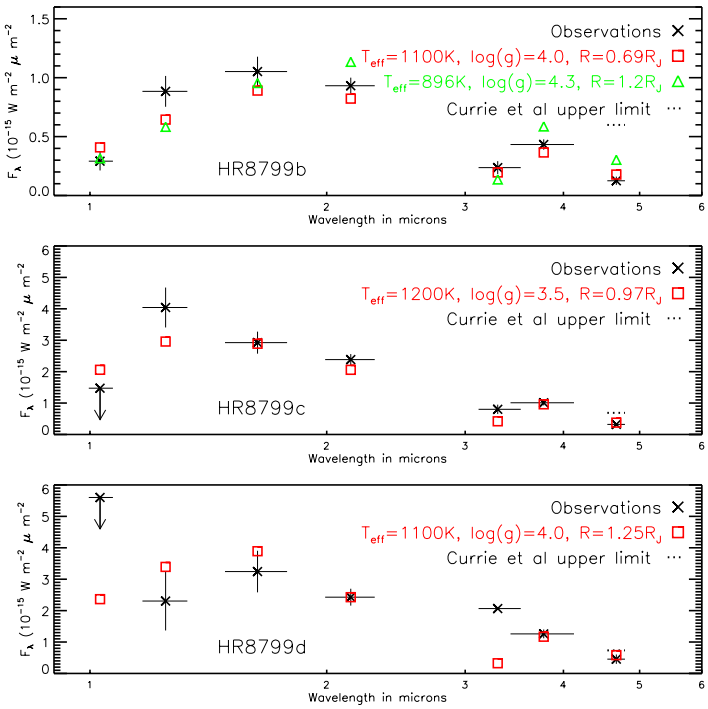

Figure 4. Comparison between the best solar-abundance model (red squares) and the broadband photometry (black cross) for HR 8799b(top), c (middle), and d (bottom). For planet b, the photometry from the 10 times more metal-rich case described in Barman et al. (2011) is plotted in green triangles. The photometric measurements other than for the M-band are from Marois et al. (2008b, 2010b) and Currie et al. (2011). We also show Currie et al. (2011) upper limits for the M-band photometry as a dotted line.

(A color version of this figure is available in the online journal.)

radius ($\sim 0.7\ R_j$) to match the observed bolometric luminosity; nearly a factor of two smaller than predicted by traditional hot-start models (Baraffe et al. 2003). For planets c and d, we find temperatures and gravities that are fairly close to the expected values from evolution models (Marois et al. 2008b). Barman et al. (2011) argue that increasing the metallicity to 10 times solar could bring the $T_{\rm eff}/\log(g)$ derived from atmosphere and evolution models for planet b into better agreement. The photometry from this metal-rich, evolution-consistent, model is also shown in Figure 4. This model, however, predicts an M-band flux that is 3.5σ brighter than observed (while all other bands agree to 2σ or better). This may indicate an even higher overall metallicity and/or that a non-solar C-to-O ratio is required. A broader exploration of the possible metal abundances for all four planets will be left to a future paper.

6. CONCLUSIONS

In this Letter, we have estimated for the first time the M-band fluxes of three of the currently four known HR 8799 planets. These detections were made possible due to the use of an innovative LOCI-based background subtraction routine that has allowed for a factor of three gain in contrast (factor of nine in integration time) compared to a classical background subtraction using a median. This new background subtraction routine can be used to subtract the background noise in any infrared data.

We have detected HR 8799b, c, and d at M-band from 3 to 8σ. From a $K' - L'$ and $L' - M'$ color diagram, we confirm that the three planets are located near the end of the L-type sequence, close to the L- and T-dwarf transition region. We then derived new atmosphere model fits for the three planets. For planets c and d, temperatures and surface gravities are close to the expected values from evolutionary models. For planet b, the solar-abundance model fits well the broadband photometry from 1 to $5\,\mu$m but it requires a very small planetary radius to match the bolometric luminosity and is thus in contradiction with the planet evolution models. The metal-rich evolution-consistent model overpredicts the M-band flux, which may indicate an even higher overall metallicity and/or a non-solar C-to-O ratio. Higher S/N images will help disentangle the different physical and chemical parameters.

The authors thank S. Leggett for kindly providing the Figure 3 field brown dwarf data. Portions of this work were performed under the auspices of the U.S. Department of Energy by Lawrence Livermore National Laboratory under Contract DE-AC52-07NA27344. The data presented herein were obtained at the W. M. Keck Observatory, which is operated as a scientific partnership among the California Institute of Technology, the University of California, and the National Aeronautics and Space Administration. The Observatory was made possible by the generous financial support of the W. M. Keck Foundation. The authors wish to recognize and acknowledge the very significant cultural role and reverence that the summit of Mauna Kea has always had within the indigenous Hawaiian community. We are most fortunate to have the opportunity to conduct observations from this mountain.

REFERENCES

Baraffe, I., Chabrier, G., Barman, T. S., Allard, F., & Hauschildt, P. H. 2003, A&A, 402, 701
Barman, T., Macintosh, B., Konopacky, Q. M., & Marois, C. 2011, ApJ, 733, 65
Bowler, B. P., Liu, M. C., Dupuy, T. J., & Cushing, M. C. 2010, ApJ, 723, 850
Cox, A. N., & Pilachowski, C. A. 2000, Physics Today, 53, 77
Currie, T., Burrows, A., Itoh, Y., et al. 2011, ApJ, 729, 128
Cushing, M. C., Roellig, T. L., Marley, M. S., et al. 2006, ApJ, 648, 614
Gray, R. O., & Kaye, A. B. 1999, AJ, 118, 2993
Hinz, P. M., Rodigas, T. J., Kenworthy, M. A., et al. 2010, ApJ, 716, 417
Janson, M., Bergfors, C., Goto, M., Brandner, W., & Lafrenière, D. 2010, ApJ, 710, L35
Kalas, P., Graham, J. R., Chiang, E., et al. 2008, Science, 322, 1345
Lafrenière, D., Marois, C., Doyon, R., & Barman, T. 2009, ApJ, 694, L148
Lafrenière, D., Marois, C., Doyon, R., Nadeau, D., & Artigau, É. 2007, ApJ, 660, 770
Lagrange, A. M., Gratadour, D., Chauvin, G., et al. 2009, A&A, 493, L21
Leeuwen, E. V. 2007, A&A, 474, 653
Leggett, S., Saumon, D., Marley, M. S., et al. 2007, ApJ, 655, 1079
Lloyd-Hart, M. 2000, PASP, 112, 264
Marois, C., Lafrenière, D., Doyon, R., Macintosh, B., & Nadeau, D. 2006, ApJ, 641, 556
Marois, C., Lafrenière, D., Macintosh, B., & Doyon, R. 2008a, ApJ, 673, 647
Marois, C., Macintosh, B., Barman, T., et al. 2008b, Science, 322, 1348
Marois, C., Macintosh, B., & Véran, J.-P. 2010a, Proc. SPIE, 7736, 77361J
Marois, C., Zuckerman, B., Konopacky, Q. M., Macintosh, B., & Barman, T. 2010b, Nature, 468, 1080
McLean, I. S., & Sprayberry, D. 2003, Proc. SPIE, 4841, 1
Metchev, S., Marois, C., & Zuckerman, B. 2009, ApJ, 705, L204
Rhee, J. H., Song, I., Zuckerman, B., & McElwain, M. 2007, ApJ, 660, 1556
Saumon, D., Marley, M. S., Lodders, K., & Freedman, R. S. 2003, in IAU Symp. 211, Brown Dwarfs, ed. E. Martín (San Francisco, CA: ASP), 345
Su, K. Y. L., Rieke, G. H., Stapelfeldt, K. R., et al. 2009, ApJ, 705, 314
Yelda, S., Lu, J. R., Ghez, A. M., et al. 2010, ApJ, 725, 331
Zuckerman, B., Rhee, J. H., Song, I., & Bessell, M. S. 2011, ApJ, 732, 61

Chapitre 3

Galicher et al., 2014, AA, 565, L4

Détection et caractéristation en proche infrarouge avec l'instrument *Gemini Planet Imager* de l'exoplanète HD 95086 b (paragraphe 3.1.2.3 du dossier de synthèse).

A&A 565, L4 (2014)
DOI: 10.1051/0004-6361/201423839

Astronomy & Astrophysics

L E

Near-infrared detection and characterization of the exoplanet HD 95086 b with the Gemini Planet Imager⋆

R. Galicher[1], J. Rameau[2], M. Bonnefoy[2], J.-L. Baudino[1], T. Currie[3], A. Boccaletti[1], G. Chauvin[2], A.-M. Lagrange[2], and C. Marois[4]

[1] LESIA, CNRS, Observatoire de Paris, Univ. Paris Diderot, UPMC, 5 place Jules Janssen, 92190 Meudon, France
e-mail: raphael.galicher@obspm.fr
[2] UJF-Grenoble 1/CNRS-INSU, Institut de Planétologie et d'Astrophysique de Grenoble (IPAG) UMR 5274, 38041 Grenoble, France
[3] Department of Astronomy and Astrophysics, Univ. of Toronto, 50 St. George St., Toronto M5S 1A1, Canada
[4] National Research Council of Canada Herzberg, 5071 West Saanich Road, Victoria V9E 2E7, Canada

Received 18 March 2014 / Accepted 15 April 2014

ABSTRACT

HD 95086 is an intermediate-mass debris-disk-bearing star. VLT/NaCo 3.8 μm observations revealed it hosts a $5 \pm 2\ M_{\rm Jup}$ companion (HD 95086 b) at ≃56 AU. Follow-up observations at 1.66 and 2.18 μm yielded a null detection, suggesting extremely red colors for the planet and the need for deeper direct-imaging data. In this Letter, we report H-(1.7 μm) and K_1-(2.05 μm) band detections of HD 95086 b from Gemini Planet Imager (GPI) commissioning observations taken by the GPI team. The planet position in both spectral channels is consistent with the NaCo measurements and we confirm it to be comoving. Our photometry yields colors of $H - L' = 3.6 \pm 1.0$ mag and $K_1 - L' = 2.4 \pm 0.7$ mag, consistent with previously reported 5-σ upper limits in H and Ks. The photometry of HD 95086 b best matches that of 2M 1207 b and HR 8799 cde. Comparing its spectral energy distribution with the BT-SETTL and LESIA planet atmospheric models yields $T_{\rm eff} \sim$ 600–1500 K and $\log g \sim$ 2.1–4.5. Hot-start evolutionary models yield $M = 5 \pm 2\ M_{\rm Jup}$. Warm-start models reproduce the combined absolute fluxes of the object for M = 4–14 $M_{\rm Jup}$ for a wide range of plausible initial conditions ($S_{\rm init}$ = 8–13 $k_{\rm B}$/baryon). The color−magnitude diagram location of HD 95086 b and its estimated $T_{\rm eff}$ and $\log g$ suggest that the planet is a peculiar L–T transition object with an enhanced amount of photospheric dust.

Key words. planets and satellites: atmospheres – planets and satellites: detection – stars: individual: HD 95086 – instrumentation: adaptive optics

1. Introduction

HD 95086 b is a directly imaged planet ($5 \pm 2\ M_{\rm J}$, $a_{\rm proj} = 55.7 \pm 2.5$ AU) discovered by Rameau et al. (2013a) in L' (3.8 μm) with VLT/NaCo (Lenzen et al. 2003; Rousset et al. 2003) orbiting the young A8 star HD 95086 ($M \sim 1.6\ M_\odot$), a member of the Lower Centaurus Crux subgroup (17 ± 4 Myr, Pecaut et al. 2012; Meshkat et al. 2013). Additional L' images taken later in 2013 confirmed that the object is comoving with its star (Rameau et al. 2013b).

NaCo Ks (2.18 μm) and NICI (Chun et al. 2008) H-band (1.65 μm) observations failed to reveal the planet (Rameau et al. 2013a; Meshkat et al. 2013). However, 5σ lower limits of Ks-L′ = 1.2 ± 0.5 mag and $H - L' = 3.1 \pm 0.5$ mag suggest that the planet may have extremely red colors, similar to the young planets HR 8799 bcde and 2M 1207 b (Chauvin et al. 2004; Marois et al. 2008, 2010a), which have very dusty/cloudy atmospheres (Barman et al. 2011; Currie et al. 2011). Higher contrast near-IR data able to detect HD 95086 b can provide better comparisons with these objects and better constrain its atmosphere.

In this Letter, we present detections of HD 95086 b with the recently installed Gemini Planet Imager (GPI, Macintosh et al. 2014) on Gemini South from public data as a part of GPI commissioning observations (Perrin et al. 2014). The data (acquired and reduced by the GPI team), their analysis, and the detections are presented in Sect. 2. In Sect. 3, we combine GPI H and K_1 photometry with NaCo L' photometry to constrain the physical properties of HD 95086 b.

2. Observations and data reduction

The GPI is a new instrument for imaging and characterizing planets around young nearby bright stars, combining an extreme adaptive optics system, coronagraphs, and an integrated field spectrograph (IFS). The IFS platescale is 14.3 ± 0.3 mas px^{-1} for a 2.8″ field-of-view (FOV) and the true North position angle is given within 1 deg[1].

The HD 95086 spectral data were obtained at H (1.5−1.8 μm, R = 44–49) and K_1 (1.9–2.19 μm, R = 62–70) in 2013 December using apodized Lyot coronagraphs (Table 1) and angular differential imaging (ADI, Marois et al. 2006a). Conditions were good: 0.43″ and 0.6″ DIMM seeing, air masses of 1.32 and 1.34, and coherence times of 19 ms and 17 ms, respectively. The GPI commissioning team used their pipeline for bad-pixel removal, destriping, non-linearity and persistence corrections, flat-fielding, wavelength calibration, and converting the data into spectral data cubes. We used the data cubes relying on the GPI pipeline quality. The data are made of 21 and 17 spectral

⋆ Based on public data taken at the GPI commissioning.

[1] http://planetimager.org/

Table 1. Observing log of HD 95086 with GPI.

Date	Filter	Coro mask diam (mas)	DIT(s) × NDITS × Nb_λ	Nb images	FOV rotation (°)
2013/12/10	K_1-coro	306	119.29278 × 1 × 37	17	11.7
2013/12/11	H-coro	246	119.29278 × 1 × 37	21	15.0

Notes. Date, filter, occulting mask diameter, exposure, numbers of coadds, of spectral channels, of images, and FOV rotation.

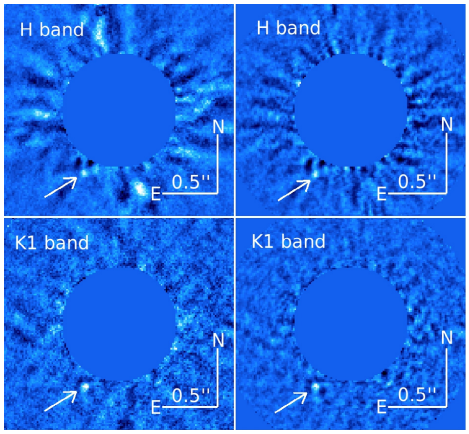

Fig. 1. Final images of the HD 95086 system at H (*top*) and K_1 (*bottom*) bands from two of our pipelines. The planet (arrow) is detected in all images. The bright speckles are masked up to 500 mas from the central star.

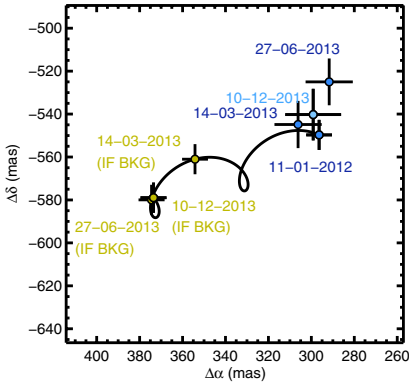

Fig. 2. HD 95086 b positions from its star in RA ($\Delta\alpha$) and Dec ($\Delta\delta$). GPI and NaCo measurements are marked in blue and expected positions of a background object in yellow.

cubes at H and K_1 bands, respectively, consisting of 37 spectral channels each.

To further process the data, we registered each slice of the spectral cubes using the barycenter of the four satellite spots (attenuated replica of the central star PSF induced by a grid placed in a pupil plane, Marois et al. 2006b). Then, we minimized the speckle noise in each slice using independent pipelines each adopting various methods (Marois et al. 2006a; Lafrenière et al. 2007; Lagrange et al. 2010; Boccaletti et al. 2012; Chauvin et al. 2012; Soummer et al. 2012; Currie et al. 2013; Marois et al. 2014) used for ADI and spectral differential imaging (SSDI, Racine et al. 1999). Finally, all slices were mean-combined to yield an integrated broad-band image to maximize the signal-to-noise ratio (S/N) of any off-axis source. Binning images in wavelength and suppressing the speckles (ADI), or suppressing the speckles in each spectral channel (ADI/ADI+SSDI) and binning images give similar results, and all our pipelines recover HD 95086 b, which is the sole bright spot at the expected separation. Thus, we provide the first detections at H and K_1 bands (Fig. 1) with an S/N of ~3–4 and 5–6, respectively. The central bright speckles are masked up to 500 mas. These are the first detections of HD 95086 b with an instrument that is not NaCo/VLT. No spectrum can be extracted given the low S/N.

To estimate the planet flux and position, we needed unsaturated GPI PSFs. As GPI cannot acquire off-axis observations of the star, we calibrated photometry and astrometry using the satellite spots, which are expected to have same shape and brightness for a given filter. In the laboratory the spot-to-central-star flux ratios were 2.035×10^{-4} (9.23 mag) and 2.695×10^{-4} (8.92 mag) at H and K_1 bands[1]. To check these values, we compared H and K photometry of HD 8049 B (VLT/ NACO-SINFONI, Zurlo et al. 2013) with our measurements derived from public GPI HD 8049 data. Assuming that the object is not photometrically variable with time and considering the laboratory spot contrasts, GPI and VLT photometry are consistent within $\epsilon_1 = 0.2$ mag, which we take as the error on the ratios. From these ratios, we assessed biases induced by our processing by injecting fake point-sources (i.e., unsaturated PSFs) into the data before applying speckle-suppression techniques (Lagrange et al. 2010; Marois et al. 2010b; Chauvin et al. 2012; Galicher et al. 2012). We obtained templates of the planet image. Adjusting the flux of the templates, we found the planet photometry and the fitting error ϵ_2, which depends on the detection quality. ϵ_2 is 0.8 mag and 0.3 mag at H and K_1. Finally, we estimated the variation ϵ_3 of stellar flux over the sequence with the variation of spot flux. ϵ_3 is 0.2 mag and 0.3 mag over the H and K_1 sequences including the variations between spots. The resulting photometric error is the quadratic error, which is dominated by the low S/N at H and is a mix of all errors at K_1.

For the astrometric error, we considered uncertainties in the centroiding accuracy of individual slices (≤0.3 pixel), the plate scale (0.02 pixel), the planet template fit (0.7 pixel at H, 0.5 pixel at K_1), and the North position angle (1 deg). The error is dominated by the low S/N of the detections and the generic GPI calibrations. The current precision is good enough to assess the comoving status of the companion (Fig. 2). We tried to use the astrometric standard HD 8049 B in GPI data to better constrain the North orientation. We did not succeed because of the high orbital motion of HD 8049 B and because there is no contemporary observation from other instruments.

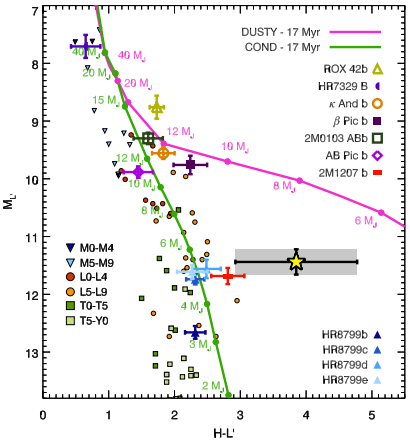

Fig. 3. Color–magnitude diagram using the new H-band photometry of HD 95086 b (yellow star) and data from Bonnefoy et al. (2013), Bonnefoy et al. (2014), and Currie et al. (2014).

Table 2. HD 95086 b photometry and astrometry at H and K_1 (GPI data) and L' (Rameau et al. 2013a,b, and revision*).

Date	Filter	Sep (mas)	PA(°)	Δm
2013/12/11	H	633 ± 17	150.6 ± 1.7	13.1 ± 0.9
2013/12/10	K_1	623 ± 15	151.4 ± 1.5	12.1 ± 0.5
2013/03/24	L'	626.1 ± 12.8	150.7 ± 1.3	9.71 ± 0.56
2012/01/11	L'	623.9 ± 7.4	151.8 ± 0.8	9.79 ± 0.40
2012/01/11	L'	623.9 ± 7.4	151.8 ± 0.8	9.48 ± 0.19*

Notes. (*) See text for details.

Final measurements are presented in Table 2. We include revised 2012 NaCo L' photometry obtained by 1) better calibrating the planet signal (as in Currie et al. 2013) and 2) precisely deriving the L' neutral density (ND) filter throughput (used to flux-calibrate HD 95086) by comparing ND and unsaturated β Pic data.

3. Characterization

Absolute magnitudes were derived from the contrast ratios (Table 2): $M_H = 15.29 \pm 0.91$ mag, $M_{K_1} = 14.11 \pm 0.51$ mag, and $M_{L'} = 11.44 \pm 0.22$ mag using the 2MASS and WISE W1 (Cutri et al. 2003, 2012) photometry of the star[2].

Combining the H band GPI data with revised NaCo L' data, we compared the $L'/H - L'$ color–magnitude diagram position of HD 95086 b with that of young companions, field dwarfs (Leggett et al. 2010, 2013), and LYON evolutionary tracks (Chabrier et al. 2000; Baraffe et al. 2003) generated for the GPI/NaCo passbands[3].

We converted the GPI measurements into H photometry by applying correction factors derived from published spectra, the filter transmissions, and a spectrum of Vega. HD 95086 b lies at the $L-T$ transition in this diagram, similar to other young (8–30 Myr) planets like HR 8799 cde (Marois et al. 2008, 2010a) and 2M1207 b (Chauvin et al. 2004). Its red $H - L'$ color compared with the sequence of field dwarf objects (Leggett et al. 2010, 2013) suggests a high content of photospheric dust (Barman et al. 2011; Currie et al. 2011), owing to reduced surface gravity (e.g. Fig. 11 of Marley et al. 2012).

Table 3. Physical parameters predicted by hot-start evolutionary models for the observed absolute magnitudes.

	SED		L'	
Model	BT-SETTL	Lesia	Dusty	Cond
$T_{\rm eff}$ (K)	1050^{+450}_{-450}	1200^{+300}_{-300}	916^{+43}_{-44}	1108^{+66}_{-65}
log g (dex)	$4.0^{+0.5}_{-0.5}$	$3.3^{+1.2}_{-1.2}$	$3.8^{+0.1}_{-0.1}$	$3.9^{+0.1}_{-0.1}$
M ($M_{\rm Jup}$)	–	–	4.5^{+1}_{-1}	$5.5^{+1.5}_{-1.5}$

We built the 1.5–4.8 μm spectral energy distribution (SED) of the planet following Bonnefoy et al. (2013) by combining the GPI photometry with the L' one. The normalized SED (at L') is best compatible with the young exoplanets HR 8799 bcde and 2M1207 b, but is redder. Its colors are also ∼1 mag redder than those of the benchmark dusty L6.5−L7.5 field dwarf 2MASS J22443167+2043433 (Dahn et al. 2002; Stephens et al. 2009).

We also compared the SED of HD 95086 b with the predictions from grids of synthetic spectra for BT-SETTL (Allard et al. 2012) and LESIA atmospheric models (Baudino et al. 2014). Each synthetic SED was normalized to that of HD 95086 b at L'. The BT-SETTL grid covers 400 K $\leq T_{\rm eff} \leq$ 3500 K with 50 to 100 K increments, $-0.5 \leq \log g \leq 6.0$ dex with 0.5 dex increments, and $M/H = 0.0$ or +0.5 dex. The BT-SETTL models that reproduce the photometry of HD 95086 b have 600 K $\leq T_{\rm eff} \leq$ 1500 K and 3.5 dex $\leq \log\ g \leq$ 4.5 dex. The three LESIA grids assume 700 K $\leq T_{\rm eff} \leq$ 2100 K, 2.1 $\leq \log g \leq$ 4.5 dex, and solar abundances: one without clouds and two with clouds of Fe and Mg_2SiO_4 particles. For each LESIA model, we selected the planet radius that minimizes χ^2 between the observed and calculated apparent magnitudes. We only kept models with a radius in a realistic range derived from evolution models (0.6 to 2 Jupiter radii, Mordasini et al. 2012). All LESIA models that reproduced the HD 950866 b photometry have 900 K $\leq T_{\rm eff} \leq$ 1500 K and 2.1 dex $\leq log\ g \leq$ 4.5 dex.

The planet mass cannot be derived from the atmosphere models, and evolutionary models are needed. Comparing the planet's L' luminosity with hot-start DUSTY and COND models for an age of 17 ± 4 Myr, we find a planet mass of $M = 5 \pm 2\ M_{\rm Jup}$ (Table 3). We did not use the H and K_1 photometries because they are poorly reproduced by the models for an object at the $L-T$ transition (larger uncertainties than for L'). The models predict $T_{\rm eff}$ and $\log g$, in agreement with those derived from the SED fit.

Alternatively, we used the warm-start models (Spiegel & Burrows 2012) to account for possible different initial conditions for the planet (parameterized by the initial entropy between 8 and 13 k_B/baryon). The models assume solar metallicity and atmospheres enriched by a factor of 3 with/without dust clouds as boundary conditions. Synthetic SEDs are generated from predicted spectra of planets[4]. For the full range of initial entropies we considered, models assuming masses of 4−14 $M_{\rm Jup}$

[2] Correction factors from the GPI/NaCo and 2MASS/WISE photometry, derived from the spectrum of an A7III star in the Pickles et al. (1998) library, are negligible.

[3] http://phoenix.ens-lyon.fr/simulator/index.faces

[4] http://www.astro.princeton.edu/~burrows/warmstart/spectra.tar.gz

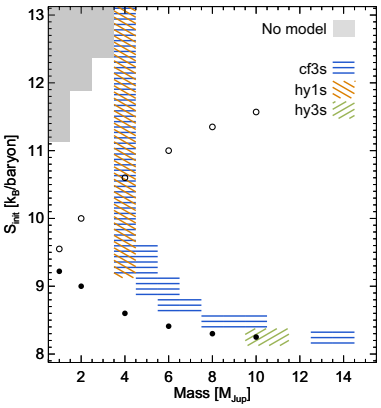

Fig. 4. Combination of initial entropies ($S_{\rm init}$) and masses (shaded areas) for which the planet 1.6–4.8 μm photometries are reproduced by the warm-start models of Spiegel & Burrows (2012) within 1σ. Three boundary conditions are considered: with (hy) and without (cf) cloudy atmospheres, at solar (1s) and 3x solar (3s) metallicity. Initial entropies for the cold-start (filled circles) and hot-start (open circles) models of Marley et al. (2007) are overlaid.

match the SED of HD 95086 b (Fig. 4). For much of this range ($S_{\rm init}$ = 9.5−13) a mass of 4 $M_{\rm Jup}$ is favored.

4. Conclusions

We reported the near-IR detections of HD 95086 b from GPI public commissioning data. We confirmed that the companion is comoving with HD 95086 and derived the first estimates of its magnitudes with respect to its star: $H = 13.1 \pm 0.9$ and $K_1 = 12.1 \pm 0.5$.

While the mid-IR luminosity of HD 95086 b is best consistent with an L−T transition object, it has redder near-IR colors than other young, imaged planet-mass companions. This is consistent with a very dusty and low surface gravity atmosphere.

Comparison with atmosphere models provided 600 K $\leq T_{\rm eff} \leq$ 1500 K and 2.1 dex $\leq \log g \leq$ 4.5 dex. Evolutionary models are consistent with a mass of $5 \pm 2\ M_{\rm Jup}$. However, the models are affected by systematic errors that are difficult to quantify because of the lack of young objects at the L−T transition.

More higher-precision spectroscopic and photometric data for HD 95086 b are required to refine the planet properties.

Acknowledgements. We thank the consortium who built the GPI instrument and the data analysis team for developing reduction tools. We are grateful to Dave Spiegel and Adam Burrows for making the warm-start models publicly available. J.R., M.B., G.C., and A.M.L. acknowledge financial support from the French National Research Agency (ANR) through project grant ANR10-BLANC0504-01. This research has benefitted from the SpeX Prism Spectral Libraries, maintained by Adam Burgasser at http://pono.ucsd.edu/~adam/browndwarfs/spexprism. J.L.B.'s PhD is funded by the LabEx "Exploration Spatiale des Environnements Planétaires" (ESEP) # 2011-LABX-030. T.C. is supported by a McLean Postdoctoral Fellowship.

References

Allard, F., Batten, A., Budding, E., et al. 2012, IAU Proc. 282, eds. M. T. Richards, & I. Hubeny, 235
Baraffe, I., Chabrier, G., Barman, T., Allard, F., & Hauschildt, P. 2003, A&A, 402, 701
Barman, T., Macintosh, B., Konopacky, Q. M., & Marois, C. 2011, ApJ, 735, L39
Baudino, J.-L., Brézard, B., Boccaletti, A., Bonnefoy, M., & Lagrange, A.-M. 2014, IAU Proc., 299, 277
Boccaletti, A., Augereau, J.-C., Lagrange, A.-M., et al. 2012, A&A, 544, A85
Bonnefoy, M., Boccaletti, A., Lagrange, A.-M., et al. 2013, A&A, 555, A107
Bonnefoy, M., Chauvin, G., Lagrange, A.-M., et al. 2014, A&A, 562, A127
Chabrier, G., Baraffe, I., Allard, F., & Hauschildt, P. 2000, ApJ, 542, 464
Chauvin, G., Lagrange, A.-M., Dumas, C., et al. 2004, A&A, 425, 29
Chauvin, G., Lagrange, A.-M., Beust, H., et al. 2012, A&A, 542, A41
Chun, M., Toomey, D., Wahhaj, Z., et al. 2008, Proc. SPIE, 7015, 70151
Currie, T., Burrows, A., Itoh, Y., et al. 2011, ApJ, 729, 128
Currie, T., Burrows, A., Madhusudhan, N., et al. 2013, ApJ, 776, 15
Currie, T., Daemgen, S., Debes, J. H., et al. 2014, ApJ, 780, L30
Cutri, R., Skrutskie, M., Van Dyk, S., et al. 2003, VizieR On-line Data Catalog: II/246
Cutri, R., Skrutskie, M., Van Dyk, S., et al. 2012, VizieR On-line Data Catalog: II/311
Dahn, C., Harris, H., Vrba, F., et al. 2002, ApJ, 124, 1170
Galicher, R., & Marois, C. 2012, Proc. of the AO4ELT conference, 25
Lafrenière, D., Marois, C., Doyon, R., Nadeau, D., & Artigau, É. 2007, ApJ, 660, 770
Lagrange, A.-M., Bonnefoy, M., Chauvin, G., et al. 2010, Science, 329, 57
Leggett, S., Burningham, B., Saumon, D., et al. 2010, ApJ, 710, 1627
Leggett, S., Morley, C., Marley, M., et al. 2013, ApJ, 763, 130
Lenzen, R., Hartung, M., Brandner, W., et al. 2003, Proc. SPIE, 4841, 944
Marley, M., Fortney, J., Hubickyj, O., Bodenheimer, P., & Lissauer, J. 2007, ApJ, 655, 541
Marley, M., Saumon, D., Cushing, M. et al. 2012, ApJ, 754, 135
Marois, C., Lafrenière, D., Doyon, R., Macintosh, B., & Nadeau, D. 2006a, ApJ, 641, 556
Marois, C., Lafrenière, D., Macintosh, B., & Doyon, R. 2006b, ApJ, 647, 612
Marois, C., Macintosh, B., Barman, T., et al. 2008, Science, 322, 1348
Marois, C., Macintosh, B., & Véran, J.-P. 2010a, Proc. SPIE, 7736, 77361
Marois, C., Zuckerman, B., Konopacky, Q., et al. 2010b, Nature, 468, 1080
Marois, C., Correia, C., Véran, J.-P., & Currie, T. 2014, IAU Symp., 299, 48
Macintosh, B., Graham, J., Ingraham, P., et al. 2014, PNAS, accepted [arXiv:1403.7520]
Meshkat, T., Bailey, V., Rameau, J., et al. 2013, ApJ, 775, L40
Mordasini, C., Alibert, Y., Georgy, C., et al. 2012, A&A, 547, A112
Pecaut, M.-J., Mamajek, E. E., & Bubar, E. J. 2012, ApJ, 746, 154
Perrin, M., & GPI Instrument and Science teams 2014, AAS Meeting Abstracts, 223, 348
Pickles 1998, PASP, 110, 863
Racine, R., Nadeau, D. & Doyon, R. 1999, ESO Conf. Proc., 56, 377
Rameau, J., Chauvin, G., Lagrange, A.-M., et al. 2013a, ApJ, 772, L15
Rameau, J., Chauvin, G., Lagrange, A.-M., et al. 2013b, ApJ, 779, L26
Rousset, G., Lacombe, F., Puget, P., et al. 2003, Proc. SPIE, 4839, 140
Soummer, R., Pueyo, L., & Larkin, J. 2012, ApJ, 755, L28
Spiegel, D., & Burrows, A. 2012, ApJ, 745, 174
Stephens, D., Leggett, S., Cushing, M., et al. 2009, ApJ, 702, 154
van Leeuwen, F. 2007, A&A, 474, 653
Zurlo, A., Vigan, A., Hagelberg, J., et al. 2013, A&A, 554., A21

Chapitre 4

Galicher et al., 2018, AA, 615, A92

Mesures et précisions astrométriques et photométriques en imagerie haute dynamique : l'outil *Sphere speckle calibration tool* (SpeCal) (paragraphe 3.1.3 du dossier de synthèse).

A&A 615, A92 (2018)
https://doi.org/10.1051/0004-6361/201832973

Astronomy & Astrophysics

Astrometric and photometric accuracies in high contrast imaging: The SPHERE speckle calibration tool (SpeCal)⋆

R. Galicher[1], A. Boccaletti[1], D. Mesa[2,3], P. Delorme[4], R. Gratton[2], M. Langlois[5,6], A.-M. Lagrange[4], A.-L. Maire[7], H. Le Coroller[5], G. Chauvin[4], B. Biller[8], F. Cantalloube[7], M. Janson[9], E. Lagadec[10], N. Meunier[4], A. Vigan[5], J. Hagelberg[4], M. Bonnefoy[4], A. Zurlo[11,12,13], S. Rocha[4], D. Maurel[4], M. Jaquet[5], T. Buey[1], and L. Weber[14]

[1] Lesia, Observatoire de Paris, PSL Research University, CNRS, Sorbonne Universités, Univ. Paris Diderot, UPMC Univ. Paris 06, Sorbonne Paris Cité, 5 place Jules Janssen, 92190 Meudon, France
e-mail: raphael.galicher@obspm.fr
[2] INAF – Osservatorio Astronomico di Padova, Vicolo della Osservatorio 5, 35122 Padova, Italy
[3] INCT, Universidad De Atacama, calle Copayapu 485, Copiapó, Atacama, Chile
[4] Université Grenoble Alpes, CNRS, IPAG, 38000 Grenoble, France
[5] Aix-Marseille Université, CNRS, LAM (Laboratoire d'Astrophysique de Marseille) UMR 7326, 13388 Marseille, France
[6] CRAL, UMR 5574, CNRS, Université de Lyon, Ecole Normale Supérieure de Lyon, 46 Allée d'Italie, 69364 Lyon Cedex 07, France
[7] Max-Planck-Institut für Astronomie, Königstuhl 17, 69117 Heidelberg, Germany
[8] Institute for Astronomy, University of Edinburgh, Blackford Hill, Edinburgh EH9 3HJ, UK
[9] Department of Astronomy, Stockholm University, 106 91 Stockholm, Sweden
[10] Université Côte d'Azur, OCA, CNRS, Lagrange, France
[11] Universidad de Chile, Camino el Observatorio 1515, Santiago, Chile
[12] Núcleo de Astronomía, Facultad de Ingeniería, Universidad Diego Portales, Av. Ejercito 441, Santiago, Chile
[13] Millenium Nucleus "Protoplanetary Disks in ALMA Early Science", Valparaiso, Chile
[14] Geneva Observatory, University of Geneva, Chemin des Mailettes 51, 1290 Versoix, Switzerland

Received 7 March 2018 / Accepted 21 April 2018

ABSTRACT

Context. The consortium of the Spectro-Polarimetric High-contrast Exoplanet REsearch installed at the Very Large Telescope (SPHERE/VLT) has been operating its guaranteed observation time (260 nights over five years) since February 2015. The main part of this time (200 nights) is dedicated to the detection and characterization of young and giant exoplanets on wide orbits.
Aims. The large amount of data must be uniformly processed so that accurate and homogeneous measurements of photometry and astrometry can be obtained for any source in the field.
Methods. To complement the European Southern Observatory pipeline, the SPHERE consortium developed a dedicated piece of software to process the data. First, the software corrects for instrumental artifacts. Then, it uses the speckle calibration tool (SpeCal) to minimize the stellar light halo that prevents us from detecting faint sources like exoplanets or circumstellar disks. SpeCal is meant to extract the astrometry and photometry of detected point-like sources (exoplanets, brown dwarfs, or background sources). SpeCal was intensively tested to ensure the consistency of all reduced images (cADI, Loci, TLoci, PCA, and others) for any SPHERE observing strategy (ADI, SDI, ASDI as well as the accuracy of the astrometry and photometry of detected point-like sources.
Results. SpeCal is robust, user friendly, and efficient at detecting and characterizing point-like sources in high contrast images. It is used to process all SPHERE data systematically, and its outputs have been used for most of the SPHERE consortium papers to date. SpeCal is also a useful framework to compare different algorithms using various sets of data (different observing modes and conditions). Finally, our tests show that the extracted astrometry and photometry are accurate and not biased.

Key words. instrumentation: high angular resolution – methods: observational – techniques: image processing – planets and satellites: detection

1. Introduction

The Spectro-Polarimetric High-contrast Exoplanet REsearch (SPHERE; Beuzit et al. 2008) is a facility-class instrument at the Very Large Telescope (VLT) dedicated to directly imaging and spectroscopically characterizing exoplanets and circumstellar disks. It combines a high-order adaptive-optics system with diverse coronagraphs. Three instruments are available: an infrared dual-band imager (IRDIS, Dohlen et al. 2008), an infrared integral field spectrometer (IFS, Claudi et al. 2008), and a visible imaging polarimeter (Zimpol, Thalmann et al. 2008).

Since first light in May 2014, SPHERE has been performing well in all observational modes, enabling numerous follow-up studies of known sub-stellar companions to stars and circumstellar disks as well as new discoveries (e.g., Boccaletti et al. 2015; de Boer et al. 2016; Ginski et al. 2016; Lagrange et al. 2016; Maire et al. 2016a, 2017; Mesa et al. 2016, 2017;

⋆ Based on observations collected at the European Organisation for Astronomical Research in the Southern Hemisphere under ESO programme 097.C-0865.

Perrot et al. 2016; Vigan et al. 2016; Zurlo et al. 2016; Chauvin et al. 2017; Bonnefoy et al. 2017; Feldt et al. 2017; Samland et al. 2017). The good performance to date results from the stability of the instrument over time and a dedicated and sophisticated software for data reduction.

The SPHERE reduction software uses the data reduction handling pipeline (DRH, Pavlov et al. 2008) that was delivered to ESO with the instrument as well as upgraded tools optimized using the first SPHERE data to derive accurate spectrophotometric and astrometric calibrations (Mesa et al. 2015; Maire et al. 2016b). The software that is implemented at the SPHERE data center (Delorme et al. 2017a) first assembles tens to thousands of images or spectra into calibrated datacubes, removing or correcting for instrumental artifacts. This includes image processing steps such as flat-fielding, bad pixels, background, frame selection, anamorphism correction, true north alignment, frame centring, and spectral transmission. The outputs of these first steps are temporal and spectral sequences of images organized in datacubes with four dimensions hereafter: coronagraphic images and the associated point-spread functions (PSF). Then, the software uses the speckle calibration tool (SpeCal) written in the IDL language and described in this paper. SpeCal was developed in the context of the SpHere INfrared survey of Exoplanets (SHINE), which is the main part of the SPHERE guaranteed observation time (GTO) and is now used to process all SPHERE data obtained with IRDIS and IFS systematically. SpeCal uses data processing algorithms proposed in the literature. Data from the Zurich imaging polarimeter (ZIMPOL) will be implemented in the future.

In Sect. 2, we describe the algorithms that SpeCal uses to optimize the exoplanet detection, while in Sect. 3 we explain how SpeCal algorithms estimate the astrometry and photometry of point-like sources like exoplanets or brown dwarfs. To address the accuracies of the data reduction in terms of astrometry and photometry we use SpeCal to reduce two sequences recorded with IRDIS (Sect. 4) and IFS (Sect. 5) during the SPHERE guaranteed time observations.

2. Calibration of the speckle pattern

2.1. Differential imaging strategies

Current high contrast imaging instruments dedicated to exoplanet detection combine an adaptive optics system to compensate for the atmospheric turbulence and coronagraphs to attenuate the flux of the central bright source (i.e. the star). Because the adaptive optics system is not perfect and because of aberrations in the optics of the telescope and instrument, part of the stellar light reaches the science detector, creating spatial interference patterns called speckles. The speckles mimic images of off-axis point-like sources, especially in narrow band filters. Other factors let stellar light go through the coronagraph preventing the detection of faint sources in the raw data: chromatism of the coronagraph, atmospheric dispersion, diffraction effects from the secondary mirror and from spiders, low wind effect, and so on. Hereafter, for convenience, the stellar speckle pattern will refer to any type of stellar light that reaches the detector even if it is not in the form of speckles.

Strategies that are routinely used to discriminate exoplanet images from the stellar speckle pattern include angular differential imaging (ADI, Marois et al. 2006), dual-band imaging, and spectral differential imaging (SDI, Rosenthal et al. 1996; Racine et al. 1999; Marois et al. 2004; Thatte et al. 2007), reference differential imaging (RDI, Beuzit et al. 1997), and polarization differential imaging (PDI, Baba & Murakami 2003; Baba et al. 2005). Each strategy relies on specific assumptions about the speckle pattern, and the efficiency of extracting the planet signal from the speckle pattern is directly related to the strengths and limitations of these assumptions. When using ADI, we assume most of the optical aberrations come from planes that are optically conjugated to the pupil plane and remain static in the course of the observation. Keeping the pupil orientation fixed (pupil tracking mode), we record a sequence of images that show a stable speckle pattern while the field of view, including an off-axis exoplanet image, rotates around the central star. Using dual-band imaging, we assume the spectrum of the star (and so, the speckles) is different from the exoplanet spectrum. Using SDI, we assume the speckles are induced by an achromatic optical path difference in a pupil plane so that we can predict the evolution of the phase aberrations that induce the speckles with wavelength. Using RDI, we observe several similar stars with a similar instrumental set-up assuming the speckle pattern is stable in time. Finally, the PDI technique assumes that, unlike the star light, the light coming from the planet is polarized. For each strategy, several algorithms exist to process the data.

The SPHERE instrument can record coronagraphic images simultaneously in two spectral filters using the IRDIS subsystem for dual-band imaging (Vigan et al. 2010) or in 39 narrow spectral channels using the IFS for SDI (Zurlo et al. 2014; Mesa et al. 2015). During the observations, ADI, dual-band imaging, and SDI can be used so that the SPHERE instrument records four-dimensional datacubes, called $I(x, y, \theta, \lambda)$: two spatial dimensions (x, y, sky coordinates), one angular dimension (θ, orientation with respect to the north direction, which evolves with time in pupil tracking mode), and one spectral dimension (λ, wavelength). In the rest of the paper, we use "spectral channel" to refer to the spectral dimension, and "angular channel" to refer to the angular dimension. Also, we use SDI for both SDI and dual-band imaging.

The SpeCal tool was developed so that all the SHINE SPHERE GTO data can be uniformly processed. We remind readers that this tool uses data processing techniques that were previously proposed in the literature. The interest of the tool is that all these techniques have been tested on several datasets to ensure that all the products are consistent (contrast curves, measurements of astrometry, and photometry of detected point-like sources). SpeCal can process data recorded using ADI, SDI, RDI, or the combination of ADI and SDI that is called ASDI hereafter (see Table 1). When SDI or ASDI is chosen, the frames $I(x, y, \theta, \lambda)$ are spatially scaled with wavelength to compensate for the spectral dispersion of the speckle position and size, the reference wavelength being the shortest one. The resulting frames are called $I_s(x, y, \theta, \lambda)$. The scaling changes the spatial sampling. An inverse scaling is performed at the end of the data processing. The ASDI option usually minimizes the speckle pattern more efficiently but it can strongly bias the photometry of the objects that are detected, as demonstrated in Maire et al. (2014) and Rameau et al. (2015).

Numerous algorithms were proposed to minimize the speckle pattern in coronagraphic images so that point-like sources (e.g., exoplanets) or extended sources (e.g., circumstellar disks) can be detected. SpeCal offers several algorithms depending on the observing strategy: classical ADI (cADI, Marois et al. 2006), classical reference differential imaging (cRDI), subtraction of a radial profile (radPro), locally optimized combination of images (Loci, Lafrenière et al. 2007), LociRDI, template-Loci

Table 1. Acronyms of the strategies of observation.

ADI	Angular differential imaging
SDI	Spectral differential imaging
PDI	Polarization differential imaging
RDI	Reference differential imaging
ASDI	Simultaneous ADI and SDI

(TLoci, Marois et al. 2014), principal component analysis (PCA, Soummer et al. 2012; Amara & Quanz 2012), and classical averaging with no subtraction (ClasImg). The objective of each algorithm, except ClasImg, is the determination of one speckle pattern $A(x, y, \theta, \lambda)$ that is then subtracted from $I(x, y, \theta, \lambda)$ to obtain a datacube $R(x, y, \theta, \lambda)$ where the stellar intensity is reduced:

$$R(x, y, \theta, \lambda) = I(x, y, \theta, \lambda) - A(x, y, \theta, \lambda). \quad (1)$$

The pattern A can be a function of the spectral dimension, of the angular dimension, and of the sky coordinates.

In the ADI cases, once the A pattern is subtracted, all frames of R are rotated to align their north axis. In the SDI case, the R frames are spatially scaled to recover the initial sampling. In the ASDI case, the R frames are both spatially scaled and rotated. Then, the frames are mean-combined to sum up the off-axis source signal. The result is a datacube $I_{\rm final}(x, y, \lambda)$. SpeCal also uses a median combination of the R frames. Hence, there are two final images for each spectral channel.

The following sections describe how SpeCal calculates the A pattern for each algorithm, the acronyms for which are given in Table 2.

2.2. Classical averaging

SpeCal can provide the average and median combinations of the rotated R frames using $A = 0$. This algorithm (ClasIm) can be useful to optimize the signal-to-noise (S/N) ratio of detections in parts of the image that are dominated by background instead of speckles.

2.3. cADI

In classical ADI, SpeCal averages the cube of frames over the angular dimension for each spectral channel (λ):

$$A_{\rm a}(x, y, \lambda) = \langle (I(x, y, \theta, \lambda) \rangle_\theta. \quad (2)$$

Equation (1) is applied and the R frames are rotated and then averaged to produce one final image $I_{\rm final,a}$ per spectral channel.

SpeCal can also remove the median of the frames instead of the average:

$$A_{\rm m}(x, y, \lambda) = ({\rm median}(I(x, y, \theta, \lambda))_\theta. \quad (3)$$

Then, it uses $A_{\rm m}$ in Eq. (1), rotates the R frames, and then applies a median combination. The final image $I_{\rm final,m}$ is less sensitive than $I_{\rm final,a}$ to uncorrected hot or bad pixels. It is however harder to accurately retrieve the photometry of a detected off-axis source from $I_{\rm final,m}$ than from $I_{\rm final,a}$ (Sect. 3).

2.4. cRDI

The reference differential imaging (RDI) is especially useful to obtain images of extended sources like circumstellar disks or to probe small angular separations to the star because it is not subject to self-subtraction unlike the other algorithms. The classical RDI (cRDI) is similar to cADI but it uses N reference frames $I_{\rm R}(x, y, n, \lambda)$ to derive the speckle pattern A, where $n = 1 \ldots N$. These reference frames are images of stars other than the one of interest ($I_{\rm R} \neq I$). The resulting A pattern is

$$A(x, y, \lambda) = ({\rm median}(I_{\rm R}(x, y, n, \lambda))_n. \quad (4)$$

Table 2. Acronyms and names of algorithms used to process the data recorded using a given strategy of observation (third column).

Acronym	Name	Strat.	Section
ClasImg	Median/average combination	All	2.2
cADI	Classical ADI	ADI	2.3
cRDI	Classical RDI	RDI	2.4
radPro	Subtraction of radial profile	ADI	2.5
Loci	Locally optimized combination of images	All	2.6
Tloci	Template-Loci	All	2.7
LociRDI	Loci using only RDI	RDI	2.8
PCA	Principal component analysis	All	2.9

Notes. If the third column shows "all", it means the algorithm can be used on ADI, or SDI, or ASDI data.

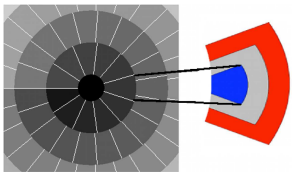

Fig. 1. Loci and TLoci regions of interest (*left figure* and central blue region in the *right figure*) and TLoci optimizing region (exterior red region in the *right figure*).

2.5. Subtraction of a radial profile

For detecting and studying extended sources, SpeCal proposes the radPro algorithm that first works out the average of the datacube over the angular dimension (Eq. (2)). Then, it calculates the azimuthally averaged profile in rings of one pixel width. Finally, the A pattern is the centro-symmetrical image that is derived from this profile.

2.6. Loci

The SpeCal Loci algorithm is described in Lafrenière et al. (2007). For a given θ, a given λ, and a given region in the field (blue in Fig. 1), the algorithm calculates the linear combination of the other frames $I_{\rm s}(x, y, \theta', \lambda')$ ($\theta' \neq \theta$ and $\lambda' \neq \lambda$ in ASDI) to build $A(x, y, \theta, \lambda)$ that minimizes $|R|$ (Eq. (1)) in the region of interest. In addition to the algorithm of Lafrenière et al. (2007), we impose the coefficients of the linear combination to be positive. Conversely to Lafrenière et al. (2007), the region of interest where A is applied and the region of optimization from which A is derived are the same in SpeCal. They are defined using:

– the radial width of the region (dr in Lafrenière et al. 2007);
– the number of PSFs inside the region (N_A in Lafrenière et al. 2007).

We use different parameters to Lafrenière et al. (2007) to select the frames that are used in the linear combination. Consider the frame $I_s(x, y, \theta, \lambda)$ (ASDI case, Sect. 2.1). First, we assume the image I_p of a putative off-axis source in I_s is the two-dimensional Gaussian function with the full width half-maximum (FWHM) estimated from the recorded PSF (see Sect. 2.10.1). If the source is in the region centered on (x_0, y_0) in $I_s(x, y, \theta, \lambda)$, it is angularly shifted by $s_\theta = r_0(\theta_i - \theta)$ and radially shifted by $s_r = r_0(1 - \lambda/\lambda_j)$ in $I_s(x, y, \theta_i, \lambda_j)$, where $r_0 = \sqrt{x_0^2 + y_0^2}$ is the angular separation from the star in FWHM unit. If only $I_s(x, y, \theta_i, \lambda_j)$ was used to build A, the normalized intensity of the off-axis source integrated within a disk of one-*FWHM* diameter in the frame R would be

$$\tau' = \frac{\iint_{r<FWHM/2} \left[I_s(x', y', \theta, \lambda) - I_s(x', y', \theta_i, \lambda_j)\right] \mathrm{d}x'\,\mathrm{d}y'}{\iint_{r<FWHM/2} I_p(x', y', \theta, \lambda)\,\mathrm{d}x'\,\mathrm{d}y'} \tag{5}$$

using $x' = x - x_0$, $y' = y - y_0$ and $r = \sqrt{x'^2 + y'^2}$. Then,

$$\tau' = 1 - \frac{\iint_{r<FWHM/2} \left[I_s(x', y', \theta_i, \lambda_j)\right] \mathrm{d}x'\,\mathrm{d}y'}{\iint_{r<FWHM/2} I_p(x', y', \theta, \lambda)\,\mathrm{d}x'\,\mathrm{d}y'}. \tag{6}$$

Using the radial and angular shifts s_r and s_θ of $I_s(x, y, \theta_i, \lambda_j)$, we find

$$\tau' = 1 - \frac{E(s_\theta)\,E(s_r)}{4\,\mathrm{erf}^2(\alpha/2)}, \tag{7}$$

where α equals $2\sqrt{\ln 2}$, and erf is the error function, and

$$E(s) = \mathrm{erf}\left(\alpha\left(s + \frac{1}{2}\right)\right) - \mathrm{erf}\left(\alpha\left(s - \frac{1}{2}\right)\right). \tag{8}$$

Here, we assume the angular motion is linear, which is a good assumption because $E(s)$ quickly decreases. The function τ' goes from 0 ($\theta = \theta_i$ and $\lambda = \lambda_j$, total self-subtraction) to 1 (no self-subtraction). In SpeCal, we set a parameter τ that can be linked to the minimum motion $\delta_{\min}$ of the putative off-axis source in Lafrenière et al. (2007). If τ' is smaller than τ, the frame $I_s(x, y, \theta_i, \lambda_j)$ is rejected. Doing so for each θ_i and λ_j, we obtain a series of frames $\{I_s\}$ that individually leave at least τ times the initial flux of the putative source in the $R(x, y, \theta, \lambda)$. Then, we select from $\{I_s\}$ the N most correlated frames (N is adjustable) to $I_s(x, y, \theta, \lambda)$ in the considered region. We obtain the linear combination of the N frames (i.e., the A pattern) that minimizes the residual energy in this region using the bounded-variables least-squares algorithm by Lawson & Hanson (1995). Finally, as the coefficients of the linear combination are positive, the flux of the putative source in the final image I_{final} is at least τ times the initial flux for any region.

The Loci algorithm can be used to reduce ADI, SDI, or ASDI data. In the ADI case, the Loci A pattern that is worked out for a given frame $I(x, y, \theta, \lambda)$ uses the other frames taken in the same spectral channel only. In the SDI case, it uses the frames taken with the same angle θ only. Finally, in the ASDI case, all frames are spatially scaled with wavelength, and they are all used to determine the A pattern.

2.7. TLoci

The SpeCal TLoci algorithm is derived from the one described in Galicher & Marois (2011) and Marois et al. (2014) assuming a flat planet spectrum in contrast. The parameters that are used to select the frames (τ and N) and to describe the regions of interest (dr and N_A) where the A pattern is applied (blue region in Fig. 1) are the same as for the Loci case (Sect. 2.6). The difference from Loci is the region where A is optimized (red region). In SpeCal, the gap between this region and the region of interest is set to 0.5 *FWHM*. Hence, the optimizing region is close enough to the region of interest so that A is efficiently optimized, and the optimizing region is far enough from the region of interest so that the flux of a source in the latter does not bias the linear combination. Moreover, the internal radii of the two regions are the same in SpeCal. Finally, an additional parameter sets the radial width of the optimizing region. As for Loci, TLoci can be associated to ADI, SDI, and ASDI.

2.8. LociRDI

A reference differential imaging algorithm using Loci is also implemented in SpeCal. It works as described in Sect. 2.6 but the frames that are used to build A are reference frames as in the cRDI case (Sect. 2.4).

2.9. PCA

For historical reasons, two PCA algorithms are implemented in SpeCal. The first version can be applied on IRDIS or IFS data using the ADI or ASDI options. This algorithm follows the equation of Soummer et al. (2012). For each frame $I(x, y, \theta, \lambda)$, we subtract its average over the field of view:

$$I_z(x, y, \theta, \lambda) = I(x, y, \theta, \lambda) - \langle I(x, y, \theta, \lambda)\rangle_{x,y}. \tag{9}$$

In the ADI case, the principal components are calculated for each spectral channel independently. Each frame $I_z(x, y, \theta, \lambda)$ is then projected onto the N first components to obtain the A pattern that is used in Eq. (1), replacing I with I_z. The N parameter is called "number of modes" hereafter. Finally, the averages that were removed (Eq. (9)) are added back to obtain the R frames of Eq. (1). In the ASDI case, the algorithm is the same but it works on I_s instead of I. We note that here there is no frame selection to minimize the self-subtraction of point-like sources when deriving the principal components.

The second version of PCA that is implemented in SpeCal is very similar to the first one but it can be applied on IFS data using the ASDI option only (Mesa et al. 2015). The two PCA versions were tested on a large amount of SPHERE data and they provide a very similar performance.

2.10. Common outputs

2.10.1. Model of unsaturated PSF

SpeCal produces common outputs whatever the chosen algorithm. First, it records the final images I_{final} normalized to the estimated maximum of an unsaturated non-coronagraphic stellar image with the same exposure time. Hence, the values of the pixels in I_{final} give the contrast ratio to the star maximum. For each spectral channel, the maximum β of the stellar non-coronagraphic image is derived from the best fit of the input

PSFs by the function

$$\mathrm{PSF}_{\mathrm{model}} = \alpha + \beta \exp\left(-\left(\frac{2\sqrt{(x-x_{\mathrm{PSF}})^2+(y-y_{\mathrm{PSF}})^2}}{\gamma}\right)^{\eta}\right), \quad (10)$$

where α is the background level, β is the star maximum, γ and η are related to the spatial extension of the PSF (and to FWHM), and $(x_{\mathrm{PSF}}, y_{\mathrm{PSF}})$ give the center of the PSF. All these parameters are fitted accounting for the photon noise in the provided PSF images. The SPHERE PSFs are usually close to two-dimensional Gaussian functions ($\eta = 2$) but can deviate from them. In the context of SHINE, PSFs are usually recorded before and after the coronagraphic sequence. SpeCal calculates the best fit to each of the PSFs ($\sim 50 \times 50$ pixels) and runs two tests on the time series of fitted parameters. First, it works out the average and standard deviation of the normalization factor β over time, records the two values, and sends a warning if the flux of the star β varies by more than 20% between distinct PSF observations of the target. Then, it sends a warning if the background level α is larger than 10% of β. These values (10% and 20%) were defined as quality requirements based on our experience with the instrument and the analysis of hundreds of datasets. Finally, SpeCal estimates and records the PSF FWHM.

2.10.2. Calibration of photometry

For algorithms that bias the photometry of off-axis sources, SpeCal estimates the throughput of the technique at each position in the field. For cADI, radPro, and PCA, SpeCal creates a datacube of fake planets that are on a linear spiral centered on the star (one planet per 2 *FWHM*). For each planet, we use the recorded PSF and its flux equals ten times the local residual flux in I_{final}. The fake planet datacube is added to the datacube $I(x, y, \theta, \lambda)$. Then, SpeCal combines the frames as the $I(x, y, \theta, \lambda)$ were combined to get I_{final}. For each planet, the ratio of the flux in the resulting image to the flux of the fake planet is calculated to obtain the 1D-throughput as a function of the angular separation. For Loci and TLoci, the throughput τ_R is estimated in each frame R as the average of all τ' of Eq. (7), weighting $E(s_\theta)$ and $E(s_r)$ by the coefficients used to obtain I_{final}. We average all τ_R to obtain the 1D-throughput as a function of the angular separation. Finally, the throughput map T is the centro-symmetrical image created from the 1D-throughput. SpeCal also calculates the throughput-corrected final image I_{final}/T.

2.10.3. S/N and detection maps

For each spectral channel, the image I_{final}/T is divided into annulii of 0.5 *FWHM* width. Then, in each annulus (i.e., at each angular separation), we calculate the standard deviation that is set to be the 1 σ contrast. S/N maps are also created. Each pixel gives the ratio of the flux in I_{final}/T to the standard deviation of I_{final}/T calculated in annulii of 1 *FWHM* centered on the star. This correction is valid only for point-like sources. For example, this correction is not valid for an extended source like a disk. Finally, SpeCal also provides local detection maps giving the local standard deviation in boxes of 2 *FWHM* radial size and of a total area of 5 $FWHM^2$.

3. Astrometry and photometry of point-like sources

All algorithms, except RDI and ClasImg, distort the image of an off-axis point-like source in I_{final} (Sect. 3.1). Thus, the estimation of the position and flux of such a source cannot be done directly from I_{final} (Marois et al. 2010; Lagrange et al. 2010; Galicher & Marois 2011; Maire et al. 2014; Rameau et al. 2015). However, SpeCal can fit a model of an off-axis source image to the detected source in I_{final} (Sect. 3.2), or it can inject a negative point-like source into the initial datacube I and adjust the position and flux of this negative source to locally minimize the flux in I_{final} (Sect. 3.3).

3.1. Planet image

Say there is a planet whose intensity is described by $I_{\mathrm{p}}(x, y, \theta, \lambda)$ whereas the stellar intensity is $I_*(x, y, \theta, \lambda)$. The A pattern is derived from the cube

$$I(x, y, \theta, \lambda) = I_*(x, y, \theta, \lambda) + I_{\mathrm{p}}(x, y, \theta, \lambda) \quad (11)$$

and part of the A pattern is composed of planet signal. For example, when using cADI, Loci, TLoci, or radPro on ADI, SDI, or ASDI data, the A pattern can be expressed as

$$A(x, y, \theta, \lambda) = \sum_i \sum_j c_{i,j}\, I(x, y, \theta_i, \lambda_j), \quad (12)$$

$$A(x, y, \theta, \lambda) = \sum_i \sum_j \left[c_{i,j}\, I_*(x, y, \theta_i, \lambda_j) + c_{i,j}\, I_{\mathrm{p}}(x, y, \theta_i, \lambda_j)\right], \quad (13)$$

$$A(x, y, \theta, \lambda) = A_*(x, y, \theta, \lambda) + A_{\mathrm{p}}(x, y, \theta, \lambda), \quad (14)$$

where coefficients $c_{i,j}$ are real numbers that can be a function of (x, y), and

$$\begin{cases} A_*(x, y, \theta, \lambda) = \sum_i \sum_j c_{i,j}\, I_*(x, y, \theta_i, \lambda_j) \\ A_{\mathrm{p}}(x, y, \theta, \lambda) = \sum_i \sum_j c_{i,j}\, I_{\mathrm{p}}(x, y, \theta_i, \lambda_j). \end{cases} \quad (15)$$

Hence, the A pattern is contaminated by planet signal and, when subtracting the A pattern from the initial frames I, part of the planet signal self-subtracts. The R frames is then

$$R = (I_* - A_*) + (I_{\mathrm{p}} - A_{\mathrm{p}}), \quad (16)$$

where all terms depend on x, y, θ, and λ. A perfect algorithm – that does not exist – would be such that $A_* = I_*$ and $A_{\mathrm{p}} = 0$.

As the planet image moves in the field from one frame to another (radially for SDI or azimuthally for ADI), the subtracted signal is shifted with respect to the astrophysical position of the planet. This results in a positive-negative pattern of the planet in each frame of R and as a consequence in the final image I_{final} (left in Fig. 2). This pattern is not always centered on the planet position. The distortions of the planet image can be minimized by carefully selecting the frames that are used to build A (so that $A_{\mathrm{p}} \to 0$) but it usually reduces the efficiency of the speckle attenuation at the same time (increasing $|I_* - A_*|$). In the case of PCA algorithms, $I(x, y, \theta_i, \lambda_i)$ in Eq. (12) is replaced by the principal components, which are also contaminated by the planet signal.

3.2. Model of planet images

The first way of extracting the astrometry and the photometry of an off-axis point-like source like a planet in an ADI, SDI, or ASDI reduced image consists of building a model of the planet image (Galicher & Marois 2011). First, we estimate the position of the detected source in I_{final} with a pixel accuracy. Then, we use the measured stellar PSF to build a sequence of

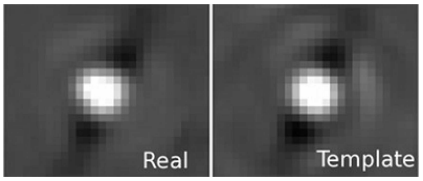

Fig. 2. Real (*left*) and estimated (*right*) images of an off-axis source in an ADI reduced image showing the negative wings due to self-subtraction of the planet flux.

frames $I_{\rm fp}(x, y, \theta, \lambda)$ with only one fake planet image at the rough position accounting for the field-of-view rotation. We do not account for the smearing that affects images. This effect may be non-negligible at the edges of the IRDIS images if the field-of-view rotation is fast and the exposures are long, which is rare. We combine the frames $I_{\rm fp}$ in the same way the frames I were combined using the same $c_{i,j}$ and we get an estimation of $A_{\rm p}$ (Eq. (15)). Rotating (ADI case), spatially scaling (SDI case), and averaging the frames result in a model of the planet image (right in Fig. 2). The planet image has negative wings due to the self-subtraction of the planet flux (Sect. 3.1).

Then, the flux and the position of this synthetic image are adjusted to best fit the real planet image within a disk of diameter 3 *FWHM* so that it includes the positive and the negative parts of the image. The optimization is done using $I_{\rm final}$, which is derived from the average of the R frames after rotation and spatial scaling (and not the one obtained using the median-combination that does not preserve linearity). Rigorously, we should calculate the synthetic image each time we test a new planet position. To optimize computation time, we shift the synthetic planet image that was obtained with the rough position. We noticed no significant difference as long as the shifts are smaller than ∼1 *FWHM*.

Once the optimization is done, we look for the excursion of each parameter that increases the minimum residual level by a factor of 1.15. We set these excursions to be the $1\,\sigma$ accuracies due to the fitting errors in the SpeCal outputs. The value of 1.15 is empirical but it was tested on numerous cases (high or low S/N detection, strong or weak negative wings, Loci, TLoci, PCA, and others). Another SpeCal output is the standard deviation in time of the averaged flux in the coronagraphic images. To avoid saturated parts of the images and background dominated parts, the averaged flux is calculated inside an annulus centered on the star and going from 30 pixels to 50 pixels in radius.

SpeCal can use this technique to extract astrometry and spectro-photometry in images obtained with any algorithm (cADI/radPro/Loci/TLoci/PCA/averaging) and any of ADI, SDI, or ASDI. It can also be used on cRDI, LociRDI, and ClasImg final images. In these cases, the planet image model is the stellar PSF shifted at the position of the detection with no negative wings as the $A_{\rm p}$ pattern is null (classical fit of a non-coronagraphic image).

3.3. Negative planets

Another technique – the fake negative planet – (Lagrange et al. 2010; Chauvin et al. 2012) is implemented in SpeCal to retrieve the photometry and astrometry of point-like sources. First, we build the sequence of frames $I_{\rm fp}$ with the fake planet only, as done in Sect. 3.2. Then, we subtract this datacube from the initial data I. We apply the algorithm and get the final image from the $I - I_{\rm fp}$ frames. In this final image, we measure the standard deviation of the residual intensity inside a disk of 3 *FWHM* diameter centered on the rough position of the detected planet. Modifying the fake planet position and flux, we minimize the residual intensity. The uncertainties on the best values are estimated as the ones in Sect. 3.2. The negative planet technique is more time-consuming than the model of planet image technique because it calculates the $c_{i,j}$ for all the tested fake planet positions and fluxes. It is, however, needed in some cases for which the model of planet image technique is biased (Sect. 4.2).

Table 3. Separations to the central star in pixels towards east (ΔRA) and north (ΔDec), angular separations in mas and flux ratio with respect to the star (C) for each fake planet added to the IRDIS data.

Id	ΔRA (pixel)	ΔDec (pixel)	Sepa (mas)	Band	$C \times$ 1e6
1	52.90	2.70	649.4	$H2$	3.000
				$H3$	2.400
2	−25.80	8.40	318.0	$H2$	6.000
				$H3$	3.000
3	−72.00	−71.20	1250.1	$H2$	1.000
				$H3$	3.000

4. Reduction of IRDIS data

In Sects. 4 and 5, we use SpeCal to reduce two datasets as examples. In Sect. 4, we consider one sequence recorded during the SPHERE GTO on 2016 September 16 observing HIP2578 in IRDIS $H2/H3$ mode. There are 80 images of 64 s exposure time and the field of view rotates by 31.5°. The seeing was about 0.5 arcsec and the average wind speed was 7.4 m s^{-1}.

All algorithms are applied on the same datacube provided by the first part of the SPHERE pipeline (background, flat-fielding, bad pixels, registration, wavelength calibration, astrometric calibration; Pavlov et al. 2008; Zurlo et al. 2014; Maire et al. 2016b). The datacube is a $1024 \times 1024 \times 80 \times 2$ array. The last dimension stands for the two spectral channels ($H2$ and $H3$). We also added three fake planets to the data (see Table 3) using the recorded stellar PSFs. We chose the position and the flux to have three typical cases. Planets 1 and 2 are in the speckle dominated part of the image, planet 2 being surrounded by brighter speckles. Planet 3 is in a region dominated by the background and not by speckles.

4.1. Calibration of the speckle pattern

We apply several algorithms to the two spectral channels independently (no use of SDI) and we show the average of the two final images in Fig. 3 for cADI, TLoci, Loci, and two PCA (5 and 10 modes). Images are corrected from the technique throughput T (self-subtraction of a putative planet, Sect. 2.10.2) and from the coronagraph transmission. All images provide similar sensitivities except for cADI, which is less efficient inside the AO correction area that is dominated by speckles. The three fake planets are well detected in all images. The corresponding 5σ contrast curves are plotted in Figs. 4 ($H2$) and 5 ($H3$), where the three planets are represented by plus symbols. The curves are corrected for the throughput T of each technique and from the coronagraph transmission (Guerri et al. 2011). The latter is a

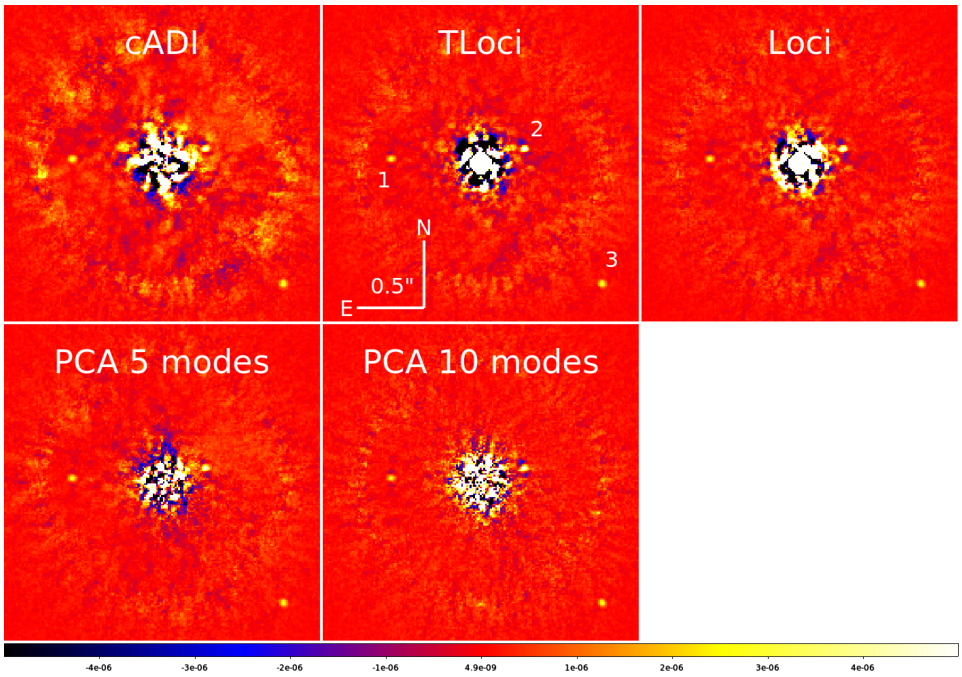

Fig. 3. IRDIS example: final images using cADI, Tloci, Loci, PCA (5 and 10 modes). Images are corrected from the technique throughput and from the coronagraph transmission. The color scale, which is the same for all images, shows the contrast to the star ratio. The spatial scale is the same for all images.

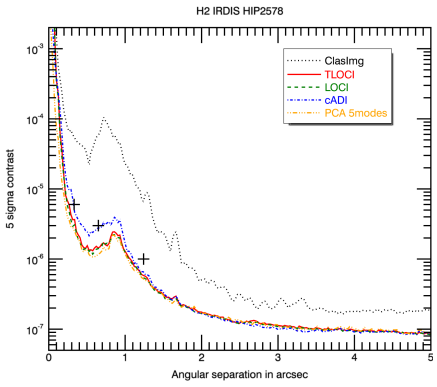

Fig. 4. Contrast curves at 5 σ before (ClasImg) and after minimization of the stellar light using different algorithms (cADI, Tloci, Loci, PCA 5 modes) on $H2$ data. The curves are corrected from the technique attenuation and from the coronagraph transmission. The fake planets are represented by plus symbols.

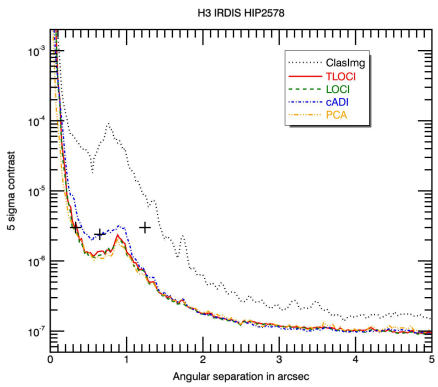

Fig. 5. Same as Fig. 4 for $H3$-band.

function of angular separation and it was calibrated at the telescope and via numerical simulations. We also overplot the contrast before any a posteriori speckle minimization with a dotted line (ClasImg). The utility of a speckle calibration during the data processing is obvious since none of the planets are detected in the images with no subtraction (ClasImg). In this example, all the algorithms except cADI give similar performances in terms of contrast level. For some sequences, one algorithm reaches better contrast levels but there is no algorithm in SpeCal that is always better than the others.

The small sample statistic bias (Mawet et al. 2014) that mainly affects separations at less than 0.2″ will be implemented in the next version of the tool. This correction will affect all the algorithm reductions the same way.

Table 4. Measured astrometry and photometry in IRDIS images for each planet (same Id as in Table 3) using the model of planet image technique (Sect. 3.2).

Algorithm	Id	Band	ΔRA (pixel)	E	ΔDec (pixel)	E	$C \times$ 1e6	E
cADI	1	$H2$	52.70 ± 0.21	0.95	2.54 ± 0.20	0.80	2.775 ± 0.206	1.09
		$H3$	53.02 ± 0.22	0.55	2.48 ± 0.22	1.00	2.272 ± 0.163	0.79
	2	$H2$	−25.94 ± 0.42	0.33	8.60 ± 0.37	0.54	5.163 ± 0.694	1.21
		$H3$	−25.75 ± 1.17	0.04	8.59 ± 1.03	0.18	2.723 ± 0.946	0.29
	3	$H2$	−71.98 ± 0.27	0.07	−71.09 ± 0.28	0.39	1.175 ± 0.098	1.79
		$H3$	−71.94 ± 0.15	0.40	−71.10 ± 0.15	0.67	2.938 ± 0.162	0.38
TLoci	1	$H2$	52.96 ± 0.17	0.35	2.59 ± 0.12	0.92	2.883 ± 0.175	0.67
		$H3$	53.10 ± 0.23	0.87	2.62 ± 0.16	0.50	2.201 ± 0.147	1.35
	2	$H2$	−25.82 ± 0.21	0.10	8.55 ± 0.15	1.00	5.602 ± 0.394	1.01
		$H3$	−25.91 ± 0.40	0.28	8.61 ± 0.29	0.72	2.643 ± 0.295	1.21
	3	$H2$	−71.90 ± 0.23	0.43	−71.00 ± 0.22	0.91	0.993 ± 0.082	0.09
		$H3$	−71.97 ± 0.13	0.23	−71.17 ± 0.13	0.23	3.016 ± 0.166	0.10
Loci	1	$H2$	53.01 ± 0.17	0.65	2.58 ± 0.12	1.00	2.847 ± 0.176	0.87
		$H3$	52.95 ± 0.20	0.25	2.59 ± 0.15	0.73	2.231 ± 0.145	1.17
	2	$H2$	−25.72 ± 0.20	0.40	8.54 ± 0.15	0.93	5.945 ± 0.392	0.14
		$H3$	−25.76 ± 0.36	0.11	8.63 ± 0.27	0.85	2.952 ± 0.294	0.16
	3	$H2$	−71.91 ± 0.22	0.41	−71.08 ± 0.21	0.57	0.995 ± 0.078	0.06
		$H3$	−71.95 ± 0.13	0.38	−71.15 ± 0.13	0.38	2.884 ± 0.157	0.74
PCA5modes	1	$H2$	52.90 ± 0.16	0.00	2.58 ± 0.12	1.00	2.748 ± 0.160	1.58
		$H3$	52.85 ± 0.17	0.29	2.56 ± 0.13	1.08	2.292 ± 0.135	0.80
	2	$H2$	−25.76 ± 0.21	0.19	8.47 ± 0.15	0.47	6.595 ± 0.430	1.38
		$H3$	−25.94 ± 0.45	0.31	8.56 ± 0.33	0.48	3.432 ± 0.361	1.20
	3	$H2$	−72.00 ± 0.24	0.00	−71.17 ± 0.24	0.12	0.908 ± 0.075	1.23
		$H3$	−71.92 ± 0.13	0.62	−71.15 ± 0.13	0.38	2.908 ± 0.157	0.59

Notes. Measurements are given with their 1 σ uncertainties. For each measurement, we compare it to the true value using the E criteria that is given in Eq. (17).

Table 5. Extracted astrometry and photometry for each planet (same Id than in Table 3) using the model of planet image technique (Sect. 3.2) and the negative planet technique (Sect. 3.3) on the final image provided by PCA 10 modes.

Extraction	Id	Band	ΔRA (pixel)	E	ΔDec (pixel)	E	$C \times$ 1e6	E
Model of planet image	1	$H2$	52.87 ± 0.21	0.14	2.51 ± 0.15	1.27	2.108 ± 0.148	6.03
		$H3$	52.92 ± 0.23	0.09	2.56 ± 0.16	0.88	1.650 ± 0.118	6.36
	2	$H2$	−25.77 ± 0.19	0.16	8.35 ± 0.14	0.36	4.634 ± 0.290	4.71
		$H3$	−26.00 ± 0.33	0.61	8.34 ± 0.21	0.29	2.182 ± 0.204	4.01
	3	$H2$	−72.07 ± 0.23	0.30	−71.03 ± 0.23	0.74	0.787 ± 0.070	3.04
		$H3$	−71.93 ± 0.15	0.47	−71.15 ± 0.15	0.33	2.365 ± 0.143	4.44
Negative planet	1	$H2$	52.90 ± 0.10	0.00	2.58 ± 0.07	1.71	2.781 ± 0.146	1.50
		$H3$	52.84 ± 0.12	0.50	2.56 ± 0.08	1.75	2.298 ± 0.126	0.81
	2	$H2$	−25.74 ± 0.10	0.60	8.47 ± 0.08	0.88	6.338 ± 0.321	1.05
		$H3$	−25.93 ± 0.18	0.72	8.56 ± 0.13	1.23	3.116 ± 0.190	0.61
	3	$H2$	−72.06 ± 0.28	0.21	−71.28 ± 0.19	0.42	0.915 ± 0.086	0.99
		$H3$	−71.91 ± 0.09	1.00	−71.13 ± 0.09	0.78	2.919 ± 0.162	0.50

Notes. For each measurement, we compare it to the true value using the E criteria that is given in Eq. (17).

4.2. Measurements of astrometry and photometry

We extract the astrometry and photometry for each detected point-like source using the technique of the model of planet image (Sect. 3.2). The estimated contrasts to the star are gathered in Table 4 with the associated 1 σ uncertainties. Each measurement C is compared to the true value C_R using

$$E = \frac{|C - C_R|}{Err}, \tag{17}$$

with Err the estimated 1 σ uncertainty on C.

All the astrometric measurements are at less than 1 σ from the true values (Table 3), which corresponds to an accuracy of ∼0.2 pixel (i.e., ∼2 mas); and all photometric measurements are

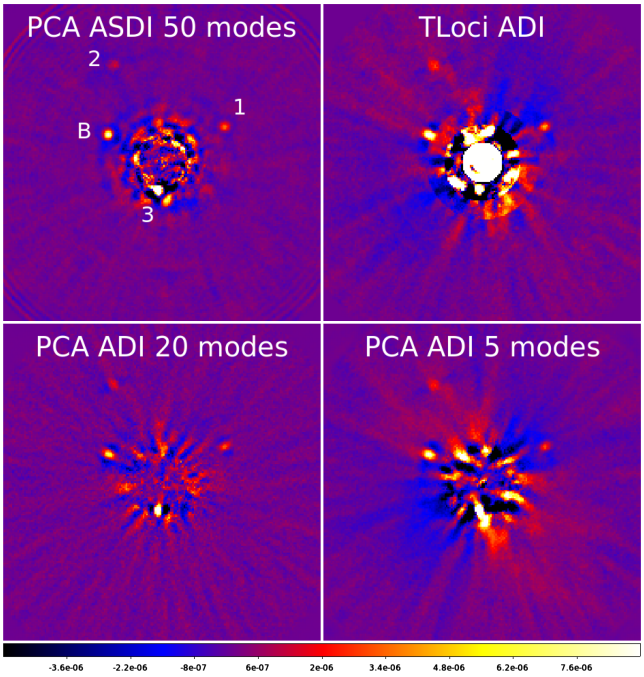

Fig. 6. IFS example: final images using PCA/ASDI (50 modes), PCA/ADI (20 and 5 modes), and TLoci. Images are corrected from the technique throughput and from the coronagraph transmission. The color scale. which is the same for all images, shows the contrast to the star ratio. The spatial scale is the same for all images.

Table 6. Fake planets injected in the IFS data: separation from the central star in pixels toward east (ΔRA) and toward north (ΔDec), angular separation in mas, and averaged contrast over the 39 spectral channels.

Id	ΔRA(pix)	ΔDec(pix)	Sepa(mas)	$C \times 1e6$
1	−36.70	21.20	316.2	4.3
2	29.00	57.30	479.1	4.5
3	2.40	−16.90	127.3	3.3

at less than $1.8\,\sigma$ from the true value C_R. In the case of PCA images, the model of planet image technique can be biased in the current version of SpeCal, especially when using more than approximately ten modes. We are still investigating to understand why. To overcome this bias, we use the negative planet technique (Sect. 3.3) that can be time-consuming but which provides more accurate measurements as showed in Table 5: the measurements are at less than $1.5\,\sigma$ from the true values whereas they were at $6\,\sigma$ using the planet image technique.

To conclude, SpeCal meets the requirements in terms of extracted astrophysical signals because the measured astrometry and photometry of point-like sources (e.g., exoplanets or brown dwarfs) are accurate and unbiased. This is essential to correctly interpret the observations (fit of the planet orbits or of their spectra). Moreover, SpeCal enables the use of several algorithms to provide a global dispersion of these measurements and a cross-check between measurements to prevent any systematic errors.

5. Reduction of IFS data

We now use SpeCal to reduce one sequence recorded during the SPHERE GTO on 2016 September 16 observing HD206893 in IFS YJH mode. There are 80 images of 64 s exposure time and the field of view rotates by 75.6°. The seeing was about 0.7 arcsec and the average wind speed was 8.4 ms^{-1}.

As for the IRDIS data, all algorithms are applied on the same datacube provided by the first part of the SPHERE pipeline (Pavlov et al. 2008; Mesa et al. 2015; Maire et al. 2016b). The datacube is a $290 \times 290 \times 80 \times 39$ array. The last dimension is the number of IFS spectral channels. We also added three fake planets to the data (see Table 6) using the recorded stellar PSFs. As for IRDIS, we chose the position and spectra to be representative of three common cases. The spectra of planets 1 and 2 show strong variations between $0.9\,\mu$m and $1.7\,\mu$m. Planet 1 is closer to the star and its image is located in a region with bright speckles. Planet 3 is located in a region with very bright speckles and its spectrum in contrast is flatter than the others.

5.1. Calibration of the speckle pattern

First, we apply ASDI PCA to detect point-like sources as it efficiently minimizes the speckle pattern (Fig. 6). We detect four point-like sources: the three fake planets (1–3) and one real object HD 206893 B that we do not study in this paper (see Delorme et al. 2017b; Milli et al. 2017). It is hard to accurately retrieve the planet photometry from ASDI images when the planet spectrum is unknown, as demonstrated in Maire et al. (2014) and Rameau et al. (2015). Therefore, we also apply several algorithms using ADI resulting in 39 final images $I_{\rm final}(x, y, \lambda)$ for each algorithm. The averages over the 39 channels are shown in Fig. 6 for PCA/ADI (5 and 20 modes) and TLoci/ADI. We clearly detect the four objects in all images.

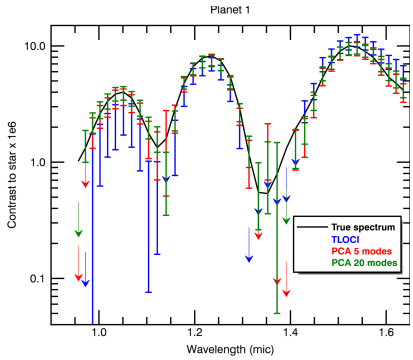

Fig. 7. Spectra of planet-to-star contrast extracted from the PCA/ADI 5 modes (red), PCA/ADI 20 modes (green), and TLoci/ADI (blue) images compared to the true spectrum that was used for fake planet 1 (black full line). Error bars and upper limits are given at 1 σ.

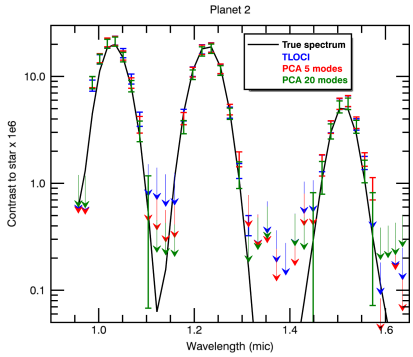

Fig. 8. Same as Fig. 7 for the fake planet 2.

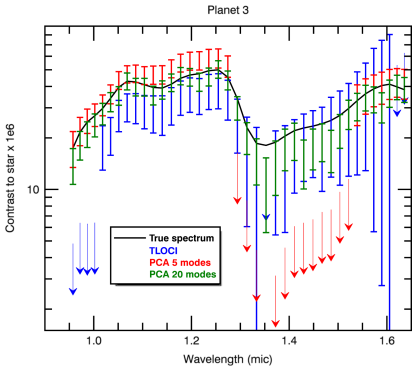

Fig. 9. Same as Fig. 7 for the fake planet 3.

5.2. Measurements of photometry

For TLoci and PCA/ADI 5 mode images, we use the model of planet image technique (Sect. 3.2) to extract the photometry and the astrometry of the three fake planets. For the PCA/ADI 20 mode image, we use the negative planet technique (Sect. 3.3) to avoid the photometry underestimation that was noticed in Sect. 4.2. When considering the spectral channels where the planet is detected, the astrometry measurements are accurate with 1 σ uncertainties of 0.6, 0.3, and 0.5 pixel for planets 1, 2, and 3 respectively. These values correspond to 4.5, 2.3, and 3.8 mas respectively.

We plot the extracted spectrophotometry in Figs. 7–9 for the TLoci/ADI (blue), the PCA/ADI 5 modes (red), and the PCA/ADI 20 modes (green) cases, as well as the true spectra that we used for the fake planets (full line). The arrows give the 1 σ upper limits when the planet is not detected, and the error bars correspond to the estimated 1 σ uncertainties.

All algorithms retrieve the spectra of the three fake planets with similar uncertainties and no bias. In the case of planet 3, which is in a region with bright speckles, there are spectral channels below 1 μm for which TLoci give an upper limit only (no detection). For the same planet, the PCA algorithm using 5-modes does not detect the object between 1.3 μm and 1.5 μm, whereas it does below 1 μm. Such a situation often happens: several algorithms detect the planet in different spectral channels. Thus, it is essential to use several algorithms in parallel to optimize the detection and the measured spectrum.

6. Conclusion

The Speckle Calibration tool (SpeCal) was developed by the SPHERE/VLT consortium in the context of a large survey (SHINE), the main objective of which is to search for and measure the astrometry and spectrophotometry of exoplanets at large separations (>5 au). SpeCal provides high contrast images using a variety of algorithms (cADI, PCA, Loci, TLoci) enabling the study of exoplanets, brown dwarfs, and circumstellar disks. SpeCal has been intensively tested on SPHERE guaranteed time observations (GTO) and calibration data since 2013. It is implemented in the SPHERE data center (Delorme et al. 2017a) to produce the final reduction for public data releases. The final reductions will be available in the SPHERE target database (TDB[1]). Finally, SpeCal and the DC are able to process all GTO data obtained with IRDIS/SPHERE (dual-band imaging) and IFS/SPHERE (integral field spectrometer) automatically.

SpeCal delivers major outputs for the survey and feeds the SPHERE database with final images, contrast curves, S/N maps, astrometry, and photometry of detected point-like sources in the field (exoplanets, brown dwarfs, background sources, and all sub-stellar or stellar candidates). This material has been used for the study of exoplanets and circumstellar disks primarily based on SPHERE data (de Boer et al. 2016; Ginski et al. 2016; Lagrange et al. 2016; Maire et al. 2016a, 2017; Mesa et al. 2016, 2017; Perrot et al. 2016; Vigan et al. 2016; Zurlo et al. 2016; Benisty et al. 2017; Bonavita et al. 2017; Bonnefoy et al. 2017; Feldt et al. 2017; Pohl et al. 2017; Samland et al. 2017).

In this paper, we investigated the astrometric and photometric performance for point-like sources considering objects at a contrast of $\sim 3 \times 10^{-6}$ in the separation range of 3–26 *FWHM*. Using the techniques of positive and negative fake planets, we demonstrated the ability to achieve a measurement of the astrometry with an accuracy of ~0.2 pixel (i.e., ~2 mas) for IRDIS and

[1] http://cesam.lam.fr/spheretools/

0.5 pixel (i.e., ∼4 mas) for IFS. Similarly the photometric accuracy reaches ∼10%.

We are planning to upgrade SpeCal with other algorithms like Andromeda (Cantalloube et al. 2015) or inverse approaches (Devaney & Thiébaut 2017), and other observing modes (polarimetry, ZIMPOL). Finally, a specific tool to model the ADI self-subtraction of circumstellar disks with simple geometries will also be implemented.

Acknowledgements. SPHERE is an instrument designed and built by a consortium consisting of IPAG (Grenoble, France), MPIA (Heidelberg, Germany), LAM (Marseille, France), LESIA (Paris, France), Laboratoire Lagrange (Nice, France), INAF – Osservatorio di Padova (Italy), Observatoire astronomique de l'Université de Genève (Switzerland), ETH Zurich (Switzerland), NOVA (Netherlands), ONERA (France), and ASTRON (Netherlands), in collaboration with ESO. SPHERE was funded by ESO, with additional contributions from the CNRS (France), MPIA (Germany), INAF (Italy), FINES (Switzerland), and NOVA (Netherlands). SPHERE also received funding from the European Commission Sixth and Seventh Framework Programs as part of the Optical Infrared Coordination Network for Astronomy (OPTICON) under grant number RII3-Ct-2004-001566 for FP6 (2004–2008), grant number 226604 for FP7 (2009–2012), and grant number 312430 for FP7 (2013–2016). This work has made use of the SPHERE data center, jointly operated by Osug/Ipag (Grenoble), Pytheas/Lam/Cesam (Marseille), OCA/Lagrange (Nice), and Observatoire de Paris/Lesia (Paris) and supported by a grant from Labex OSUG@2020 (Investissements d'avenir – ANR10 LABX56). We acknowledge financial support from the French ANR GIPSE, ANR-14-CE33-0018. Dino Mesa acknowledges support from the ESO-Government of Chile Joint Committee program "Direct imaging and characterization of exoplanets".

References

Amara, A., & Quanz, S. P. 2012, MNRAS, 427, 948
Baba, N., & Murakami, N. 2003, PASP, 115, 1363
Baba, N., Murakami, N., Tate, Y., Sato, Y., & Tamura, M. 2005, Proc. SPIE, 5905, 347
Benisty, M., Stolker, T., Pohl, A., et al. 2017, A&A, 597, A42
Beuzit, J.-L., Mouillet, D., Lagrange, A.-M., & Paufique, J. 1997, A&AS, 125, 175
Beuzit, J.-L., Feldt, M., Dohlen, K., et al. 2008, Proc. SPIE, 7014, 701418
Boccaletti, A., Thalmann, C., Lagrange, A.-M., et al. 2015, Nature, 526, 230
Bonavita, M., D'Orazi, V., Mesa, D., et al. 2017, A&A, 608, A106
Bonnefoy, M., Milli, J., Ménard, F., et al. 2017, A&A, 597, L7
Cantalloube, F., Mouillet, D., Mugnier, L. M., et al. 2015, A&A, 582, A89
Chauvin, G., Lagrange, A.-M., Beust, H., et al. 2012, A&A, 542, A41
Chauvin, G., Desidera, S., Lagrange, A.-M., et al. 2017, A&A, 605, L9
Claudi, R. U., Turatto, M., Gratton, R. G., et al. 2008, Proc. SPIE, 7014, 70143E
de Boer, J., Salter, G., Benisty, M., et al. 2016, A&A, 595, A114
Delorme, P., Meunier, N., Albert, D., et al. 2017a, SF2A Proc. of the Annual meeting of the French Society of Astronomy and Astrophysics, 347
Delorme, P., Schmidt, T., Bonnefoy, M., et al. 2017b, A&A, 608, A79
Devaney, N., & Thiébaut, É. 2017, MNRAS, 472, 3734
Dohlen, K., Langlois, M., Saisse, M., et al. 2008, Proc. SPIE, 7014, 70143L
Feldt, M., Olofsson, J., Boccaletti, A., et al. 2017, A&A, 601, A7
Galicher, R., & Marois, C. 2011, 2nd Int. Conf. on Adaptive Optics for Extremely Large Telescopes, P25 http://ao4elt2.lesia.obspm.fr
Ginski, C., Stolker, T., Pinilla, P., et al. 2016, A&A, 595, A112
Guerri, G., Daban, J.-B., Robbe-Dubois, S., et al. 2011, Exp. Astron., 30, 59
Lafrenière, D., Marois, C., Doyon, R., Nadeau, D., & Artigau, É. 2007, ApJ, 660, 770
Lagrange, A.-M., Bonnefoy, M., Chauvin, G., et al. 2010, Science, 329, 57
Lagrange, A.-M., Langlois, M., Gratton, R., et al. 2016, A&A, 586, L8
Lawson, C., & Hanson, R. 1995, Solving Least Squares Problems (Philadelphia: Society for Industrial and Applied Mathematics)
Maire, A.-L., Boccaletti, A., Rameau, J., et al. 2014, A&A, 566, A126
Maire, A.-L., Bonnefoy, M., Ginski, C., et al. 2016a, A&A, 587, A56
Maire, A.-L., Langlois, M., Dohlen, K., et al. 2016b, Proc. SPIE, 9908, 990834
Maire, A.-L., Stolker, T., Messina, S., et al. 2017, A&A, 601, A134
Marois, C., Racine, R., Doyon, R., Lafrenière, D., & Nadeau, D. 2004, ApJ, 615, L61
Marois, C., Lafrenière, D., Doyon, R., Macintosh, B., & Nadeau, D. 2006, ApJ, 641, 556
Marois, C., Macintosh, B., & Véran, J. 2010, Proc. SPIE, 7736, 77361J
Marois, C., Correia, C., Véran, J.-P., & Currie, T. 2014, IAU Symp., 299, 48
Mawet, D., Milli, J., Wahhaj, Z., et al. 2014, ApJ, 792, 97
Mesa, D., Gratton, R., Zurlo, A., et al. 2015, A&A, 576, A121
Mesa, D., Vigan, A., D'Orazi, V., et al. 2016, A&A, 593, A119
Mesa, D., Zurlo, A., Milli, J., et al. 2017, MNRAS, 466, L118
Milli, J., Hibon, P., Christiaens, V., et al. 2017, A&A, 597, L2
Pavlov, A., Möller-Nilsson, O., Feldt, M., et al. 2008, Proc. SPIE, 7019, 701939
Perrot, C., Boccaletti, A., Pantin, E., et al. 2016, A&A, 590, L7
Pohl, A., Sissa, E., Langlois, M., et al. 2017, A&A, 605, A34
Racine, R., Walker, G. A. H., Nadeau, D., Doyon, R., & Marois, C. 1999, PASP, 111, 587
Rameau, J., Chauvin, G., Lagrange, A.-M., et al. 2015, A&A, 581, A80
Rosenthal, E. D., Gurwell, M. A., & Ho, P. T. P. 1996, Nature, 384, 243
Samland, M., Mollière, P., Bonnefoy, M., et al. 2017, A&A, 603, A57
Soummer, R., Pueyo, L., & Larkin, J. 2012, ApJ, 755, L28
Thalmann, C., Schmid, H. M., Boccaletti, A., et al. 2008, Proc. SPIE, 7014, 70143F
Thatte, N., Abuter, R., Tecza, M., et al. 2007, MNRAS, 378, 1229
Vigan, A., Moutou, C., Langlois, M., et al. 2010, MNRAS, 407, 71
Vigan, A., Bonnefoy, M., Ginski, C., et al. 2016, A&A, 587, A55
Zurlo, A., Vigan, A., Mesa, D., et al. 2014, A&A, 572, A85
Zurlo, A., Vigan, A., Galicher, R., et al. 2016, A&A, 587, A57

Chapitre 5

Delorme et al., 2016 ; AA, 588, A136.pdf

Analyse de surface d'onde en plan focal en large bande spectrale (paragraphe 3.2.1 du dossier de synthèse et paragraphe 1.5 de la note d'accompagnement).

A&A 588, A136 (2016)
DOI: 10.1051/0004-6361/201527657

Astronomy & Astrophysics

Focal plane wavefront sensor achromatization: The multireference self-coherent camera

J. R. Delorme[1], R. Galicher[1], P. Baudoz[1], G. Rousset[1], J. Mazoyer[2], and O. Dupuis[1]

[1] LESIA, Observatoire de Paris, CNRS and University Denis Diderot Paris 7, 5 place Jules Janssen, 92195 Meudon, France
e-mail: jacques-robert.delorme@obspm.fr
[2] Space Telescope Science Institute, 3700 San Martin Drive, 21218 Baltimore MD, USA

Received 28 October 2015 / Accepted 5 January 2016

ABSTRACT

Context. High contrast imaging and spectroscopy provide unique constraints for exoplanet formation models as well as for planetary atmosphere models. But this can be challenging because of the planet-to-star small angular separation (<1 arcsec) and high flux ratio (>10^5). Recently, optimized instruments like VLT/SPHERE and Gemini/GPI were installed on 8m-class telescopes. These will probe young gazeous exoplanets at large separations ($\gtrsim$1 au) but, because of uncalibrated phase and amplitude aberrations that induce speckles in the coronagraphic images, they are not able to detect older and fainter planets.
Aims. There are always aberrations that are slowly evolving in time. They create quasi-static speckles that cannot be calibrated a posteriori with sufficient accuracy. An active correction of these speckles is thus needed to reach very high contrast levels (>10^6−10^7). This requires a focal plane wavefront sensor. Our team proposed a self coherent camera, the performance of which was demonstrated in the laboratory. As for all focal plane wavefront sensors, these are sensitive to chromatism and we propose an upgrade that mitigates the chromatism effects.
Methods. First, we recall the principle of the self-coherent camera and we explain its limitations in polychromatic light. Then, we present and numerically study two upgrades to mitigate chromatism effects: the optical path difference method and the multireference self-coherent camera. Finally, we present laboratory tests of the latter solution.
Results. We demonstrate in the laboratory that the multireference self-coherent camera can be used as a focal plane wavefront sensor in polychromatic light using an 80 nm bandwidth at 640 nm (bandwidth of 12.5%). We reach a performance that is close to the chromatic limitations of our bench: 1σ contrast of 4.5×10^{-8} between 5 and 17 λ_0/D.
Conclusions. The performance of the MRSCC is promising for future high-contrast imaging instruments that aim to actively minimize the speckle intensity so as to detect and spectrally characterize faint old or light gaseous planets.

Key words. techniques: high angular resolution – instrumentation: high angular resolution – instrumentation: adaptive optics

1. Introduction

During the last few years, the imaging of circumstellar disks and exoplanets has become one of the priorities to be able to constrain models of planetary system formation and of planetary atmospheres. However, direct imaging of faint sources around bright objects is very challenging. For example, in the visible and near-infrared light, the contrast ranges from 10^3 for bright debris disks down to 10^{10} for Earth-like planets (Seager & Deming 2010). The study of this type of object therefore requires dedicated techniques, such as coronagraphs, that attenuate the light from the host star (Marois et al. 2010; Lagrange et al. 2009).

A lot of coronagraphs associate a focal plane mask and a pupil diaphragm called a Lyot stop to filter the stellar light and minimize the star intensity in the science image (Rouan et al. 2000; Soummer et al. 2003; Mawet et al. 2005; Murakami et al. 2008). However, as a result of aberrations, part of the stellar light goes through the Lyot stop and produces speckles in the science image. These speckles are usually brighter than the planet signal that we are looking for and it is necessary to reduce their intensity.

With ground-based telescopes, most of the speckles are due to atmospheric turbulence. These dynamic wavefront errors are estimated and corrected by conventional adaptive optics (AO) systems that measure the wavefront error using a wavefront sensor in a dedicated optical channel. Because of beam splitting, quasi-static, non-common path aberrations (NCPA) are generated by the instrument optics between the wavefront-sensing channel and the science-image channel, which limits the accuracy of the AO correction (Hartung et al. 2003). Like P1640 (Hinkley et al. 2011) and SCExAO (Jovanovic et al. 2014), VLT/SPHERE (Beuzit et al. 2008) and Gemini/GPI (Macintosh et al. 2008) are two instruments designed to detect young Jupiter-like planets. They minimize the quasi-static NCPA in open loop before the observations but cannot control them during the observations. However, as NCPAs evolve during the observations, the calibration degrades with time and the contrast performance is limited by quasi-static speckles to 10^{-4}–10^{-5} at 0.5″ in raw images. Space-based telescopes are free of atmospheric turbulence but the variations of temperature and gravity also create quasi-static aberrations. Dedicated real-time methods are required to estimate and compensate for quasi-static aberrations in a closed loop. First, these can be implemented into current ground-based high-contrast imaging instruments to enhance the contrast in the science images. Secondly, we could integrate these techniques in the design of high-contrast instruments for future ground-based extremely large telescopes (ELTs) and space-based telescopes, e.g. WFIRST-AFTA Spergel et al. (2015) or HDST, see Dalcanton et al. (2015).

Dedicated strategies for observations (Marois et al. 2004, 2006) have been implemented to overcome the quasi-static speckle limitation. They use the correlation between speckles

in time or in wavelength. Their performance were demonstrated on-sky, enabling exoplanets to be detected by direct imaging (Marois et al. 2008, 2010; Lagrange et al. 2009). However, as the aberrations and the speckle pattern slowly evolve in time, a posteriori calibrations cannot calibrate all the speckles and an active control of the speckle field is requiered to achieve contrast that is better than 10^{-5} in the raw data.

This type of control can be done using at least one deformable mirror (DM) upstream from the coronagraph. Since DMs have a finite number of actuators, they can only correct speckles in a bounded area in the focal plane image (Sect. 2 and Malbet et al. 1995). To correct the speckles without being limited by NCPA, we also need to estimate the aberrations (i.e., the complex electric field of the speckles) directly from the science image using a focal plane wavefront sensor (FPWFS).

Several FPWFSs have been proposed. Some of them are based on temporal modulations of speckles like the electrical field conjugation method (Give'on et al. 2006, 2007; Bordé & Traub 2006) or phase diversity method (Sauvage et al. 2012; Paul et al. 2013). There are also FPWFSs that are based on spatial modulations of the speckles such as the Asymetric Pupil Fourier wavefront sensor (Martinache 2013) or the self-coherent camera (SCC, Baudoz et al. 2006; Galicher et al. 2008b). The SCC creates Fizeau interference to spatially modulate the speckle intensity in the coronagraphic images. Thus, it can retrieve the complex electric field from one coronagraphic image (i.e., the science image) without NCPA. We discuss the SCC principle and performance (Mazoyer et al. 2013b) in Sect. 3. As with all FPWFSs, the SCC is limited by the chromatism of the images. In this paper, we propose two methods to make it work in polychromatic light. The first method is an upgrade of the SCC in which the optical path difference (OPD) between the two beams of the Fizeau interferometer is not null. The second solution, called the multireference self-coherent camera (MRSCC), is another upgrade of the SCC, which uses more than two interfering beams. We present both methods and discuss their performance and limitations in Sects. 4 and 5. In Sect. 6, we present the très haute dynamique (THD) laboratory bench and the expected performance of the MRSCC. Finally, in Sect. 7, we demonstrate in the laboratory that the MRSCC can control, in closed loop, a DM that minimizes the speckle intensity in wide spectral band images (12.5% bandpass).

2. Dark hole and estimation of the contrast

A DM has a limited number of actuators and only modify speckles in a bounded area of the image that we call the influence area. Assuming an N by N actuator DM in pupil plane, the size of the influence area is a $N\lambda_0/D$ by $N\lambda_0/D$ square centered on the optical axis, where λ_0 is the central wavelength and D the diameter of the pupil. The part of the influence area where we try to minimize the speckle intensity is called dark hole (DH, Malbet et al. 1995). If only one DM is used and set in a pupil plane, we can choose to control only the phase aberrations to reduce the speckle intensity in the full influence area, or both phase and amplitude aberrations by limiting the DH to half of the influence area (Bordé & Traub 2006). Because the aberrations are never solely phase aberrations in the experimental set up, we use the second option in this paper.

Once the speckle minimization have been performed, we estimate its performance in a contrast computation area. We define this area within the DH removing $1.5\lambda_0/D$ on each side. Indeed, since we do not use a pupil apodizer, the diffraction pattern of the uncorrected bright speckles that are located just outside of the DH spreads light inside the DH.

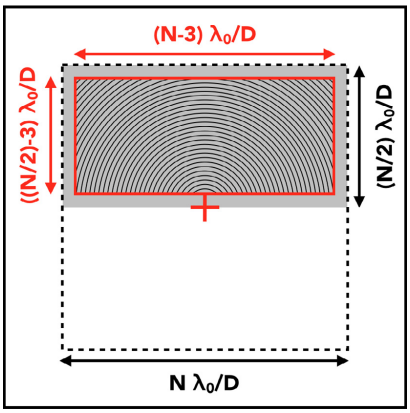

Fig. 1. Influence area of the DM (dashed line), DH (gray area) and computation area (red solid line). The annuli of $\frac{\lambda_0}{2D}$ width in the computation area are used to compute the contrast curves. The red cross represents the optical axis.

Figure 1 is a scheme of the main sizes of the three areas that have been introduced previously. The influence area is delineated by a dashed line, with the DH represented as a gray area and the computation area delineated by a red solid line. The computation area covers a range of separations from $1.5\lambda_0/D$ to $\left((N-3)/\sqrt{2}\right)\lambda_0/D$.

To estimate by how much the speckle intensity is reduced after correction, we use two criteria: the contrast curve and the cumulative function of the intensity, both of which are computed in the computation area. The contrast curves are the azimuthal standard deviation of the image intensity, computed in annuli of $\lambda_0/2D$ width (annuli in Fig. 1) centered on the optical axis (red cross). It gives the 1σ detection limit as a function of the angular separation. To obtain cumulative functions, we compute the ratio between the number of pixels with an intensity lower than a given value and the total number of pixels within the computation area. These two criteria are complementary. The cumulative function gives information about the statistics of the residual intensity (median and dispersion) while the contrast curve shows how the standard deviation evolves with the angular separation to the star.

3. The self-coherent camera

In this section, we recall the principles of the SCC and explain the origin of its sensitivity to chromatism.

3.1. Principle of the SCC in monochromatic light

The SCC can be used as an FPWFS downstream from a coronagraph for high contrast imaging (Galicher et al. 2008b; Mazoyer et al. 2014). It uses a small reference hole that is added to the Lyot stop plane (Fig. 2, top). We call the separation between the classical Lyot stop and the reference hole ξ_0, D_L the diameter of the classical Lyot stop, and γ the ratio between D_L and the diameter of the reference hole. We consider $\gamma \gg 1$ (Galicher et al. 2010). The angle θ_H between the reference hole and the horizontal axis of the Lyot stop plane does not impact on the

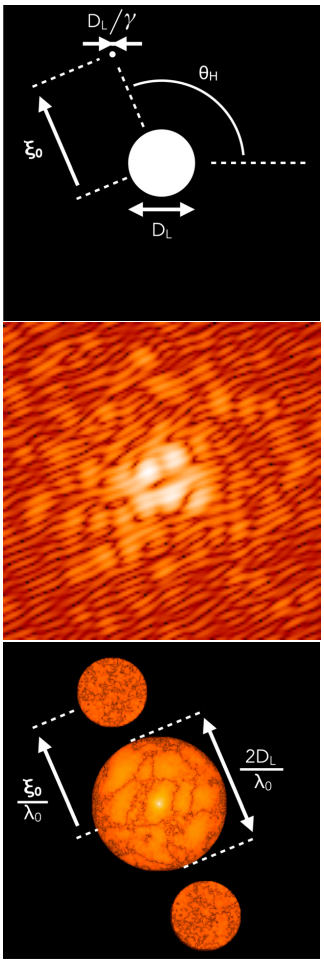

Fig. 2. *Top*: SCC Lyot stop. *Middle*: numerically simulated SCC image showing spatially modulated stellar speckles. Field of view: $20\lambda_0/D$ by $20\lambda_0/D$. *Bottom*: fourier transformation of the SCC image.

performance of the instrument. We use an angle of +115° in this paper, which is the value for our laboratory experiments (Sect. 6).

Owing to aberrations, part of the stellar light is not filtered by the coronagraph and goes through the classical Lyot stop, which induces speckles in the image. A small part of the stellar light that is diffracted by the coronagraph is selected by the SCC reference hole. The two coherent beams are recombined in the image plane, which form Fizeau fringes that spatially modulate the speckles. As for a planet, its image is off the coronagraph mask and its light only goes through the classical Lyot stop. As it is not coherent with the stellar light of the reference hole, the companion image is not spatially modulated by fringes. Figure 2 (middle) is an SCC image with no planet. In this image, we artificially increased the flux from the reference to underline the fringes.

We can write the intensity I in an SCC image as follows:

$$I(\boldsymbol{\alpha}) = |A_S(\boldsymbol{\alpha})|^2 + |A_C(\boldsymbol{\alpha})|^2 + |A_R(\boldsymbol{\alpha})|^2 + 2Re\left[A_S(\boldsymbol{\alpha}) A_R^*(\boldsymbol{\alpha}) \exp\left(\frac{2i\pi\boldsymbol{\alpha}.\boldsymbol{\xi}_0}{\lambda_0}\right)\right], \quad (1)$$

where $\boldsymbol{\alpha}$ is the focal plane coordinate. A_S is the complex electric field of the speckles we want to estimate and minimize, A_C the complex electric field of the companion and A_R the complex electric field associated with the SCC reference hole and A_R^* the conjugate of A_R. These complex electric fields in the focal plane are wavelength-dependent and we account for these dependences in all numerical simulations. In the second member of Eq. (1), the first term is the speckle pattern (i.e., coronagraphic residue) that we want to minimize, the second term is the companion image that we want to detect, the third term is the intensity associated with the SCC reference hole and, finally, the last term corresponds to the spatial modulation of the speckles.

Once the image is recorded, we apply a numerical Fourier transform (Fig. 2, bottom) to differentiate the fringed speckles from the companion image and we obtain:

$$\begin{aligned}\mathcal{F}^{-1}[I](\boldsymbol{u}) = {} & \mathcal{F}^{-1}\left[|A_S|^2 + |A_C|^2 + |A_R|^2\right] * \delta(\boldsymbol{u}) \\ & + \mathcal{F}^{-1}\left[A_S^* A_R\right] * \delta\left(\boldsymbol{u} + \frac{\boldsymbol{\xi}_0}{\lambda_0}\right) \\ & + \mathcal{F}^{-1}\left[A_S A_R^*\right] * \delta\left(\boldsymbol{u} - \frac{\boldsymbol{\xi}_0}{\lambda_0}\right), \end{aligned} \quad (2)$$

where $\boldsymbol{u}$ is the spatial frequency plane coordinate, $\mathcal{F}$ the Fourier transform operator and $\mathcal{F}^{-1}$ its inverse. The first term, which is the central peak of the Fourier transform, is the sum of the autocorrelations of the electric field in the classical Lyot stop and in the reference hole. The radius of the central peak is D_L/λ_0 because $\gamma \gg 1$. The other two terms, which correspond to the two lateral peaks of the Fourier transform, are the correlation between the stellar electric fields in the classical Lyot stop and in the reference hole. The two peaks are conjugated and contain the same information and the same contribution of noise. The radius of these peaks is $D_L(1 + 1/\gamma)/(2\lambda_0)$. Thus, the three peaks do not overlap if the separation $\|\boldsymbol{\xi}_0\|$ between the classical Lyot stop and the SCC reference hole is large enough (Galicher et al. 2010):

$$\|\boldsymbol{\xi}_0\| > \frac{D_L}{2}\left(3 + \frac{1}{\gamma}\right). \quad (3)$$

To estimate the complex electric field A_S, we select one of the lateral peaks and we recenter it. The Fourier Transform of this correlation peak, called I_-, is

$$I_- = A_S A_R^*. \quad (4)$$

This contains the information on the complex electric field A_S of the stellar speckles multiplied by the reference A_R^*. Because the reference beam is created in the Lyot plane of the instrument and goes through the same optics as the beam of the classical Lyot stop, A_R^* is very stable with respect to A_S. Moreover, the point spread function (PSF) $|A_R|^2$ has a full width at half maximum (FWHM) of $\gamma\,\lambda_0/D$. So, if the reference pupil is small enough, ($\gamma \gg 1$) $|A_R|^2$ does not go to zero inside the influence area of the DM. With these hypotheses, if we minimize I_-, as done in this paper, we also minimize A_S and the speckle intensity (Mazoyer 2014).

To control the DM on our bench, we reform the real and imaginary parts of I_- as vectors and we concatenate them in one unique vector. To convert I_- in a command to the DM we make use of a linear approach that is based on a control matrix (Boyer et al. 1990; Mazoyer et al. 2013a). To build the control matrix, we define the set of sine and cosine functions that the DM can produce. The number of functions equals the number of degrees of freedom available with the DM. We apply each of these functions successively to the DM and record the corresponding SCC image and compute the corresponding vector I_-. With all the I_-, we build an interaction matrix. Finally, we invert this using a singular value decomposition to obtain the control matrix that can be used in a closed loop.

During the correction, we register one SCC image at each iteration. To only correct speckles in the DH (and not in the entire influence area), we multiply the SCC image by a numerical mask (Butterworth type) reproducing the DH. The resulting image is processed to extract I_-. The numerical mask allows us to be able to saturate part of the image outside the DH with limited impacts on the estimated I_-. The multiplication of I_- by the control matrix leads to the DM command increment that is multiplied by a gain and added to the previous iteration command. After a few iterations the correction has been done and is stable.

Usually, the active correction is not limited by the SCC and the speckles inside the DH are still modulated by fringes. We can then apply the a posteriori SCC data processing to enhance the contrast (Baudoz et al. 2013). In this paper we do not use the a posteriori calibration and we focus on the performance of the active correction. Consequently, after the active correction is done, we can close the reference aperture to record the coronagraphic image (with no stellar light from the reference hole). We normalize the SCC and coronagraphic images by the maximum intensity of the non-coronagraphic PSF that was recorded with the stellar source off the coronagraph axis. All the images shown in this paper are normalized in flux.

3.2. Simulated performance in monochromatic light

Below we derive a typical performance for the SCC in monochromatic light ($\lambda_0 = 640$ nm) from numerical simulations. This result is used when studying the performance in polychromatic light (Sect. 3.4).

We assume a perfect achromatic coronagraph (Cavarroc et al. 2006) without any apodization. To simulate the SCC, we numerically add a reference hole, assuming $\gamma = 25$ and $\xi_0 = 1.8D$, which obey Eq. (3). The flux inside of the reference beam is similar to the flux measured in our laboratory, which is 4.8×10^{-8} times the energy in the pupil upstream from the coronagraph. The simulated phase aberrations have a power spectral density (PSD), which varyies as $f^{-2.3}$ (with f the spatial frequencies) and a standard deviation of 10 nm rms inside the pupil, since it is the case in our laboratory experiment. We also assume amplitude aberrations of 5% rms with a PSD, which varies as f^{-1}. Levels and PSD chosen for phase and amplitude are similar to those we measured in our laboratory. We assume a 32 by 32 actuator DM and we correct phase and amplitude aberrations in a DH of 16 by 32 λ_0/D. The simulated detector is similar to the one that we used in our laboratory. This has a readout noise (RON) of 3.2 e^- per pixel and a full well capacity of 60 000 e^- per pixel.

In this paper, we reproduce the readout noise of the detector and the photon noise. To set the flux level, we use our experimental conditions (see Sect. 7), with 17 e^- for a normalized intensity of 2×10^{-8}. We use this conversion factor in the numerical simulations. We also reproduce the saturation of the detector. All the corrected images presented in this paper are coronagraphic images.

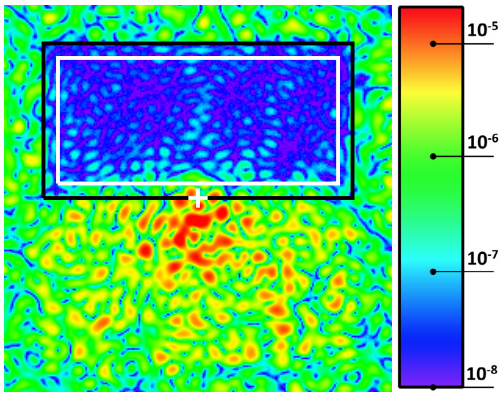

Fig. 3. Numerically simulated coronagraphic image obtained after an SCC correction in monochromatic light. Simulation parameters are given in Table 1. Black line: DH (16 λ_0/D by 32 λ_0/D). White line: computation area (13 λ_0/D by 29 λ_0/D). White cross: optical axis. Field of view: 40 λ_0/D by 40 λ_0/D. The color bar associated with this image is the same for all the coronagraphic images in the paper.

Table 1. Set of parameters used to simulate the image of Fig. 3.

Light source	$\lambda_0 = 640$ nm
Phase aberrations	PSD: $f^{-2.3}$, 10 nm rms
Amplitude aberrations	PSD: f^{-1}, 5% rms
Deformable mirror	32 by 32 actuators
Coronagraph	Perfect coronagraph
Lyot stop	$\gamma = 25$, $\xi_0 = 1.8\ D_L$, $\theta_H = +115°$
Readout noise	3.2 e^-/pixel
Saturation level	60 000 e^-/pixel
Normalized intensity	$2 \times 10^{-8} \longleftrightarrow 17$ e^-/pixel
DM influence area	32 by 32 λ_0/D
Dark hole	16 by 32 λ_0/D
Computation area	13 by 29 λ_0/D
Sampling	6.25 pixels per λ_0/D

Figure 3 presents the coronagraphic image obtained after correction. In monochromatic light, the intensity of all the speckles located inside the computation area (white line) is efficiently reduced. The perfect coronagraph that we simulated does not include any apodization. As a consequence, the bright speckles close to optical axis (white cross) spread light at small angular separations in the DH.

Figure 4 presents the contrast curve (top) and the cumulative function (bottom) associated with the image of Fig. 3. The average of the 1σ contrast is 2.9×10^{-8} between $5\lambda_0/D$ and $20\lambda_0/D$ and between $6\lambda_0/D$ and $17\lambda_0/D$. From the cumulative function the normalized intensity is better than 2.8×10^{-8} in 50% of the computation area (i.e., the median-normalized intensity). Moreover, the cumulative curve shows that the dispersion of the speckle intensity is small as observed in Fig. 3 where the contrast level inside the DH is almost uniform. The achieved contrast level depends on the level of phase and amplitude aberrations assumed in the simulation.

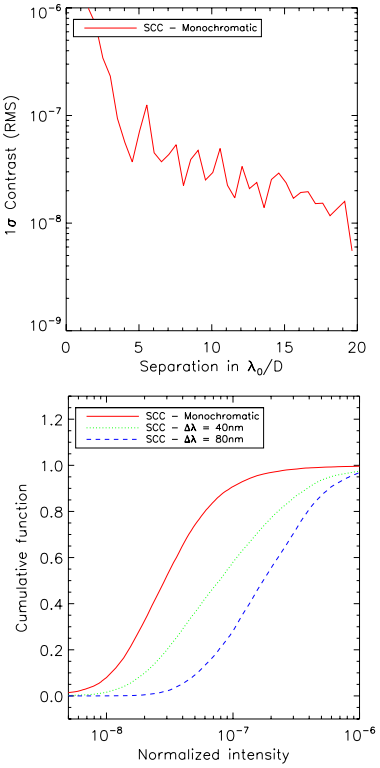

Fig. 4. Contrast curve (*top*) computed from the coronagraphic image that was obtained with the SCC in monochromatic light (Fig. 3) and spatial cumulative function (*bottom*) associated with images obtained with the SCC in monochromatic light (red solid line) and in polychromatic light, assuming $\Delta\lambda = 40$ nm (green dotted line) and 80 nm (blue dashed line).

Mazoyer et al. (2014) demonstrated that the limitation of the correction obtained in monochromatic light in the laboratory was that the amplitude aberrations cannot be corrected with only one deformable mirror. In other words, the SCC electric field estimation is accurate but the correction with a finite number of actuators is limited. The results presented here assumed a clear circular aperture. For a pupil with central obscuration, spiders, or segmentation, as long as the coronagraph rejects part of the stellar light in the reference hole, the SCC should then provide an accurate estimation of the electric field that needs to be corrected. However, discountinuities in the pupil produce effects in the focal plane that could be addressed using dedicated coronagraphs (e.g., N'Diaye et al. 2014) or special correction techniques with several DMs in cascade, see Pueyo & Norman (2013).

3.3. SCC in polychromatic light

To spectrally characterize the very faint neighborhood of bright stars like exoplanets and increase the signal to noise ratio of the detections, one solution is to make observations with a large bandwidth (5–20%). As a consequence, an efficient coronagraphic instrument has to work with large bandwidths as well as the associated focal plane wavefront sensor. In this section, we assume a perfectly achromatic coronagraph to study the impact of a finite bandwidth on the SCC wavefront estimation.

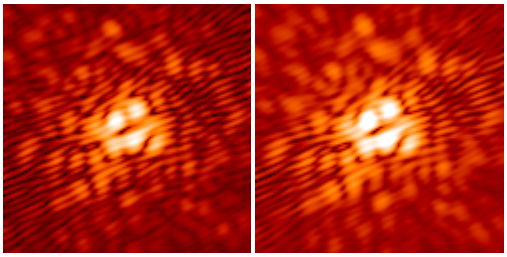

Fig. 5. Numerically simulated SCC images obtained before correction for $\Delta\lambda = 40$ nm (*left*) and $\Delta\lambda = 80$ nm (*right*) at $\lambda_0 = 640$ nm. Field of view: 20 by 20 λ_0/D.

Figure 5 presents SCC images obtained before correction, using the same parameters as for the monochromatic case (Table 1) but with larger bandwidths: $\Delta\lambda = 40$ nm (left) and $\Delta\lambda = 80$ nm (right). As for Fig. 2 (middle), to highlight the fringes, we numerically increased the flux into the reference beams to obtain these two SCC images. We observe that the fringes are only located around the central fringe with a width that is proportional to the coherence length of the light ($\lambda_0^2/\Delta\lambda$). Indeed, in polychromatic light, the intensity recorded on the detector in the focal plane is

$$I_{\Delta\lambda}(\boldsymbol{\alpha}) = \int_{\Delta\lambda} \left[|A_S|^2 + |A_C|^2 + |A_R|^2\right] \mathrm{d}\lambda + \int_{\Delta\lambda} 2Re\left[A_S A_R^* \exp\left(\frac{2i\pi\boldsymbol{\alpha}.\boldsymbol{\xi}_0}{\lambda}\right)\right] \mathrm{d}\lambda, \quad (5)$$

where $\int_{\Delta\lambda}$ represents the integration over the range $\lambda_0 \pm \Delta\lambda/2$. As in Eq. (1), the last term corresponds to the spatial modulation of the speckles. The fringe pattern is now a superposition of monochromatic fringe patterns. As the fringe spacing is wavelength-dependent, the resulting pattern becomes blurred far from the central fringe (Fig. 5), and the larger the bandwidth, the faster the fringes become blurred.

Figure 6 is the Fourier transform of the SCC image obtained in polychromatic light for $\Delta\lambda = 80$ nm around $\lambda_0 = 640$ nm. The associated equation of this Fourier transform is:

$$\mathcal{F}^{-1}\left[I_{\Delta\lambda}\right](\boldsymbol{u}) = \int_{\Delta\lambda} \mathcal{F}^{-1}\left[|A_S|^2 + |A_C|^2 + |A_R|^2\right] * \delta(\boldsymbol{u})\, \mathrm{d}\lambda + \int_{\Delta\lambda} \mathcal{F}^{-1}\left[A_S^* A_R\right] * \delta\left(\boldsymbol{u} - \frac{\boldsymbol{\xi}_0}{\lambda}\right) \mathrm{d}\lambda + \int_{\Delta\lambda} \mathcal{F}^{-1}\left[A_S A_R^*\right] * \delta\left(\boldsymbol{u} + \frac{\boldsymbol{\xi}_0}{\lambda}\right) \mathrm{d}\lambda. \quad (6)$$

The first term, corresponding to the central peak, now has a radius of D_L/λ_{min}. This is determined by the smallest wavelength $\lambda_{min} = \lambda_0 - \Delta\lambda/2$. We still assume $\gamma \gg 1$. Each lateral peak is the sum of all the monochromatic lateral peaks. Their size and distance to the central peak are a function of the wavelength. The closest of these to the central peak has a radius $D_L(1 + 1/\gamma)/(2\lambda_{max})$ with $\lambda_{max} = \lambda_0 + \Delta\lambda/2$. Thus, in

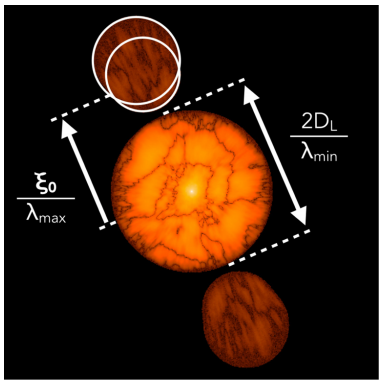

Fig. 6. Fourier transform of the SCC image obtained by numerical simulations, assuming polychromatic light ($\Delta\lambda$ = 80 nm at λ_0 = 640 nm).

polychromatic light, the lateral and central peaks do not overlap if and only if

$$||\boldsymbol{\xi}_0|| > D_L\left(\frac{\lambda_{max}}{\lambda_{min}} + \frac{1}{2} + \frac{1}{2\gamma}\right). \quad (7)$$

If the condition of Eq. (7) is fulfilled, we can select the elongated lateral peak by using a circular oversized mask and extract I_- using the procedure described for the monochromatic case (see Sect. 3.1).

3.4. Performance of the SCC in polychromatic light

In this section we use the SCC in polychromatic light (Eq. (7) fulfilled) to create a DH as performed in monochromatic light (Sect. 3.2). We assume the parameters of Table 1 and we obtain the image of Fig. 7 for a bandwidth of 40 nm (top) and for $\Delta\lambda$ = 80 nm (bottom). In both cases, $|A_R|^2$ have the same characteristics as in monochromatic light (maximum at 4.8×10^{-8} in normalized intensity).

Figure 7 highlights the limitation of the SCC in polychromatic light. When increasing the bandwidth, the SCC estimation is less and less efficient and speckles inside the DH are measured and are therefore not corrected (top left of the DH). Comparing these images with the images obtained before correction (Fig. 5), we observe that in the area where the fringes are blurred, the SCC estimation is disturbed. In other words, if speckles are not spatially modulated, the associated complex field A_S cannot be estimated and thus, it cannot be minimized. As a consequence, the area of the DH where the correction is efficient quickly decreases as the bandwidth increases.

The cumulative functions associated with Fig. 7 are given in Fig. 4 (top). The performance degrades by a factor of three for the $\Delta\lambda$ = 40 nm (7.8×10^{-8}) and six for $\Delta\lambda$ = 80 nm (1.7×10^{-7}). These values confirm that the larger the bandwidth, the worse the correction.

To overcome the limitation of the SCC in polychromatic light, Galicher et al. (2008a) proposed two methods: working with an integral field spectrometer (IFS) at modest spectral resolution (R = 30 to 100) or faking the use of a short bandpass filter using a Wynne compensator (Wynne 1979). However, both methods have drawbacks that led us to develop new methods to make the SCC more achromatic. The Wynne compensator is a very invasive device composed of two triplets of lenses and the IFS is not available in all current coronagraphic instruments.

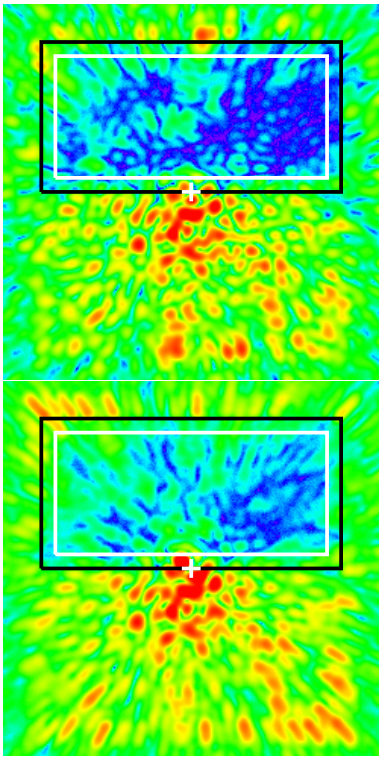

Fig. 7. Numerically simulated coronagraphic images after correction with the SCC for $\Delta\lambda$ = 40 nm (*top*) and $\Delta\lambda$ = 80 nm (*bottom*).

In this paper, we propose two other solutions to work with polychromatic light. The first method presented in Sect. 4 is based on the introduction of a non-null OPD between the reference hole and the classical Lyot stop. The second method, called the multireference self-coherent camera, uses several reference holes, instead of just one (Sect. 5).

4. Optical path difference between reference hole and Lyot stop

bearing in mind that we reduce the DH to half of the influence area of the DM, part of the fringe pattern is located in the half plane that we do not try to correct. One solution to improve the performance of the SCC in polychromatic light consists of shifting the pattern of fringes inside the DH. To do so, we can introduce an achromatic OPD between the beam that goes through the classical Lyot stop and the beam that goes through the reference hole. Calling δ the OPD, Eq. (5) becomes:

$$I_{\Delta\lambda}(\boldsymbol{\alpha}) = \int_{\Delta\lambda}\left[|A_S|^2 + |A_C|^2 + |A_R|^2\right]d\lambda + \int_{\Delta\lambda} 2Re\left[A_S A_R^* \exp\left(\frac{2i\pi\,(\boldsymbol{\alpha}.\boldsymbol{\xi}_0 + \delta)}{\lambda}\right)\right]d\lambda. \quad (8)$$

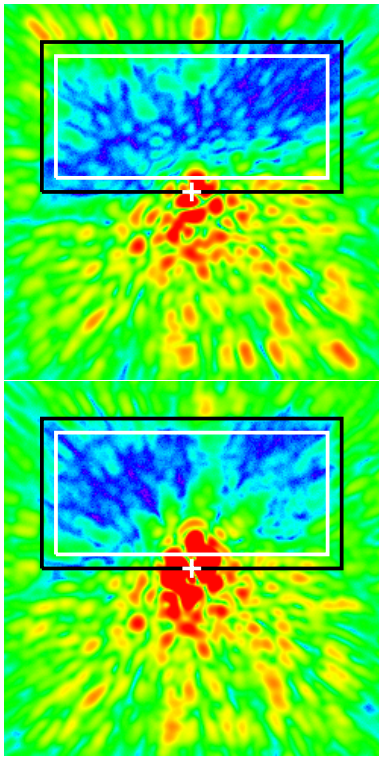

Fig. 8. Numerically simulated coronagraphic images for different OPD: (*top*) $\delta = 8\lambda_0$ and (*bottom*) $\delta = 16\lambda_0$. Bandwidth: $\Delta\lambda = 80$ nm.

When applying a constant OPD in the conditions of Fig. 7 (bottom) the fringe pattern can be shifted inside the DH. This increase of the fringe visibility inside the DH should improve the SCC estimation. Introducing an OPD of $\delta = 8\lambda_0$ or $\delta = 16\lambda_0$ shifts the central fringe by 8 or 16 fringes which corresponds to $\sim 4.4\lambda_0/D$ and $\sim 8.9\lambda_0/D$ in our numerical simulation (1.8 fringes per speckle). We obtain images of Fig. 8 using the assumptions of Table 1 and $\Delta\lambda = 80$ nm.

Compared with Fig. 7, we find that non-null OPD improves the SCC correction. Figure 9 presents the cumulative curves associated with the images of Figs. 3, 7 (bottom), and 8. In the case with no OPD, the median of the speckle intensity is 1.7×10^{-7}, while we find 9.4×10^{-8} and 1.4×10^{-7} for $\delta = 8\lambda_0$ and $\delta = 16\lambda_0$. We find the $\delta = 16\lambda_0$ case is less efficient than the $\delta = 8\lambda_0$ case. Indeed, even if the fringe pattern is in the middle of the DH when $\delta = 16\lambda_0$, the visibility of the SCC fringes is not uniform in the DH. Visibility is low close to the optical axis because the speckles are a lot brighter than the $|A_R|^2$ there. That is why the central part of the DH is not well corrected in the $\delta = 16\lambda_0$ case. The best value of the OPD is when the white fringe is closer to the axis: a smaller OPD.

Even if the OPD solution can improve the contrast inside the DH, we noticed in our numerical simulations that the performance strongly depends on the initial speckles pattern and when low order aberrations are too large, the correction does not converge. This technique would then be difficult to use and we propose another solution to improve the performance of the SCC estimation and correction: the MRSCC.

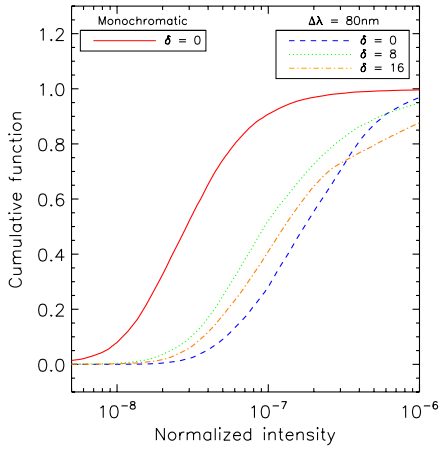

Fig. 9. Cumulative functions associated with the images obtained by numerical simulations in monochromatic light (red solid line) and in polychromatic light ($\Delta\lambda = 80$ nm at 640 nm) assuming $\delta = 0$ (blue dashed line), $\delta = 8\lambda_0$ (green dotted line) or $\delta = 16\lambda_0$ (orange mixed line)

5. Multireference self-coherent camera

The MRSCC is designed to mitigate the chromatic limitation of the SCC. In this section we introduce the formalism of the MRSCC and study the performance as a function of the bandwidth from numerical simulations.

5.1. Formalism of the MRSCC

The fringe pattern produced by the reference hole of the SCC gets blurred far from the central fringe in polychromatic light. In these blurred areas, the speckles cannot be corrected. To increase the area of the DH where the speckles are spatially modulated, we introduce additional fringe patterns by adding reference holes in the Lyot stop (Fig. 10, top). As for the SCC reference hole, the stellar light selected by the new reference holes interferes with the stellar coronagraphic residue in the image plane, which creates Fizeau fringes on the speckles. The orientation and the fringe spacing of these new patterns depend on the positions of the reference holes with respect to the Lyot stop. By placing them shrewdly it is possible to spatially modulate areas of the DH where the fringes that are induced by the SCC hole are blurred. Thus, the MRSCC can increase the area where speckles are correctly modulated.

Figure 10 (middle) presents one MRSCC image obtained with a Lyot stop that was composed of three reference holes in addition to the classical Lyot stop (Fig. 10, top). In this MRSCC image, we numerically increased the flux into the reference holes to highlight the fringes. The distances and the diameter ratio between the reference holes and the Lyot stop pupil are the same ($\xi_1 = \xi_2 = \xi_3 = 1.8D_L$ and $\gamma_1 = \gamma_2 = \gamma_3 = 25$).

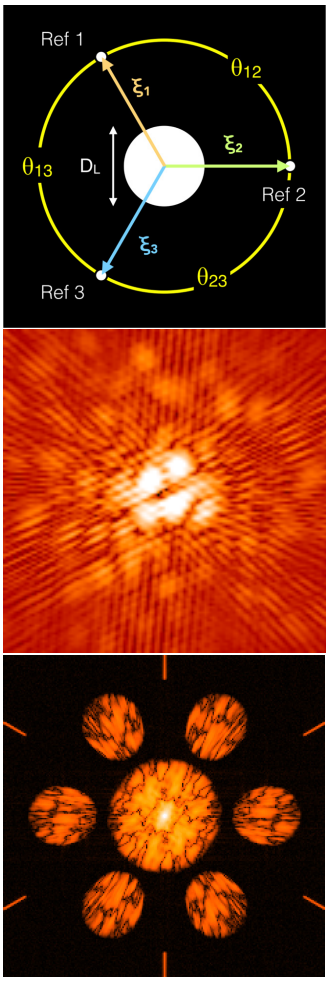

Fig. 10. *Top*: MRSCC Lyot stop with three reference holes. *Middle*: numerically simulated MRSCC image showing the three fringe patterns before correction. Field of view: 20 by 20 λ_0/D. *Bottom*: fourier transform of the MRSCC image.

They obey Eq. (7) for $\Delta\lambda = 80$ nm. The angle between each couple of reference holes is 120°. We can write the intensity in the MRSCC image as

$$I_{\Delta\lambda}(\boldsymbol{\alpha}) = \int_{\Delta\lambda}\left[|A_S|^2 + |A_C|^2 + \sum_{i=1}^{n}|A_{R_i}|^2\right]d\lambda + \sum_{i=1}^{n}\int_{\Delta\lambda} 2Re\left[A_S A_{R_i}^* \exp\left(\frac{2i\pi\boldsymbol{\alpha}.\boldsymbol{\xi}_i}{\lambda}\right)\right]d\lambda + \sum_{j=1}^{n}\sum_{i>j}^{n}\int_{\Delta\lambda} 2Re\left[A_{R_j} A_{R_i}^* \exp\left(\frac{2i\pi\boldsymbol{\alpha}.\boldsymbol{\xi}_{ij}}{\lambda}\right)\right]d\lambda, \quad (9)$$

where n is the number of reference holes and $\boldsymbol{\xi}_{ij} = \boldsymbol{\xi}_i - \boldsymbol{\xi}_j$. The second term is the sum of the modulations of the speckle electric field A_S by each reference beam $A_{R_i}^*$. The third term contains the sum of the fringe patterns that are due to the interference between reference holes. Indeed, beams coming from two reference holes also form Fizeau fringes in the MRSCC image. To order to estimate the complex amplitude A_S we apply the Fourier transform to the image (Fig. 10, bottom):

$$\mathcal{F}^{-1}\left[I_{\Delta\lambda}\right](\boldsymbol{u}) = \int_{\Delta\lambda}\left(\mathcal{F}^{-1}\left[|A_S|^2 + |A_C|^2\right] + \sum_{i=1}^{n}\mathcal{F}^{-1}\left[|A_{R_i}|^2\right]\right) * \delta(\boldsymbol{u})\,d\lambda + \int_{\Delta\lambda}\sum_{i=1}^{n}\mathcal{F}^{-1}\left[A_S^* A_{R_i}\right] * \delta\left(\boldsymbol{u} - \frac{\boldsymbol{\xi}_i}{\lambda}\right)d\lambda + \int_{\Delta\lambda}\sum_{i=1}^{n}\mathcal{F}^{-1}\left[A_S A_{R_i}^*\right] * \delta\left(\boldsymbol{u} + \frac{\boldsymbol{\xi}_i}{\lambda}\right)d\lambda + \int_{\Delta\lambda}\sum_{j=1}^{n}\sum_{\substack{i=1\\ i\neq j}}^{n}\mathcal{F}^{-1}\left[A_{R_j}^* A_{R_i}\right] * \delta\left(\boldsymbol{u} - \frac{\boldsymbol{\xi}_{ij}}{\lambda}\right)d\lambda. \quad (10)$$

The first term is the central peak of the spatial frequency plane. The second and third term contain the lateral correlation peaks of A_S and $A_{R_i}^*$ and their conjugate. There are a couple of conjugated correlation peaks per reference hole. This is the information we want to extract to control the DM and create the DH. Finally, the last term contains the correlation peaks between reference holes. They do not disturb the estimation of the electric field if they do not overlap the correlation peaks used to do the estimation of I_- (see Fig. 10 bottom, six small sections of straight line at the border of the Fourier image). The size and the position of each correlation peak depend on the spectral bandwidth and on the position of the reference holes in the Lyot stop plane.

To estimate the electric field, we extract each lateral peak of the second term. Then, using the algorithm described in Sect. 3.1 we obtain one I_- for each reference hole. In polychromatic light, these estimations are different and complementary because each reference beam modulates different speckles (i.e., different parts of the focal plane image). We build a new polychromatic estimator which is the concatenation of the n estimators provided by the n reference beams. Using this new estimation of the electric field is the only change from the SCC correction loop described in Sect. 3.1.

For an efficient estimation of the speckle electric field, we ensure that the different components in the spatial frequency plane do not overlap. First, the distances between reference holes and the Lyot stop pupil obey Eq. (7). Then, the correlation peaks do not overlap. Finally, the position of each reference hole is chosen so that the secondary lateral correlation peaks do not overlap the primary correlation peaks.

5.2. Performance of the MRSCC

In this section, we simulate an MRSCC with three reference holes assuming monochromatic light $\lambda_0 = 640$ nm and two bandwidths ($\Delta\lambda = 40$ nm and $\Delta\lambda = 80$ nm) around $\lambda_0 = 640$ nm. The angle θ_H between the first reference and the horizontal axis in the Lyot stop plane is +115°. The angle between the first reference hole and the second one θ_{12} is −135° and there is an angle θ_{13} of +105° between the first reference hole and the third one. These angles correspond to the ones used in our laboratory experiment (see Sect. 7). Separations between the classical Lyot

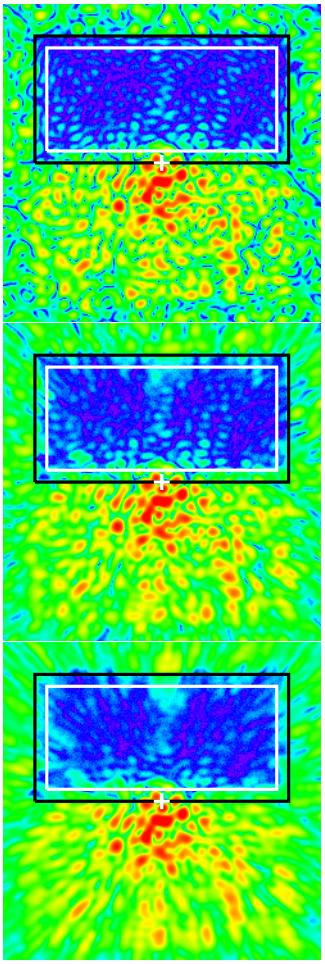

Fig. 11. Numerically simulated coronagraphic images obtained after correction with the MRSCC in monochromatic light (*top*; $\lambda_0 = 640$ nm) and in polychromatic light ($\Delta\lambda = 40$ nm (*middle*) and $\Delta\lambda = 80$ nm (*bottom*) around $\lambda_0 = 640$ nm).

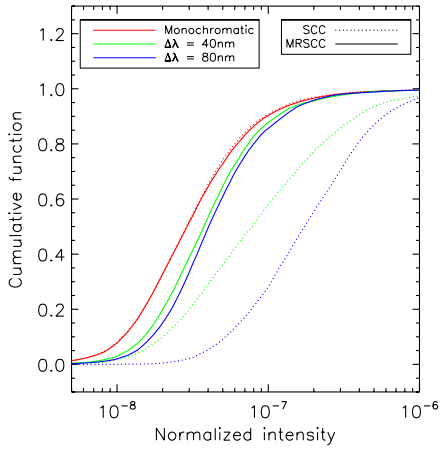

Fig. 12. Cumulative functions associated with the images obtained by numerical simulations with the SCC (dashed curve) and with the MRSCC (solid curves). In monochromatic light (red curves) the cumulatives functions of the both SCC and MRSCC are the same.

stop and reference holes are: $\xi_i = 1.8 D_L$. We assume $\gamma_i = 25$. Because we simulate a perfect coronagraph, we numerically add the reference beams and we set their flux to the one measured in our laboratory. The maximum normalized intensity level of $|A_{R_i}|^2$ is 4.8×10^{-8}. Finally, the other parameters are the same as previously (see Table 1).

Figure 11 presents the images after correction of the speckles using the MRSCC as a focal plane wavefront sensor. At the top, the image was obtained after correction in monochromatic light. If we compare this image and the image obtained in monochromatic light with the SCC (Fig. 3), we can see that they are almost the same. Indeed, in monochromatic light, fringes do not get blurred and adding reference holes bring no new information on A_S.

The middle and bottom images were obtained after correction in polychromatic light: $\Delta\lambda = 40$ nm and $\Delta\lambda = 80$ nm around $\lambda_0 = 640$ nm. They show that, when increasing the bandwidth, speckles in the DH of the MRSCC images are well corrected for bandwidth up to 80 nm.

Figure 12 presents the cumulative functions associated with these three images (solid lines) and to the images obtained with the SCC of Figs. 3 and 7 (dotted lines). In monochromatic light, the performances are almost the same using one or three reference holes. The slight difference can be explained by the fact that photon noise is greater for the MRSCC (three reference beams) than for the SCC (one reference beam). In polychromatic light, MRSCC always provides images with deeper contrast levels because speckles that were not well estimated with the unique reference hole of the SCC are estimated using the second or the third reference hole of the MRSCC. The median of the speckle intensity inside the DH is 3.8×10^{-8} for $\Delta\lambda = 40$ nm and 4.1×10^{-8} for $\Delta\lambda = 80$ nm. We find a gain of ~2 for $\Delta\lambda = 40$ nm and ~4 for $\Delta\lambda = 80$ nm in contrast to the SCC performance (see Sect. 3.4). Thus, the MRSCC significantly mitigates the chromatic effects of the SCC and its performance is almost insensitive to the bandwidth up to $\Delta\lambda = 80$ nm. The small difference is the result of a few bright speckles located close to the border of the DH.

Unlike the OPD method (Sect. 4), the MRSCC performance does not depend on the initial map of phase and amplitude aberrations. It also reaches deeper contrast levels in numerical simulations. Of course MRSCC is not insensitive to chromatism. Its performance decreases gradually when the bandwidth is widened. However, from preliminary numerical simulations that are not presented in this paper, it can be used to control contrast levels in the DH by working with bandwidths up to 150 nm in visible light. For larger bandwidths, we may add a fourth reference hole, bearing in mind the constraints presented in Sect. 5.1. Another solution could be a combination of the OPD method although it may be complicated to achromatically control the OPD. In the following sections we probe the MRSCC performance in the laboratory.

6. The THD bench and expected performance

In this section we present our laboratory optical bench called the THD-bench. We use it to derive the expected performance of the MRSCC from numerical simulations.

6.1. The THD bench

The SCC and MRSCC are tested in our laboratory at the Observatoire de Paris. A complete description of the optical bench is given in Mas et al. (2010). Here, we only list main components:

- Two light sources. A quasi-monochromatic laser diode emitting at $\lambda_0 = 637$ nm ($\Delta\lambda < 1$ nm) and a supercontinuum Fianium source (SC450) with a calibrated spectral filter ($\lambda_0 = 640$ nm $\Delta\lambda = 80$ nm).
- A tip-tilt mirror. Control of pointing errors down to $6.5 \times 10^{-2} \lambda_0/D$ (Mas et al. 2012).
- A Boston Micromachines Corporation DM of 32 by 32 actuators in a square array. This is set in a pupil plane that is upstream of the coronagraph focal mask and we use only 27 actuators across the pupil diameter.
- a dual-zone phase mask (DZPM) coronagraph composed of an apodizer in pupil plane and a phase mask in focal plane (Soummer et al. 2003; N'Diaye et al. 2012) that are optimized to reach 1σ contrast under 2.8×10^{-8} for an angular separation greater than 5 λ_0/D and for a bandwidth of 133 nm around 665 nm.
- A Lyot stop (Fig. 10, top) with a classical Lyot stop aperture with a $D_L = 8$ mm diameter for a $\varnothing_p = 8.1$ mm entrance pupil (98.7% filtering) and three reference holes (see Fig. 10 top: $\theta_H = +115°$, $\theta_{12} = -146°$, $\theta_{13} = +103°$, $\gamma_1 = \gamma_2 = \gamma_3 = 26.6$, $\xi_1 = 1.76 D_L$, $\xi_2 = 1.89 D_L$ and $\xi_3 = 1.93 D_L$).
- An Andor camera with a readout noise of 3.2 e^- rms per pixel and a full well capacity of 60 000 e^- per pixel. We used 400 by 400 pixel images and the resolution element λ_0/D_L is sampled by 6.25 pixels.

The only component modified to switch from the SCC to the MRSCC is the Lyot stop. By not disturbing the optical path thanks to a motorised mount, we can open or close the reference holes. We note that we did not use the motor to produce a temporal modulation as Give'on et al. (2012). As with the SCC, the MRSCC uses spatial modulation and it only needs a single image to retrieve the complex amplitude of the speckle field.

With 27 actuators across the pupil diameter, we can control a 13.5 by 27 λ_0/D DH area with the use of only one DM to correct the effects of both phase and amplitude aberrations (Fig. 13). Even in an ideal case (without aberrations), the DZPM coronagraph does not perfectly cancel the star. In Fig. 14, the red curve represents the theorerical limit of the DZPM coronagraph in monochromatic light ($\lambda_0 = 640$ nm) and the blue dashed curve shows a bandwidth of $\Delta\lambda = 133$ nm around $\lambda_0 = 665$ nm. Because of the design specifications, most of the speckles below 5 λ_0/D are very bright and some saturate the detector. To prevent the SCC estimation being biased, we numerically reduce the speckles' impact by multiplying the SCC images by a Butterworth-type spatial filter, shaped like a disk centered on the optical axis. This numerical mask multiplies the half-DH Butterworth mask and the resulting mask attenuates the central speckles by a factor of 3 and those located at 5 λ_0/D by a factor 1.5. The computation area is represented by a solid red line. To obtain this area, we remove a band of $1.5\lambda_0/D$ on each side of the DH. To avoid the bright speckles, which result from the DZPM, we remove a disk centered on the optical axis of $<10\lambda_0/D$ diameter and because of bright speckles at the top of the DH (Sect. 7) we also remove a disk centered at 22 λ_0/D from the optical axis and with a radius of $12.5\lambda_0/D$.

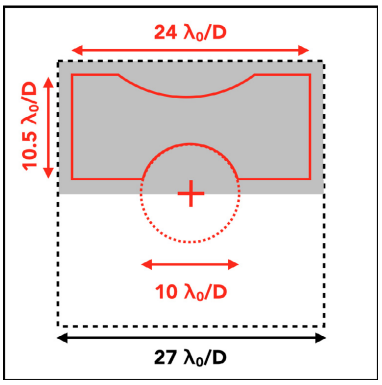

Fig. 13. Main dimensions used in our laboratory experiment. The influence area of the DM is delineated by a dashed line, the DH is represented by a gray area and the computation area is delineated by a red solid line. The optical axis is represented by the red cross.

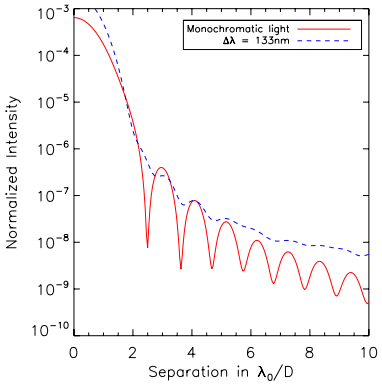

Fig. 14. Radial intensity profiles computed from coronagraphic images obtained by numerical simulations without phase and amplitude aberrations. The red solid curve is the profile associated with an image obtained in monochromatic light while, the blue dashed lines are obtained in polychromatic light ($\Delta\lambda = 133$ nm around $\lambda_0 = 665$ nm).

6.2. Numerical simulations of the THD bench

In this section, we run numerical simulations of the MRSCC in polychromatic light ($\lambda_0 = 640$ nm $- \Delta\lambda = 80$ nm) using the parameters that best reproduce the optical configuration of the THD bench (see Sect. 6.1). Amplitude aberrations are derived from a laboratory measurement (Mazoyer et al. 2013a). Phase aberrations have a standard deviation of 10 nm and a power spectral density of $f^{-2.3}$, which best reproduce the speckles' intensity distribution in non-corrected images. We numerically simulate the electric field produced by the DZPM coronagraph inside the classical Lyot stop, as well as inside each reference hole. We find that the flux inside the reference beams are similar to the flux

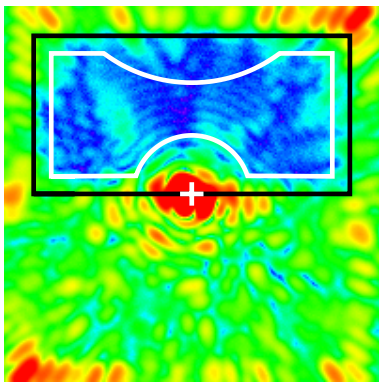

Fig. 15. Numerical simulated image obtained after correction using a MRSCC in polychromatic light $\Delta\lambda = 80$ nm and assuming the optical configuration of the THD bench. Field of view: 32 by 32 λ_0/D.

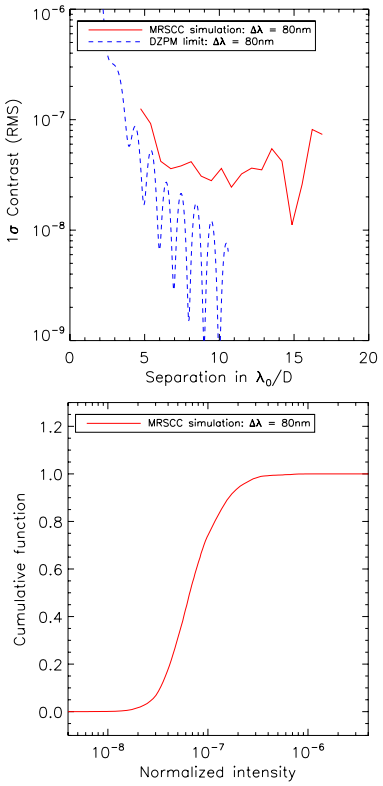

Fig. 16. Contrast curve (*top*) and spatial cumulative function (*bottom*) associated with the MRSCC image obtained by numerical simulations assuming the optical configuration of the bench. The blue dashed curve is the theorerical limit of the DZPM coronagraph for a bandwidth of $\Delta\lambda = 80$ nm around $\lambda_0 = 640$ nm.

measured on the THD bench. Finally we use the measured spectrum of the 80 nm source (close to a flat spectrum) that was used during the experiments (Sect. 7).

Figure 15 presents a coronagraphic image obtained by using the MRSCC with $\Delta\lambda = 80$ nm. The correction is efficient almost everywhere in the DH. Figure 16 presents the associated contrast curve (top) and the cumulative function (bottom). Below $5\lambda_0/D$ contrast is limited by DZPM coronagraph performance (blue dashed curve). In these numerical simulations, the MRSCC reaches a 1σ contrast level of 3.6×10^{-8} between $5\lambda_0/D$ and $17\lambda_0/D$ and a median of the speckle intensity of 6.5×10^{-8}. Thus, we expect the MRSCC to significantly reduce the speckle intensity inside the DH in polychromatic light in our laboratory.

7. Laboratory performances

7.1. Chromatism of the bench

Before testing the SCC and the MRSCC in polychromatic light, we estimate the chromatism of the optical bench. To obtain this information we use the SCC in monochromatic light (laser source – $\lambda_0 = 637\,\text{nm} - \Delta\lambda < 1$ nm) to reach the deepest contrast that our bench can provide inside the DH. After the correction in closed loop, we record the image, which is presented in Fig. 17 (top). Then, we keep the DM shape frozen and we switch the light source from the monochromatic light to the polychromatic light ($\lambda_0 = 640$ nm $- \Delta\lambda = 80$ nm). The resulting image is presented in Fig. 17 (bottom). The only difference between the two images is the bandwidth used to record the two images. The two images are very similar and we study their contrast curves and cumulative functions as given in Fig. 18.

The contrast curves (top) are not plotted below 5 λ_0/D because the computation area excludes the central saturated spot (Fig. 13). The average 1σ contrast level measured between 5 and 17 λ_0/D is 2.1×10^{-8} for the image recorded in monochromatic light and 2.7×10^{-8} for the image recorded in polychromatic light. If we only consider the contrast curves, we conclude that there is no significant chromatic evolution of the aberrations on the THD bench below a contrast of 2.7×10^{-8}.

The cumulative functions are plotted at the bottom. The median intensity of the speckles is 2.7×10^{-8} for the image recorded in monochromatic light and 6.3×10^{-8} for the image recorded in polychromatic light. The difference between the two cumulative curves is larger than that between the contrast curves. It means that uniform offset in intensity exists in the polychromatic image. This may be due to chromatism effects of the DZPM, or the outband of the spectral filter or chromatism of the THD optics. We conclude that the THD bench (optical components and coronagraph) is achromatic at a 6.3×10^{-8} level in normalized intensity and at a 2.7×10^{-8} level contrast. These levels give an idea of the deepest contrast that we can achieve in polychromatic light ($\Delta\lambda = 80$ nm around $\lambda_0 = 640$ nm) on the THD bench, whichever technique is used to control the DM.

7.2. SCC vs. MRSCC in polychromatic light

In this section we compare the SCC and MRSCC performance in the laboratory using a bandwidth of 80 nm around $\lambda_0 = 640$ nm. First, we create a DH using the SCC in polychromatic light starting from a given voltage map for the DM (i.e., a given surface shape) and we record the best correction of the speckle field (Fig. 19, top). Then, starting from the same given initial DM shape, we use the MRSCC and we obtain the DH of Fig. 19 (bottom). As expected, in the SCC image, a lot of speckles are

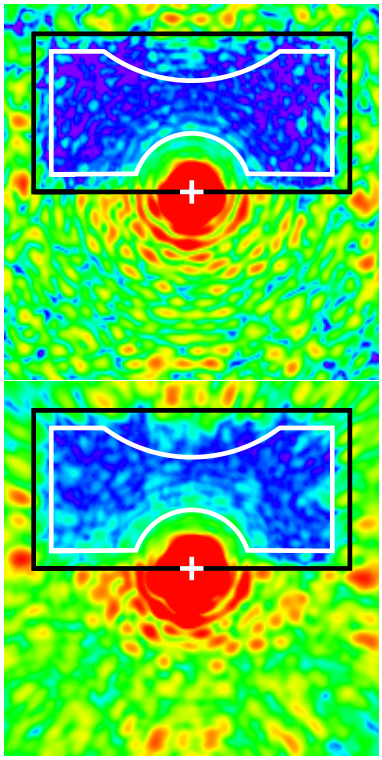

Fig. 17. Laboratory images obtained after SCC correction of the speckles in monochromatic light, (*top*) recorded in monochromatic light (λ_0 = 640 nm) and (*bottom*) recorded in polychromatic light ($\Delta\lambda$ = 80 nm at λ_0 = 640 nm).

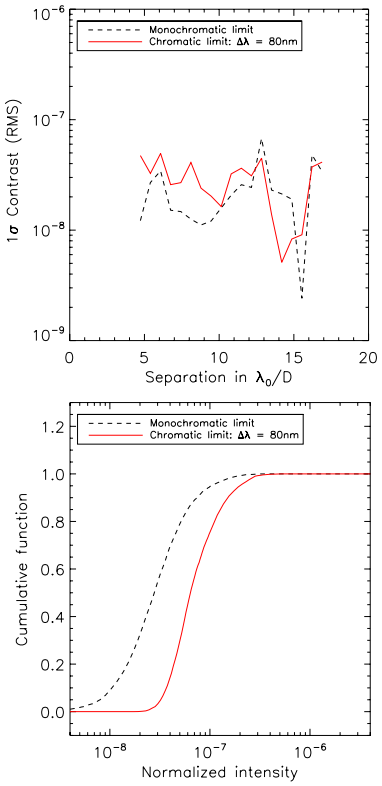

Fig. 18. Contrast curve (*top*) and spatial cumulative function (*bottom*) associated with the laboratory images recorded in monochromatic light (black dashed curve) and in polychromatic light (red solid curve)

not corrected, whereas the correction is almost uniform with the MRSCC. Figure 20 presents the contrast (top) and cumulative (bottom) curves computed from these images. The orange dotted curves are associated with the laboratory image obtained with the SCC (Fig. 19, top) and the blue dashed curves to the laboratory image obtained with the MRSCC (Fig. 19, bottom). We overplot the curves associated with the chromatic limit of the bench (red solid curves, Sect. 7.1) and associated with the numerical simulations of the bench (mixed green curves, Sect. 6.2).

All these laboratory results demonstrate the gain in contrast brought by the MRSCC compared to the SCC. For SCC, the average 1σ contrast is never better than 10^{-7} and the median intensity is 2.7×10^{-7}. In the MRSCC images we measure an average 1σ contrast of 4.5×10^{-8} between 5 and 17 λ_0/D and a median intensity of 8.3×10^{-8}. These performances are close to the numerical simulations prediction: 3.6×10^{-8} and 6.5×10^{-8} respectively.

If we compare the images obtained with the MRSCC (Fig. 19, bottom) and the image that is limited by the chromatism of the bench (Fig. 17, bottom), the levels are equivalent, except at the top of the DH, where some speckles are not well corrected because all the fringe patterns of the MRSCC are blurred. These types of bright uncorrected speckles also exist in the numerical simulated image (top right corner of the DH in Fig. 15). From numerical simulations we find that the location of these speckles depends on the initial phase and amplitude aberrations. It may be possible to correct them by adding a fourth reference hole or by optimizing the orientations of the reference holes. However, none of these solutions were available during our laboratory experiments.

8. Conclusions

In this paper, we proposed two methods to make the SCC more achromatic: the MRSCC and the OPD method. We tested these two methods by numerical simulations and proved that they improve the performance of the SCC in polychromatic light. We found that the OPD method performance depends on the initial aberration map and that it is not robust enough to be used.

Then, we demonstrated in the laboratory that the MRSCC can be used to control a DM in polychromatic light (bandwidth of 80 nm around 640 nm – 12.5%) to reach an average 1σ contrast of approximately 4.5×10^{-8} between 5 and 17 λ_0/D from the star and a median contrast of 8.3×10^{-8}. The performances obtained on the THD bench with the DZPM coronagraph are close to the chromatic limitation of our bench, meaning that the MRSCC may be able to control the speckle intensity at even deeper contrast levels.

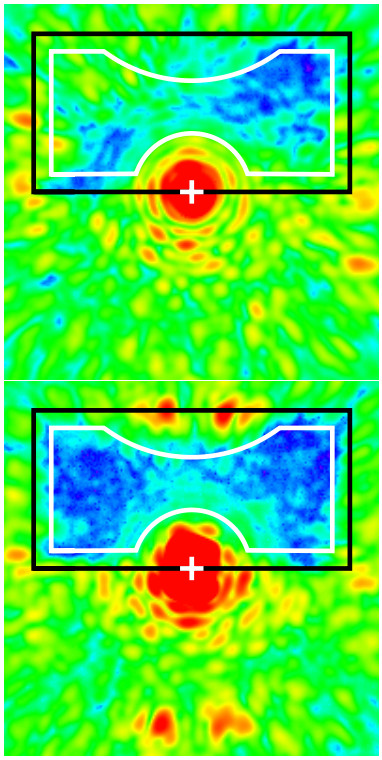

Fig. 19. Laboratory image obtained on the THD bench after speckle correction in polychromatic light ($\Delta\lambda$ = 80 nm at λ_0 = 640 nm) using a SCC (*top*) and the MRSCC (*bottom*).

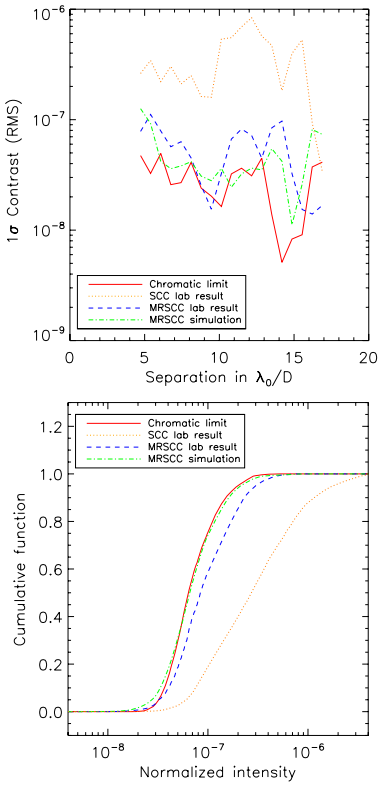

Fig. 20. Contrast curves (*top*) and spatial cumulative functions (*bottom*) for $\Delta\lambda$ = 80 nm, associated with the expected performance from numerical simulations (mixed green line) and to three laboratory images: chromatic limit of the THD bench (red solid line), SCC correction (orange dotted curves) and MRSCC correction (blue dashed curves).The cumulative curves have been computed inside the computation area presented Fig. 13.

The MRSCC has all the advantages of the SCC. It is a focal plane wavefront sensor, which is able to work in closed loop. It is easy to implement by adding only small holes in the Lyot stop plane and it can be associated with several phase-mask coronagraphs. Also, only one focal plane image is mandatory for estimating the electric field instead of the several images that are needed by techniques that are based on temporal modulation.

This study was realized using a clear circular aperture. In the case of an arbitrary telescope aperture, the sensing with the MRSCC can still be undertaken as long as the coronagraph diffracts enough stellar light into the reference hole.

The attractive features of the MRSCC make this FPWFS a serious candidate for a possible upgrade of the current high-contrast imaging instruments and could be used with future instruments for space-based missions and extremely large telescopes.

Finally, several improvements may be possible in the future. Among them, we will explore more sophisticated algorithms to measure the electric field from the MRSCC image. We also indend to correct speckles close to the optical axis by using another phase-mask coronagraph like a vortex (Mawet et al. 2005). Finally, Mazoyer et al. (2013a) demonstrate that the contrast level of the THD bench is determined mainly by amplitude aberrations. To improve its performance and increase the size of the DH, we will control both the phase and amplitude aberrations in the full influence area with an upgraded version of our bench by adding DMs.

Acknowledgements. We wish to thank M. N'Diaye, A. Caillat and K. Dohlen for their collaboration on the design of the DZPM used to obtain laboratory results and for sharing the code used to numerically simulate it. This work was carried out at the Observatoire de Paris (France) under contract number DA-10091195 with the CNES (Toulouse, France). We also thank the referee for his very constructive remarks on the manuscript of the paper.

References

Baudoz, P., Boccaletti, A., Baudrand, J., & Rouan, D. 2006, in IAU Colloq. 200: Direct Imaging of Exoplanets: Science Techniques, eds. C. Aime, & F. Vakili, 553

Baudoz, P., Mazoyer, J., & Galicher, R. 2013, in Proc. Third AO4ELT Conf., eds. S. Esposito, & L. Fini, 109

Beuzit, J.-L., Feldt, M., Dohlen, K., et al. 2008, in SPIE Conf. Ser., 7014, 18

Bordé, P. J., & Traub, W. A. 2006, ApJ, 638, 488

Boyer, C., Michau, V., & Rousset, G. 1990, in Amplitude and Intensity Spatial Interferometry, ed. J. B. Breckinridge, SPIE Conf. Ser., 1237, 406

Cavarroc, C., Boccaletti, A., Baudoz, P., Fusco, T., & Rouan, D. 2006, A&A, 447, 397

Dalcanton, J., Seager, S., Aigrain, S., et al. 2015, ArXiv e-prints [arXiv:1507.04779]
Galicher, R., Baudoz, P., & Rousset, G. 2008a, in SPIE Conf. Ser., 7015, 6
Galicher, R., Baudoz, P., & Rousset, G. 2008b, A&A, 488, L9
Galicher, R., Baudoz, P., Rousset, G., Totems, J., & Mas, M. 2010, A&A, 509, A31
Give'on, A., Kasdin, N. J., Vanderbei, R. J., & Avitzour, Y. 2006, J. Opt. Soc. Am. A, 23, 1063
Give'on, A., Kern, B., Shaklan, S., Moody, D. C., & Pueyo, L. 2007, in Am. Astron. Soc. Meet. Abst., BAAS, 39, 135.20
Give'on, A., Shaklan, S., Kern, B., et al. 2012, in SPIE Conf. Ser., 8442
Hartung, M., Blanc, A., Fusco, T., et al. 2003, A&A, 399, 385
Hinkley, S., Oppenheimer, B. R., Zimmerman, N., et al. 2011, PASP, 123, 746
Jovanovic, N., Guyon, O., Martinache, F., et al. 2014, in SPIE Conf. Ser., 9147, 1
Lagrange, A.-M., Kasper, M., Boccaletti, A., et al. 2009, A&A, 506, 927
Macintosh, B. A., Graham, J. R., Palmer, D. W., et al. 2008, in SPIE Conf. Ser., 7015, 18
Malbet, F., Yu, J. W., & Shao, M. 1995, PASP, 107, 386
Marois, C., Racine, R., Doyon, R., Lafrenière, D., & Nadeau, D. 2004, ApJ, 615, L61
Marois, C., Lafrenière, D., Doyon, R., Macintosh, B., & Nadeau, D. 2006, ApJ, 641, 556
Marois, C., Macintosh, B., Barman, T., et al. 2008, Science, 322, 1348
Marois, C., Zuckerman, B., Konopacky, Q. M., Macintosh, B., & Barman, T. 2010, Nature, 468, 1080
Martinache, F. 2013, PASP, 125, 422
Mas, M., Baudoz, P., Rousset, G., Galicher, R., & Baudrand, J. 2010, in SPIE Conf. Ser., 7735, 66
Mas, M., Baudoz, P., Mazoyer, J., Galicher, R., & Rousset, G. 2012, in SPIE Conf. Ser., 8446
Mawet, D., Riaud, P., Absil, O., & Surdej, J. 2005, ApJ, 633, 1191
Mazoyer, J. 2014, Ph.D. Thesis, University Paris 7 – Denis Diderot
Mazoyer, J., Baudoz, P., Galicher, R., Mas, M., & Rousset, G. 2013a, A&A, 557, A9
Mazoyer, J., Baudoz, P., Galicher, R., & Rousset, G. 2013b, in Proc. Third AO4ELT Conference, eds. S. Esposito, & L. Fini
Mazoyer, J., Baudoz, P., Galicher, R., & Rousset, G. 2014, A&A, 564, L1
Murakami, N., Uemura, R., Baba, N., et al. 2008, PASP, 120, 1112
N'Diaye, M., Dohlen, K., Cuevas, S., et al. 2012, A&A, 538, A55
N'Diaye, M., Pueyo, L., Soummer, R., & Carlotti, A. 2014, in SPIE Conf. Ser., 9143, 4
Paul, B., Sauvage, J.-F., & Mugnier, L. M. 2013, A&A, 552, A48
Pueyo, L., & Norman, C. 2013, ApJ, 769, 102
Rouan, D., Riaud, P., Boccaletti, A., Clénet, Y., & Labeyrie, A. 2000, PASP, 112, 1479
Sauvage, J.-F., Fusco, T., Petit, C., et al. 2012, in SPIE Conf. Ser., 8447, 15
Seager, S., & Deming, D. 2010, ARA&A, 48, 631
Soummer, R., Dohlen, K., & Aime, C. 2003, A&A, 403, 369
Spergel, D., Gehrels, N., Baltay, C., et al. 2015, ArXiv e-prints [arXiv:1503.03757]
Wynne, C. G. 1979, Opt. Comm., 28, 21

Table des figures

Liste des tableaux

Bibliographie

Alonso, Roi. 2018. *Characterization of Exoplanets : Secondary Eclipses*. Springer International Publishing AG. Page 40.

Alonso-Floriano, F. J., Sánchez-López, A., Snellen, I. A. G., López-Puertas, M., Nagel, E., Amado, P. J., Bauer, F. F., Caballero, J. A., Czesla, S., & Nortmann, L. 2019. Multiple water band detections in the CARMENES near-infrared transmission spectrum of HD 189733 b. *Astronomy & Astrophysics*, **621**(Jan), A74.

Amara, A., & Quanz, S. P. 2012. PYNPOINT : an image processing package for finding exoplanets. *Monthly Notices of the Royal Astronomical Society*, **427**(Dec.), 948–955.

Baba, N., & Murakami, N. 2003. A Method to Image Extrasolar Planets with Polarized Light. *Publications of the Astronomical Society of the Pacific*, **115**(Dec.), 1363–1366.

Baudoz, P., Boccaletti, A., Baudrand, J., & Rouan, D. 2006. The Self-Coherent Camera : a new tool for planet detection. *Pages 553–558 of :* Aime, C., & Vakili, F. (eds), *IAU Colloq. 200 : Direct Imaging of Exoplanets : Science Techniques*.

Baudoz, P., Mazoyer, J., Mas, M., Galicher, R., & Rousset, G. 2012 (Sept.). Dark hole and planet detection : laboratory results using the self-coherent camera. *In : Society of Photo-Optical Instrumentation Engineers (SPIE) Conference Series*. Society of Photo-Optical Instrumentation Engineers (SPIE) Conference Series, vol. 8446.

Baudoz, P., Galicher, R., Potier, A., Dupuis, O., Thijs, S., & Patru, F. 2018a (July). Optimization and performance of multi-deformable mirror correction on the THD2 bench. *Page 107062O of : Advances in Optical and Mechanical Technologies for Telescopes and Instrumentation III*. Society of Photo-Optical Instrumentation Engineers (SPIE) Conference Series, vol. 10706.

Baudoz, P., Galicher, R., Patru, F., Dupuis, O., & Thijs, S. 2018b. Status and performance of the THD2 bench in multi-deformable mirror configuration. *arXiv e-prints*, Jan.

Beaulieu, M., Abe, L., Martinez, P., Baudoz, P., Gouvret, C., & Vakili, F. 2017. High-contrast imaging at small separations : impact of the optical configuration of two deformable mirrors on dark holes. *Monthly Notices of the Royal Astronomical Society*, **469**(1), 218–230.

Bennett, David P. 2008. *Detection of Extrasolar Planets by Gravitational Microlensing*. Springer Praxis Books. Page 47.

Beuzit, J.-L., Mouillet, D., Lagrange, A.-M., & Paufique, J. 1997. A stellar coronograph for the COME-ON-PLUS adaptive optics system. *Astronomy & Astrophysics Supplement series*, **125**(Oct.).

Beuzit, J. L., Vigan, A., Mouillet, D., Dohlen, K., Gratton, R., Boccaletti, A., Sauvage, J. F., Schmid, H. M., Langlois, M., Petit, C., Baruffolo, A., Feldt, M., Milli, J., Wahhaj, Z., Abe, L., Anselmi, U., Antichi, J., Barette, R., Baudrand, J., Baudoz, P., Bazzon, A., Bernardi, P., Blanchard, P., Brast, R., Bruno, P., Buey, T., Carbillet, M., Carle, M., Cascone, E., Chapron, F., Charton, J., Chauvin, G., Claudi, R., Costille, A., De Caprio, V., de Boer, J., Delboulbé, A., Desidera, S., Dominik, C., Downing, M., Dupuis, O., Fabron, C., Fantinel, D., Farisato, G., Feautrier, P., Fedrigo, E., Fusco, T., Gigan, P., Ginski, C., Girard, J., Giro, E., Gisler, D., Gluck, L., Gry, C., Henning, T., Hubin, N., Hugot, E., Incorvaia, S., Jaquet, M., Kasper, M., Lagadec, E., Lagrange, A. M., Le Coroller, H., Le Mignant, D., Le Ruyet, B., Lessio, G., Lizon, J. L., Llored, M., Lundin, L., Madec, F., Magnard, Y., Marteaud, M., Martinez, P., Maurel, D., Ménard, F., Mesa, D., Möller-Nilsson, O., Moulin, T., Moutou, C., Origné, A., Parisot, J., Pavlov, A., Perret, D., Pragt, J., Puget, P., Rabou, P., Ramos, J., Reess, J. M., Rigal, F., Rochat, S., Roelfsema, R., Rousset, G., Roux, A., Saisse, M., Salasnich, B., Santambrogio, E., Scuderi, S., Segransan, D., Sevin, A., Siebenmorgen, R., Soenke, C., Stadler, E., Suarez, M., Tiphène, D., Turatto, M., Udry, S., Vakili, F., Waters, L. B. F. M., Weber, L., Wildi, F., Zins, G., & Zurlo, A. 2019. SPHERE : the exoplanet imager for the Very Large Telescope. *Astronomy & Astrophysics paper*, **631**(Nov), A155.

Bhowmik, T., Boccaletti, A., Thébault, P., Kral, Q., Mazoyer, J., Milli, J., Maire, A. L., van Holstein, R. G., Augereau, J. C., Baudoz, P., Feldt, M., Galicher, R., Henning, T., Lagrange, A. M., Olofsson, J., Pantin, E., & Perrot, C. 2019. Spatially resolved spectroscopy of the debris disk HD 32297. Further evidence of small dust grains. *Astronomy & Astrophysics*, **630**(Oct.), A85.

Boccaletti, A., Chauvin, G., Mouillet, D., Absil, O., Allard, F., Antoniucci, S., Augereau, J. C., Barge, P., Baruffolo, A., Baudino, J. L., Baudoz, P., Beaulieu, M., Benisty, M., Beuzit, J. L., Bianco, A., Biller, B., Bonavita, B., Bonnefoy, M., Bos, S., Bouret, J. C., Brandner, W., Buchschache, N., Carry, B., Cantalloube, F., Cascone, E., Carlotti, A., Charnay, B., Chiavassa, A., Choquet, E., Clenet, Y., Crida, A., De Boer, J., De Caprio, V., Desidera, S., Desert, J. M., Delisle, J. B., Delorme, P., Dohlen, K., Doelman, D., Dominik, C., Orazi, V. D, Dougados, C., Doute, S., Fedele, D., Feldt, M., Ferreira, F., Fontanive, C., Fusco, T., Galicher, R., Garufi, A., Gendron, E., Ghedina, A., Ginski, C., Gonzalez, J. F., Gratadour, D., Gratton, R., Guillot, T., Haffert, S., Hagelberg, J., Henning, T., Huby, E., Janson, M., Kamp, I., Keller, C., Kenworthy, M., Kervella, P., Kral, Q., Kuhn, J., Lagadec, E., Laibe, G., Langlois, M., Lagrange, A. M., Launhardt, R., Leboulleux, L., Le Coroller, H., Li Causi, G., Loupias, M., Maire, A. L., Marleau, G., Martinache, F., Martinez, P., Mary, D., Mattioli, M., Mazoyer, J., Meheut, H., Menard, F., Mesa, D., Meunier, N., Miguel, Y., Milli, J., Min, M., Molliere, P., Mordasini, C., Moretto, G., Mugnier, L., Muro Arena, G., Nardetto, N., Diaye, M. N, Nesvadba, N., Pedichini, F., Pinilla, P., Por, E., Potier, A., Quanz, S., Rameau, J., Roelfsema, R., Rouan, D., Rigliaco, E., Salasnich, B., Samland, M., Sauvage, J. F., Schmid, H. M., Segransan, D., Snellen, I., Snik, F., Soulez, F., Stadler, E., Stam, D., Tallon, M., Thebault, P., Thiebaut, E., Tschudi, C., Udry, S., van Holstein, R., Vernazza, P., Vidal, F., Vigan, A., Waters, R., Wildi, F., Willson, M., Zanutta, A., Zavagno, A., & Zurlo, A. 2020a. SPHERE+ : Imaging young Jupiters down to the snowline. *arXiv e-prints*, Mar., arXiv :2003.05714.

Boccaletti, A., Chauvin, G., Mouillet, D., Absil, O., Allard, F., Antoniucci, S., Augereau, J. C., Barge, P., Baruffolo, A., Baudino, J. L., Baudoz, P., Beaulieu, M., Benisty, M., Beuzit, J. L., Bianco, A., Biller, B., Bonavita, B., Bonnefoy, M., Bos, S., Bouret, J. C., Brandner, W., Buchschache, N., Carry, B., Cantalloube, F., Cascone, E., Carlotti, A., Charnay, B., Chiavassa, A.,

Choquet, E., Clenet, Y., Crida, A., De Boer, J., De Caprio, V., Desidera, S., Desert, J. M., Delisle, J. B., Delorme, P., Dohlen, K., Doelman, D., Dominik, C., Orazi, V. D, Dougados, C., Doute, S., Fedele, D., Feldt, M., Ferreira, F., Fontanive, C., Fusco, T., Galicher, R., Garufi, A., Gendron, E., Ghedina, A., Ginski, C., Gonzalez, J. F., Gratadour, D., Gratton, R., Guillot, T., Haffert, S., Hagelberg, J., Henning, T., Huby, E., Janson, M., Kamp, I., Keller, C., Kenworthy, M., Kervella, P., Kral, Q., Kuhn, J., Lagadec, E., Laibe, G., Langlois, M., Lagrange, A. M., Launhardt, R., Leboulleux, L., Le Coroller, H., Li Causi, G., Loupias, M., Maire, A. L., Marleau, G., Martinache, F., Martinez, P., Mary, D., Mattioli, M., Mazoyer, J., Meheut, H., Menard, F., Mesa, D., Meunier, N., Miguel, Y., Milli, J., Min, M., Molliere, P., Mordasini, C., Moretto, G., Mugnier, L., Muro Arena, G., Nardetto, N., Diaye, M. N, Nesvadba, N., Pedichini, F., Pinilla, P., Por, E., Potier, A., Quanz, S., Rameau, J., Roelfsema, R., Rouan, D., Rigliaco, E., Salasnich, B., Samland, M., Sauvage, J. F., Schmid, H. M., Segransan, D., Snellen, I., Snik, F., Soulez, F., Stadler, E., Stam, D., Tallon, M., Thebault, P., Thiebaut, E., Tschudi, C., Udry, S., van Holstein, R., Vernazza, P., Vidal, F., Vigan, A., Waters, R., Wildi, F., Willson, M., Zanutta, A., Zavagno, A., & Zurlo, A. 2020b. SPHERE+ : Imaging young Jupiters down to the snowline. *arXiv e-prints*, Mar., arXiv :2003.05714.

Bonafous, M., Galicher, R., Baudoz, P., Firminy, J., & Boussaha, F. 2016 (Jul). Development and characterization of Four-Quadrant Phase Mask coronagraph (FQPM). *Page 99126J of : Proceedings of the SPIE*. Society of Photo-Optical Instrumentation Engineers (SPIE) Conference Series, vol. 9912.

Bordé, P. J., & Traub, W. A. 2006. High-Contrast Imaging from Space : Speckle Nulling in a Low-Aberration Regime. *Astrophysical Journal*, **638**(Feb.), 488–498.

Boss, A. P. 2006a. Gas Giant Protoplanets Formed by Disk Instability in Binary Star Systems. *The Astrophysical Journal*, **641**(Apr.), 1148–1161.

Boss, A. P. 2006b. On the Formation of Gas Giant Planets on Wide Orbits. *The Astrophysical Journal*, **637**(Feb.), L137–L140.

Boss, A. P. 2006c. Rapid Formation of Gas Giant Planets around M Dwarf Stars. *The Astrophysical Journal*, **643**(May), 501–508.

Bottom, M., Shelton, J. C., Wallace, J. K., Bartos, R., Kuhn, J., Mawet, D., Mennesson, B., Burruss, R., & Serabyn, E. 2016. Stellar Double Coronagraph : A Multistage Coronagraphic Platform at Palomar Observatory. *Publication of the Astronomical Society of Pacific*, **128**(7), 075003.

Bryden, Geoffrey, Traub, Wesley, Roberts, Lewis C., Jr., Bruno, Robin, Unwin, Stephen, Backovsky, Stan, Brugarolas, Paul, Chakrabarti, Supriya, Chen, Pin, Hillenbrand, Lynne, Krist, John, Lillie, Charles, Macintosh, Bruce, Mawet, Dimitri, Mennesson, Bertrand, Moody, Dwight, Rahman, Zahidul, Rey, Justin, Stapelfeldt, Karl, Stuchlik, David, Trauger, John, & Vaischt, Gautam. 2011 (Oct.). Zodiac II : debris disk science from a balloon. *Page 81511E of : SPIE Conference Series*. Society of Photo-Optical Instrumentation Engineers (SPIE) Conference Series, vol. 8151.

Cady, Eric, Balasubramanian, Kunjithapatham, Gersh-Range, Jessica, Kasdin, Jeremy, Kern, Brian, Lam, Raymond, Mejia Prada, Camilo, Moody, Dwight, Patterson, Keith, Poberezhskiy, Ilya, Riggs, A. J. Eldorado, Seo, Byoung-Joon, Shi, Fang, Tang, Hong, Trauger, John, Zhou,

Hanying, & Zimmerman, Neil. 2017 (Sep). Shaped pupil coronagraphy for WFIRST : high-contrast broadband testbed demonstration. *Page 104000E of : Proceedings of the SPIE*. Society of Photo-Optical Instrumentation Engineers (SPIE) Conference Series, vol. 10400.

Cantalloube, F., Mouillet, D., Mugnier, L. M., Milli, J., Absil, O., Gomez Gonzalez, C. A., Chauvin, G., Beuzit, J.-L., & Cornia, A. 2015. Direct exoplanet detection and characterization using the ANDROMEDA method : Performance on VLT/NaCo data. *Astronomy & Astrophysics*, **582**(Oct.), A89.

Cavarroc, C., Boccaletti, A., Baudoz, P., Fusco, T., & Rouan, D. 2006. Fundamental limitations on Earth-like planet detection with extremely large telescopes. *Astronomy & Astrophysics*, **447**(Feb.), 397–403.

Charbonneau, David, Allen, Lori E., Megeath, S. Thomas, Torres, Guillermo, Alonso, Roi, Brown, Timothy M., Gilliland, Ronald L., Latham, David W., Mandushev, Georgi, O'Donovan, Francis T., & Sozzetti, Alessandro. 2005. Detection of Thermal Emission from an Extrasolar Planet. *The Astrophysical Journal*, **626**(1), 523–529.

Charnay, B., Bézard, B., Baudino, J. L., Bonnefoy, M., Boccaletti, A., & Galicher, R. 2018. A Self-consistent Cloud Model for Brown Dwarfs and Young Giant Exoplanets : Comparison with Photometric and Spectroscopic Observations. *The Astrophysical Journal*, **854**(2), 172.

Chauvin, G., Lagrange, A.-M., Bonavita, M., Zuckerman, B., Dumas, C., Bessell, M. S., Beuzit, J.-L., Bonnefoy, M., Desidera, S., Farihi, J., Lowrance, P., Mouillet, D., & Song, I. 2010. Deep imaging survey of young, nearby austral stars . VLT/NACO near-infrared Lyot-coronographic observations. *Astronomy & Astrophysics*, **509**(Jan.), A52.

Cheetham, A., Bonnefoy, M., Desidera, S., Langlois, M., Vigan, A., Schmidt, T., Olofsson, J., Chauvin, G., Klahr, H., Gratton, R., D'Orazi, V., Henning, T., Janson, M., Biller, B., Peretti, S., Hagelberg, J., Ségransan, D., Udry, S., Mesa, D., Sissa, E., Kral, Q., Schlieder, J., Maire, A.-L., Mordasini, C., Menard, F., Zurlo, A., Beuzit, J.-L., Feldt, M., Mouillet, D., Meyer, M., Lagrange, A.-M., Boccaletti, A., Keppler, M., Kopytova, T., Ligi, R., Rouan, D., Le Coroller, H., Dominik, C., Lagadec, E., Turatto, M., Abe, L., Antichi, J., Baruffolo, A., Baudoz, P., Blanchard, P., Buey, T., Carbillet, M., Carle, M., Cascone, E., Claudi, R., Costille, A., Delboulbé, A., De Caprio, V., Dohlen, K., Fantinel, D., Feautrier, P., Fusco, T., Giro, E., Gluck, L., Hubin, N., Hugot, E., Jaquet, M., Kasper, M., Llored, M., Madec, F., Magnard, Y., Martinez, P., Maurel, D., Le Mignant, D., Möller-Nilsson, O., Moulin, T., Origné, A., Pavlov, A., Perret, D., Petit, C., Pragt, J., Puget, P., Rabou, P., Ramos, J., Rigal, F., Rochat, S., Roelfsema, R., Rousset, G., Roux, A., Salasnich, B., Sauvage, J.-F., Sevin, A., Soenke, C., Stadler, E., Suarez, M., Weber, L., & Wildi, F. 2018. Discovery of a brown dwarf companion to the star HIP 64892. *Astronomy & Astrophysics*, **615**(Aug.), A160.

Chilcote, Jeffrey K., Bailey, Vanessa P., De Rosa, Rob, Macintosh, Bruce, Nielsen, Eric, Norton, Andrew, Millar-Blanchaer, Maxwell A., Graham, James, Marois, Christian, Pueyo, Laurent, Rameau, Julien, Savransky, Dmitry, & Veran, Jean-Pierre. 2018 (July). Upgrading the Gemini planet imager : GPI 2.0. *Page 1070244 of : SPIE Conference Series*. Society of Photo-Optical Instrumentation Engineers (SPIE) Conference Series, vol. 10702.

Chun, M., Toomey, D., Wahhaj, Z., Biller, B., Artigau, E., Hayward, T., Liu, M., Close, L., Hartung, M., Rigaut, F., & Ftaclas, C. 2008 (July). Performance of the near-infrared corona-

graphic imager on Gemini-South. *In : SPIE Conference Series.* SPIE Conference Series, vol. 7015.

Claudi, R. U., Turatto, M., Gratton, R. G., Antichi, J., Bonavita, M., Bruno, P., Cascone, E., De Caprio, V., Desidera, S., Giro, E., Mesa, D., Scuderi, S., Dohlen, K., Beuzit, J. L., & Puget, P. 2008 (July). SPHERE IFS : the spectro differential imager of the VLT for exoplanets search. *Page 70143E of : Ground-based and Airborne Instrumentation for Astronomy II.* SPIE proceedings, vol. 7014.

Close, Laird M., Males, Jared R., Morzinski, Katie M., Esposito, Simone, Riccardi, Armando, Briguglio, Runa, Follette, Kate B., Wu, Ya-Lin, Pinna, Enrico, Puglisi, Alfio, Xompero, Marco, Quiros, Fernando, & Hinz, Phil M. 2018 (Jul). Status of MagAO and review of astronomical science with visible light adaptive optics. *Page 107030L of : Proceedings of the SPIE.* Society of Photo-Optical Instrumentation Engineers (SPIE) Conference Series, vol. 10703.

Cook, Timothy, Cahoy, Kerri, Chakrabarti, Supriya, Douglas, Ewan, Finn, Susanna C., Kuchner, Marc, Lewis, Nikole, Marinan, Anne, Martel, Jason, Mawet, Dimitri, Mazin, Benjamin, Meeker, Seth R., Mendillo, Christopher, Serabyn, Gene, Stuchlik, David, & Swain, Mark. 2015. Planetary Imaging Concept Testbed Using a Recoverable Experiment-Coronagraph (PICTURE C). *Journal of Astronomical Telescopes, Instruments, and Systems*, **1**(Oct.), 044001.

Côté, Olivier, Allain, Guillaume, Brousseau, Denis, Lord, Marie-Pier, Ouahbi, Samy, Ouellet, Mireille, Patel, Deven, Thibault, Simon, Vallée, Cédric, Belikov, Ruslan, Bendek, Eduardo, Blain, Célia, Bradley, Collin, Daigle, Olivier, de Jong, Chris, Doelman, David, Doyon, René, Grand mont, Frédéric, Helmbrecht, Michael, Kenworthy, Matthew, Lafrenière, David, Marchis, Frank, Marois, Christian, Montminy, Steeve, Snik, Frans, Vasisht, Gautam, Véran, Jean-Pierre, & Vincent, Philippe. 2018 (July). A precursor mission to high contrast imaging balloon system. *Page 1070248 of : Society of Photo-Optical Instrumentation Engineers (SPIE) Conference Series.* Society of Photo-Optical Instrumentation Engineers (SPIE) Conference Series, vol. 10702.

de Boer, J., Salter, G., Benisty, M., Vigan, A., Boccaletti, A., Pinilla, P., Ginski, C., Juhasz, A., Maire, A.-L., Messina, S., Desidera, S., Cheetham, A., Girard, J. H., Wahhaj, Z., Langlois, M., Bonnefoy, M., Beuzit, J.-L., Buenzli, E., Chauvin, G., Dominik, C., Feldt, M., Gratton, R., Hagelberg, J., Isella, A., Janson, M., Keller, C. U., Lagrange, A.-M., Lannier, J., Menard, F., Mesa, D., Mouillet, D., Mugrauer, M., Peretti, S., Perrot, C., Sissa, E., Snik, F., Vogt, N., Zurlo, A., & SPHERE Consortium. 2016. Multiple rings in the transition disk and companion candidates around RX J1615.3-3255. High contrast imaging with VLT/SPHERE. *Astronomy & astrophysics*, **595**(Nov.), A114.

de Jonge, Chris, Baudoz, Pierre, Galicher, Raphaël., Huisman, Robert, Peletier, Reynier, & Jayawardhana, Bayu. 2018 (July). Effect of multiple deformable mirrors in broadband high-contrast coronagraphs. *Page 107035D of : Adaptive Optics Systems VI.* Society of Photo-Optical Instrumentation Engineers (SPIE) Conference Series, vol. 10703.

Delorme, J. R., Galicher, R., Baudoz, P., Rousset, G., Mazoyer, J., N'Diaye, M., Dohlen, K., & Caillat, A. 2014 (July). High-contrast imaging in wide spectral band with a self-coherent camera and achromatic coronagraphs. *Page 91515Q of : Advances in Optical and Mechanical Technologies for Telescopes and Instrumentation.* Society of Photo-Optical Instrumentation Engineers (SPIE) Conference Series, vol. 9151.

Delorme, J. R., Galicher, R., Baudoz, P., Rousset, G., Mazoyer, J., & Dupuis, O. 2016a. Focal plane wavefront sensor achromatization : The multireference self-coherent camera. *Astronomy & Astrophysics*, **588**(Apr.), A136.

Delorme, J. R., N'Diaye, M., Galicher, R., Dohlen, K., Baudoz, P., Caillat, A., Rousset, G., Soummer, R., & Dupuis, O. 2016b. Laboratory validation of the dual-zone phase mask coronagraph in broadband light at the high-contrast imaging THD testbed. *Astronomy & Astrophysics*, **592**(Aug.), A119.

Delorme, P., Schmidt, T., Bonnefoy, M., Desidera, S., Ginski, C., Charnay, B., Lazzoni, C., Christiaens, V., Messina, S., D'Orazi, V., Milli, J., Schlieder, J. E., Gratton, R., Rodet, L., Lagrange, A.-M., Absil, O., Vigan, A., Galicher, R., Hagelberg, J., Bonavita, M., Lavie, B., Zurlo, A., Olofsson, J., Boccaletti, A., Cantalloube, F., Mouillet, D., Chauvin, G., Hambsch, F.-J., Langlois, M., Udry, S., Henning, T., Beuzit, J.-L., Mordasini, C., Lucas, P., Marocco, F., Biller, B., Carson, J., Cheetham, A., Covino, E., De Caprio, V., Delboulbe, A., Feldt, M., Girard, J., Hubin, N., Maire, A.-L., Pavlov, A., Petit, C., Rouan, D., Roelfsema, R., & Wildi, F. 2017. In-depth study of moderately young but extremely red, very dusty substellar companion HD 206893B. *Astronomy & Astrophysics*, **608**(Dec.), A79.

Delorme, P., Meunier, N., Albert, D., Lagadec, E., Le Coroller, H., Galicher, R., Mouillet, D., Boccaletti, A., Mesa, D., Meunier, J.-C., Beuzit, J.-L., Lagrange, a.-L., Chauvin, G., Sapone, A., Langlois, M., Maire, A.-L., Montargès, M., Gratton, R., Vigan, A., Surae, C., Moreau, C., & Fenouillet, T. 2017b. The SPHERE Data Center : a reference for high contrast imaging processing. *SF2A*.

Deming, Drake, Seager, Sara, Richardson, L. Jeremy, & Harrington, Joseph. 2005. Infrared radiation from an extrasolar planet. *Nature*, **434**(7034), 740–743.

Dohlen, K., Langlois, M., Saisse, M., Hill, L., Origne, A., Jacquet, M., Fabron, C., Blanc, J.-C., Llored, M., Carle, M., Moutou, C., Vigan, A., Boccaletti, A., Carbillet, M., Mouillet, D., & Beuzit, J.-L. 2008 (July). The infra-red dual imaging and spectrograph for SPHERE : design and performance. *Page 70143L of : Ground-based and Airborne Instrumentation for Astronomy II.* SPIE Proceedings, vol. 7014.

Espinoza, Néstor, Rackham, Benjamin V., Jordán, Andrés, Apai, Dániel, López-Morales, Mercedes, Osip, David J., Grimm, Simon L., Hoeijmakers, Jens, Wilson, Paul A., & Bixel, Alex. 2019. ACCESS : a featureless optical transmission spectrum for WASP-19b from Magellan/IMACS. *Monthly Notices of the Royal Astronomical Society*, **482**(2), 2065–2087.

Flasseur, Olivier, Denis, Loïc, Thiébaut, Éric, & Langlois, Maud. 2018. Exoplanet detection in angular differential imaging by statistical learning of the nonstationary patch covariances. The PACO algorithm. *Astronomy & Astrophysics*, **618**(Nov.), A138.

Fusco, T., Sauvage, J. F., Mouillet, D., Costille, A., Petit, C., Beuzit, J. L., Dohlen, K., Milli, J., Girard, J., & Kasper, M. 2016 (Jul). SAXO, the SPHERE extreme AO system : on-sky final performance and future improvements. *Page 99090U of : Adaptive Optics Systems V.* Society of Photo-Optical Instrumentation Engineers (SPIE) Conference Series, vol. 9909.

Gaia Collaboration, Prusti, T., de Bruijne, J. H. J., Brown, A. G. A., Vallenari, A., Babusiaux, C., Bailer-Jones, C. A. L., Bastian, U., Biermann, M., Evans, D. W., Eyer, L., Jansen, F., Jordi, C., Klioner, S. A., Lammers, U., Lindegren, L., Luri, X., Mignard, F., Milligan, D. J., Panem,

C., Poinsignon, V., Pourbaix, D., Randich, S., Sarri, G., Sartoretti, P., Siddiqui, H. I., Soubiran, C., Valette, V., van Leeuwen, F., Walton, N. A., Aerts, C., Arenou, F., Cropper, M., Drimmel, R., Høg, E., Katz, D., Lattanzi, M. G., O'Mullane, W., Grebel, E. K., Holland, A. D., Huc, C., Passot, X., Bramante, L., Cacciari, C., Castañeda, J., Chaoul, L., Cheek, N., De Angeli, F., Fabricius, C., Guerra, R., Hernández, J., Jean-Antoine-Piccolo, A., Masana, E., Messineo, R., Mowlavi, N., Nienartowicz, K., Ordóñez-Blanco, D., Panuzzo, P., Portell, J., Richards, P. J., Riello, M., Seabroke, G. M., Tanga, P., Thévenin, F., Torra, J., Els, S. G., Gracia-Abril, G., Comoretto, G., Garcia-Reinaldos, M., Lock, T., Mercier, E., Altmann, M., Andrae, R., Astraatmadja, T. L., Bellas-Velidis, I., Benson, K., Berthier, J., Blomme, R., Busso, G., Carry, B., Cellino, A., Clementini, G., Cowell, S., Creevey, O., Cuypers, J., Davidson, M., De Ridder, J., de Torres, A., Delchambre, L., Dell'Oro, A., Ducourant, C., Frémat, Y., García-Torres, M., Gosset, E., Halbwachs, J. L., Hambly, N. C., Harrison, D. L., Hauser, M., Hestroffer, D., Hodgkin, S. T., Huckle, H. E., Hutton, A., Jasniewicz, G., Jordan, S., Kontizas, M., Korn, A. J., Lanzafame, A. C., Manteiga, M., Moitinho, A., Muinonen, K., Osinde, J., Pancino, E., Pauwels, T., Petit, J. M., Recio-Blanco, A., Robin, A. C., Sarro, L. M., Siopis, C., Smith, M., Smith, K. W., Sozzetti, A., Thuillot, W., van Reeven, W., Viala, Y., Abbas, U., Abreu Aramburu, A., Accart, S., Aguado, J. J., Allan, P. M., Allasia, W., Altavilla, G., Álvarez, M. A., Alves, J., Anderson, R. I., Andrei, A. H., Anglada Varela, E., Antiche, E., Antoja, T., Antón, S., Arcay, B., Atzei, A., Ayache, L., Bach, N., Baker, S. G., Balaguer-Núñez, L., Barache, C., Barata, C., Barbier, A., Barblan, F., Baroni, M., Barrado y Navascués, D., Barros, M., Barstow, M. A., Becciani, U., Bellazzini, M., Bellei, G., Bello García, A., Belokurov, V., Bendjoya, P., Berihuete, A., Bianchi, L., Bienaymé, O., Billebaud, F., Blagorodnova, N., Blanco-Cuaresma, S., Boch, T., Bombrun, A., Borrachero, R., Bouquillon, S., Bourda, G., Bouy, H., Bragaglia, A., Breddels, M. A., Brouillet, N., Brüsemeister, T., Bucciarelli, B., Budnik, F., Burgess, P., Burgon, R., Burlacu, A., Busonero, D., Buzzi, R., Caffau, E., Cambras, J., Campbell, H., Cancelliere, R., Cantat-Gaudin, T., Carlucci, T., Carrasco, J. M., Castellani, M., Charlot, P., Charnas, J., Charvet, P., Chassat, F., Chiavassa, A., Clotet, M., Cocozza, G., Collins, R. S., Collins, P., Costigan, G., Crifo, F., Cross, N. J. G., Crosta, M., Crowley, C., Dafonte, C., Damerdji, Y., Dapergolas, A., David, P., David, M., De Cat, P., de Felice, F., de Laverny, P., De Luise, F., De March, R., de Martino, D., de Souza, R., Debosscher, J., del Pozo, E., Delbo, M., Delgado, A., Delgado, H. E., di Marco, F., Di Matteo, P., Diakite, S., Distefano, E., Dolding, C., Dos Anjos, S., Drazinos, P., Durán, J., Dzigan, Y., Ecale, E., Edvardsson, B., Enke, H., Erdmann, M., Escolar, D., Espina, M., Evans, N. W., Eynard Bontemps, G., Fabre, C., Fabrizio, M., Faigler, S., Falcão, A. J., Farràs Casas, M., Faye, F., Federici, L., Fedorets, G., Fernández-Hernández, J., Fernique, P., Fienga, A., Figueras, F., Filippi, F., Findeisen, K., Fonti, A., Fouesneau, M., Fraile, E., Fraser, M., Fuchs, J., Furnell, R., Gai, M., Galleti, S., Galluccio, L., Garabato, D., García-Sedano, F., Garé, P., Garofalo, A., Garralda, N., Gavras, P., Gerssen, J., Geyer, R., Gilmore, G., Girona, S., Giuffrida, G., Gomes, M., González-Marcos, A., González-Núñez, J., González-Vidal, J. J., Granvik, M., Guerrier, A., Guillout, P., Guiraud, J., Gúrpide, A., Gutiérrez-Sánchez, R., Guy, L. P., Haigron, R., Hatzidimitriou, D., Haywood, M., Heiter, U., Helmi, A., Hobbs, D., Hofmann, W., Holl, B., Holland , G., Hunt, J. A. S., Hypki, A., Icardi, V., Irwin, M., Jevardat de Fombelle, G., Jofré, P., Jonker, P. G., Jorissen, A., Julbe, F., Karampelas, A., Kochoska, A., Kohley, R., Kolenberg, K., Kontizas, E., Koposov, S. E., Kordopatis, G., Koubsky, P., Kowalczyk, A., Krone-Martins, A., Kudryashova, M., Kull, I., Bachchan, R. K., Lacoste-Seris, F., Lanza, A. F., Lavigne, J. B., Le Poncin-Lafitte, C., Lebreton, Y., Lebzelter, T., Leccia, S., Leclerc, N., Lecoeur-Taibi, I., Lemaitre, V., Lenhardt, H., Leroux, F., Liao, S., Licata, E., Lindstrøm, H. E. P., Lister, T. A., Livanou, E., Lobel, A., Löffler, W., López, M., Lopez-Lozano, A., Lorenz, D.,

Loureiro, T., MacDonald, I., Magalhães Fernandes, T., Managau, S., Mann, R. G., Mantelet, G., Marchal, O., Marchant, J. M., Marconi, M., Marie, J., Marinoni, S., Marrese, P. M., Marschalkó, G., Marshall, D. J., Martín-Fleitas, J. M., Martino, M., Mary, N., Matijevič, G., Mazeh, T., McMillan, P. J., Messina, S., Mestre, A., Michalik, D., Millar, N. R., Miranda, B. M. H., Molina, D., Molinaro, R., Molinaro, M., Molnár, L., Moniez, M., Montegriffo, P., Monteiro, D., Mor, R., Mora, A., Morbidelli, R., Morel, T., Morgenthaler, S., Morley, T., Morris, D., Mulone, A. F., Muraveva, T., Musella, I., Narbonne, J., Nelemans, G., Nicastro, L., Noval, L., Ordénovic, C., Ordieres-Meré, J., Osborne, P., Pagani, C., Pagano, I., Pailler, F., Palacin, H., Palaversa, L., Parsons, P., Paulsen, T., Pecoraro, M., Pedrosa, R., Pentikäinen, H., Pereira, J., Pichon, B., Piersimoni, A. M., Pineau, F. X., Plachy, E., Plum, G., Poujoulet, E., Prša, A., Pulone, L., Ragaini, S., Rago, S., Rambaux, N., Ramos-Lerate, M., Ranalli, P., Rauw, G., Read, A., Regibo, S., Renk, F., Reylé, C., Ribeiro, R. A., Rimoldini, L., Ripepi, V., Riva, A., Rixon, G., Roelens, M., Romero-Gómez, M., Rowell, N., Royer, F., Rudolph, A., Ruiz-Dern, L., Sadowski, G., Sagristà Sellés, T., Sahlmann, J., Salgado, J., Salguero, E., Sarasso, M., Savietto, H., Schnorhk, A., Schultheis, M., Sciacca, E., Segol, M., Segovia, J. C., Segransan, D., Serpell, E., Shih, I. C., Smareglia, R., Smart, R. L., Smith, C., Solano, E., Solitro, F., Sordo, R., Soria Nieto, S., Souchay, J., Spagna, A., Spoto, F., Stampa, U., Steele, I. A., Steidelmüller, H., Stephenson, C. A., Stoev, H., Suess, F. F., Süveges, M., Surdej, J., Szabados, L., Szegedi-Elek, E., Tapiador, D., Taris, F., Tauran, G., Taylor, M. B., Teixeira, R., Terrett, D., Tingley, B., Trager, S. C., Turon, C., Ulla, A., Utrilla, E., Valentini, G., van Elteren, A., Van Hemelryck, E., van Leeuwen, M., Varadi, M., Vecchiato, A., Veljanoski, J., Via, T., Vicente, D., Vogt, S., Voss, H., Votruba, V., Voutsinas, S., Walmsley, G., Weiler, M., Weingrill, K., Werner, D., Wevers, T., Whitehead, G., Wyrzykowski, Ł., Yoldas, A., Žerjal, M., Zucker, S., Zurbach, C., Zwitter, T., Alecu, A., Allen, M., Allende Prieto, C., Amorim, A., Anglada-Escudé, G., Arsenijevic, V., Azaz, S., Balm, P., Beck, M., Bernstein, H. H., Bigot, L., Bijaoui, A., Blasco, C., Bonfigli, M., Bono, G., Boudreault, S., Bressan, A., Brown, S., Brunet, P. M., Bunclark, P., Buonanno, R., Butkevich, A. G., Carret, C., Carrion, C., Chemin, L., Chéreau, F., Corcione, L., Darmigny, E., de Boer, K. S., de Teodoro, P., de Zeeuw, P. T., Delle Luche, C., Domingues, C. D., Dubath, P., Fodor, F., Frézouls, B., Fries, A., Fustes, D., Fyfe, D., Gallardo, E., Gallegos, J., Gardiol, D., Gebran, M., Gomboc, A., Gómez, A., Grux, E., Gueguen, A., Heyrovsky, A., Hoar, J., Iannicola, G., Isasi Parache, Y., Janotto, A. M., Joliet, E., Jonckheere, A., Keil, R., Kim, D. W., Klagyivik, P., Klar, J., Knude, J., Kochukhov, O., Kolka, I., Kos, J., Kutka, A., Lainey, V., LeBouquin, D., Liu, C., Loreggia, D., Makarov, V. V., Marseille, M. G., Martayan, C., Martinez-Rubi, O., Massart, B., Meynadier, F., Mignot, S., Munari, U., Nguyen, A. T., Nordlander, T., Ocvirk, P., O'Flaherty, K. S., Olias Sanz, A., Ortiz, P., Osorio, J., Oszkiewicz, D., Ouzounis, A., Palmer, M., Park, P., Pasquato, E., Peltzer, C., Peralta, J., Péturaud, F., Pieniluoma, T., Pigozzi, E., Poels, J., Prat, G., Prod'homme, T., Raison, F., Rebordao, J. M., Risquez, D., Rocca-Volmerange, B., Rosen, S., Ruiz-Fuertes, M. I., Russo, F., Sembay, S., Serraller Vizcaino, I., Short, A., Siebert, A., Silva, H., Sinachopoulos, D., Slezak, E., Soffel, M., Sosnowska, D., Straižys, V., ter Linden, M., Terrell, D., Theil, S., Tiede, C., Troisi, L., Tsalmantza, P., Tur, D., Vaccari, M., Vachier, F., Valles, P., Van Hamme, W., Veltz, L., Virtanen, J., Wallut, J. M., Wichmann, R., Wilkinson, M. I., Ziaeepour, H., & Zschocke, S. 2016. The Gaia mission. *Astronomy & Astrophysics*, **595**(Nov.), A1.

Galicher, R. 2009. *Études de techniques d'imagerie à haut contraste basées sur la cohérence.* Ph.D. thesis, Université Denis Diderot (P7).

Galicher, R., & Baudoz, P. 2007. Expected performance of a self-coherent camera. *Comptes*

Rendus Physique, **8**(Apr.), 333–339.

Galicher, R., Guyon, O., Otsubo, M., Suto, H., & Ridgway, S. 2005. Laboratory Demonstration and Numerical Simulations of the Phase-Induced Amplitude Apodization. *Publications of the Astronomical Society of the Pacific*, **117**(Apr.), 411–420.

Galicher, R., Baudoz, P., & Rousset, G. 2008 (July). Self-Coherent Camera : active correction and post-processing for Earth-like planet detection. *In : Society of Photo-Optical Instrumentation Engineers (SPIE) Conference Series.* Society of Photo-Optical Instrumentation Engineers (SPIE) Conference Series, vol. 7015.

Galicher, R., Baudoz, P., & Rousset, G. 2008. Wavefront error correction and Earth-like planet detection by a self-coherent camera in space. *Astronomy & Astrophysics*, **488**(Sept.), L9–L12.

Galicher, R., Baudoz, P., Rousset, G., Totems, J., & Mas, M. 2010. Self-coherent camera as a focal plane wavefront sensor : simulations. *Astronomy & Astrophysics*, **509**(Jan.), A31+.

Galicher, R., Baudoz, P., & Baudrand, J. 2011. Multi-stage four-quadrant phase mask : achromatic coronagraph for space-based and ground-based telescopes. *Astronomy & Astrophysics*, **530**(June), A43+.

Galicher, R., Delorme, J. R., Baudoz, P., & Mazoyer, J. 2013a (Dec.). Focal Plane Wavefront Sensing with a self-coherent camera. *In :* Esposito, S., & Fini, L. (eds), *Proceedings of the Third AO4ELT Conference.*

Galicher, R., Marois, C., Zuckerman, B., & Macintosh, B. 2013b. Fomalhaut b : Independent Analysis of the Hubble Space Telescope Public Archive Data. *Astrophysical Journal*, **769**(May), 42.

Galicher, R., Baudoz, P., Delorme, J. R., Mazoyer, J., Rousset, G., Firminy, J., Boussaha, F., N'Diaye, M., Dohlen, K., & Caillat, A. 2014 (Aug.). High contrast imaging on the THD bench : progress and upgrades. *Page 91435A of : Space Telescopes and Instrumentation 2014 : Optical, Infrared, and Millimeter Wave.* Society of Photo-Optical Instrumentation Engineers (SPIE) Conference Series, vol. 9143.

Galicher, R., Marois, C., Macintosh, B., Zuckerman, B., Barman, T., Konopacky, Q., Song, I., Patience, J., Lafrenière, D., Doyon, R., & Nielsen, E. L. 2016. The International Deep Planet Survey. II. The frequency of directly imaged giant exoplanets with stellar mass. *Astronomy & Astrophysics*, **594**(Oct.), A63.

Galicher, R., Boccaletti, A., Mesa, D., Delorme, P., Gratton, R., Langlois, M., Lagrange, A.-M., Maire, A.-L., Le Coroller, H., Chauvin, G., Biller, B., Cantalloube, F., Janson, M., Lagadec, E., Meunier, N., Vigan, A., Hagelberg, J., Bonnefoy, M., Zurlo, A., Rocha, S., Maurel, D., Jaquet, M., Buey, T., & Weber, L. 2018. Astrometric and photometric accuracies in high contrast imaging : The SPHERE speckle calibration tool (SpeCal). *Astronomy & Astrophysics*, **615**(July), A92.

Galicher, R., Baudoz, P., Delorme, J. R., Mawet, D., Bottom, M., Wallace, J. K., Serabyn, E., & Shelton, C. 2019. Minimization of non-common path aberrations at the Palomar telescope using a self-coherent camera. *Astronomy & Astrophysics*, **631**(Nov.), A143.

Galicher, R., Huby, E., Baudoz, P., & Dupuis, O. 2020. A family of phase masks for broadband coronagraphy example of the wrapped vortex phase mask theory and laboratory demonstration. *Astronomy & Astrophysics*, **635**(Mar.), A11.

Gaspar, Andras, & Rieke, George. 2020. New HST data and modeling reveal a massive planetesimal collision around Fomalhaut. *Proceedings of the National Academy of Science*, **117**(18), 9712–9722.

Gaudi, B. Scott, Seager, Sara, Mennesson, Bertrand, Kiessling, Alina, Warfield, Keith, Cahoy, Kerri, Clarke, John T., Domagal-Goldman, Shawn, Feinberg, Lee, Guyon, Olivier, Kasdin, Jeremy, Mawet, Dimitri, Plavchan, Peter, Robinson, Tyler, Rogers, Leslie, Scowen, Paul, Somerville, Rachel, Stapelfeldt, Karl, Stark, Christopher, Stern, Daniel, Turnbull, Margaret, Amini, Rashied, Kuan, Gary, Martin, Stefan, Morgan, Rhonda, Redding, David, Stahl, H. Philip, Webb, Ryan, Alvarez-Salazar, Oscar, Arnold, William L., Arya, Manan, Balasubramanian, Bala, Baysinger, Mike, Bell, Ray, Below, Chris, Benson, Jonathan, Blais, Lindsey, Booth, Jeff, Bourgeois, Robert, Bradford, Case, Brewer, Alden, Brooks, Thomas, Cady, Eric, Caldwell, Mary, Calvet, Rob, Carr, Steven, Chan, Derek, Cormarkovic, Velibor, Coste, Keith, Cox, Charlie, Danner, Rolf, Davis, Jacqueline, Dewell, Larry, Dorsett, Lisa, Dunn, Daniel, East, Matthew, Effinger, Michael, Eng, Ron, Freebury, Greg, Garcia, Jay, Gaskin, Jonathan, Greene, Suzan, Hennessy, John, Hilgemann, Evan, Hood, Brad, Holota, Wolfgang, Howe, Scott, Huang, Pei, Hull, Tony, Hunt, Ron, Hurd, Kevin, Johnson, Sandra, Kissil, Andrew, Knight, Brent, Kolenz, Daniel, Kraus, Oliver, Krist, John, Li, Mary, Lisman, Doug, Mandic, Milan, Mann, John, Marchen, Luis, Marrese-Reading, Colleen, McCready, Jonathan, McGown, Jim, Missun, Jessica, Miyaguchi, Andrew, Moore, Bradley, Nemati, Bijan, Nikzad, Shouleh, Nissen, Joel, Novicki, Megan, Perrine, Todd, Pineda, Claudia, Polanco, Otto, Putnam, Dustin, Qureshi, Atif, Richards, Michael, Eldorado Riggs, A. J., Rodgers, Michael, Rud, Mike, Saini, Navtej, Scalisi, Dan, Scharf, Dan, Schulz, Kevin, Serabyn, Gene, Sigrist, Norbert, Sikkia, Glory, Singleton, Andrew, Shaklan, Stuart, Smith, Scott, Southerd, Bart, Stahl, Mark, Steeves, John, Sturges, Brian, Sullivan, Chris, Tang, Hao, Taras, Neil, Tesch, Jonathan, Therrell, Melissa, Tseng, Howard, Valente, Marty, Van Buren, David, Villalvazo, Juan, Warwick, Steve, Webb, David, Westerhoff, Thomas, Wofford, Rush, Wu, Gordon, Woo, Jahning, Wood, Milana, Ziemer, John, Arney, Giada, Anderson, Jay, Maíz-Apellániz, Jesús, Bartlett, James, Belikov, Ruslan, Bendek, Eduardo, Cenko, Brad, Douglas, Ewan, Dulz, Shannon, Evans, Chris, Faramaz, Virginie, Feng, Y. Katherina, Ferguson, Harry, Follette, Kate, Ford, Saavik, García, Miriam, Geha, Marla, Gelino, Dawn, Götberg, Ylva, Hildebrand t, Sergi, Hu, Renyu, Jahnke, Knud, Kennedy, Grant, Kreidberg, Laura, Isella, Andrea, Lopez, Eric, Marchis, Franck, Macri, Lucas, Marley, Mark, Matzko, William, Mazoyer, Johan, McCandliss, Stephan, Meshkat, Tiffany, Mordasini, Christoph, Morris, Patrick, Nielsen, Eric, Newman, Patrick, Petigura, Erik, Postman, Marc, Reines, Amy, Roberge, Aki, Roederer, Ian, Ruane, Garreth, Schwieterman, Edouard, Sirbu, Dan, Spalding, Christopher, Teplitz, Harry, Tumlinson, Jason, Turner, Neal, Werk, Jessica, Wofford, Aida, Wyatt, Mark, Young, Amber, & Zellem, Rob. 2020. The Habitable Exoplanet Observatory (HabEx) Mission Concept Study Final Report. *arXiv e-prints*, Jan., arXiv :2001.06683.

Gerard, Benjamin, Marois, Christian, Galicher, Raphael, & Veran, Jean-Pierre. 2019a (Jan). The Future of Exoplanet Imaging : the Fast Atmospheric Self-Coherent Camera Technique. *Page 104.07 of : American Astronomical Society Meeting Abstracts #233.* American Astronomical Society Meeting Abstracts, vol. 233.

Gerard, Benjamin L., & Marois, Christian. 2020. Focal Plane Wavefront Sensing with the FAST TGV Coronagraph. *Publications of the Astronomical Society of the Pacific*, **132**(1012), 064401.

Gerard, Benjamin L., Marois, Christian, & Galicher, Raphaël. 2018. Fast Coherent Differential Imaging on Ground-based Telescopes Using the Self-coherent Camera. *The Astronomical Journal*, **156**(3), 106.

Gerard, Benjamin L., Marois, Christian, Galicher, Raphaël, Baudoz, Pierre, Patapis, Polychronis, & Kühn, Jonas. 2019b. The Fast Atmospheric Self-Coherent Camera Technique : Laboratory Results and Future Directions. *arXiv e-prints*, Oct., arXiv :1910.04554.

Gibbs, Aidan, Wagner, Kevin, Apai, Daniel, Moór, Attila, Currie, Thayne, Bonnefoy, Mickäel, Langlois, Maud, & Lisse, Carey. 2019. VLT/SPHERE Multiwavelength High-contrast Imaging of the HD 115600 Debris Disk : New Constraints on the Dust Geometry and the Presence of Young Giant Planets. *The Astronomical Journal*, **157**(1), 39.

Ginski, C., Stolker, T., Pinilla, P., Dominik, C., Boccaletti, A., de Boer, J., Benisty, M., Biller, B., Feldt, M., Garufi, A., Keller, C. U., Kenworthy, M., Maire, A. L., Ménard, F., Mesa, D., Milli, J., Min, M., Pinte, C., Quanz, S. P., van Boekel, R., Bonnefoy, M., Chauvin, G., Desidera, S., Gratton, R., Girard, J. H. V., Keppler, M., Kopytova, T., Lagrange, A. M., Langlois, M., Rouan, D., & Vigan, A. 2016. Direct detection of scattered light gaps in the transitional disk around HD 97048 with VLT/SPHERE. *Astronomy & Astrophysics*, **595**(Nov.), A112.

Ginski, C., Benisty, M., van Holstein, R. G., Juhász, A., Schmidt, T. O. B., Chauvin, G., de Boer, J., Wilby, M., Manara, C. F., Delorme, P., Ménard, F., Pinilla, P., Birnstiel, T., Flock, M., Keller, C., Kenworthy, M., Milli, J., Olofsson, J., Pérez, L., Snik, F., & Vogt, N. 2018. First direct detection of a polarized companion outside a resolved circumbinary disk around CS Chamaeleonis. *Astronomy & Astrophysics*, **616**(Aug.), A79.

Give'On, A., Belikov, R., Shaklan, S., & Kasdin, J. 2007. Closed loop, DM diversity-based, wavefront correction algorithm for high contrast imaging systems. *Optics Express*, **15**, 12338–+.

Goebel, Sean B., Guyon, Olivier, Hall, Donald N. B., Jovanovic, Nemanja, Lozi, Julien, & Martinache, Frantz. 2018. Measurements of Speckle Lifetimes in Near-infrared Extreme Adaptive Optics Images for Optimizing Focal Plane Wavefront Control. *Publications of the Astronomical Society of the Pacific*, **130**(992), 104502.

Goldreich, P., & Tremaine, S. 1980. Disk-satellite interactions. *The Astrophysical Journal*, **241**(Oct.), 425–441.

Gong, Qian, Bolcar, Matthew R., Corsetti, James A., Crooke, Julie A., Generie, Joseph, Groff, Tyler D., Hylan, Jason, Jones, Andrew, Parramon, Roser Juanola, Mand ell, Avi M., West, Garrett J., & Zimmerman, Neil T. 2019. Optical design of the Extreme Coronagraph for Living Planetary Systems instrument for the LUVOIR mission study. *Journal of Astronomical Telescopes, Instruments, and Systems*, **5**(Apr.), 025002.

Gravity Collaboration, Abuter, R., Accardo, M., Amorim, A., Anugu, N., Ávila, G., Azouaoui, N., Benisty, M., Berger, J. P., Blind, N., Bonnet, H., Bourget, P., Brandner, W., Brast, R., Buron, A., Burtscher, L., Cassaing, F., Chapron, F., Choquet, É., Clénet, Y., Collin, C., Coudé Du Foresto, V., de Wit, W., de Zeeuw, P. T., Deen, C., Delplancke-Ströbele, F., Dembet, R.,

Derie, F., Dexter, J., Duvert, G., Ebert, M., Eckart, A., Eisenhauer, F., Esselborn, M., Fédou, P., Finger, G., Garcia, P., Garcia Dabo, C. E., Garcia Lopez, R., Gendron, E., Genzel, R., Gillessen, S., Gonte, F., Gordo, P., Grould, M., Grözinger, U., Guieu, S., Haguenauer, P., Hans, O., Haubois, X., Haug, M., Haussmann, F., Henning, Th., Hippler, S., Horrobin, M., Huber, A., Hubert, Z., Hubin, N., Hummel, C. A., Jakob, G., Janssen, A., Jochum, L., Jocou, L., Kaufer, A., Kellner, S., Kendrew, S., Kern, L., Kervella, P., Kiekebusch, M., Klein, R., Kok, Y., Kolb, J., Kulas, M., Lacour, S., Lapeyrère, V., Lazareff, B., Le Bouquin, J. B., Lèna, P., Lenzen, R., Lévêque, S., Lippa, M., Magnard, Y., Mehrgan, L., Mellein, M., Mérand, A., Moreno-Ventas, J., Moulin, T., Müller, E., Müller, F., Neumann, U., Oberti, S., Ott, T., Pallanca, L., Panduro, J., Pasquini, L., Paumard, T., Percheron, I., Perraut, K., Perrin, G., Pflüger, A., Pfuhl, O., Phan Duc, T., Plewa, P. M., Popovic, D., Rabien, S., Ramírez, A., Ramos, J., Rau, C., Riquelme, M., Rohloff, R. R., Rousset, G., Sanchez-Bermudez, J., Scheithauer, S., Schöller, M., Schuhler, N., Spyromilio, J., Straubmeier, C., Sturm, E., Suarez, M., Tristram, K. R. W., Ventura, N., Vincent, F., Waisberg, I., Wank, I., Weber, J., Wieprecht, E., Wiest, M., Wiezorrek, E., Wittkowski, M., Woillez, J., Wolff, B., Yazici, S., Ziegler, D., & Zins, G. 2017. First light for GRAVITY : Phase referencing optical interferometry for the Very Large Telescope Interferometer. *Astronomy & Astrophysics*, **602**(June), A94.

Gravity Collaboration, Lacour, S., Nowak, M., Wang, J., Pfuhl, O., Eisenhauer, F., Abuter, R., Amorim, A., Anugu, N., Benisty, M., Berger, J. P., Beust, H., Blind, N., Bonnefoy, M., Bonnet, H., Bourget, P., Brandner, W., Buron, A., Collin, C., Charnay, B., Chapron, F., Clénet, Y., Coudé Du Foresto, V., de Zeeuw, P. T., Deen, C., Dembet, R., Dexter, J., Duvert, G., Eckart, A., Förster Schreiber, N. M., Fédou, P., Garcia, P., Garcia Lopez, R., Gao, F., Gendron, E., Genzel, R., Gillessen, S., Gordo, P., Greenbaum, A., Habibi, M., Haubois, X., Haußmann, F., Henning, Th., Hippler, S., Horrobin, M., Hubert, Z., Jimenez Rosales, A., Jocou, L., Kendrew, S., Kervella, P., Kolb, J., Lagrange, A. M., Lapeyrère, V., Le Bouquin, J. B., Léna, P., Lippa, M., Lenzen, R., Maire, A. L., Mollière, P., Ott, T., Paumard, T., Perraut, K., Perrin, G., Pueyo, L., Rabien, S., Ramírez, A., Rau, C., Rodríguez-Coira, G., Rousset, G., Sanchez-Bermudez, J., Scheithauer, S., Schuhler, N., Straub, O., Straubmeier, C., Sturm, E., Tacconi, L. J., Vincent, F., van Dishoeck, E. F., von Fellenberg, S., Wank, I., Waisberg, I., Widmann, F., Wieprecht, E., Wiest, M., Wiezorrek, E., Woillez, J., Yazici, S., Ziegler, D., & Zins, G. 2019. First direct detection of an exoplanet by optical interferometry. Astrometry and K-band spectroscopy of HR 8799 e. *Astronomy & Astrophysics*, **623**(Mar.), L11.

Harman, Chester E., & Domagal-Goldman, Shawn. 2018. *Biosignature False Positives*. Springer International Publishing AG. Page 71.

Harvey, E. Newton, & Stevens, Kenneth P. 1928. THE BRIGHTNESS OF THE LIGHT OF THE WEST INDIAN ELATERID BEETLE, PYROPHORUS . *Journal of General Physiology*, **12**(2), 269–272.

Herscovici-Schiller, O., Mugnier, L. M., Baudoz, P., Galicher, R., Sauvage, J. F., & Paul, B. 2018a. Experimental validation of joint phase and amplitude wave-front sensing with coronagraphic phase diversity for high-contrast imaging. *Astronomy & Astrophysics*, **614**(June), A142.

Herscovici-Schiller, Olivier, Mugnier, Laurent M., Baudoz, Pierre, Galicher, Raphaël., Sauvage, Jean-François, Patru, Fabien, Leboulleux, Lucie, Vigan, Arthur, Dohlen, Kjetil, Fusco, Thierry, Pueyo, Laurent, Soummer, Rémi, & Le Duigou, Jean-Michel. 2018b (July). Towards the experimental validation of the non-linear dark hole on the THD bench. *Page 1070329 of :*

Adaptive Optics Systems VI. Society of Photo-Optical Instrumentation Engineers (SPIE) Conference Series, vol. 10703.

Hodapp, K. W., Jensen, J. B., Irwin, E. M., Yamada, H., Chung, R., Fletcher, K., Robertson, L., Hora, J. L., Simons, D. A., Mays, W., Nolan, R., Bec, M., Merrill, M., & Fowler, A. M. 2003. The Gemini Near-Infrared Imager (NIRI). *The Publications of the Astronomical Society of the Pacific*, **115**(Dec.), 1388–1406.

Huby, E., Baudoz, P., Mawet, D., & Absil, O. 2015. Post-coronagraphic tip-tilt sensing for vortex phase masks : The QACITS technique. *Astronomy & Astrophysics*, **584**(Dec.), A74.

Janson, M., Carson, J. C., Lafrenière, D., Spiegel, D. S., Bent, J. R., & Wong, P. 2012. Infrared Non-detection of Fomalhaut b : Implications for the Planet Interpretation. *The Astrophysical Journal*, **747**(Mar.), 116.

Jovanovic, N., Cvetojevic, N., Schwab, C., Norris, B., Lozi, J., Gross, S., Betters, C., Singh, G., Guyon, O., Martinache, F., Doughty, D., & Tuthill, P. 2016 (Aug.). Efficiently feeding single-mode fiber photonic spectrographs with an extreme adaptive optics system : on-sky characterization and preliminary spectroscopy. *Page 99080R of : SPIE conference series*. Society of Photo-Optical Instrumentation Engineers (SPIE) Conference Series, vol. 9908.

Jovanovic, Nemanja, Absil, Olivier, Baudoz, Pierre, Beaulieu, Mathilde, Bottom, Michael, Cady, Eric, Carlomagno, Brunella, Carlotti, Alexis, Doelman, David, Fogarty, Kevin, Galicher, Raphaël., Guyon, Olivier, Haffert, Sebastiaan, Huby, Elsa, Jewell, Jeffrey, Keller, Christoph, Kenworthy, Matthew A., Knight, Justin, Kühn, Jonas, Miller, Kelsey, Mazoyer, Johan, N'Diaye, Mamadou, Por, Emiel, Pueyo, Laurent, Riggs, A. J. E., Ruane, Garreth, Sirbu, Dan, Snik, Frans, Wallace, J. K., Wilby, Michael, & Ygouf, Marie. 2018 (Jul). Review of high-contrast imaging systems for current and future ground-based and space-based telescopes : Part II. Common path wavefront sensing/control and coherent differential imaging. *Page 107031U of : Proceedings of the SPIE*. Society of Photo-Optical Instrumentation Engineers (SPIE) Conference Series, vol. 10703.

Kalas, P., Graham, J. R., Chiang, E., Fitzgerald, M. P., Clampin, M., Kite, E. S., Stapelfeldt, K., Marois, C., & Krist, J. 2008. Optical Images of an Exosolar Planet 25 Light-Years from Earth. *Science*, **322**(Nov.), 1345–.

Kasper, Markus, Verinaud, Christophe, & Mawet, Dimitri. 2013 (Dec.). Roadmap for PCS, the Planetary Camera and Spectrograph for the E-ELT. *Page 8 of :* Esposito, Simone, & Fini, Luca (eds), *Proceedings of the Third AO4ELT Conference*.

Kasting, James F., Whitmire, Daniel P., & Reynolds, Ray T. 1993. Habitable Zones around Main Sequence Stars. *Icarus*, **101**(1), 108–128.

Lafrenière, D., Marois, C., Doyon, R., Nadeau, D., & Artigau, É. 2007a. A New Algorithm for Point-Spread Function Subtraction in High-Contrast Imaging : A Demonstration with Angular Differential Imaging. *The Astrophysical Journal*, **660**(May), 770–780.

Lafrenière, D., Doyon, R., Marois, C., Nadeau, D., Oppenheimer, B. R., Roche, P. F., Rigaut, F., Graham, J. R., Jayawardhana, R., Johnstone, D., Kalas, P. G., Macintosh, B., & Racine, R. 2007b. The Gemini Deep Planet Survey. *The Astrophysical Journal*, **670**(Dec.), 1367–1390.

Lagrange, A. M. 2014. Direct imaging of exoplanets. *Philosophical Transactions of the Royal Society of London Series A*, **372**(2014), 20130090–20130090.

Launhardt, R., Henning, Th., Quirrenbach, A., Ségransan, D., Avenhaus, H., van Boekel, R., Brems, S. S., Cheetham, A. C., Cugno, G., Girard, J., Godoy, N., Kennedy, G. M., Maire, A. L., Metchev, S., Müller, A., Musso Barcucci, A., Olofsson, J., Pepe, F., Quanz, S. P., Queloz, D., Reffert, S., Rickman, E. L., Ruh, H. L., & Samland, M. 2020. ISPY-NACO Imaging Survey for Planets around Young stars. Survey description and results from the first 2.5 years of observations. *Astronomy & astrophysics*, **635**(Mar.), A162.

Lenzen, Rainer, Hartung, Markus, Brandner, Wolfgang, Finger, Gert, Hubin, Norbert N., Lacombe, Francois, Lagrange, Anne-Marie, Lehnert, Matthew D., Moorwood, Alan F. M., & Mouillet, David. 2003. NAOS-CONICA first on sky results in a variety of observing modes. *Pages 944–952 of :* Iye, Masanori, & Moorwood, Alan F. M. (eds), *Society of Photo-Optical Instrumentation Engineers (SPIE) Conference Series*. Society of Photo-Optical Instrumentation Engineers (SPIE) Conference Series, vol. 4841.

Lin, D. N. C., Bodenheimer, P., & Richardson, D. C. 1996. Orbital migration of the planetary companion of 51 Pegasi to its present location. *Nature*, **380**(6575), 606–607.

Lozi, Julien, Guyon, Olivier, Jovanovic, Nemanja, Goebel, Sean, Pathak, Prashant, Skaf, Nour, Sahoo, Ananya, Norris, Barnaby, Martinache, Frantz, N'Diaye, Mamadou, Mazin, Ben, Walter, Alex B., Tuthill, Peter, Kudo, Tomoyuki, Kawahara, Hajime, Kotani, Takayuki, Ireland, Michael, Cvetojevic, Nick, Huby, Elsa, Lacour, Sylvestre, Vievard, Sébastien, Groff, Tyler D., Chilcote, Jeffrey K., Kasdin, Jeremy, Knight, Justin, Snik, Frans, Doelman, David, Minowa, Yosuke, Clergeon, Christophe, Takato, Naruhisa, Tamura, Motohide, Currie, Thayne, Takami, Hideki, & Hayashi, Masa. 2018 (July). SCExAO, an instrument with a dual purpose : perform cutting-edge science and develop new technologies. *Page 1070359 of : SPIE conference series*. Society of Photo-Optical Instrumentation Engineers (SPIE) Conference Series, vol. 10703.

Macintosh, B., Poyneer, L., Sivaramakrishnan, A., & Marois, C. 2005 (Aug.). Speckle lifetimes in high-contrast adaptive optics. *Pages 170–177 of :* Tyson, R. K., & Lloyd-Hart, M. (eds), *Society of Photo-Optical Instrumentation Engineers (SPIE) Conference Series*. Society of Photo-Optical Instrumentation Engineers (SPIE) Conference Series, vol. 5903.

Macintosh, B., Graham, J. R., Ingraham, P., Konopacky, Q., Marois, C., Perrin, M., Poyneer, L., Bauman, B., Barman, T., Burrows, A. S., Cardwell, A., Chilcote, J., De Rosa, R. J., Dillon, D., Doyon, R., Dunn, J., Erikson, D., Fitzgerald, M. P., Gavel, D., Goodsell, S., Hartung, M., Hibon, P., Kalas, P., Larkin, J., Maire, J., Marchis, F., Marley, M. S., McBride, J., Millar-Blanchaer, M., Morzinski, K., Norton, A., Oppenheimer, B. R., Palmer, D., Patience, J., Pueyo, L., Rantakyro, F., Sadakuni, N., Saddlemyer, L., Savransky, D., Serio, A., Soummer, R., Sivaramakrishnan, A., Song, I., Thomas, S., Wallace, J. K., Wiktorowicz, S., & Wolff, S. 2014. First light of the Gemini Planet Imager. *Proceedings of the National Academy of Science*, **111**(Sept.), 12661–12666.

Macintosh, Bruce, Chilcote, Jeffery K., Bailey, Vanessa P., de Rosa, Rob, Nielsen, Eric, Norton, Andrew, Poyneer, Lisa, Wang, Jason, Ruffio, J. B., Graham, J. R., Marois, Christian, Savransky, Dmitry, & Veran, Jean-Pierre. 2018 (July). The Gemini Planet Imager : looking back over five years and forward to the future. *Page 107030K of : SPIE conference series*. Society of Photo-Optical Instrumentation Engineers (SPIE) Conference Series, vol. 10703.

Maire, A. L., Stolker, T., Messina, S., Müller, A., Biller, B. A., Currie, T., Dominik, C., Grady, C. A., Boccaletti, A., Bonnefoy, M., Chauvin, G., Galicher, R., Millward, M., Pohl, A., Brandner, W., Henning, T., Lagrange, A. M., Langlois, M., Meyer, M. R., Quanz, S. P., Vigan, A., Zurlo, A., van Boekel, R., Buenzli, E., Buey, T., Desidera, S., Feldt, M., Fusco, T., Ginski, C., Giro, E., Gratton, R., Hubin, N., Lannier, J., Le Mignant, D., Mesa, D., Peretti, S., Perrot, C., Ramos, J. R., Salter, G., Samland, M., Sissa, E., Stadler, E., Thalmann, C., Udry, S., & Weber, L. 2017. Testing giant planet formation in the transitional disk of SAO 206462 using deep VLT/SPHERE imaging. *Astronomy & Astrophysics paper*, **601**(May), A134.

Malbet, F., Yu, J. W., & Shao, M. 1995. High-Dynamic-Range Imaging Using a Deformable Mirror for Space Coronography. *Publications of the Astronomical Society of the Pacific*, **107**(Apr.), 386.

Marois, C., Lafrenière, D., Doyon, R., Macintosh, B., & Nadeau, D. 2006. Angular Differential Imaging : A Powerful High-Contrast Imaging Technique. *The Astrophysical Journal*, **641**(Apr.), 556–564.

Marois, C., Correia, C., Véran, J.-P., & Currie, T. 2014 (Jan.). TLOCI : A Fully Loaded Speckle Killing Machine. *Pages 48–49 of :* Booth, M., Matthews, B. C., & Graham, J. R. (eds), *Exploring the Formation and Evolution of Planetary Systems*. IAU Symposium, vol. 299.

Mas, M., Baudoz, P., Rousset, G., Galicher, R., & Baudrand, J. 2010 (July). Self-coherent camera : first results of a high-contrast imaging bench in visible light. *In : Society of Photo-Optical Instrumentation Engineers (SPIE) Conference Series*. Society of Photo-Optical Instrumentation Engineers (SPIE) Conference Series, vol. 7735.

Mas, M., Baudoz, P., Mazoyer, J., Galicher, R., & Rousset, G. 2012a (Sept.). Experimental results on wavefront correction using the self-coherent camera. *In : Society of Photo-Optical Instrumentation Engineers (SPIE) Conference Series*. Society of Photo-Optical Instrumentation Engineers (SPIE) Conference Series, vol. 8446.

Mas, M., Baudoz, P., Rousset, G., & Galicher, R. 2012b. Tip-tilt estimation and correction using FQPM coronagraphic images. *Astronomy & Astrophysics*, **539**(Mar.), A126.

Mawet, D., Shelton, C., Wallace, J., Bottom, M., Kuhn, J., Mennesson, B., Burruss, R., Bartos, R., Pueyo, L., Carlotti, A., & Serabyn, E. 2014 (Aug.). Demonstration of vortex coronagraph concepts for on-axis telescopes on the Palomar Stellar Double Coronagraph. *Page 91432T of : Space Telescopes and Instrumentation 2014 : Optical, Infrared, and Millimeter Wave*. Proceedings of the SPIE, vol. 9143.

Mawet, D., Bond, C. Z., Delorme, J. R., Jovanovic, N., Cetre, S., Chun, M., Echeverri, D., Hall, D., Lilley, S., Wallace, J. K., & Wizinowich, P. 2018 (July). Keck Planet Imager and Characterizer : status update. *Page 1070306 of : SPIE conference series*. Society of Photo-Optical Instrumentation Engineers (SPIE) Conference Series, vol. 10703.

Mawet, Dimitri, Fitzgerald, Michael, Konopacky, Quinn, Beichman, Charles, Jovanovic, Nemanja, Dekany, Richard, Hover, David, Chisholm, Eric, Ciardi, David, Artigau, Étienne, Banyal, Ravinder, Beatty, Thomas, Benneke, Björn, Blake, Geoffrey A., Burgasser, Adam, Canalizo, Gabriela, Chen, Guo, Do, Tuan, Doppmann, Greg, Doyon, René, Dressing, Courtney, Fang, Min, Greene, Thomas, Hillenbrand, Lynne, Howard, Andrew, Kane, Stephen, Kataria, Tiffany, Kempton, Eliza, Knutson, Heather, Kotani, Takayuki, Lafrenière, David, Liu,

Chao, Nishiyama, Shogo, Pand ey, Gajendra, Plavchan, Peter, Prato, Lisa, Rajaguru, S. P., Robertson, Paul, Salyk, Colette, Sato, Bun'ei, Schlawin, Everett, Sengupta, Sujan, Sivarani, Thirupathi, Skidmore, Warren, Tamura, Motohide, Terada, Hiroshi, Vasisht, Gautam, Wang, Ji, & Zhang, Hui. 2019 (Sept.). High-resolution Infrared Spectrograph for Exoplanet Characterization with the Keck and Thirty Meter Telescopes. *Page 134 of : Bulletin of the American Astronomical Society*, vol. 51.

Mayor, M., & Queloz, D. 1995. A Jupiter-Mass Companion to a Solar-Type Star. *Nature*, **378**(Nov.), 355–+.

Mazoyer, J., Baudoz, P., Mas, M., Rousset, G., & Galicher, R. 2012 (Sept.). Experimental parametric study of the self-coherent camera. *In : Society of Photo-Optical Instrumentation Engineers (SPIE) Conference Series.* Society of Photo-Optical Instrumentation Engineers (SPIE) Conference Series, vol. 8442.

Mazoyer, J., Baudoz, P., Galicher, R., Mas, M., & Rousset, G. 2013. Estimation and correction of wavefront aberrations using the self-coherent camera : laboratory results. *Astronomy & Astrophysics*, **557**(Sept.), A9.

Mazoyer, J., Baudoz, P., Galicher, R., & Rousset, G. 2014. High-contrast imaging in polychromatic light with the self-coherent camera. *Astronomy & Astrophysics*, **564**(Apr.), L1.

Mazoyer, Johan. 2014 (Sept.). *High-Contrast Direct Imaging of Exoplanets and Circumstellar Disks : From the Self-Coherent Camera to NICI Data Analysis.* Ph.D. thesis, LESIA, Observatoire de Paris, CNRS, UPMC and Univ. Paris Diderot.

Mazoyer, Johan, Baudoz, Pierre, Belikov, Ruslan, Crill, Brendan, Fogarty, Kevin, Galicher, Raphaël, Groff, Tyler, Guyon, Olivier, Juanola-Parramon, Roser, Kasdin, Jeremy, Leboulleux, Lucie, Sayson, Jorge Llop, Mawet, Dimitri, Prada, Camilo Mejia, Mennesson, Bertrand, N'Diaye, Mamadou, Perrin, Marshall, Pueyo, Laurent, Roberge, Aki, Ruane, Garreth, Serabyn, Eugene, Shaklan, Stuart, Siegler, Nicholas, Sirbu, Dan, Soummer, Rémi, Stark, Chris, Trauger, John, & Zimmerman, Neil. 2019 (Sept.). High-Contrast Testbeds for Future Space-Based Direct Imaging Exoplanet Missions. *Page 101 of : Bulletin of the American Astronomical Society*, vol. 51.

McLean, I. S., & Sprayberry, D. 2003 (Mar.). Instrumentation at the Keck observatory. *Pages 1–6 of :* M. Iye & A. F. M. Moorwood (ed), *SPIE Conference Series.* SPIE Conference, vol. 4841.

Méndez, Abel, Rivera-Valentín, Edgard G., Schulze-Makuch, Dirk, Filiberto, Justin, Ramírez, Ramses, Wood, Tana E., Dávila, Alfonso, McKay, Chris, Ortiz Ceballos, Kevin, Jusino-Maldonado, Marcos, Nery, Guillermo, Heller, René, Byrne, Paul, Malaska, Michael J., Nathan, Erica, Filipa Simões, Marta, Antunes, André, Martínez-Frías, Jesús, Carone, Ludmila, Izenberg, Noam R., Atri, Dimitra, Carvajal Itic Chitty, Humberto, Nowajewski-Barra, Priscilla, Rivera-Hernández, Frances, Brown, Corine, Lynch, Kennda, Chen, Howard, González, Grizelle, Kashyap Jagadeesh, Madhu, Zuluaga, Jorge, Cockell, Charles S., Haqq-Misra, Jacob, & Barnes, Rory. 2020. Habitability Models for Planetary Sciences. *arXiv e-prints*, July, arXiv :2007.05491.

Mennesson, Bertrand, Debes, J., Douglas, E., Nemati, B., Stark, C., Kasdin, J., Macintosh, B., Turnbull, M., Rizzo, M., Roberge, A., Zimmerman, N., Cahoy, K., Krist, J., Bailey, V.,

Trauger, J., Rhodes, J., Moustakas, L., Frerking, M., Zhao, F., Poberezhskiy, I., & Demers, R. 2018 (Aug.). The WFIRST coronagraph instrument : a major step in the exploration of sun-like planetary systems via direct imaging. *Page 106982I of : SPIE Conference*. Society of Photo-Optical Instrumentation Engineers (SPIE) Conference Series, vol. 10698.

Miller, Kelsey, Males, Jared R., Guyon, Olivier, Close, Laird M., Doelman, David, Snik, Frans, Por, Emiel, Wilby, Michael J., Bohlman, Chris, Lumbres, Jennifer, Van Gorkom, Kyle, Kautz, Maggie, Rodack, Alexander, Knight, Justin, Jovanovic, Nemanja, Morzinski, Katie, & Schatz, Lauren. 2018 (July). Focal plane wavefront sensing and control strategies for high-contrast imaging on the MagAO-X instrument. *Page 107031T of : SPIE conference series*. Society of Photo-Optical Instrumentation Engineers (SPIE) Conference Series, vol. 10703.

Milli, J., Banas, T., Mouillet, D., Mawet, D., Girard, J. H., Vigan, A., Boccaletti, A., Kasper, M., Wahhaj, Zahed, Lagrange, A. M., Beuzit, J. L., Fusco, T., Sauvage, J. F., & Galicher, R. 2016 (July). Speckle lifetime in XAO coronagraphic images : temporal evolution of SPHERE coronagraphic images. *Page 99094Z of : SPIE conference series*. Society of Photo-Optical Instrumentation Engineers (SPIE) Conference Series, vol. 9909.

Mordasini, C., Alibert, Y., & Benz, W. 2009. Extrasolar planet population synthesis. I. Method, formation tracks, and mass-distance distribution. *Astronomy & Astrophysics*, **501**(3), 1139–1160.

Murakami, Naoshi, Nishikawa, Jun, Akaiwa, Natsumi, Komuro, Yusuke, Baba, Naoshi, & Tamura, Motohide. 2016 (Jul). A three-layer eight-octant phase mask towards broadband high-contrast observations. *Page 99126G of : Advances in Optical and Mechanical Technologies for Telescopes and Instrumentation II*. Society of Photo-Optical Instrumentation Engineers (SPIE) Conference Series, vol. 9912.

Patru, F., Baudoz, P., Galicher, R., Boussaha, F., Firminy, J., Cao, Q., Wang, K., Xing, L., Bonafous, M., & Potier, A. 2018 (July). In-lab testing of six-level phase mask coronagraphs onto the high-contrast imaging THD2 bench. *Page 107032L of : Adaptive Optics Systems VI*. Society of Photo-Optical Instrumentation Engineers (SPIE) Conference Series, vol. 10703.

Paul, B., Mugnier, L. M., Sauvage, J. F., Ferrari, M., & Dohlen, K. 2013. High-order myopic coronagraphic phase diversity (COFFEE) for wave-front control in high-contrast imaging systems. *Optics Express*, **21**(26), 31751.

Perrot, C., Boccaletti, A., Pantin, E., Augereau, J.-C., Lagrange, A.-M., Galicher, R., Maire, A.-L., Mazoyer, J., Milli, J., Rousset, G., Gratton, R., Bonnefoy, M., Brandner, W., Buenzli, E., Langlois, M., Lannier, J., Mesa, D., Peretti, S., Salter, G., Sissa, E., Chauvin, G., Desidera, S., Feldt, M., Vigan, A., Di Folco, E., Dutrey, A., Péricaud, J., Baudoz, P., Benisty, M., De Boer, J., Garufi, A., Girard, J. H., Menard, F., Olofsson, J., Quanz, S. P., Mouillet, D., Christiaens, V., Casassus, S., Beuzit, J.-L., Blanchard, P., Carle, M., Fusco, T., Giro, E., Hubin, N., Maurel, D., Moeller-Nilsson, O., Sevin, A., & Weber, L. 2016. Discovery of concentric broken rings at sub-arcsec separations in the HD 141569A gas-rich, debris disk with VLT/SPHERE. *Astronomy & astrophysics*, **590**(May), L7.

Perryman, Michael, Hartman, Joel, Bakos, Gáspár Á., & Lindegren, Lennart. 2014. Astrometric Exoplanet Detection with Gaia. *The Astrophysical Journal*, **797**(1), 14.

Pohl, A., Sissa, E., Langlois, M., Müller, A., Ginski, C., van Holstein, R. G., Vigan, A., Mesa, D., Maire, A.-L., Henning, T., Gratton, R., Olofsson, J., van Boekel, R., Benisty, M., Biller, B., Boccaletti, A., Chauvin, G., Daemgen, S., de Boer, J., Desidera, S., Dominik, C., Garufi, A., Janson, M., Kral, Q., Ménard, F., Pinte, C., Stolker, T., Szulágyi, J., Zurlo, A., Bonnefoy, M., Cheetham, A., Cudel, M., Feldt, M., Kasper, M., Lagrange, A.-M., Perrot, C., & Wildi, F. 2017. New constraints on the disk characteristics and companion candidates around T Chamaeleontis with VLT/SPHERE. *Astronomy & Astrophysics paper*, **605**(Sept.), A34.

Pollack, James B., Hubickyj, Olenka, Bodenheimer, Peter, Lissauer, Jack J., Podolak, Morris, & Greenzweig, Yuval. 1996. Formation of the Giant Planets by Concurrent Accretion of Solids and Gas. *Icarus*, **124**(1), 62–85.

Potier, A., Baudoz, P., Galicher, R., Patru, F., & Thijs, S. 2018 (Aug). Current limitation of the THD2 bench : the scatter issue. *Page 106986G of : Proceedings of the SPIE*. Society of Photo-Optical Instrumentation Engineers (SPIE) Conference Series, vol. 10698.

Potier, A., Baudoz, P., Galicher, R., Singh, G., & Boccaletti, A. 2020a. Comparing focal plane wavefront control techniques : Numerical simulations and laboratory experiments. *Astronomy & Astrophysics*, **635**(Mar.), A192.

Potier, A., Galicher, R., Baudoz, P., Huby, E., Milli, J., Wahhaj, Z., Boccaletti, A., Vigan, A., N'Diaye, M., & Sauvage, J. F. 2020b. Increasing the raw contrast of VLT/SPHERE with the dark hole technique. I. Simulations and validation on the internal source. *Astronomy & Astrophysics*, **638**(June), A117.

Pueyo, Laurent, Kay, Jason, Kasdin, N. Jeremy, Groff, Tyler, McElwain, Michael, Give'on, Amir, & Belikov, Ruslan. 2009. Optimal dark hole generation via two deformable mirrors with stroke minimization. *Applied Optics*, **48**(32), 6296.

Racine, R., Walker, G. A. H., Nadeau, D., Doyon, R., & Marois, C. 1999. Speckle Noise and the Detection of Faint Companions. *Publications of the Astronomical Society of the Pacific*, **111**(May), 587–594.

Ramirez, Ramses M. 2018. A More Comprehensive Habitable Zone for Finding Life on Other Planets. *Geosciences*, **8**(8), 280.

Rousset, Gerard, Lacombe, Francois, Puget, Pascal, Hubin, Norbert N., Gendron, Eric, Fusco, Thierry, Arsenault, Robin, Charton, Julien, Feautrier, Philippe, Gigan, Pierre, Kern, Pierre Y., Lagrange, Anne-Marie, Madec, Pierre-Yves, Mouillet, David, Rabaud, Didier, Rabou, Patrick, Stadler, Eric, & Zins, Gerard. 2003. NAOS, the first AO system of the VLT : on-sky performance. *Pages 140–149 of :* Wizinowich, Peter L., & Bonaccini, Domenico (eds), *Society of Photo-Optical Instrumentation Engineers (SPIE) Conference Series*. Society of Photo-Optical Instrumentation Engineers (SPIE) Conference Series, vol. 4839.

Ruane, G., Riggs, A., Mazoyer, J., Por, E. H., N'Diaye, M., Huby, E., Baudoz, P., Galicher, R., Douglas, E., Knight, J., Carlomagno, B., Fogarty, K., Pueyo, L., Zimmerman, N., Absil, O., Beaulieu, M., Cady, E., Carlotti, A., Doelman, D., Guyon, O., Haffert, S., Jewell, J., Jovanovic, N., Keller, C., Kenworthy, M. A., Kuhn, J., Miller, K., Sirbu, D., Snik, F., Wallace, J. Kent, Wilby, M., & Ygouf, M. 2018 (Aug.). Review of high-contrast imaging systems for current and future ground- and space-based telescopes I : coronagraph design methods and optical performance metrics. *Page 106982S of : SPIE conference series*. Society of Photo-Optical Instrumentation Engineers (SPIE) Conference Series, vol. 10698.

Ruane, G., Patterson, K., Seo, B. J., Mejia Prada, C., Crill, B., & Siegler, N. 2019 (Dec.). The Decadal Survey Testbed : Demonstrating Technology for Imaging Earth-like Exoplanets with Future Space Telescopes. *Pages P51H–3446 of : AGU Fall Meeting Abstracts*, vol. 2019.

Safronov, V. S. 1972. *Evolution of the protoplanetary cloud and formation of the earth and planets.* Keter Publishing House.

Santos, N. C. 2008. Extra-solar planets : Detection methods and results. *New Astronomy Review*, **52**(June), 154–166.

Santos, Nuno C., & Faria, João P. 2018 (Jan). Exoplanetary Science : An Overview. *Page 165 of : Asteroseismology and Exoplanets : Listening to the Stars and Searching for New Worlds*, vol. 49.

Sauvage, Jean-François, Fusco, Thierry, Petit, Cyril, Mugnier, Laurent, Paul, Baptiste, & Costille, Anne. 2012 (July). Focal-plane wave front sensing strategies for high contrast imaging : experimental validations on SPHERE. *Page 844715 of : Adaptive Optics Systems III.* Society of Photo-Optical Instrumentation Engineers (SPIE) Conference Series, vol. 8447.

Schneider, G., Thompson, R. I., Smith, B. A., & Terrile, R. J. 1998 (Aug.). Exploration of the environments of nearby stars with the NICMOS coronagraph : instrumental performance considerations. *Pages 222–233 of :* Bely, P. Y., & Breckinridge, J. B. (eds), *Society of Photo-Optical Instrumentation Engineers (SPIE) Conference Series.* Society of Photo-Optical Instrumentation Engineers (SPIE) Conference Series, vol. 3356.

Schneider, G., Smith, B. A., Becklin, E. E., Koerner, D. W., Meier, R., Hines, D. C., Lowrance, P. J., Terrile, R. J., Thompson, R. I., & Rieke, M. 1999. NICMOS Imaging of the HR 4796A Circumstellar Disk. *The Astrophysical Journal*, **513**(Mar.), L127–L130.

Singh, Garima, Martinache, Frantz, Baudoz, Pierre, Guyon, Olivier, Matsuo, Taro, Jovanovic, Nemanja, & Clergeon, Christophe. 2014. Lyot-based Low Order Wavefront Sensor for Phase-mask Coronagraphs : Principle, Simulations and Laboratory Experiments. *Publications of the Astronomical Society of the Pacific*, **126**(940), 586.

Singh, Garima, Galicher, Raphaël, Baudoz, Pierre, Dupuis, Olivier, Ortiz, Manuel, Potier, Axel, Thijs, Simone, & Huby, Elsa. 2019. Active minimization of non-common path aberrations in long-exposure imaging of exoplanetary systems. *Astronomy & Astrophysics paper*, **631**(Nov), A106.

Sissa, E., Olofsson, J., Vigan, A., Augereau, J. C., D'Orazi, V., Desidera, S., Gratton, R., Langlois, M., Rigliaco, E., Boccaletti, A., Kral, Q., Lazzoni, C., Mesa, D., Messina, S., Sezestre, E., Thébault, P., Zurlo, A., Bhowmik, T., Bonnefoy, M., Chauvin, G., Feldt, M., Hagelberg, J., Lagrange, A. M., Janson, M., Maire, A. L., Ménard, F., Schlieder, J., Schmidt, T., Szulágyi, J., Stadler, E., Maurel, D., Delboulbé, A., Feautrier, P., Ramos, J., & Rigal, F. 2018. New disk discovered with VLT/SPHERE around the M star GSC 07396-00759. *Astronomy & Astrophysics paper*, **613**(May), L6.

Snellen, Ignas A. G., de Kok, Remco J., de Mooij, Ernst J. W., & Albrecht, Simon. 2010. The orbital motion, absolute mass and high-altitude winds of exoplanet HD209458b. *Nature*, **465**(7301), 1049–1051.

Soummer, R., Pueyo, L., & Larkin, J. 2012. Detection and Characterization of Exoplanets and Disks Using Projections on Karhunen-Loève Eigenimages. *The Astrophysical Journal Letter*, **755**(Aug.), L28.

Soummer, Rémi. 2005. Apodized Pupil Lyot Coronagraphs for Arbitrary Telescope Apertures. *The Astrophysical Journal*, **618**(2), L161–L164.

Stolker, T., Dominik, C., Avenhaus, H., Min, M., de Boer, J., Ginski, C., Schmid, H. M., Juhasz, A., Bazzon, A., Waters, L. B. F. M., Garufi, A., Augereau, J. C., Benisty, M., Boccaletti, A., Henning, Th., Langlois, M., Maire, A. L., Ménard, F., Meyer, M. R., Pinte, C., Quanz, S. P., Thalmann, C., Beuzit, J. L., Carbillet, M., Costille, A., Dohlen, K., Feldt, M., Gisler, D., Mouillet, D., Pavlov, A., Perret, D., Petit, C., Pragt, J., Rochat, S., Roelfsema, R., Salasnich, B., Soenke, C., & Wildi, F. 2016. Shadows cast on the transition disk of HD 135344B. Multiwavelength VLT/SPHERE polarimetric differential imaging. *Astronomy & Astrophysics*, **595**(Nov.), A113.

Thatte, N., Abuter, R., Tecza, M., Nielsen, E. L., Clarke, F. J., & Close, L. M. 2007. Very high contrast integral field spectroscopy of AB Doradus C : 9-mag contrast at 0.2arcsec without a coronagraph using spectral deconvolution. *Monthly Notices of the Royal Astronomical Society*, **378**(July), 1229–1236.

Vievard, Sebastien, Bos, Steven, Cassaing, Frederic, Ceau, Alban, Guyon, Olivier, Jovanovic, Nemanja, Keller, Christoph U., Lozi, Julien, Martinache, Frantz, Montmerle-Bonnefois, Aurelie, Mugnier, Laurent, NDiaye, Mamadou, Norris, Barnaby, Sahoo, Ananya, Sauvage, Jean-Francois, Snik, Frans, Wilby, Michael J., & Wong, Alisson. 2019. Overview of focal plane wavefront sensors to correct for the Low Wind Effect on SUBARU/SCExAO. *arXiv e-prints*, Dec., arXiv :1912.10179.

Vigan, A., N'Diaye, M., Dohlen, K., Sauvage, J. F., Milli, J., Zins, G., Petit, C., Wahhaj, Z., Cantalloube, F., Caillat, A., Costille, A., Le Merrer, J., Carlotti, A., Beuzit, J. L., & Mouillet, D. 2019. Calibration of quasi-static aberrations in exoplanet direct-imaging instruments with a Zernike phase-mask sensor. III. On-sky validation in VLT/SPHERE. *Astronomy & Astrophysics*, **629**(Sept.), A11.

Vigan, Arthur. 2019 (July). HiRISE : Bringing high-spectral. *Page 39 of : The Very Large Telescope in 2030.*

von Essen, C., Mallonn, M., Welbanks, L., Madhusudhan, N., Pinhas, A., Bouy, H., & Weis Hansen, P. 2019. An optical transmission spectrum of the ultra-hot Jupiter WASP-33 b. First indication of aluminum oxide in an exoplanet. *Astronomy & Astrophysics*, **622**(Feb), A71.

Winn, J. N. 2010. *Exoplanet Transits and Occultations.* University of Arizona Press. Pages 55–77.

Wolszczan, Alexander. 2015. *Pulsar Planets.* Springer Berlin Heidelberg. Pages 2089–2092.

Wright, Jason T., & Gaudi, B. Scott. 2013. *Exoplanet Detection Methods.* Springer Science+Business Media Dordrecht. Page 489.

Résumé

Depuis 2004, mes travaux de recherche ont tous un lien avec l'imagerie des exoplanètes ou des disques de poussières qui orbitent autour des étoiles du voisinage solaire ($< 100\,\mathrm{pc}$).

J'utilise les instruments travaillant dans le visible et l'infrarouge, comme Sphere/VLT et GPI/Gemini, pour étudier les exoplanètes géantes gazeuses (plusieurs masses joviennes) et jeunes (moins de quelques 100 millions d'années). L'imagerie fournit des mesures astrométriques à partir desquelles on détermine l'orbite exoplanétaire, et des mesures photométriques ou spectrométriques qui nous informent sur la température et la nature de l'atmosphère de l'exoplanète. L'imagerie permet également d'étudier les disques circumstellaires, berceaux de la formation planétaire. Enfin, à partir de grandes campagnes d'observation, on peut déterminer la fréquence des géantes gazeuses dans la partie externe des systèmes exoplanétaires.

En parallèle de ce travail astrophysique, je développe de nouvelles techniques d'observation pour améliorer les instruments actuels d'imagerie ou en proposer de nouveaux pour les futurs télescopes optiques au sol (*extremely large telescope*) ou dans l'espace. L'objectif est d'être capable de détecter des exoplanètes plus légères, plus matures que des géantes gazeuses de quelques 100 millions d'années, par exemple, des jumelles de la Terre. Ces développements instrumentaux vont de la proposition d'un concept à la démonstration sur télescope.

Dans les deux domaines, astrophysique et instrumentation, j'ai la chance de travailler en collaboration avec de nombreux collègues d'autres instituts que le mien et en étroite collaboration avec l'ensemble de l'équipe d'imagerie à haute dynamique du Lesia.

Mots-clés: exoplanètes, disques circumstellaires, imagerie haute dynamique, haute résolution angulaire, coronographie, traitement d'images, analyseur de surface d'onde, optique adaptative

Abstract

Since 2004, my research focuses on imaging exoplanets and circumstellar disks around nearby stars (closer than 100 pc).

I use current visible and infrared imagers like Sphere/VLT or GPI/Gemini to study giant young gaseous planets (several Jupiter masses and $\lesssim 100$ million years). Astrometry help constraining the exoplanet orbits and, photometry and spectrometry provide information on the effective temperature and the nature of the exoplanet atmosphere. Imaging is also essential to study circumstellar disks where exoplanets form. Finally, from large imaging survey, one can determine the occurrence of giant gaseous planets in the exoplanetary systems.

I also develop new techniques for high contrast imaging for upgrading current instruments or creating new ones for the next generation of ground- or space-based telescopes. The objective is the imaging of Earth-like planets that are $10^3 - 10^4$ fainter than the current imaged planets. My instrumental participation goes from theoretical ideas to demonstrations at the telescope.

In both projects, astrophysics and instrumentation, I have the pleasure to collaborate with several colleagues all around the world and to be part of the very united and active high contrast imaging team at Lesia.

Keywords: exoplanets, circumstellar disks, high contrast imaging, high angular resolution, coronagraph, post-processing imaging, wavefront sensor, adaptive optics